Coherent two-dimensional spectroscopy: implementation and applications to lineshape analysis.

Samuel Palato

Department of Chemistry
McGill University
Montréal, Québec, Canada
October 2018

A thesis submitted to McGill University in partial fulfillment of the requirements of the degree of Doctor of Philosophy

À Katherine, qui a gentiment accepté de se joindre à l'aventure.

Abstract

Spectra are usually interpreted in terms of transition energies and intensities. The lineshape is not discussed as often; yet it reveals fluctuations and disorder in the system. Nowhere is this analysis more powerful than in nonlinear spectroscopy, which enables resolution of lineshapes along multiple time-frequency axes. In some cases, the study of multidimensional lineshapes lays bare the origin of dephasing, such as coupling to coherent vibrational excitation. In the more common case, lineshapes and their dynamics provide important clues to the dynamics of materials. The interpretation of lineshapes requires solid theoretical foundations, which are introduced. The spectrometer allowing the observation of lineshape dynamics is then detailed. The bandwidth of the spectrometer is obtained by self-phase modulation in Argon. The response of Ar is instantaneous; this simple temporal response enables efficient modeling. The application of broadband two-dimensional spectroscopy to the analysis of coherent lineshape dynamics in CdSe nanocrystals (NCs) is reported. Two salient observations are made. First, modulations arising from the LO phonon are observed, and confirmed to be vibrational in nature by coherence mapping. Second, no electronic coherence are observed. This runs contrary to the predictions of continuum models of NCs. The lack of electronic coherence can be explained by the occurrence of intrinsic disorder present in a realistic NC. Finally, the general application of lineshape analysis is demonstrated by studying the time-resolved photoluminescence of dual-emitting NCs. The data suggests the existence of two surface states and electron transfer dynamics at the surface of the NCs, on a timescale of >10 ns, longer than previously thought.

Résumé

Les données spectroscopiques sont généralement interprétées en vue d'obtenir l'énergie et l'intensité des transitions. Le profil des raies est rarement discuté, bien qu'il révèle les fluctuations et le désordre du système. L'analyse des profils de raies est d'une efficacité particulière en spectroscopie bidimensionelle (2D), qui résout ce profil selon plusieurs axes temp-fréquence. Dans certains cas, la dynamique de profil met à nu les processus à l'origine du déphasage. C'est le cas du couplage à aux dynamiques vibrationnelles cohérentes. En général, les profils et leur dynamiques fournissent des indices supplémentaires sur les dynamiques électroniques. L'interprétation du profil des raies spectrales requiert une solide fondation théorique, qui ouvre l'ouvrage. S'ensuit la présentation d'un spectromètre 2D optique permettant d'observer de telles dynamiques. L'appareil met à profit l'automodulation de phase dans l'Argon, gaz à réponse instantanée. Le spectromètre 2D à lumière blanche est utilisé afin d'analyser les dynamiques cohérentes des profils de raie de nanocristaux (NC) de CdSe. Cette analyse donne lieu à deux observations. Premièrement, une modulation du profil due au phonon longitudinal optique (LO) est observée. Son origine vibrationnelle est confirmée grâce à la méthode de profilage cohérent. Deuxièmement, aucune cohérence électronique ne peut être observée, en contradiction avec les modèles continus des NC. Cette criante absence est expliquée par le désordre intrinsèque d'un NC réaliste. Finalement, la portée générale de l'analyse des profils de raie est démontrée par l'étude de la photoluminescence résolue en temps (tPL) de NC double-émetteurs. Les données suggèrent l'existence de deux états de surface ainsi que du transfert d'électrons à la surface des NC sur une échelle temporelle plus longue que généralement anticipé.

Acknowledgements

In a thesis as in most things, it is the journey that matters more than the destination. I was blessed to carry out this voyage in such an excellent company.

First thanks go to my supervisor, Pat Kambhampati. I have learned many lessons from him, some I'm not yet aware of, and some he's not. At all points during this thesis, I have been granted full autonomy and responsibility. This was an excellent way to learn, if a bit scary at times. I enjoyed the plentiful discussions on topics scientific, meta-scientific and entirely unscientific.

Next, I want to thank my thesis committee, Brad Siwick and David Ronis, for their support. Their continuing guidance and wise words helped me to steer my research projects in the correct direction at important times. Their enthusiasm for different aspects of my research has been motivating.

I now want to thank Hélène Seiler for all the time spent together during our theses. At times, this was a long and arduous journey, and her continuing support and motivation has proved necessary to march on. We managed to tackle rather difficult projects and challenges together. This was the start of a friendship like few.

The Siwick-Kambhampati office can seem a bit uninviting, with the small windows and dead plants. It is nevertheless an excellent environment to carry out science thanks to the great people sharing this space. In bulk, thanks to M. Krause, J. Saari, J. Mooney, B. Walsh, M. Stern, T. Mack, L. Jethi, T. Kipp, C. Sonnichsen, P. Brosseau, M. Otto, L.R. de Cotret, H. Baker and D. Strandell. I have learned a lot at your contact. I thoroughly enjoyed the many discussions we had, and the food.

Special thanks to Hélène Seiler, Harry Baker and Laurent-René de Cotret who have provided detailed feedback on this thesis.

I also thank Chantal Marotte for her continuous support as well as for many discussions. Her quick and efficient work was the best help one can hope for.

Last but not least, I want to thank Ophélie, Isaac and Katherine, who have *provided* much needed distraction from the obsession of the PhD, at any time of the day or night. I am forever in your debt.

Preface

This thesis describes my contribution to the installation, development and use of two-dimensional electronic spectroscopy and time-resolved photoluminescence spectroscopy in the Kambhampati lab. The first two chapters are required to introduce the concepts and tools used in the rest of the thesis. Chapter 4, presenting the characterization of a broadband white-light source, is adapted from a manuscript currently undergoing peer review: S. Palato, *et al.*, Hollow-core fiber for femtosecond visible spectroscopy, of which I am the first author. Chapter 5 is adapted from an article currently undergoing peer review: S. Palato, H. Seiler, P. Nijjar, O. Prezhdo, P. Kambhampati, Atomic disorder gives rise to dissipation of electronic coherences in semiconductor nanocrystals, of which I am the first author. Chapter 6, reporting on the time-resolved emission from dual emitting CdSe NCs, has been adapted from a published article, Palato, S. *et al.* Electron Dynamics at the Surface of Semiconductor Nanocrystals. *The Journal of Physical Chemistry C* **121,** 26519–26527 (Nov. 2017), of which I am the first author.

Table of Contents

List of tables

List of figures

CHAPTER 1

Introduction: Light-matter interaction

Light is one of the primary media by which humans perceive the external world. Beyond the almost universal experience of vision, a detailed understanding of the processes governing light and its interaction with matter enables powerful measurements, both extensive and detailed of things visible and invisible. Microscopes require an understanding of refraction; lasers, of quantum mechanics. Measurements involving light permeate most areas of knowledge concerned with the physical world. The understanding and control of light relatedly enables modern technologies such as metrology, precision manufacturing and fiber-optics telecommunications. Reflections on the nature of light itself are a source of fundamental interrogation and innovation, as demonstrated by the theories of relativity and the modern field of quantum information.

The potential technological or scientific use of a beam of light depends strongly on the region of the electromagnetic spectrum it occupies. Light visible to the human eye spans the region known as the visible spectrum. It is usually defined as comprising light with wavelength from 400 nm to 700 nm, larger than the largest viruses but smaller than the smallest cells. The corresponding periods are 1.33 fs to 2.33 fs, which is extremely short. The response of matter to light in the visible range thus reveals processes occurring on the timescale of a few femtoseconds. As far as the period of electromagnetic waves are concerned, the human eye can resolve differences of a fraction of a femtosecond. This duration is unfathomably short to our not-so-humble brains — albeit this sensitivity suffers from a few constraints.

In order to reliably obtain femtosecond resolution, pulsed lasers need to be used. Recent advances in the generation, manipulation and measurement of femtosecond pulses provide the humble physical chemist with an extensive set of tools. It is a privilege we shall indulge in. Femtosecond pulsed lasers emit a stroboscopic stream of pulses with individual duration on the order of 10 to 100 fs. Although the average power is typically low (a few W), the peak power of each pulse easily reach the GW regime. The amplification of femtosecond pulses to this power regime was a breakthrough honored by the most recent Nobel prize in physics [1, 2]. The high field strengths enhance nonlinear light-matter interactions. These nonlinear effects form the basis of most of the control and measurement of fs pulses. Nonlinear optical processes allow control over many properties of light, such as frequency, phase and pulse duration. Nonlinear interactions also form the basis of nonlinear spectroscopy such as Transient Absorption (TA) and coherent multidimensional spectroscopy (CMDS). Perhaps surprisingly, the common fluorescence spectrum is rigorously described as a third order process. Depending on the point of view and the experiment carried out, nonlinear light-matter interaction can reveal a lot about matter, or about light.

1.1 Spectroscopy probes the material response.

Spectroscopic experiments probe the response of the materials to electromagnetic radiation. The strongest interactions occur when the frequency of the light field is resonant with an excitation in the material. The information obtained using spectroscopy thus depends on the region of the spectrum used. Visible, as well as near

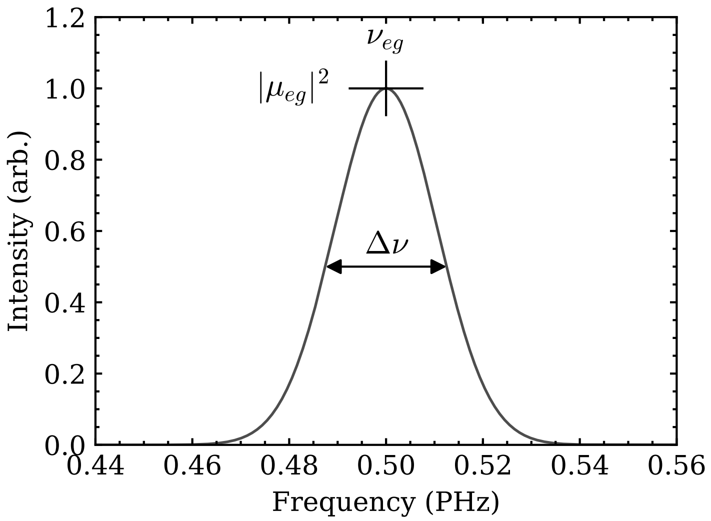

Figure 1.1: Minimal absorption spectrum consisting of a single band. The transition dipole μ_{eg} controls the height of the peak. The position of the peak corresponds to the energy spacing $E_{eg} = h\nu_{eg}$. The lineshape can be very complex, here a simple Gaussian is used. A simple measure of the linewidth such as the FWHM is typically reported.

infrared (IR) and near ultraviolet (UV), probes the dynamics of valence electrons in semiconductors and molecular systems.

The simplest spectroscopic measurement that can be carried out is the usual absorption spectrum. This is a first order experiment, linear in the electric field. An example absorption spectrum for a two-level system is shown in Fig 1.1. Such a peak can roughly be described using three parameters. The transition dipole μ_{eg} controls the intensity of the response. The peak's height thus reveals the magnitude of charge reorganization between the two states. The resonance frequency $\nu_{eg} = \omega_{eg}/2\pi$ dictates the position of the peak. It is related to the energy difference between the two states via the Planck constant $E_e - E_g = E_{eg} = \hbar\omega_{eg} = h\nu_{eg}$. The theoretical description of the absorption spectrum of Fig 1.1 is usually carried out using a form of Fermi's Golden rule [3, 4]:

$$\varepsilon''(\omega) = \frac{\pi\rho}{\varepsilon_0\hbar\omega}\sum_{a,b} P(a)\omega_{ba}\left|\mu_{ba}\right|^2\left[\delta(\omega-\omega_{ba})+\delta(\omega+\omega_{ba})\right] \tag{1.1}$$

$$= \frac{\pi\rho}{\varepsilon_0\hbar\omega}\sum_{a<b}\left[P(a)-P(b)\right]\omega_{ba}\left|\mu_{ba}\right|^2\delta(\omega-\omega_{ba}) \tag{1.2}$$

where $\varepsilon''(\omega)$ is the absorption coefficient, ρ is the density of oscillators, ε_0 is the vacuum permittivity, a and b are eigenstates of the system, $P(a)$ is the probability of the system being in state a, $\omega_{ba} = \left(E_b - E_a\right)/\hbar$, μ_{ab} is the transition dipole moment and $\delta(\omega)$ is the Dirac delta function. The second equality can be derived from the first by realizing $\omega_{ba} = -\omega_{ab}$ and running the sum over a given pair of states only once. This can be achieved by considering the set of eigenstates to be arbitrarily ordered.

Spectroscopy is usually concerned with the position and intensities of the spectroscopic bands; the shape of the bands is less often subject to analysis and interpretation. Indeed, it is approximated as an infinitely sharp peak in eq 1.2. In general, a single resonance can have a complicated shape, called the lineshape. Often, a simple measurement of the peak width is reported, such as the full width at half maximum (FWHM). This width depends on fluctuations of the spectroscopic response, both dynamical and in the ensemble. In the simplest case, fluctuations of the resonance frequency dominates and the width is proportional to the standard deviation $\Delta\nu$. Even a simple linear absorption spectrum thus contains a wealth of information related to charge reorganization, resonance frequencies and their fluctuations. Information contained in the lineshape cannot be interpreted unambiguously however. Processes occurring on multiple timescales can yield similar or even identical signals. For example, relaxation back to the ground state can yield a spectrum identical to fast fluctuations of the resonance frequency.

Time-resolved spectroscopy can be used to gain further insight into the processes initiated by light absorption. A common scheme is the pump-probe experiment, in which two short pulses (pump and probe) interact in succession with the sample. The change induced by the pump beam is monitored using the probe. The experiment is repeated for varying interpulse delays, thus recording the ultrafast dynamics in a manner similar to stop motion. The first famous application of this technique was to settle a dispute regarding the gallop of horses[1]. Using this scheme, the resolution of the experiment is limited by the pulse duration, not by the speed of the detector. It can be applied with any type of pumps and probe pulses, be they optical pulses, electron bursts, etc. The all-optical pump-probe experiment is often refered to as Transient Absorption (TA), which measures changes in the absorption spectrum of the sample. Time-resolved spectra can reveal changes in any of the previously mentioned parameters. Changes in peak heights are typically interpreted as indicative of population dynamics. Changes in peak positions can be due to nuclear reorganization; a time-dependent change in ω_{eg} is often called a dynamical Stokes shift. Lineshape dynamics yield more information about the processes giving rise to line-broadening and can help discriminate between competing explanations.

Pump-probe spectroscopy has been successfully applied to a wide range of materials. The common implementation of pump-p Typically, the technique uses a probe with a broad bandwidth to monitor the absorption spectrum over a wide range. The pump is usually obtained using optical parametric amplification (OPA), which readily generates high power pulses with a single color (a narrow bandwidth). Control over the center frequency, bandwidth and fluence of the pump pulse allows the design

---

[1] Funding criteria have changed.

of experiments to extract detailed information about the dynamics of the sample. The pump pulse is also a source of constraints for the technique: the temporal and spectral properties of the pump are related by the Fourier Transform. In particular, the temporal duration and spectral bandwidth are related by the time-bandwidth product:

$$\Delta t \Delta \nu = a \tag{1.3}$$

where Δt is the FWHM of the pulse temporal intensity, $\Delta \nu$ is the FWHM of the spectral intensity and a is a constant depending on the pulse shape. For a perfect Gaussian pulse, a=0.44. A shorter pulse thus requires a proportionally broader bandwidth. The time-bandwidth product imposes a strong constraint on TA experiments. The measurement of ever shorter events requires ever shorter pulses, and thus of inversely broader spectra. Furthermore, a 10 fs pulse centered at 500 THz (600 nm, 2.07 eV) requires a bandwidth of over 182 meV. A pulse with such a wide spectrum is difficult to maintain, a source of much experimental frustration. Furthermore, materials with congested (and thus interesting) spectra will often exhibit multiple bands of interest in this bandwidth. Broad spectra will thus simultaneously excite multiple transitions. The observed signal will thus be a mix of all these excitations, and the data will be hard to understand. Lineshape variations will be nearly impossible to analyze. Essentially, TA experiments suffer from a trade-off between time resolution and pump energy resolution. This problem is not academic, it is very real in the case of semiconductor NCs, which have smooth, congested spectra, which will be discussed later.

The basic TA experiment described above probes the third order response. The third order response can be characterized by up to three time or frequency axes. In a TA experiment, these can be controlled using the pump center wavelength, pump-probe delay and probe wavelength. This gives rise to the time-bandwidth product limit discussed previously. Alternatively, the measurement can be carried out using an interferometric pulse pair for the pump, carrying out the measurement in the time-time-frequency domain. Two-dimensional electronic spectroscopy (2DE) is such an experiment. Upon Fourier transformation to the frequency-time-frequency domain, this experimental scheme provides resolution along excitation energy without the limits imposed by time-bandwidth product.

Two-dimensional spectroscopy is a form of coherent multidimensional spectroscopy (CMDS) that uses 3 or 4 pulses to measure the third order response. Typically, the results are presented in the frequency-time-frequency domain, a stack of 2D spectra at varying pump-probe delays. The dataset is essentially a 3 dimensional volume, and Fourier transformations allow the conversion of any axis between time and frequency. A single peak thus has lineshapes along all 3 axes, which are not entirely independent. 2D spectroscopy unravels the lineshape contributions in a way that is entirely inaccessible to linear spectroscopy.

The results of 2D spectroscopy are usually expressed in the frequency-time-frequency domain as $S(E_1, t_2, E_3)$. The data can be interpreted as the change in the absorbance, measured at E_3, due to excitation at E_1, with duration t_2 between the two events. E_1 is often referred as the excitation energy, t_2 the waiting time or population time and E_3 the detection or emission energy. There are many related variants of 2D spectra, and even more conventions on how to represent the data. Here, we opt to use E_1 as the horizontal axis, and E_3 as the vertical axis, for a fixed value of t_2. Such a spectrum is represented on Fig 1.2e. The spectrum is dominated by bleach, a reduction in the absorbance. It is indicated in red. This feature is somewhat square,

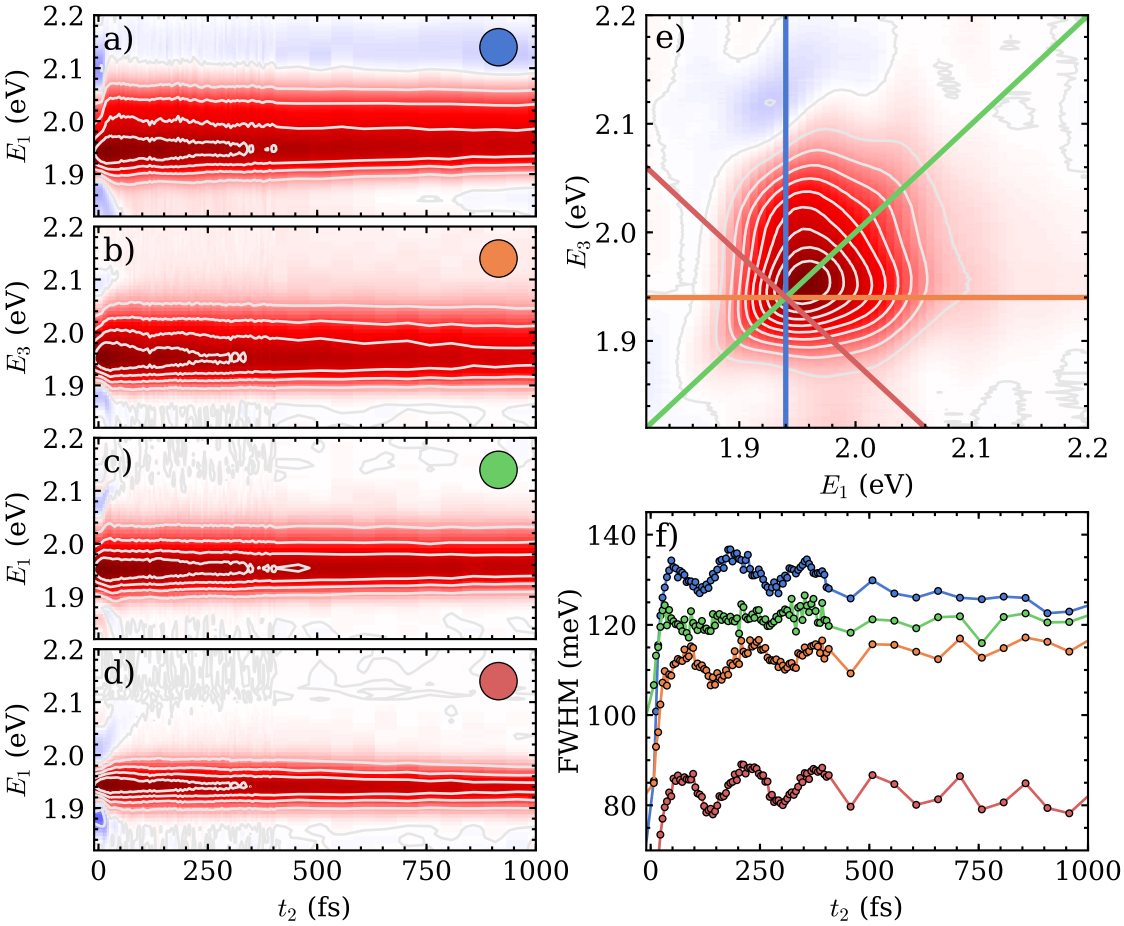

Figure 1.2: The results of a 2D experiment can be viewed along multiple angles. Shown is the real absorptive 2D spectrum of CdSe NCs. (a) Pseudo-TA slice, at fixed $E_1 = 1.94$ eV. This data is analogous to the result of a TA experiment. (b) Pump-resolved absorption spectrum, at fixed $E_3 = 1.94$ eV. (c) Diagonal cut of the 2D spectrum, $E_1 = E_3$. (d) Anti-diagonal cut of a 2D spectrum, $E_3 - 1.94 = 1.94 - E_1$. (e) 2D spectrum at fixed $t_2 = 500$ fs. The horizontal axis is E_1, corresponding to excitation energy. The vertical axis is E_3, corresponding to detection energy. (f) FWHM of the slices in panels (a-d). The modulation due to the LO phonon is visible in 3 cases. The anti-diagonal FWHM is reasonably smaller: 2DE is a hole-burning experiment.

as it arises from the two diagonal and two cross peaks of the X_1 and X_2 transitions, located at 1.94 and 2.01 eV. An induced absorption feature is visible at higher values of E_3 ($\approx$ 2.05 eV), consistent with results from TA.

The spectrum can also be cut in multiple other planes. Fig 1.2a shows the spectrum at a fixed value of $E_1 = 1.94$ eV. This dataset is comparable to the result of a TA experiment, and is sometimes called a pseudo-TA slice. Panel b shows the data for fixed $E_3 = 1.94$ eV. It represents the change of absorbance as a function of excitation energy, a pump-resolved absorption spectrum. This data cannot be obtained any other way. The spectrum can also be cut at angles. As will be introduced later, the diagonal and antidiagonal cuts usually reveal the inhomogeneous and homogeneous broadening, respectively. The diagonal and antidiagonal cuts are shown on Fig 1.2c and d, respectively.

At first sight, it seems not much is happening; semiconductor NCs are essentially little rocks which don't do much. Closer inspection, however, reveals dynamics arising from the coherent LO phonon. For example, the dynamic FWHM of the slices in panels a-d are reported on panel f. The widths are all modulated by the LO phonon, except the diagonal linewidth.

1.2 Lineshape analysis in materials: CdSe Nanocrystals as a model system

A good spectroscopy experiment has no use without an interesting sample to study. As a model sample, this thesis focuses on CdSe colloidal nanocrystals (NC), also known as quantum dots (QD, CQD: colloidal QD). Colloidal NCs have dimensions on the nanometer scale, down to 1 nm radius. The shape of the NC can be adjusted using synthesis parameters, although spheres are a common occurrence. The core material can be surrounded by a shell of a different material. This shell can play a number of roles, such as protecting the excited charges from environmental

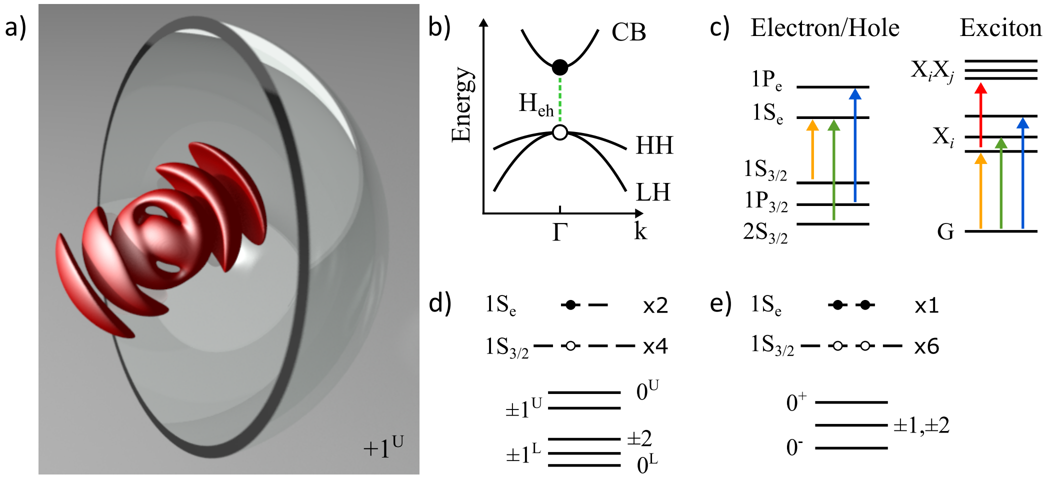

Figure 1.3: Electronic structure of CdSe Nanocrystals a) Excitons as particle in a sphere. The glass shell indicates the boundary of the NCs. The exciton orbital is $+1^U$. b) Bands of bulk CdSe. c) Confinement yields a manifold of hydrogenoid states of the electrons and holes. Electron-hole interactions yield the exciton basis. d) Configurations for the ground state exciton X_1. The eight possible states mix, resulting in a fine structure. e) Configurations for the ground state biexciton.

fluctuations or selectively delocalize electrons or holes. In order to maintain colloidal stability, the surface of the NC is coordinated with organic ligands, often aliphatic amines or thiols. This layer of grease forms an insulating layer that electrons can hardly traverse [5–7].

The electronic structure of nanocrystal is related to that of the bulk semiconductor. It is illustrated on Fig 1.3b. Upon optical excitation, the electron is promoted from the valence to the conduction band. The corresponding vacancy in the valence band is described as a hole, a quasi-particle. In CdSe NC, the vertical transition occurs at the Γ point. The electron can occupy a single state in the conduction band (CB). The valence band contains two bands with different spin states. Different angular momenta of the holes result in bands with different effective masses, called the heavy hole (HH) and light hole (LH). Due to attractive Coulomb interactions, the electron and hole can bind to form an exciton. The exciton can be described similarly to an Hydrogen atom. Its Bohr radius is dependent on material properties, in bulk CdSe it is 5.6 nm [8].

In NCs, the charged particles are trapped by the surrounding insulating medium, enhancing their interaction and thus the occurrence of excitons. For small NCs, the extent of the exciton can exceed that of its host. When the NC radius is smaller or comparable to the bulk Bohr radius of the exciton, confinement effects dominate. This regime is known as *strong confinement*. As a result, the exciton is confined in the nanocrystal in a manner similar to the standard problem of a particle in a box. The electronic structure of nanostructures can thus be obtained by confining the bulk states in a spherical volume. This standard theoretical treatment is called the $k \cdot p$ effective mass approximation (EMA) theory [9]. It is conceptually enlightening and helps in understanding experimental trends, sometimes with good theoretical treatment. This description is outlined here.

Under the influence of confinement, the conduction and valence bands are split into hydrogen-like states, shown on Fig 1.3c. Colored arrows indicate optically active transitions. The system can equivalently be expressed in the exciton basis, with excitons X_i corresponding to specific electron-hole states. The eigenstates of the exciton form a discrete set of states similar to atomic orbitals. The band-edge exciton X_1 is formed of the two-fold degenerate $1\mathrm{S}_\mathrm{e}$ electron state and the four-fold degenerate $1\mathrm{S}_{3/2}$ hole state, as shown on Fig 1.3d. There is thus a total of 8 possible exciton states. Exchange interaction and crystal-field splitting results lifts degeneracy and results in the fine structure indicated on the bottom of panel d.

The formation of another exciton results in the formation of a biexciton $\mathrm{X}_i\mathrm{X}_j$. Biexcitons can have a coarse structure, as indicated Fig 1.3c, which arises from the multiple possible combinations of single excitons. Similarly to single excitons, biexcitons have a fine structure. The fine structure of the X_1^2 biexciton is indicated on Fig 1.3e. In this case, the conduction band is saturated. The fine structure of the biexciton thus arises from the six hole configurations: the two holes must be placed in 4 states. Again, exchange and crystal field effects result in the fine-structure indicated in on the bottom of panel e [10]. Multiexciton states can be formed in a similar way. We note that the saturation of the conduction band states prevents the formation of another X_1 exciton, such that X_1^3 cannot be formed. Interestingly, the X_1 exciton is an 8-fold degenerate state that behaves like a two-fold degenerate state in spectroscopic saturation experiments.

The EMA model treats the nanocrystal as a continuous medium. It entirely neglects the atomistic structure of NCs. Other treatments built the NC from the bottom up, using explicit atomic positions and *ab initio* quantum mechanical tools to compute the properties of a NC. Multiple groups have reported calculations of the electronic structure using specialized pseudopotentials or standard density-functional theory (DFT) [11–14]. These techniques explicitly include atoms, and thus includes details that are ignored by the EMA theory. As a result, the symmetry of the NC breaks and the exciton states of the EMA model mix. The exact electronic structure is sensitive to details of the NC structure, such as facets size and orientation, etc. Using these approaches, one now contemplates much more directly the difficulty of the problem: the observed experimental result depends on an ensemble average over these structural details.

The inclusion of thermal agitation demands the inclusion of dynamical fluctuations of the structure, which renders such atomistic calculations very expansive. When carried out, *ab initio* molecular dynamics naturally include the impact of thermal fluctuations on the electronic properties [15, 16]. This approach will be used in chapter 5. However powerful atomistic calculations may be, their complexities make it hard to extract robust trends. As a consequence, the continuum EMA model forms the standard theoretical model underpinning the work on NC nanocrystals.

Strongly confined NCs exist on a length scale between bulk semiconductor and molecule. This regime bends the rules, giving rise to novel phenomena arising from the same physics. In order to relax, a hot electron can transfer its excess energy to the hole, or to phonons which will be discussed later. The first case is known as Auger relaxation. Due to confinement, the increased electron-hole interaction opens up Auger relaxation pathways not normally present in bulk semiconductors. Transferring the excess energy to the hole circumvents the phonon bottleneck for electrons [14, 17–19]. Accelerated Auger relaxation pathways prove experimentally challenging to study using transient absorption: studying fast dynamics require short pump pulses. As previously discussed, short pulses imply broad bandwidth. The broad bandwidth of the pump pulse precludes the control over the initial population, which in turns prevent the careful study of Auger pathways. 2DE circumvents this time-bandwidth problem, and thus should reveal more clearly such Auger pathways[1].

Semiconductor NCs are excellent systems in which to study many-body effects. A NC can host multiple excitons, which can bind to form biexcitons due to stabilizing Coulomb and exchange interactions [10, 20–23]. The energetics and dynamics of biexcitons in NCs are relatively hard to investigate due to their small binding energy, typically estimated at around 10 meV in CdSe. Biexcitons can be studied by spectroscopy, both in absorption and emission. Their spectral signatures are small peak shifts and subtle lineshape changes due to a biexciton sideband, shifted by

---

[1] For relaxation pathways, you have to see in Hélène's thesis and articles.

the binding energy. Similarly to single excitons, biexcitons are expected to exhibit a spectrum of states, with both a coarse and a fine structure. The fast relaxation of biexcitons, which can undergo both electron-hole recombination to the exciton or exciton-exciton annihilation to the ground state, further complicates their investigation. The study of biexciton structure and dynamics by 2DE should be advantageous compared to TA[1], especially at low temperatures.

The surface of semiconductor NCs can be used to adjust their interaction with light. In particular, major efforts were undertaken to optimize the quantum yield and linewidth of NCs for light emission [7, 24, 25]. Modifications to the coordinating ligands affect coupling to the environment, notably by creating trap states lying in the band-gap of the NC. Electrons and holes in the NC can then relax to these states which impacts the performance of NCs for applications. This impact can be negative, as in the case of light emission for displays, or positive as in the case of catalysis or white-light emission. In all cases, the ligands act as the primary interface between the environment and the NC, which can potentially open up new dynamics for charges in these materials [26].

Nuclear motions in semiconductor NCs are rather simple when compared to their rich electron dynamics. Nuclear excitations are well described by the phonons of the bulk semiconductor. The prevalent phonon branches in CdSe are the longitudinal optical (LO, $\sim$200 cm^{-1}) and longitudinal acoustic (LA, $\sim$20 cm^{-1}) phonons. Other phonon modes exist in NCs. The occurrence of surface optical (SO) and transverse optical (TO) modes is a topic of current investigations [27]. Spheroid modes are sometimes discussed [28]. Contrary to electronic excitations, phonons in NCs are

---

[1] Altough, again, you'll have to read Hélène's thesis

weakly affected by size and other synthesis parameters. The confinement of the LO phonon can be observed for very small NCs, but the associated frequency shift is rather minor, ranging from 209 cm^{-1} for NCs with diameter > 6 nm to 196 cm^{-1} in pyramidal clusters with an edge length of 1.7 mn [29–31]. The robustness of the sparse phonon manifold contrasts with their rich and sensitive exciton dynamics. Electronic excitations and vibrational modes interact: excitons are subject to phonon dynamics via exciton-phonon coupling. CdSe is a polar lattice, and the coupling to the LO phonon is mostly mediated by the Fröhlich interaction. The dominant coupling mechanism to the acoustic phonons is by piezoelectric coupling [8].

As a result of exciton-phonon coupling, electronic excitation of the NCs are concurrent with phonon excitations. The phonon dynamics then modulate the electronic properties of the NCs. This results in both coherent and incoherent dynamics. According to the Frank-Condon principle, an electronic transition occurs on a timescale that is much too short for the nuclei. The electronic excitation thus acts as an impulsive excitation of the normal vibrational coordinates, where the equilibrium position has been abruptly changed. The phonon modes can be modeled as classical damped harmonic oscillators. In the case of weak damping, the impulsive excitation will yield long-lived oscillations of the vibrational coordinate. In the linear spectrum, this phenomenon gives rise to the familiar Frank-Condon progressions. In time-resolved spectroscopy, this vibrational oscillation will modulate the electronic transition frequency, yielding coherent lineshape dynamics analogous to frequency modulation. In the case of overdamped vibrational coordinates, the absorption will reveal a dynamical Stokes shift due to lattice reorganization. Coherent signatures of both the LO and LA modes have been observed in the spectroscopic signatures of CdSe NCs [28, 32–35].

The investigation of electron-phonon coupling by TA is not always straightforward. Clear time-resolved signatures are obtained for underdamped vibrational modes, with period $T_{\mathrm{vib}} = E_{\mathrm{vib}}/h$. The vibrational period sets an upper limit to the pulse duration. The associated spectrum must have a bandwidth of E_{vib}. However, the absorption spectrum consists of a Frank-Condon progression with spacing E_{vib}. The time-bandwidth trade-off of TA is again an obstacle. As will be made clear in chapter 5, this can give rise to partial cancellation of the vibrational signatures in TA. The cancellation can be complete for low energy modes. Furthermore, the vibrational sidebands can be obscured by other line-broadening mechanisms, such as inhomogeneous size distribution, making them hard to study. One has to blindly aim the pump spectrum into the sample absorption spectrum with the hope of hitting a vibrational side band. CMDS circumvent both difficulties by providing resolution within the pump bandwidth, thus yielding an unprecedented view into electron-phonon coupling. This aspect will be the main topic of chapter 5, central to this thesis.

1.3 Contents

CMDS spectroscopy is supported by a detailed theoretical framework. It is necessary to present this material first. The discussion will be rather detailed. Theory is presented in chapter 2. The description applies to coherent spectroscopies of any order, but special attention is paid to the linear and third order responses, and to the modeling of lineshapes. The experimental implementation of our 2D spectroscopy apparatus is described in chapter 3, along with a general description of the femtosecond pulse and a presentation of pulse measurement techniques. The development of the white light source, which exploits the instantaneous nonlinear response of Argon up to 11th order, is presented in chapter 4. The following chapters present experimental results obtained on a model system of CdSe colloidal nanocrystals (NCs). Coherent lineshape dynamics due to phonons and exciton superposition of states are investigated in chapter 5. Finally, the broad applicability of lineshape dynamics is further demonstrated by studying the time-resolved emission spectrum of ultrasmall CdSe NCs using a streak camera in chapter 6. Concluding remarks and directions for future work are presented in chapter 7.

References

1. Strickland, D. & Mourou, G. Compression of Ampified Chirped Optical Pulses. *Optics Communications* **55,** 447–449 (1985).
2. Strickland, D. & Mourou, G. *Nobel Prize in Physics 2018* 2018. `https://www.nobelprize.org/prizes/physics/2018/summary/`.
3. McHale, J. *Molecular Spectroscopy* (Prentice Hall, Upper Saddle River, 1999).
4. Mukamel, S. *Principles of nonlinear optical spectroscopy* xviii, 543 p. (1995).
5. Boles, M. A., Ling, D., Hyeon, T. & Talapin, D. V. The surface science of nanocrystals. *Nat Mater* **15,** 141–153 (Feb. 2016).
6. Kovalenko, M. V. *et al.* Prospects of Nanoscience with Nanocrystals. *ACS Nano* **9,** 1012–1057 (Feb. 2015).
7. Kagan, C. R., Lifshitz, E., Sargent, E. H. & Talapin, D. V. Building devices from colloidal quantum dots. *Science* **353,** aac5523–aac5523 (Aug. 2016).
8. Vasilevskiy, M. I. in *Semiconductor Nanocrystal Quantum Dots: Synthesis, Assembly, Spectroscopy and Applications* 217–256 (2008).
9. Sercel, P. C. & Efros, A. L. Band-Edge Exciton in CdSe and Other II–VI and III–V Compound Semiconductor Nanocrystals - Revisited. *Nano Letters* **18,** 4061–4068 (July 2018).
10. Rodina, A. V. & Efros, A. L. Band-edge biexciton in nanocrystals of semiconductors with a degenerate valence band. *Physical Review B - Condensed Matter and Materials Physics* **82,** 1–14 (2010).
11. Zunger, A. On the Farsightedness (hyperopia) of the Standard k . p Model. *physica status solidi (a)* **190,** 467–475 (Apr. 2002).
12. Zunger, A. Pseudopotential theory of semiconductor quantum dots. *Physica Status Solidi (B) Basic Research* **224,** 727–734 (2001).

13. Prezhdo, O. V. Photoinduced Dynamics in Semiconductor Quantum Dots: Insights from Time-Domain ab Initio Studies. *Accounts of Chemical Research* **42,** 2005–2016 (2009).
14. Prezhdo, O. V. Multiple excitons and the electron–phonon bottleneck in semiconductor quantum dots: An ab initio perspective. *Chemical Physics Letters* **460,** 1–9 (July 2008).
15. Dong, S. *et al.* Observation of an Excitonic Quantum Coherence in CdSe Nanocrystals. *Nano Letters* **15,** 6875–6882 (Oct. 2015).
16. Pal, S., Nijjar, P., Frauenheim, T. & Prezhdo, O. V. Atomistic Analysis of Room Temperature Quantum Coherence in Two-Dimensional CdSe Nanostructures. *Nano Letters* **17,** 2389–2396 (Apr. 2017).
17. Cooney, R., Sewall, S., Anderson, K., Dias, E. & Kambhampati, P. Breaking the Phonon Bottleneck for Holes in Semiconductor Quantum Dots. *Physical Review Letters* **98,** 177403 (Apr. 2007).
18. Kilina, S. V., Kilin, D. S. & Prezhdo, O. V. Breaking the Phonon Bottleneck in PbSe and CdSe Quantum Dots: Time-Domain Density Functional Theory of Charge Carrier Relaxation. *ACS Nano* **3,** 93–99 (Jan. 2009).
19. Rainò, G. *et al.* Exciton Dynamics within the Band-Edge Manifold States: The Onset of an Acoustic Phonon Bottleneck. *Nano Letters* **12,** 5224–5229 (Oct. 2012).
20. Sewall, S. L., Franceschetti, A., Cooney, R. R., Zunger, A. & Kambhampati, P. Direct observation of the structure of band-edge biexcitons in colloidal semiconductor CdSe quantum dots. *Physical Review B - Condensed Matter and Materials Physics* **80,** 1–4 (2009).

21. Achermann, M., Hollingsworth, J. A. & Klimov, V. I. Multiexcitons confined within a subexcitonic volume: Spectroscopic and dynamical signatures of neutral and charged biexcitons in ultrasmall semiconductor nanocrystals. *Physical Review B - Condensed Matter and Materials Physics* **68,** 1–5 (2003).
22. Shumway, J., Franceschetti, A. & Zunger, A. Correlation versus mean-field contributions to excitons, multiexcitons, and charging energies in semiconductor quantum dots. *Physical Review B - Condensed Matter and Materials Physics* **63,** 1–13 (Mar. 2001).
23. Korkusinski, M., Voznyy, O. & Hawrylak, P. Fine structure and size dependence of exciton and biexciton optical spectra in CdSe nanocrystals. *Physical Review B* **82,** 245304 (Dec. 2010).
24. Kambhampati, P., Mack, T. & Jethi, L. Understanding and Exploiting the Interface of Semiconductor Nanocrystals for Light Emissive Applications. *ACS Photonics* **4,** 412–423 (Mar. 2017).
25. Bowers, M. J., McBride, J. R. & Rosenthal, S. J. White-Light Emission from Magic-Sized Cadmium Selenide Nanocrystals. *Journal of the American Chemical Society* **127,** 15378–15379 (Nov. 2005).
26. Tyagi, P. *et al.* Controlling piezoelectric response in semiconductor quantum dots via impulsive charge localization. *Nano letters* **10,** 3062–7 (Aug. 2010).
27. Lin, C., Kelley, D. F., Rico, M. & Kelley, A. M. The "surface optical" phonon in CdSe nanocrystals. *ACS Nano* **8,** 3928–3938 (2014).
28. Chilla, G. *et al.* Direct observation of confined acoustic phonons in the photoluminescence spectra of a single CdSe-CdS-ZnS core-shell-shell nanocrystal. *Physical Review Letters* **100,** 1–4 (2008).

29. Hwang, Y. N., Park, S. H. & Kim, D. Size-dependent surface phonon mode of CdSe quantum dots. *Physical Review B - Condensed Matter and Materials Physics* **59,** 7285–7288 (1999).
30. Krauss, T. D. & Wise, F. W. Raman-scattering study of exciton-phonon coupling in PbS nanocrystals. *Physical Review B* **55,** 9860–9865 (1997).
31. Beecher, A. N., Dziatko, R. A., Steigerwald, M. L., Owen, J. S. & Crowther, A. C. Transition from Molecular Vibrations to Phonons in Atomically Precise Cadmium Selenide Quantum Dots. *Journal of the American Chemical Society* **138,** 16754–16763 (2016).
32. Sagar, D. M. *et al.* Size dependent, state-resolved studies of exciton-phonon couplings in strongly confined semiconductor quantum dots. *Physical Review B - Condensed Matter and Materials Physics* **77,** 235321 (June 2008).
33. Sagar, D. M., Cooney, R. R., Sewall, S. L. & Kambhampati, P. State-resolved exciton-phonon couplings in CdSe semiconductor quantum dots. *Journal of Physical Chemistry C* **112,** 9124–9127 (June 2008).
34. Gellen, T. A., Lem, J. & Turner, D. B. Probing Homogeneous Line Broadening in CdSe Nanocrystals Using Multidimensional Electronic Spectroscopy. *Nano Letters* **17,** 2809–2815 (May 2017).
35. Kelley, A. M. Electron-phonon coupling in CdSe nanocrystals. *Journal of Physical Chemistry Letters* **1,** 1296–1300 (2010).

CHAPTER 2

Classical light and quantum matter

Theoretical descriptions of the spectroscopic experiment abound. Indeed, each scientific community has a favorite description, tailored to explain its conventional experiments and observables of interest [1]. This chapter introduces the description most commonly used for nonlinear spectroscopy of molecules and materials. The material response is usually obtained using a quantum mechanical or semiclassical treatment. The presentation mostly follows the books of Hamm and Zanni [2], Mukamel [3] and Cho [4]. An attempt is made at making the presentation comprehensive and self-contained as this thesis is part of the initial generation of students working on 2DE in the Kambhampati group.

The description is anchored in response theory, making it rather convenient and general. The description of the quantum dynamics of matter are done both in Hilbert space and in Liouville space, as both are used in the thesis. The concepts are illustrated by their application to the description of spectroscopy experiments. The simpler case of linear absorption is covered first in order to introduce advanced tools such as Double-sided Feynman Diagrams. The case of 2D spectroscopy is then covered.

2.1 Response theory

Response theory is a well established element of statistical mechanics. It finds applications in a wide range of fields, from hydrodynamics to electronic circuits and, of course, spectroscopy [5, 6]. Response theory is concerned with the change in a macroscopic observable due to the application of an external perturbation. The standard description is limited to the linear response, where the perturbation is taken to be very small such that the response is approximately linear. This is essentially an expansion truncated at the linear term. We cannot afford this luxury and will need to keep a few more terms in this expansion: up to the 5th order will be discussed in this thesis. The general form of this expansion can be written as the Volterra series:

$$\begin{aligned}\Delta A(t) = &\int \mathrm{d}\tau_1 f(t-\tau_1)\chi^{(1)}(\tau_1) + \int \mathrm{d}\tau_1 \int \mathrm{d}\tau_2\, f(t-\tau_1) f(t-\tau_2)\chi^{(2)}(\tau_1,\tau_2) \\ &+ \int \mathrm{d}\tau_1 \int \mathrm{d}\tau_2 \int \mathrm{d}\tau_3\, f(t-\tau_1) f(t-\tau_2) f(t-\tau_3)\chi^{(3)}(\tau_1,\tau_2,\tau_3) + \mathcal{O}(f^4), \quad (2.1)\end{aligned}$$

where ΔA is the change in an observable A, f is an external perturbation and $\chi^{(n)}$ is the n^{th} order susceptibility or response. The specific form depends upon whether the process is described in the time or frequency domain. The n^{th} order response can take up to n time or frequency arguments. Higher order terms can be expanded into multiple contributions.

Series expansions such as eq 2.1 can be intellectually unsatisfying. It separates the components of the response by order, yet they are not independent. It implies the response to a perturbation of arbitrary magnitude is simply a matter of keeping terms until convergence, which is obviously a limited approach. For example, the numerical procedure in chapter 4 uses the nonlinear response up to 11th order in an attempt to converge the behavior of Argon in a strong electromagnetic field [7, 8]. Other, more complete approaches, do not need to rely on an expansion [9, 10].

Series expansions enable beancounting of expansion coefficients: quantitatively useful but conceptually sterile[1]. It may be tempting to use a non-approximate treatment, such as direct integration of the time-dependent Schrödinger equation. Indeed, some problems can be solved that way [11].

Expansions such as the above nevertheless have some very useful characteristics. In the case of light-matter interaction, these advantages clearly outweigh its shortcomings. First, eq 2.1 neatly separates the applied perturbation f from the response $\chi^{(n)}$ such that they can be treated independently. The response to a dynamical perturbation above holds for arbitrary perturbation $f(t)$; the total response can be derived from the impulse response, the response to $f(t) = \delta(t)$. This is to be contrasted with a full calculation using the time-independent Schrödinger equation for a molecule subject to an electromagnetic wave, which has to be redone every time properties of the EM wave are changed significantly.

In the case of nonlinear light-matter interactions, different terms in expansion 2.1 can be associated with different experiments. The higher order terms can also be expanded into multiple contributions which can be isolated experimentally, as will be outlined in the next chapter. Each of these contributions can thus be studied, interpreted or modeled independently using a representation that is the most convenient: time vs frequency domain; classical vs quantum mechanics (or in between); Hilbert vs Liouville space; Schrödinger, Heisenberg or interaction picture.

The ability to selectively measure and interpret different terms in eq 2.1 underpins both nonlinear optics and nonlinear spectroscopy. In the case of nonlinear optics, materials with relatively simple responses $\chi^{(n)}$ are used in order to focus on

---

[1] Polymer physics can be a good example of this.

the manipulation or measurement of the EM wave. Examples of this limit include pulse measurement by nonlinear optics (sections 3.3.1 and 3.3.2) and white-light generation by self-phase modulation in a noble gas (chapter 4). In the case of spectroscopy, the light field should be known in order to accurately measure the nonlinear responses $\chi^{(n)}$.

The expansion presented in eq 2.1 is now studied in the specific case of nonlinear spectroscopy. The interaction of light with polarizable media induces a time-varying polarization in the sample. For nonlinear spectroscopy, the polarization is expanded into a linear and nonlinear parts:

$$P(t) = P^{(1)}(t) + P^{(2)}(t) + P^{(3)}(t) + \dots \ , \tag{2.2}$$

where $P(t)$ is the polarization in the medium, $P^{(1)}(t)$ is the linear polarization and the rest forms the nonlinear polarization. This equations corresponds to eq 2.1. As per Maxwell's equations, the time varying polarization emits an electric field E_{sig}:

$$E_{\text{sig}}(t) = \mathrm{i}P(t), \tag{2.3}$$

which is the experimental observable. The polarization is given by the expectation value of the dipole operator:

$$P(t) \propto \langle \hat{\mu} \rangle = \langle \psi(t) \,|\, \hat{\mu} \,|\, \psi(t) \rangle \tag{2.4}$$

where a statistical average will have to be included.

Each of the terms in eq 2.2 can be expressed rather inelegantly[1] in the time domain [3]:

$$P^{(n)}(t) = \int_0^\infty \mathrm{d}t_n \int_0^\infty \mathrm{d}t_{n-1} \cdots \int_0^\infty \mathrm{d}t_1 \chi^{(n)}(t_n, t_{n-1}, \ldots, t_1)$$

$$\mathcal{E}(t - t_n)\mathcal{E}(t - t_n - t_{n-1}) \ldots \mathcal{E}(t - t_n - t_{n-1} - \cdots - t_1), \qquad (2.5)$$

where $\mathcal{E}(t)$ is the incident real electric field. It is usually convenient to use a complex electric field in the time domain: $2\mathcal{E}(t) = \Re E(t)$. For an experiment with m pulses, we have:

$$\mathcal{E}(t) = \sum_i^m \mathcal{E}_i(t) = \frac{1}{2} \sum_i^m \left[E_i(t) + E_i^\star(t)\right]. \qquad (2.6)$$

Inserting eq 2.6 in eq 2.5 results in a large number of terms. Furthermore, the material response $\chi^{(n)}$ can be expanded in 2^n terms $\chi_j^{(n)}$, as will be demonstrated in the next section. This situation seems hopeless. Luckily, each term of these $\chi_j^{(n)}$ corresponds to one term (or a few equivalent terms) in the electric field expansion. All other combinations can be neglected when carrying out the integral. This will be demonstrated later for the case of linear spectroscopy; nonlinear spectroscopy follows the same rules. Equation 2.5 is thus tractable when fully expanded.

The ensemble response of dilute NCs is isotropic, such that the the wavevector dependence can be factored out [3]. Polarization will similarly be disregarded. This is entirely justified for the linear response of an isotropic medium and for single pulse experiments, but not so much for multiple pulses experiments such as 2D spectroscopy. The response of an isotropic medium cannot depend on the absolute polarizations of the pulses, but their relative angles can be used to isolate specific

---

[1] If we were in mathematics, we would have to create a notation just for it. Series expansions can be inelegant.

contributions[2, 7, 8, 12, 13]. Nevertheless, polarization shall be ignored and left for future work.

2.2 Material response

2.2.1 The wavefunction

At the microscopic level, the behavior of molecules and materials is governed by quantum mechanics. The starting point of the derivation is thus the time-dependent Schrödinger equation (TDSE). The behavior of a microscopic quantum system affected by an electric field is indeed a case where this equation should apply. Spectroscopy of materials does not involve relativity; the TDSE acts as our equation of everything. However, the sample under study is extended and complicated. It consists of a number of particles close to Avogadro's number. Solving the TDSE for such a system is impossible and a number of physical approximations have to be made. The derivation of the nonlinear response from the TDSE aims to be rigorous enough to clearly introduce the needed physical approximations and corresponding intuition.

Dynamics of quantum systems are given by the time-dependent Schrödinger equation:

$$\frac{\partial}{\partial t}\left|\psi(t)\right\rangle = -\frac{\mathrm{i}}{\hbar}\hat{H}(t)\left|\psi(t)\right\rangle, \tag{2.7}$$

where $|\psi(t)\rangle$ is the wavefunction containing all the information about the system's state and $\hat{H}(t)$ is the system's Hamiltonian. The wavefunction is described as a linear combination of basis states:

$$\left|\psi\right\rangle = \sum_i c_i \left|i\right\rangle \tag{2.8}$$

where $|\psi\rangle$ is the total wavefunction, c_i is a complex coefficient and $|i\rangle$ is a basis function. The basis can be selected according to the task at hand. It is most convenient when the set $\{|i\rangle\}$ forms an orthonormal complete basis. In this case,

$$\langle i|j\rangle = \delta_{ij} \tag{2.9}$$

$$\langle i|\psi\rangle = c_i \tag{2.10}$$

$$\langle\psi|\psi\rangle = \sum_i |c_i|^2 = 1, \tag{2.11}$$

where the last equation is a consequence of the normalization of the wavefunction. The space spanned by $\{|i\rangle\}$ is called the Hilbert space. It is said to be complete when:

$$\sum_i |i\rangle\langle i| = \hat{I}. \tag{2.12}$$

where $\hat{I}$ is the identity operator.

Recall the value of an observable A is given by the expectation value of the corresponding operator $\langle\hat{A}\rangle$.

$$\begin{aligned}\langle\hat{A}\rangle &= \langle\psi|\hat{A}|\psi\rangle & (2.13)\\ &= \sum_{i,j} c_i^\star c_j \langle i|\hat{A}|j\rangle & (2.14)\\ &= \sum_{i,j} c_i^\star c_j A_{ij} & (2.15)\end{aligned}$$

where $\langle\hat{A}\rangle$ is the observable value of A. The value A_{ij} is a matrix element. In this thesis, operators will be designated with a pointy hat; scalar and Hilbert space vectors will be undecorated. In spectroscopy, the observable of interest is the polarization, corresponding to the operator $\hat{\mu}$.

The TDSE as written in eq 2.7 uses both a time-dependent wavefunction $|\psi(t)\rangle$ and Hamiltonian $\hat{H}(t)$. This is not necessary: the temporal evolution can be contained entirely in the wavefunction, yielding the Schrödinger picture, or in the operators, yielding the Heisenberg picture. When the time-dependence has some component in both, this is called the interaction picture. This choice is arbitrary, one can freely transform from one to the other as this amounts to a change of frame of reference. It is common to think about the time evolution of a dynamical property as arising from the evolution of the system, and the Schrödinger picture is often preferred.

The common Schrödinger picture poses problems when discussing spectroscopic results. It forces the Hamiltonian to be time-independent, thus feeding the entirety of the time evolution in the coefficients. For a continuous monochromatic wave, this naturally yields a basis of dressed states made of material wavefunctions in a field[1]. We want to interpret spectroscopic results in terms of the material Hamiltonian and its spectrum, the time-dependent electric field is merely a tool in our hands.

It is thus desirable to separate the Hamiltonian in a time-independent material part and a time-varying part due to light-matter interaction:

$$\hat{H}(t) = \hat{H}_0 + \hat{H}_E(t) \tag{2.16}$$

$$\hat{H}_E(t) = -\hat{\mu}E(t) \tag{2.17}$$

where $\hat{H}(t)$ is the full Hamiltonian, $\hat{H}_0$ is the Hamitonian of matter in the absence of a field and $\hat{H}_E(t)$ arises from light-matter interaction. This separation naturally leads to the interaction picture. In the interaction picture, both operators and states have a time-evolution. However, the separation of the Hamiltonian is based on a physical distinction, and the results will similarly lend themselves to physical intuition.

The preceding considerations naturally lead to the basis formed of the eigenstates of matter in the absence of an electric field. This choice is useful both conceptually and in derivations: $\hat{H}(t)$ induces transitions between the natural states of the

---

[1] They're called polaritons.

system. The eigenstates obey the time-independent Schrödinger equation:

$$\hat{H}_0 \left| i \right\rangle = E_i \left| i \right\rangle , \tag{2.18}$$

where $\hat{H}_0$ is the field-free Hamiltonian defined in eq 2.16 above and E_i is the energy[1] of state i. The set of eigenstates forms a physically complete basis for our spectroscopy problems.

At the fundamental level, this mathematical toolkit is all that is required. In practice, however, the TDSE cannot be integrated for a macroscopic system of N particles and the associated $6N$ degrees of freedom [14]. The first approximation to be made is that the response of the microscopic system can be obtained from the behavior of a localized microscopic system. In the case of the spectroscopy of dilute chromophores, this approximation is rather solid, and the macroscopic behavior can be described from the behavior of the microscopic system (eg: a single chromophore) and statistical mechanics. That is, we can derive the macroscopic response from the averaged microscopic response:

$$\chi^{(n)}_{\text{macro}} \propto N \left\langle \chi^{(n)}_{\text{micro}} \right\rangle , \tag{2.19}$$

where the angle brackets $\langle \ldots \rangle$ denote an ensemble average. The absolute value matters very little in the current work, we will be interested entirely on relative intensities. We will not distinguish between the macroscopic and microscopic susceptibilities, though the average will always be necessary.

---

[1] We will use similar symbols for both the electric field and the energy. Sorry.

2.2.2 The density matrix

The current description operates in Hilbert space and applies to pure states. In order to take the ensemble average and describe mixed states, it is necessary to carry out the derivation in Hilbert space first, then take the average. This is feasible for simple systems, but can become tedious when the variations are not trivial. It is beneficial to introduce an alternative representation which can include the effect of an ensemble average directly. This description is based on the density matrix. The density matrix is defined from matrix elements of the density operator:

$$\hat{\rho} = \sum_k P_k \left|\psi_k\right\rangle \left\langle\psi_k\right| , \tag{2.20}$$

where the index k represents a microscopic state as understood in statistical mechanics and P_k is the ensemble probability of state k, a real positive number such that $\sum_k P_k = 1$.

The elements of the density matrix are given by:

$$\begin{aligned} \rho_{ij} &= \sum_k P_k \left\langle i|\psi_k\right\rangle \left\langle\psi_k|j\right\rangle & (2.21) \\ &= \left\langle c_i c_j^\star \right\rangle . & (2.22) \end{aligned}$$

We can distinguish between the diagonal and off diagonal elements:

$$\begin{aligned} \rho_{ii} &= \left\langle c_i c_i^\star \right\rangle = \left\langle |c_i|^2 \right\rangle , & (2.23) \\ \rho_{ij} &= \left\langle c_i c_j^\star \right\rangle = \left\langle |c_i| \, |c_j| \exp\left(\mathrm{i}\Delta\phi_{ij}\right)\right\rangle \quad \forall \; i \neq j, & (2.24) \end{aligned}$$

where $\Delta\phi_{ij} = \phi_i - \phi_j$ is the difference in the phases of the coefficients.

The diagonal terms, presented in eq 2.23, are known as populations. They are all positive real numbers such that $\rho_{ii} \leq 1$, which results from the orthonormality of the basis set $\{|i\rangle\}$ and the normalization of the probabilities P_k. Indeed, $\sum_i \rho_{ii} = 1$.

The populations have a simple physical description. They represent the probability of finding a system in the ensemble in basis state i. This quantity is very important in the understanding of spectroscopy data as it is directly proportional to the populations found in eq 1.2.

The off-diagonal elements, equation 2.24, are known as coherences. They are complex numbers such that $|\rho_{ij}| \leq 1$. Their intuitive description is not as straightforward as for the population, even if populations have no classical analogue. The coherences represent the synchronization of the different basis coefficient in the ensemble. A coherent ensemble requires that all individual oscillators are synchronized, such that $\Delta\phi_{ij}$ has a narrow distribution.

An attempt at undersanding the concept of coherences can be made in analogy with classical oscillators. An ensemble of identical pendulums[1], all launched in an identical fashion will stay synchronized forever. They collectively exhibit a large degree of coherence. If you can measure the angle of a single pendulum, you know the angle of all the others with a reasonable accuracy. If instead the pendulums have slight differences of string length, they will slowly but certainly drift out of synchronization. After a long enough delay, they will have entirely different angles. Similarly, if the first set of perfect pendulums is launched in perfect unison, but in a room with some wind, they will end up being desynchronized. For a perhaps more remote analogy, imagine the same musical score played by either a symphony orchestra or an elementary school class. Although they produce the same notes, the results are rather different; one shows a much better degree of coherence.

---

[1] Pendula? — This is proves more contentious than I expected.

The density operator and its friends will form the basis for much of the discussion of the dynamics of matter during spectroscopy experiments. The temporal evolution of the density matrix is given by the Liouville-von Neumann equation:

$$\dot{\hat{\rho}} = \frac{\partial}{\partial t}\hat{\rho} = -\frac{\mathrm{i}}{\hbar}\left[\hat{H}, \hat{\rho}\right] \tag{2.25}$$

$$= -\frac{\mathrm{i}}{\hbar}\left(\hat{H}\hat{\rho} - \hat{\rho}\hat{H}\right) \tag{2.26}$$

where we have introduced the dot notation for time-derivatives and the commutator $\left[\hat{A}, \hat{B}\right] = \hat{A}\hat{B} - \hat{B}\hat{A}$. Indeed, the time evolution of any operator can be obtained from its commutator with the Hamiltonian [4]. The above equation is readily demonstrated by taking the partial time derivative of the density operator and substitution using the TDSE, eq 2.7.

The expectation value of an operator can also be obtained directly from the density matrix. This is derived as follows:

$$\langle A \rangle = \sum_k P_k \left\langle \psi_k \middle| \hat{A} \middle| \psi_k \right\rangle \tag{2.27}$$

$$= \sum_{k,i,j} P_k c_i^\star c_j A_{ij} \tag{2.28}$$

$$= \sum_{i,j} A_{ij} \rho_{ji} \tag{2.29}$$

$$= \mathrm{Tr}\left[\hat{A}\hat{\rho}\right] \tag{2.30}$$

where we have used the trace of a matrix $\mathrm{Tr}\, M = \sum_i M_{ii}$.

The expectation value as written in equation 2.29 is a linear combination. The density matrix allows both calculation of the dynamics using the Liouville-von Neumann equation (eq 2.25) and the expectation value of operators (eq 2.29). This suggests an alternative formulation of quantum mechanics where everything is expressed using the density matrix, or elements of the density operator. Indeed, the entirety of quantum mechanics can be written using the elements ρ_{ij} as a basis, forming what is called Liouville space. Conceptually, this amounts to unraveling the density matrix into a vector. The order of the elements is arbitrary and doesn't matter, as long as it is consistent. However, if we are now to tag each element with a single index, we will be confused. The convention is to identify vectors with two indices. Matrix elements will thus require four indices. This is called *Tetradic Notation.* The corresponding objects, the Liouville-space analogues of operators, will be called super-operators, and denoted with a double-hat: $\hat{\hat{L}}$. Apart for this notational nicety, Liouville space forms a normal linear vector space, much like our initial basis set [3].

The basis vectors in Liouville space are related to the Hilbert space basis as follows:

$$|ij) \leftrightarrow \rho_{ij} \left|i\right\rangle \left\langle j\right| \tag{2.31}$$

and operators are linear combinations in this space, ie: they are now vectors:

$$|A) = \sum_{i,j} A_{ij}|ij) \tag{2.32}$$

$$(A| = \sum_{i,j} A_{ji}(ij| = |A)^{\dagger}. \tag{2.33}$$

The scalar product can be defined as:

$$(B|A) = \mathrm{Tr}\left(B^{\dagger}A\right) \tag{2.34}$$

which corresponds to computing the statistical correlation between B and A [6]. Every manipulation that can be done in Hilbert space has an equivalent formulation in Liouville space. We thus have two ways of formulating the same problem, and can pick whichever is most convenient.

Why bother with Liouville space then? A basis set of N states in Hilbert space corresponds to a basis of $(N^2 + N)/2$ density elements in Liouville space, which seems complicated. However, the Liouville space description already has the ensemble average baked in. This allows the coherences to be treated independently from the populations. This will be a major element of the discussion going forward: coherences correspond to oscillating dipoles, populations do not. Furthermore, quantum Liouville space has a direct analogue in the form of a classical Liouville space. This provides a clear and rigorous path for semiclassical treatments. Finally, time is taken into account slightly differently in the two spaces. Calculations with multiple time arguments in Hilbert space require repeating the calculation for all permutations of the time arguments and thus includes unintuitive time orderings. This is eliminated in Liouville space, and the theoretical calculation maps directly to the experimental description of an experiment with multiple pulses.

2.2.3 Dynamics

CMDS experiments are designed to probe the dynamical response of matter. The temporal evolution of the system is usually expressed using the density matrix, since it explicitly separates incoherent population dynamics from coherent dynamics. However, the modeling tools to be introduced later are expressed in Hilbert space. Quantum dynamics will thus be derived in both Hilbert and Liouville space, yielding analogous sets of equations. The entire process relies in the separation of the Hamiltonian in a material and field part, expressing the problem in the interaction picture and truncating the resulting expansion to the desired order.

Time evolution in Hilbert space is described using the TDSE (eq 2.7). We can define a propagator $\hat{U}$ such that:

$$|\psi(t)\rangle = \hat{U}(t, t_0) \, |\psi(t_0)\rangle \, . \tag{2.35}$$

This operator can be inserted in the TDSE and integrated to yield:

$$\hat{U}(t,t_0) = 1 - \frac{\mathrm{i}}{\hbar}\int_{t_0}^{t} \mathrm{d}\tau \hat{H}(\tau)\hat{U}(\tau,t_0), \tag{2.36}$$

$\hat{U}(\tau,t_0)$ has to be determined using that exact same equation. In a manner analogous to numerical integration of differential equations, the integration can be carried out for infinitesimal time steps, and iteratively re-inserted into eq 2.36, yielding a series expansion:

$$\hat{U}(t,t_0) = 1 + \sum_{n=1}^{\infty}\left(-\frac{\mathrm{i}}{\hbar}\right)^{n}\int_{t_0}^{t}\mathrm{d}\tau_n\int_{t_0}^{\tau_n}\mathrm{d}\tau_{n-1}\ldots\int_{t_0}^{\tau_2}\mathrm{d}\tau_1\hat{H}(\tau_n)\hat{H}(\tau_{n-1})\ldots\hat{H}(\tau_1). \tag{2.37}$$

It should be noted that the Hamiltonians do not commute, and thus the order of the time arguments is very important. Indeed, $\tau_{m-1} \leq \tau_m$. This series expansion is expressed in compact form using the following notation:

$$\hat{U}(t,t_0) = \exp_{+}\left(-\frac{\mathrm{i}}{\hbar}\int_{t_0}^{t}\mathrm{d}\tau\hat{H}(\tau)\right), \tag{2.38}$$

This is called the positive-time ordered exponential; the subscript + indicates the order of the time arguments matches the above eq 2.37. Its complex conjugate has a similar notation, called the negative time-ordered exponential:

$$\hat{U}^{\dagger}(t,t_0) = \exp_{-}\left(\frac{\mathrm{i}}{\hbar}\int_{t_0}^{t}\mathrm{d}\tau\hat{H}(\tau)\right) \tag{2.39}$$

$$= 1 + \sum_{n=1}^{\infty}\left(\frac{\mathrm{i}}{\hbar}\right)^{n}\int_{t_0}^{t}\mathrm{d}\tau_n\int_{t_0}^{\tau_n}\mathrm{d}\tau_{n-1}\ldots\int_{t_0}^{\tau_2}\mathrm{d}\tau_1\hat{H}(\tau_1)\ldots\hat{H}(\tau_{n-1})\hat{H}(\tau_n). \tag{2.40}$$

Note that the order of the time arguments hasn't changed ($\tau_{m-1} \leq \tau_m$) but the order of the Hamiltonians has been reversed. Also note that:

$$\hat{U}(\tau_2,t_0)\hat{U}^{\dagger}(\tau_1,t_0) = \hat{U}(\tau_2,\tau_1). \tag{2.41}$$

An equivalent formalism can be realized in Liouville space. Recalling the Louville von-Neumann equation 2.25 for a density matrix element:

$$\begin{aligned}\frac{\mathrm{d}\rho_{ij}}{\mathrm{d}t} &= -\frac{\mathrm{i}}{\hbar}\left[(\hat{H}\hat{\rho})_{ij} - (\hat{\rho}\hat{H})_{ij}\right] && (2.42)\\ &= -\frac{\mathrm{i}}{\hbar}\sum_k \left[H_{ik}\rho_{kj} - \rho_{ik}H_{kj}\right] && (2.43)\\ &= -\frac{\mathrm{i}}{\hbar}\sum_{i',j'} L_{ij,i'j'}\rho_{i'j'} && (2.44)\\ \dot{\hat{\rho}} &= -\frac{\mathrm{i}}{\hbar}\hat{\hat{L}}\hat{\rho} && (2.45)\end{aligned}$$

where $\hat{\hat{L}}$ is the Liouville super-operator. This equation is entirely analogous to the TDSE with $\hat{\hat{L}}$ instead of $\hat{H}$. This yields the following definition of the Liouville super-operator matrix elements:

$$L_{ij,i'j'} = H_{ii'}\delta_{jj'} - H^{\dagger}_{jj'}\delta_{ii'}. \tag{2.46}$$

The above mentioned propagator can also be defined in Liouville space. In a manner entirely analogous to previously:

$$\hat{\hat{U}}(t,t_0) = \exp_{+}\left(-\frac{\mathrm{i}}{\hbar}\int_{t_0}^{t}\mathrm{d}\tau\,\hat{\hat{L}}(\tau)\right). \tag{2.47}$$

using the positive time-ordered exponential previously defined in eq 2.37.

The propagators use two time arguments. We will typically be interested in propagating the system forward for some delay, the absolute value of the time points will usually not matter. For this, we define the Green function $G(t)$ such that:

$$|\psi(t+t_0)\rangle = \hat{G}(t)\,|\psi(t_0)\rangle \qquad \text{(Hilbert space)} \tag{2.48}$$

$$\hat{\rho}(t+t_0) = \hat{\hat{G}}(t)\hat{\rho}(t_0) \qquad \text{(Liouville space)} \tag{2.49}$$

Essentially, the Green function propagates the system forward in time by delay t. It can be difficult to define $G(t)$ to obey these equation. However, its formulation is simple in the case of time-independent $\hat{H}$ (and $\hat{\hat{L}}$):

$$G(t) = \theta(t)U(t_0 + t, t_0), \tag{2.50}$$

$$\hat{G}(t) = \theta(t)\exp\left[-\frac{\mathrm{i}}{\hbar}\hat{H}t\right], \qquad \text{(Hilbert space)} \tag{2.51}$$

$$\hat{\hat{G}}(t) = \theta(t)\exp\left[-\frac{\mathrm{i}}{\hbar}\hat{\hat{L}}t\right], \qquad \text{(Liouville space)} \tag{2.52}$$

where $\theta(t)$ is the Heaviside step function. The first equation holds in both spaces, we have dropped the hats. In particular, in the absence of relaxation it can be demonstrated that:

$$\hat{\hat{G}}(t) = \theta(t)\sum_{ij} |ij)\exp\left[-\mathrm{i}\omega_{ij}t\right](ij| \tag{2.53}$$

where $\omega_{ij} = (E_i - E_j)/\hbar$ and thus:

$$|ij(t + t_0)) = \hat{\hat{G}}(t)|ij(t_0)) = e^{-\mathrm{i}\omega_{ij}t}|ij(t_0)). \tag{2.54}$$

This states that under a time-independent Hamiltonian an $|ij)$ coherence rotates with angular frequency ω_{ij}. Defining the Green function to include other phenomena — such as relaxation or lineshapes — is more complicated, but we'll still use it[1].

The equations above perform the expansion on the full Hamiltonian. This is not what is required for spectroscopic experiments: we want to fully take into account the Hamiltonian of matter and limit the perturbative treatment to the electric field. The simple path to demonstrate this is to use the interaction picture. The Hamiltonian

---

[1] As experimentalists, we'll get away with just making it up.

is split into a time independent material $\hat{H}_0$ and a field part, recall eq 2.16:

$$\hat{H} = \hat{H}_0 + \hat{H}_E(t) = \hat{H}_0 - E(t)\hat{\mu}$$

and the Liouville space analogue:

$$\hat{\hat{L}} = \hat{\hat{L}}_0 + \hat{\hat{L}}_E(t) \tag{2.55}$$

$$\hat{\hat{L}}_E = -E(t)\hat{\hat{\mu}} \tag{2.56}$$

This allows the definition of the time-evolution operator due to $\hat{H}_0$ and $\hat{\hat{L}}_0$ as before:

$$\hat{U}_0(t, t_0) = \exp\left(-\frac{\mathrm{i}}{\hbar}\hat{H}_0(t - t_0)\right), \qquad \text{(Hilbert space)} \tag{2.57}$$

$$\hat{\hat{U}}_0(t, t_0) = \exp\left(-\frac{\mathrm{i}}{\hbar}\hat{\hat{L}}_0(t - t_0)\right). \qquad \text{(Liouville space)} \tag{2.58}$$

The corresponding Green functions are also similarly defined.

In the interaction picture, both operators and vectors are time-dependent. Specifically, we define an interaction picture version of every operator using U_0:

$$\hat{A}(t) = \hat{U}_0^{\dagger}(t, t_0)\hat{A}\hat{U}_0(t, t_0) \tag{2.59}$$

where $\hat{A}(t)$ is the interaction-picture operator (now time-dependent) corresponding to the Schrödinger-picture, time-independent operator $\hat{A}$. An entirely analogous equation exists for super-operators. In particular, the dipole operator and super-operator:

$$\hat{\mu}(\tau) = \exp\left(\frac{\mathrm{i}}{\hbar}\hat{H}_0\tau\right)\hat{\mu}\exp\left(-\frac{\mathrm{i}}{\hbar}\hat{H}_0\tau\right) \qquad \text{(Hilbert space)} \tag{2.60}$$

$$\hat{\hat{\mu}}(\tau) = \exp\left(\frac{\mathrm{i}}{\hbar}\hat{\hat{L}}_0\tau\right)\hat{\hat{\mu}}\exp\left(-\frac{\mathrm{i}}{\hbar}\hat{\hat{L}}_0\tau\right) \qquad \text{(Liouville space).} \tag{2.61}$$

The interaction picture is used to obtain a version of the time-ordered expansion (eq 2.37) using only the field part. This demonstration is carried out in Liouville space, although an equivalent one can also be made in Hilbert space. This is achieved by (briefly) defining the field part of $\hat{\hat{L}}_E$ in the interaction picture:

$$\hat{\hat{L}}'_E(\tau) = \hat{\hat{U}}_0^\dagger(\tau, t_0)\hat{\hat{L}}_E(\tau)\hat{\hat{U}}_0(\tau, t_0) \tag{2.62}$$

such that

$$\hat{\hat{U}}(t, t_0) = \hat{\hat{U}}_0(t, t_0) \exp_+ \left(-\frac{\mathrm{i}}{\hbar}\int_{t_0}^{t} \mathrm{d}\hat{\hat{L}}'_E(\tau)\right) \tag{2.63}$$

$$\begin{aligned}\hat{\hat{U}}(t, t_0) = \hat{\hat{U}}_0(t, t_0) + \sum_{n=1}^{\infty}\left(\frac{\mathrm{i}}{\hbar}\right)^n \int_{t_0}^{t}\mathrm{d}\tau_n \int_{t_0}^{\tau_n}\mathrm{d}\tau_{n-1}\ldots\int_{t_0}^{\tau_2}\mathrm{d}\tau_1 \\ \hat{\hat{U}}_0(t, \tau_n)\hat{\hat{L}}_E(\tau_n)\hat{\hat{U}}_0(\tau_n, \tau_{n-1})\hat{\hat{L}}_E(\tau_{n-1})\ldots\hat{\hat{U}}_0(\tau_2, \tau_1)\hat{\hat{L}}_E(\tau_1)\hat{\hat{U}}_0(\tau_1, t_0)\end{aligned} \tag{2.64}$$

where eq 2.41 has been used to condense the propagators. (You can now forget about $\hat{\hat{L}}'_E(t)$).

Using this result to expand the density matrix, we get:

$$\hat{\rho}^{(n)}(t) = \left(\frac{\mathrm{i}}{\hbar}\right)^n \int_{t_0}^{t}\mathrm{d}\tau_n \int_{t_0}^{\tau_n}\mathrm{d}\tau_{n-1}\ldots\int_{t_0}^{\tau_2}\mathrm{d}\tau_1 E(\tau_n)E(\tau_{n-1})\ldots E(\tau_1) \tag{2.65}$$

$$\hat{\hat{G}}(t-\tau_n)\hat{\hat{\mu}}\hat{\hat{G}}(\tau_n-\tau_{n-1})\hat{\hat{\mu}}\ldots\hat{\hat{G}}(\tau_2-\tau_1)\hat{\hat{\mu}}\hat{\rho}_{\mathrm{eq}} \tag{2.66}$$

where we used the definition of the Green function (eq 2.49) and $\hat{\hat{G}}(t)\hat{\rho}_{\mathrm{eq}} = \hat{\rho}_{\mathrm{eq}}$ by definition of $\hat{\rho}_{\mathrm{eq}}$.

The response is obtained by computing the resulting polarization:

$$\chi^{(n)}(t_n, t_{n-1}\ldots t_1) = (\mu|\rho^{(n)}(t_n, t_{n-1}\ldots t_1)) \tag{2.67}$$

$$\chi^{(n)}(t_n, t_{n-1}\ldots t_1) = (\mu|\hat{\hat{G}}(t_n)\hat{\hat{\mu}}\hat{\hat{G}}(t_{n-1})\hat{\hat{\mu}}\ldots\hat{\hat{G}}(t_1)\hat{\hat{\mu}}|\rho_{\mathrm{eq}}) \tag{2.68}$$

where $t_m = \tau_{m+1} - \tau_m$ and $t_n = t - \tau_n$. This formulation forms the basis of the description of CMDS experiments. Note in particular that the electric field operator expands to two terms (eq 2.6). The expansion of order n thus expands to 2^n terms, half of which are the complex conjugates of the other half. Furthermore, both $\hat{\hat{\mu}}$ and

$\hat{\hat{G}}$ are Liouville space matrices. The number of non-zero elements depends on the number of allowed transitions (off-diagonal elements of $\hat{\mu}$) as well as the number of relaxation pathways (off-diagonal elements of $\hat{\hat{G}}$). This compact expression expands to multiple different interaction terms, and to all possible pathways the system can take under the action of the pulses. The total number of terms can be very large ($>$1000)!

2.2.4 The system and the bath

Spectroscopic experiments reveal only part of the molecular response, the part that falls in the bandwidth observable to the apparatus. For example, the visible bandwidth corresponds to excitations of the valence electrons. However, the light-induced excitation can drive the motion of secondary degrees of freedom if a coupling exists. The complete response to an optical excitation is thus made of the electronic resonance and all modes it is coupled to. This is especially important for the understanding of lineshapes and their dynamics. Ordering the modes by their direct or indirect susceptibility can be used to greatly simplify the active space necessary to a rigorous description of the system. Most modes are entirely uncoupled to both the visible light field and the resulting excitation of the valence electrons. Core electrons, rotational motion and spin excitations often fall in this category, as well as subatomic physics. They can be eliminated directly.

The motion of nuclei is more complicated. Some vibrational modes are strongly coupled to electronic motion, giving rise to Raman modes. The change of the equilibrium geometry in the electronic excited state can give rise to slow but large rearrangements of the molecule. The nuclear rearrangements following electronic excitation can be so large as to induce photochemical reactions. Vibrational modes can also be coupled among themselves, further entangling the response. Nuclear motions thus have to be taken into account when determining the electronic response. They cause fluctuations of the electronic response, and thus modulate the linewidth.

It is common to separate the system in two parts, a system and a bath, that are treated differently. One point that requires emphasis is that the system bath partitioning can be done arbitrarily without any loss of generality [6, 15–17]. There is thus no physics arising directly from the system-bath partitioning, but also no constraints to limit the flexibility of said partitioning. One is free to define the system out of convenience, in order to simplify the description. One rule is commonly obeyed in the spectroscopy literature: the spectroscopic response must be contained in the system, and have no response from the bath. This maps well to a spectroscopic experiment where the response arises from a chromophore and the background signal is absent or removed through experimental design. Furthermore, it is desirable to select the bath such that it obeys simple statistics with a well-known analytical description, such as Gaussian fluctuations. The orthodox system-bath partition of theoretical nonlinear spectroscopy does not make full use of this flexibility. The system is always taken to be the spectroscopically active degrees of freedom, and every other mode is in the bath, even if it is an important component of the dynamics. This results in obscure jargon, misunderstandings and some confusion[1].

The complete set of basis functions for the whole system can be partitioned with the use of projection operators. Formally, the partitioning requires a pair, the operator $\hat{P}$ for the system and $\hat{Q}$ for the bath:

$$\hat{P} = \sum_{i=1}^{n} |i\rangle \langle i| \tag{2.69}$$

---

[1] It can be funny to observe the heated arguments made over ill-defined jargon.

$$\hat{Q} = \sum_{i=n+1} |i\rangle \langle i| \tag{2.70}$$

where the system is composed of n basis functions and the second sum runs over the remaining basis vectors. In matrix form, $\hat{P}$ would have some diagonal elements be 1, everything else would be 0; $\hat{Q}$ would have 1s in the remaining diagonal elements and zeros everywhere else. Note that this may require some care when selecting the basis. The equations above keep every mode in its quantum form, the classical limit can be taken later. These deceptively simple operators form the basis of a formal derivation of the reduced equations of motion for an open quantum system subject to environmental fluctuations.

The projection operators have the following properties:

$$\hat{P} + \hat{Q} = 1 \tag{2.71}$$

$$\hat{P}^2 = \hat{P} \tag{2.72}$$

$$\hat{Q}^2 = \hat{Q} \tag{2.73}$$

$$\hat{P}\hat{Q} = \hat{Q}\hat{P} = 0, \tag{2.74}$$

where eq 2.71 is a completeness relation (no states were forgotten or counted twice), eqs 2.72 and 2.73 states the operators are idempotent (applying them more than once doesn't change anything) and eq 2.74 is an orthogonality relation (no states are in both system and bath). Using these properties, we can readily see that $\hat{P}$ and $\hat{Q}$ partition the wavefunction and the operators into a system and a bath part:

$$|\psi\rangle = \left(\hat{P} + \hat{Q}\right) |\psi\rangle \tag{2.75}$$

$$= \hat{P} |\psi\rangle + \hat{Q} |\psi\rangle \tag{2.76}$$

$$= |\psi\rangle_{\text{sys}} + |\psi\rangle_{\text{bath}} . \tag{2.77}$$

Indeed, conditions 2.71 to 2.74 are all the conditions that a system-bath partitioning need to obey.

The projection operators can be used to obtain equations of motions specific to the system. By using the TDSE (eq 2.7) and property eq 2.71 above, we get:

$$
\begin{aligned}
|\dot{\psi}\rangle &= -\frac{\mathrm{i}}{\hbar}\hat{H}\left(\hat{P}+\hat{Q}\right)|\psi\rangle \\
\hat{P}|\dot{\psi}\rangle &= -\frac{\mathrm{i}}{\hbar}\left(\hat{P}\hat{H}\hat{P}+\hat{P}\hat{H}\hat{Q}\right)|\psi\rangle \\
\hat{P}|\dot{\psi}\rangle &= -\frac{\mathrm{i}}{\hbar}\left(\hat{P}\hat{H}\hat{P}^2+\hat{P}\hat{H}\hat{Q}^2\right)|\psi\rangle \\
|\dot{\psi}\rangle_{\mathrm{sys}} &= -\frac{\mathrm{i}}{\hbar}\left(\hat{P}\hat{H}\hat{P}\,|\psi\rangle_{\mathrm{sys}}+\hat{P}\hat{H}\hat{Q}\,|\psi\rangle_{\mathrm{bath}}\right) \\
|\dot{\psi}\rangle_{\mathrm{sys}} &= -\frac{\mathrm{i}}{\hbar}\left(\hat{H}_{\mathrm{sys}}\,|\psi\rangle_{\mathrm{sys}}+\hat{H}_{\mathrm{sb}}\,|\psi\rangle_{\mathrm{bath}}\right) \qquad (2.78)
\end{aligned}
$$

where $\hat{H}_{\mathrm{sys}} = \hat{P}\hat{H}\hat{P}$ is the system Hamiltonian and $\hat{H}_{\mathrm{sb}} = \hat{P}\hat{H}\hat{Q}$ is the Hamiltonian describing the action of the bath on the system. The second equation is obtained by multiplying from the left by $\hat{P}$ and the third is obtained by using eqs 2.72 and 2.73. This can be used to define arbitrary system bath partitions and rigorously solve for their dynamics and to partition operators into parts corresponding to the system, to the bath and to system-bath coupling (both effect of the bath on the system and effect of the system on the bath).

A similar formulation can be made for the density matrix. The projection operator is typically defined as:

$$\hat{P}\hat{\rho} = \rho_B^0\,\mathrm{Tr}_B\,\hat{\rho} = \rho_B^0\hat{\rho}_{\mathrm{sys}} \qquad (2.79)$$

where Tr_B indicates a trace over the bath modes and ρ_B^0 is the equilibrium density matrix of the bath modes. This operation defines the reduced density operator ρ_{sys} after both ensemble averaging and averaging over the equilibrium distribution of the bath modes. The definition used above, however, contains an approximation that eq 2.69 doesn't. Namely, it explicitly assumes the bath distribution is fixed at the equilibrium distribution, and thus that any force the system applies on the bath is negligible.

The equations in this section will not be used directly in this thesis, which reports on experimental work. The inclusion of this section aims at covering the concept of system-bath partitioning which occurs frequently in the field of spectroscopy. It is the rigorous framework underlying the theory of quantum open system. These concepts are used to develop the multimode brownian oscillator model below (sec 2.3.4).

2.3 Linear Spectroscopy

The interpretation and modeling of CMDS experiments involves advanced tools such as double-sided Feynman diagrams (DSFD) and multi-point correlation functions of the transition dipole. The Liouville space DSFD are a powerful tool of spectrocopic assignment applicable to nonlinear spectroscopy. The multi-point correlation functions enable the rigorous inclusion of lineshapes, including cases that will induce coherent lineshape dynamics. These concepts are introduced for the simpler case of linear spectroscopy, in order to focus on the tools themselves.

2.3.1 Linear spectroscopy in Liouville space

The Hamiltonian for an isolated chromophore in an external, time-varying electric field is given by eq 2.16, Recall:

$$\hat{H}(t) = \hat{H}_0 + \hat{H}_E = \hat{H}_0 - \hat{\mu}E(t).$$

The previous section shows how this can be used to obtain the series expansion of the nonlinear polarization from an expansion of the density matrix in terms of $\hat{H}_E$:

$$P(t) = (\mu|\rho(t)) = \sum_n (\mu|\rho^{(n)}(t)) \tag{2.80}$$

$$P^{(n)}(t) = (\mu|\rho^{(n)}(t)) \tag{2.81}$$

In a linear absorption experiment, the emitted signal field propagates along the same vector as the incident field, and their interference is detected using a square-law detector:

$$I(\omega) = |E(\omega) + E_{\text{sig}}(\omega)|^2 \tag{2.82}$$

$$= |E(\omega)|^2 + |E_{\text{sig}}(\omega)|^2 + 2\Re\left[E(\omega)E^{\star}_{\text{sig}}(\omega)\right] \tag{2.83}$$

The linear signal arises from the first term[1] in this series, $P^{(1)}(t)$. The absorption spectrum can be computed from:

$$(\mu|\rho^{(1)}(t_1)) = (\mu|\hat{\hat{G}}(t_1)\hat{\hat{\mu}}|\rho_{\text{eq}}). \tag{2.84}$$

The perturbative expansion allows for transitions of either the bra or ket. For a multilevel system, the dipole super-operator can be expressed as:

$$\hat{\hat{\mu}} = \sum \mu_{ii'}\delta_{jj'}|ij)(i'j'| - \mu^{\star}_{jj'}\delta_{ii'}|ij)(i'j'| \tag{2.85}$$

where the first term comes from operating on the ket and the second term comes from operating on the bra (remember, it is a commutator). Each dipole operator gives rise to two terms, one of which is negative. The operator projects populations into coherences and coherences into either different coherences or into populations, but only a single index of the density matrix is allowed to change.

---

[1] $(\mu|\rho_{\text{eq}}) = 0$ by definition of the equilibrium.

For a multilevel system initially in equilibrium such that:

$$|\rho_{\text{eq}}) = \sum_g P(g)|gg) \tag{2.86}$$

equation 2.80 above can be expanded as follows:

$$\begin{align}
\chi^{(1)}(t_1) &= (\mu|\rho^{(1)}(t_1)) \tag{2.87}\\
&= \frac{\mathrm{i}}{\hbar}(\mu|\hat{\hat{G}}(t_1)\hat{\hat{\mu}}|\rho_{\text{eq}}) \tag{2.88}\\
&= \frac{\mathrm{i}}{\hbar}\sum_g P(g)(\mu|\hat{\hat{G}}(t_1)\hat{\hat{\mu}}|gg) \tag{2.89}\\
&= \frac{\mathrm{i}}{\hbar}\sum_{g,a} P(g)\left[\mu_{ag}(\mu|\hat{\hat{G}}(t_1)|ag) - \mu_{ga}(\mu|\hat{\hat{G}}(t_1)|ga)\right] \tag{2.90}\\
&= \frac{\mathrm{i}}{\hbar}\sum_{g,a} P(g)\theta(t_1)\left[\mu_{ag}e^{-\mathrm{i}\omega_{ag}t_1}(\mu|ag) - \mu_{ga}e^{-\mathrm{i}\omega_{ga}t_1}(\mu|ga)\right] \tag{2.91}\\
&= \frac{\mathrm{i}}{\hbar}\sum_{g,a} P(g)\theta(t_1)\left[\mu_{ag}\mu_{ga}e^{-\mathrm{i}\omega_{ag}t_1} - \mu_{ga}\mu_{ag}e^{-\mathrm{i}\omega_{ga}t_1}\right] \tag{2.92}\\
&= \frac{\mathrm{i}}{\hbar}\sum_{g,a} P(g)\theta(t_1)\left|\mu_{ag}\right|^2\left[e^{-\mathrm{i}\omega_{ag}t_1} - e^{\mathrm{i}\omega_{ag}t_1}\right] \tag{2.93}\\
&= \chi_1^{(1)} + \chi_2^{(1)} \tag{2.94}
\end{align}$$

with $\omega_{ag} = (E_a - E_g)/\hbar = -\omega_{ga}$. This is the sum of two terms, which we denote $\chi_1^{(1)}$ and $\chi_2^{(1)}$.

Note that there is a difference between the Liouville space superoperator $(\rho|\hat{\hat{\mu}}|\rho)$ and the Liouville space vector (Hilbert space operator) $(\mu|\rho)$[1]. This difference is not only notational, the last step in this expansion is:

$$(\mu|ga) = \langle a|\hat{\mu}|g\rangle = \mu_{ag}, \tag{2.95}$$

---

[1] In the book of Cho, they are referred to as the *cause* and *effect* operators, respectively.

$$(\mu|ag) = \langle g|\hat{\mu}|a\rangle = \mu_{ga} \tag{2.96}$$

In matrix notation, it is obvious that it sends the coherence back to the ground state density matrix element $|gg)$. The demonstration above thus takes the system through a series of elements in Liouville space:

$$\begin{gathered}|gg) \rightarrow |ga) \rightarrow |gg)\\ |gg) \rightarrow |ag) \rightarrow |gg)\end{gathered}$$

where the second path is the conjugate of the first. This string of density matrix elements is called a Liouville space path. The total response is made of the sum over all possible such paths, which involve two states. The path needs to start in the ground state, and end in a population state as the expectation value in Liouville space is given by a trace.

The discussion started some pages ago with a statement of the spectrum as typically derived from Fermi's Golden rule, equation 1.2. It is easily demonstrated from the above result (eq 2.93):

$$\begin{aligned}\chi^{(1)}(t_1) &= \frac{\mathrm{i}}{\hbar}\sum_{g,a} P(g)\left|\mu_{ag}\right|^2 \Im e^{-\mathrm{i}\omega_{ag}t_1}\\ &= \frac{\mathrm{i}}{\hbar}\sum_{g,a} P(g)\left|\mu_{ag}\right|^2 \sin\left(\omega_{ag}t_1\right)\end{aligned}$$

This equation is readily Fourier Transformed to yield equation 1.2 (up to constant scaling factors). The second version of eq 1.2 can be obtained by realizing $\omega_{ga} = -\omega_{ag}$, which flips the sign of the sine:

$$\chi^{(1)}(t_1) = \frac{\mathrm{i}}{\hbar}\sum_{g<a} \left[P(g) - P(a)\right]\left|\mu_{ag}\right|^2 \sin\left(\omega_{ag}t_1\right).$$

where it is now required that the energy difference is thermally accessible, and thus both g and a are potential inital states. This is not the typical case in visible spectroscopy[1], but is important in the analysis of NMR and far IR spectroscopy. It seems important to show our analysis applies to well-established spectroscopy techniques.

The next step in deriving the total polarization is now to multiply equation 2.93 by the electric field. The linear polarization for a two-level system of states e, g initially in the ground state g with unit transition dipole is given by:

$$\begin{aligned}
P^{(1)}(t) &= \int_0^\infty \mathrm{d}t_1 \mathcal{E}(t-t_1)\chi^{(1)}(t_1) && (2.97)\\
&= \int_0^\infty \mathrm{d}t_1 \left(E(t-t_1) + E^\star(t-t_1)\right)\chi^{(1)}(t_1) && (2.98)\\
&= \frac{\mathrm{i}}{\hbar}\int_0^\infty \mathrm{d}t_1 \left[E(t-t_1) + E^\star(t-t_1)\right]\left(e^{-\mathrm{i}\omega_{eg}t_1} - e^{\mathrm{i}\omega_{eg}t_1}\right) && (2.99)\\
-\mathrm{i}\hbar P^{(1)}(t) &= \int_0^\infty \mathrm{d}t_1 E(t-t_1)e^{-\mathrm{i}\omega_{eg}t_1} + \int_0^\infty \mathrm{d}t_1 E^\star(t-t_1)e^{-\mathrm{i}\omega_{eg}t_1}\\
&\quad + \int_0^\infty \mathrm{d}t_1 E(t-t_1)e^{\mathrm{i}\omega_{eg}t_1} + \int_0^\infty \mathrm{d}t_1 E^\star(t-t_1)e^{\mathrm{i}\omega_{eg}t_1} && (2.100)\\
&= e^{-\mathrm{i}\omega t}\int_0^\infty \mathrm{d}t_1 A(t-t_1)e^{-\mathrm{i}(\omega_{eg}-\omega)t_1}\\
&\quad + e^{\mathrm{i}\omega t}\int_0^\infty \mathrm{d}t_1 A^\star(t-t_1)e^{-\mathrm{i}(\omega_{eg}+\omega)t_1}\\
&\quad + e^{-\mathrm{i}\omega t}\int_0^\infty \mathrm{d}t_1 A(t-t_1)e^{\mathrm{i}(\omega_{eg}+\omega)t_1}\\
&\quad + e^{\mathrm{i}\omega t}\int_0^\infty \mathrm{d}t_1 A^\star(t-t_1)e^{\mathrm{i}(\omega_{eg}-\omega)t_1} && (2.101)
\end{aligned}$$

using $E(t) = A(t)e^{-\mathrm{i}\omega t}$. The polarization contains 4 terms, two of which rotate with frequency $\omega_{eg}-\omega$, two with $\omega_{eg}+\omega$. Since $\omega \approx \omega_{eg}$, latter two terms can be neglected. This is called the rotating wave approximation. Note that we are assuming $\omega_{eg} > 0$,

---

[1] Trip suggestion: Set the Controls for the Earth of the Sun

ie: $E_e > E_g$. This is the case for visible spectroscopy, but may not necessarily be the case for NMR or far IR. In that latter case, the other two terms will vanish, and the situation is the same.

The equation above reduces to:

$$P^{(1)}(t) = \frac{\mathrm{i}}{\hbar}\int_0^\infty \mathrm{d}t_1 E(t-t_1)\chi_1^{(1)}(t_1) - \frac{\mathrm{i}}{\hbar}\int_0^\infty \mathrm{d}t_1 E^\star(t-t_1)\chi_2^{(1)}(t_1) \tag{2.102}$$

The second term is the complex conjugate of the first. We have reduced our expansion to a single term:

$$P^{(1)}(t) = \frac{1}{\hbar}\int_0^\infty \mathrm{d}t_1 \Re E(t-t_1)\left(\mu|\hat{\hat{G}}(t_1)\hat{\hat{\mu}}|\rho_{\mathrm{eq}}\right) \tag{2.103}$$

This tedious derivation was carried out for the linear spectrum for a two-level system (single transition!). Luckily, this can be generalized to higher orders. The response of order n will expand into 2^n terms. For m states, each of these further expands into around $(m-1)^n$ possible Liouville pathways. Expanding the field $E(t)$ into a sum of k pulses also results in a multitude of terms. Despite the large number of combinations, the total result reduces to a limited number of terms thanks to the rotating wave approximation. Luckily, the bookkeeping of both the system and the field can be systematically done using a representation called Double-Sided Feynmann Diagrams (DSFD).

2.3.2 Double-sided Feynman diagrams

A DSFD represents the evolution of the system in Liouville space. Vertical lines represent the evolution of the ket and the bra. Incoming and outgoing arrows indicate excitation or de-excitation. By following a few simple rules which match physical intuition, these diagrams enable the meticulous exhaustion of all possible responses

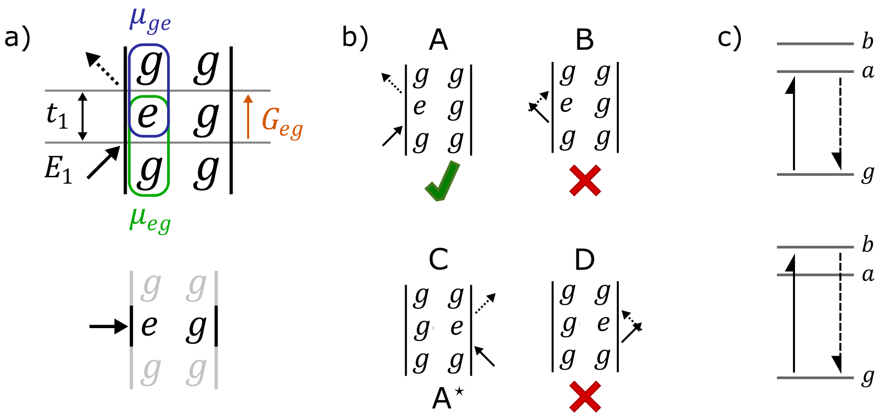

Figure 2.1: Representation of the linear response using double-sided Feynman diagrams. (a) The diagram representing the linear response for a two-level system is dissected. See text. An abbreviated version is shown below. (b) Four terms in the linear response of a two-level system are reduced to a single term. (c) When multi-level systems are discussed, it may be useful to use an energy level diagram with arrows indicating the transitions. In this representation, time runs to the right and the arrowhead side indicates interaction with the ket (left) or bra (right).

in the system. Despite their nice graphical design, diagrammatic representations such as DSFD rigorously translate into equations, such as eq 2.104 below [3, 4, 6].

Example DSFD are represented on Fig 2.1. A diagram, corresponding to the linear absorption eq 2.103 is dissected on panel a. This diagram obeys the following rules:

1. Vertical lines indicate the evolution of the ket (left) and bra (right).
2. Time goes up.
3. Labels indicate the density matrix elements.
4. Arrows indicate light-matter interactions, which can operate on the ket (left) or bra (right) but not both.
5. Right-going arrow indicates interaction with $E(t)$, left-going indicates $E^\star(t)$.
6. An arrow pointing towards the system corresponds to absorption and thus an excitation. Conversely, an arrow pointing away corresponds to de-excitation.

7. The last arrow is an expectation value, not a light-matter interaction. It corresponds to the polarization of matter. It usually has a different style.
8. By convention, last arrow operates on the ket. It is thus an outgoing arrow on the left side.
9. The measurement corresponds to taking a trace, the final state must be a population.
10. The diagram has a sign, corresponding to $(-1)^n$ where n is the number of interactions with the bra.

These rules make it easy to write the DSFD: systematically write all the permutations of arrows and states, and cross out those that do not obey the above rules. With some practice, it becomes easy to write all the possible valid diagrams without wasting too much time with the wrong ones[1].

The diagrams can be simplified somewhat. Due to rule 4 above, the initial and final states can be deduced directly from the first and last rows (respectively). Usually, consecutive arrows correspond to consecutive light-matter interaction. When this convention is obeyed, we will not indicate the index of the light pulses. For easy typesetting, the upwards pointing arrow will be converted to the horizontal and moved up to align with the density matrix elements. This results in the abbreviated diagram at the bottom of panel 2.1a.

An example of diagram elimination is shown on Fig 2.1b. The four diagrams represented there correspond to the four terms of 2.101. As demonstrated, two of them (B, D) vanish due to the rotating wave approximation, corresponding to rule 6 for diagrams. The two remaining diagrams, corresponding to eq 2.102 are mirror

---

[1] Hint: start with the final state and work your way backwards.

images of one another, and thus complex-conjugates. Rule 8 lets us draw only diagram A as long as we remember to take the real part. This is equivalent to eq 2.103.

As shown in eq 2.93, the response of a multi-level system can be decomposed into a sum over paths involving two-levels. The DSFD make it easy to inspect the signal from a given path, but it can quickly become confusing when multiple paths are available, especially in the presence of relaxation. In this case, it can be useful to enumerate the possible pathways through the manifold of states on an energy-level diagram. This formulation is not the subject of a strong convention in the field of CMDS. In the current work, time will go horizontal to the right, harpoons indicate light-matter interaction. The side of the arrowhead indicates interaction with the ket (left) or bra (right). Arrow style can be used to distinguish the types of interactions. The linear response for a three-level system consisting of a ground state g and two singly excited states a, b is shown on Fig 2.1c.

The DSFD make it easy to write down the corresponding response. Laser-induced transitions correspond to transition dipoles, which are read vertically (green, blue boxes on Fig 2.1a). The different rows of the density matrix correspond to different time intervals. During delay t_1, the system evolves in a coherence and the corresponding Green function (orange). Reading the diagram in Fig 2.1, we can directly write the susceptibility. We can even add dephasing phenomenologically by setting:

$$\hat{\hat{G}}_{eg}(t) = \exp\left[-\mathrm{i}\omega_{eg}t - t/T_2\right] \qquad \text{(Homogeneous dephasing)} \tag{2.104}$$

$$\chi^{(1)}(t) = \left|\mu_{eg}\right|^2 \exp\left[-\mathrm{i}\omega_{eg}t - t/T_2\right] \tag{2.105}$$

which Fourier transforms to a Lorentzian lineshape of width $1/T_2$. The process stays similarly straightforward for higher-order responses, allowing us to include the complicated three dimensional lineshapes phenomenologically[1].

2.3.3 Cumulant expansion: coherent lineshapes in Hilbert space

The description in terms of Liouville pathways and DSFD dominates the field of CMDS for good reason. It allows the inclusion of lineshapes using varying levels of rigor [2, 18]. However, it is unable to represent a coherent evolution of the vibrational modes and the resulting coherent lineshape dynamics. The reason seems baked in the orthodox system-bath partition. This partition puts all optically active degrees of freedom in the system, and everything else in the bath. The Liouville pathway formulation does not account for the state of the bath, which is thus reset at every step of the process. This is perfectly fine for incoherent lineshape dynamics, but prevents the inclusion of coherent vibrational motion. In order to circumvent this limitation, the calculation is carried out in Hilbert space. This also allows the rigorous derivation of the origin of lineshapes, within some approximations. The calculation for linear spectroscopy is reasonably simple, but serves to introduce the concepts.

The linear response, eq 2.103 can be equivalently expressed in Hilbert space using commutators and the interaction picture transition dipole operator, eq 2.60. Recall:

$$\begin{aligned}
\chi^{(1)}(\tau_1) &= \frac{\mathrm{i}}{\hbar}\left\langle [\hat{\mu}(\tau_1), [\hat{\mu}(\tau_0), \rho(\tau_0)]] \right\rangle && (2.106)\\
&= \frac{\mathrm{i}}{\hbar}\left\langle [\hat{\mu}(\tau_1), \hat{\mu}(\tau_0)]\, \rho_{\mathrm{eq}} \right\rangle && (2.107)\\
&= \frac{\mathrm{i}}{\hbar}\left\langle \hat{\mu}(\tau_1)\hat{\mu}(\tau_0)\rho_{\mathrm{eq}} \right\rangle - \frac{\mathrm{i}}{\hbar}\left\langle \hat{\mu}(\tau_0)\hat{\mu}(\tau_1)\rho_{\mathrm{eq}} \right\rangle && (2.108)
\end{aligned}$$

---

[1] Easy, isn't it?

$$= \frac{\mathrm{i}}{\hbar} \langle \hat{\mu}(\tau_1)\hat{\mu}(\tau_0)\rho_{\mathrm{eq}} \rangle - \frac{\mathrm{i}}{\hbar} \langle \rho_{\mathrm{eq}}\hat{\mu}(\tau_0)\hat{\mu}(\tau_1) \rangle \tag{2.109}$$

$$= \frac{1}{\hbar}\Re \langle \hat{\mu}(\tau_1)\hat{\mu}(\tau_0)\rho_{\mathrm{eq}} \rangle \tag{2.110}$$

due to the invariance of the trace under cyclic permutation. This formulation also reduces to a single term, $\langle \hat{\mu}(\tau_1)\hat{\mu}(\tau_0)\rho_{\mathrm{eq}} \rangle$, which is known as the two-point correlation function of the transition dipole moment.

This equation will now be simplified using the so-called cumulant expansion to second order. The energy of state i is separated in an average and a fluctuating part, similarly for the angular frequency:

$$E_i(t) = \overline{E}_i + \delta E_i(t) \tag{2.111}$$

$$\omega_{ij}(t) = \overline{\omega}_{ij} + \delta\omega_{ij}(t). \tag{2.112}$$

An important subtlety arises when defining the corresponding Hamiltonian. The Hamiltonian can be separated in a fixed and a fluctuating part, typically arising from system-bath interaction:

$$\hat{H}_{\mathrm{mat}}(t) = \hat{H}_0 + \hat{V}(t) \tag{2.113}$$

where $\hat{H}_0$ is the fixed part and $\hat{V}(t)$ is the fluctuating part, for example the system-bath Hamiltonian. This Hamiltonian lends itself to another use of the interaction picture.

The reference frame has to be selected carefully in order to simplify the derivation. Two possible frames of references are depicted in Fig 2.2. The first panel, Fig 2.2a, uses the average ground state energy as a reference. Both the ground and excited states fluctuate. This corresponds to an intuitive picture. The second panel shows the same trajectories, setting the time-varying ground state Hamiltonian as

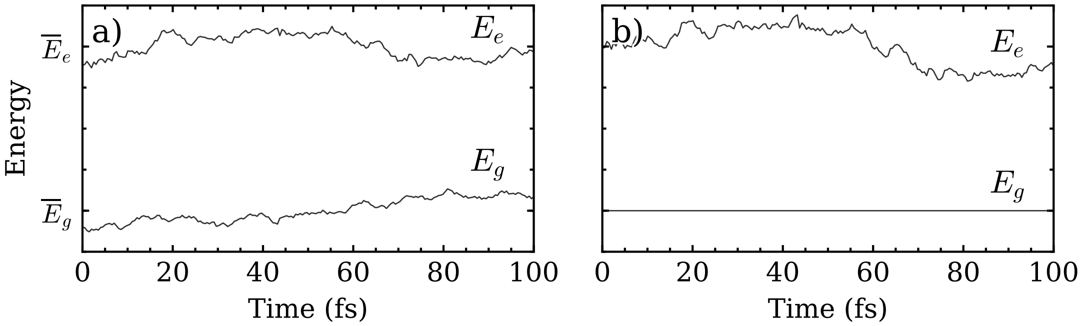

Figure 2.2: Two equivalent frames of reference. (a) The average ground state energy is taken as a reference. Both the energy of the ground and excited state fluctuate. (b) The fluctuating ground state energy is taken as a reference. All fluctuations are in the excited state.

a reference. This way, all the fluctuations are contained in the excited states, the ground state stays at a fixed energy. This makes no difference for spectroscopy, as only the energy gap can be probed. The fluctuations involved in our derivations will always be the fluctuations of the states[1]. There is an equivalent formulation where the fluctuations are taken for the energy gaps[2]. This is simply a change of reference frame. However, using states is more convenient. A system with N states will require $(N^2+N)/2$ correlation functions. The same system has $M = (N^2-N)/2$ transitions, which require $(M^2+M)/2$ correlation functions, which is a much larger number.

This choice of reference frame yields the excited states Hamiltonian:

$$\hat{H}_i(t) = \hat{H}_i + \hat{V}_{ig}(t) \tag{2.114}$$

$$\hat{H}_i = \hat{H}_g + \hbar\overline{\omega}_{ig} \tag{2.115}$$

---

[1] This work follows the book of Cho.

[2] In the book of Mukamel. This requires having a different reference for every pair of states...

$$\hat{V}_{ig}(t) = \hat{V}_i(t) - \hat{V}_g(t) \tag{2.116}$$

$$\hat{V}_{gg}(t) = 0 \tag{2.117}$$

$$\left\langle \hat{V}_{ig}(t) \right\rangle_{\text{eq}} = 0 \tag{2.118}$$

where the $\langle \ldots \rangle_{\text{eq}}$ in the last equation indicates the average. $\hat{V}_{ig}(t)$ is thus the instantaneous fluctuation of the energy of state i. Usually, the fluctuations are taken to be due to fluctuating nuclear coordinates, ie: $\hat{V}_{ij}(t) = \hat{V}_{ij}(\boldsymbol{q}(t))$.

This can be used to define the time-dependent transition dipole moment, now taking into account the evolution with respect to the ground state Hamiltonian:

$$\begin{aligned}
\hat{\mu}_{ij}(\tau) &= \left\langle i \left| \exp\left(\mathrm{i}\hat{H}_0\tau\right) \hat{\mu} \exp\left(-\mathrm{i}\hat{H}_0\tau\right) \right| j \right\rangle && (2.119)\\
&= \mu_{ij} \exp\left(\mathrm{i}\hat{H}_i\tau\right) \exp\left(-\mathrm{i}\hat{H}_j\tau\right) && (2.120)\\
&= \mu_{ij} \exp\left(-\mathrm{i}\overline{\omega}_{ij}\tau\right) \exp_+ \left[-\frac{\mathrm{i}}{\hbar}\int_0^\tau \mathrm{d}\tau' V_{ij}(\tau')\right] && (2.121)
\end{aligned}$$

where we have implicitly assumed that $\hat{\mu}$ has no time-varying part from other sources. In the context of fluctuations induced by motions from a nuclear bath, this amounts to assuming the transition dipole does not depend on nuclear coordinates, ie: $\mu_{ij}(\boldsymbol{q}) = \mu_{ij} \forall \boldsymbol{q}$. This is the Condon approximation.

The result above can be inserted in eq 2.110 to yield the linear response in the presence of fluctuations:

$$\begin{aligned}
\langle \hat{\mu}(t)\hat{\mu}(0) \rangle_{\text{eq}} &= \sum_{g,a} \langle \hat{\mu}_{ga}(t)\hat{\mu}_{ag}(0) \rangle_{\text{eq}} && (2.122)\\
&= \frac{\mathrm{i}}{\hbar}\sum_{g,a} |\mu_{ag}|^2 e^{-\mathrm{i}\overline{\omega}_{ga}t} \left\langle \exp_+\left[-\frac{\mathrm{i}}{\hbar}\int_0^t \mathrm{d}\tau \hat{V}_{ga}(\tau)\right] \right\rangle_{\text{eq}} && (2.123)\\
&= \frac{\mathrm{i}}{\hbar}\sum_{g,a} |\mu_{ag}|^2 e^{-\mathrm{i}\overline{\omega}_{ga}t} \left\langle 1 - \frac{\mathrm{i}}{\hbar}\int_0^t \mathrm{d}\tau \hat{V}_{ga}(\tau) \right.
\end{aligned}$$

$$-\frac{1}{\hbar^2}\int_0^t \mathrm{d}\tau \int_0^\tau \mathrm{d}\tau' \hat{V}_{ga}(\tau)\hat{V}_{ga}(\tau') + \ldots \Big\rangle_{\mathrm{eq}} . \tag{2.124}$$

The first order term vanishes by definition, see eq 2.118. We can now define the lineshape function:

$$\begin{aligned} g_{ij}(t) &= \frac{1}{\hbar^2}\int_0^t \mathrm{d}\tau \int_0^\tau \mathrm{d}\tau' \left\langle \hat{V}_{ig}(\tau)\hat{V}_{jg}(\tau')\right\rangle_{\mathrm{eq}} && (2.125)\\ &= \int_0^t \mathrm{d}\tau \int_0^\tau \mathrm{d}\tau' \left\langle \delta\omega_{ig}(\tau)\delta\omega_{jg}(\tau')\right\rangle_{\mathrm{eq}} && (2.126)\\ &= \int_0^t \mathrm{d}\tau \int_0^\tau \mathrm{d}\tau' \left\langle \delta\omega_{ig}(\tau')\delta\omega_{jg}(0)\right\rangle_{\mathrm{eq}} && (2.127)\\ &= \int_0^t \mathrm{d}\tau \int_0^\tau \mathrm{d}\tau' C_{ij}(\tau') && (2.128) \end{aligned}$$

where $C_{ij}(t) = \langle \delta\omega_{ig}(\tau')\delta\omega_{jg}(0)\rangle_{\mathrm{eq}}$ is known as the frequency-frequency correlation function (FFCF), and $g_{ij}(t)$ is the lineshape function. Using the lineshape function in eq 2.124, then assuming it is the first term in the series expansion of $e^{-g(t)}$ yields:

$$\langle \hat{\mu}(t)\hat{\mu}(0)\rangle_{\mathrm{eq}} = \frac{\mathrm{i}}{\hbar}\sum_{g,a} |\mu_{ag}|^2 e^{-\mathrm{i}\overline{\omega}_{ag}t} e^{-g_{aa}(t)}. \tag{2.129}$$

This equation can describe complicated lineshapes. The FFCF can be computed using one's favorite tools and used to obtain a model linear absorption spectrum, including the lineshape. The equation above involves only the autocorrelation functions, but nonlinear spectroscopy will require the inclusion of cross-correlation functions C_{ij} where $i \neq j$. Since this result was obtained using an expansion truncated to the second order term, the technique is called the cumulant expansion to second order.

The lineshape functions corresponding to common dephasing processes are listed below.

$$g^{(\mathrm{H})}(t) = \gamma t \tag{2.130}$$

$$g^{(\mathrm{I})}(t) = \frac{1}{2}\sigma^2 t \tag{2.131}$$

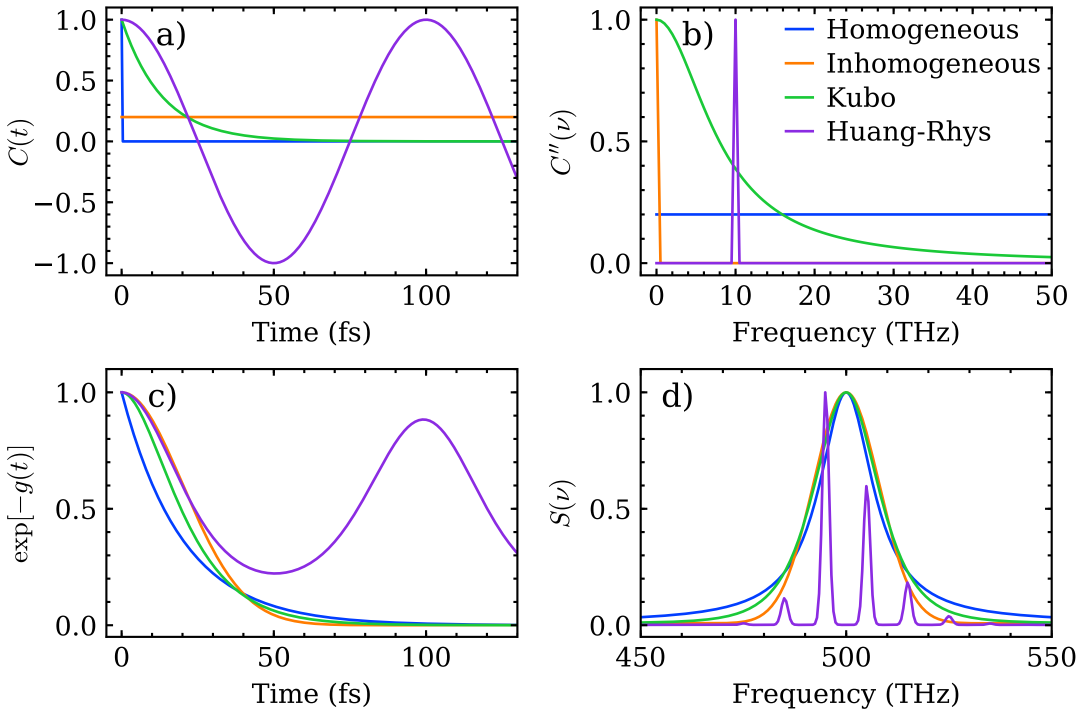

Figure 2.3: Common lineshapes functions: Homogeneous dephasing (blue), Inhomogeneous dephasing (orange), Kubo ansatz (green), Huang-Rhys coupling to vibrations (red). (a) Correlation functions in the time domain. (b) Spectral densities of the associated fluctuations. (c) Dephasing envelope $e^{-g(t)}$. (d) Linear spectrum with $\overline{\nu}_{eg} = 500$ THz. A small amount of inhomogeneous dephasing was added to the Huang-Rhys case to prevent Fourier leakage.

$$g^{(\mathrm{K})}(t) = \sigma^2\tau^2\left(e^{-t/\tau} + t/\tau - 1\right) \tag{2.132}$$

$$g^{(\mathrm{HR})}(t) = S\left(\coth\left[\frac{\hbar\omega_{\mathrm{vib}}}{2k_BT}\right]\left[1 - \cos\left(\omega_{\mathrm{vib}}t\right)\right] + \mathrm{i}\left[\sin\left(\omega_{\mathrm{vib}}t\right) - \omega_{\mathrm{vib}}t\right]\right). \tag{2.133}$$

These lineshape functions are illustrated on Fig 2.3.

The lineshape $g^{(\mathrm{H})}$ corresponds to homogeneous dephasing; it yields a Lorentzian lineshape with linewidth parameter γ. A Gaussian distribution of oscillators with a fixed transition frequency can be modeled using inhomogeneous dephasing $g^{(\mathrm{I})}$, where σ is the standard deviation of the energy levels, in units of angular frequency.

Both cases correspond to limits of the Kubo lineshape function, $g^{(\mathrm{K})}$. This lineshape function can be obtained from the correlation function:

$$C^{(K)}(t) = \sigma^2 e^{-|t|/\tau} \tag{2.134}$$

where σ^2 is the variance of the fluctuations and τ is a decorrelation timescale. This correlation function corresponds to the Ornstein-Uhlenbeck process. This describes the behavior of an overdamped oscillator subject to random kicks. Taking the limit of $\tau \gg t$ yields the inhomogenous case, whereas $\tau \ll 1/\nu_{eg}$ yields the homogeneous case.

The Huang-Rhys lineshape function $g^{(\mathrm{HR})}$ corresponds to Franck-Condon coupling between the electronic excitation and a vibrational mode. The equation above, although somewhat long, has only 3 parameters: the Huang-Rhys coupling parameter S, the mode frequency ω_{vib} and temperature T. The spectrum obtained using the Huang-Rhys lineshape function corresponds to the usual Frank-Condon progression. Inspection of Fig 2.3d reveals the 0-phonon line is slightly red-shifted. This is a consequence of the definition of our fluctuations: the transition energy entering in eq 2.129 is the average transition energy, ie: the barycenter, not the pure electronic gap. Indeed, the inclusion of Frank-Condon transitions shifts the barycenter of a band by $S\hbar\omega_{\mathrm{vib}}$ [19]. In order to keep the 0-phonon line fixed, it is necessary to blueshift the average transition energy by the same amount.

The red-shift in the Huang-Rhys parameter arises from the imaginary part of eq 2.133. Contrary to the other cases, this function is complex. Indeed, in general lineshape functions are complex, a fact that arises from the symmetry properties of quantum correlation functions, which differ slightly from those of classical correlation functions (see [3] chap. 8). The real part induces dephasing, whereas the imaginary part indicates frequency shifts. The most straightforward way to enforce the symmetry constraints is to use the spectral density corresponding to the fluctuations. The correlation function can be computed from the Fourier-domain representation of the energy fluctuations:

$$\delta E_i(\omega) = \mathcal{F}\delta E_i(t) \tag{2.135}$$

$$C''_{ij}(\omega) = \frac{1}{\hbar^2}\frac{\hbar\omega}{2k_BT}\delta E_i(\omega)\delta E^\star_j(\omega) \tag{2.136}$$

$$C_{ij}(\omega) = \left[1 + \coth\left(\frac{\hbar\omega}{2k_BT}\right)\right] C''_{ij}(\omega) \tag{2.137}$$

$$C_{ij}(\omega) = \mathcal{F}C_{ij}(t) \tag{2.138}$$

where $C''(\omega)$ is the odd part of $C(\omega)$ and $\delta E_i(t)$ is the trajectory the energy of state i. Equation 2.136 is a statement of the Wiener-Khinchin theorem. The demonstration of equation 2.137 is not carried out here, it relies on the symmetry properties of quantum correlation functions. See [3] chapter 8. The lineshape function can be obtained directly from $C(\omega)$ using:

$$g_{ij}(t) = -\frac{1}{2\pi}\int_{-\infty}^{\infty} \mathrm{d}\omega \frac{C_{ij}(\omega)}{\omega^2}\left[e^{-\mathrm{i}\omega t} + \mathrm{i}\omega t - 1\right]. \tag{2.139}$$

This allows the determination of lineshape from arbitrary spectral densities of the energy level fluctuations [3, 20]. This approach will be demonstrated in chapter 5.

2.3.4 The Multimode Brownian Oscillator model.

The equations outlined above allow the computation of lineshape functions from arbitrary sources, such as detailed numerical calculations. It is interesting to establish a way to assemble lineshape functions corresponding to common processes. Experimental spectroscopists already do this to make up model energy level diagrams[1]; it is desirable to do the same for lineshapes. This can be achieved by using the Multimode Brownian Oscillator model (MBO), as presented by Mukamel [3].

This model partitions the total system in 3 domains: the electronic system (the system), primary nuclear coordinates q_k and secondary nuclear coordinates x_l. Fluctuations of the energy levels arise from coupling to the fluctuating primary nuclear coordinates, which are themselves coupled to the secondary coordinates:

$$\delta E_i(t) = \sum_k \xi_{ik} \delta q_k(t) \tag{2.140}$$

$$m_k \ddot{q}_k(t) = -m_k \omega_k^2 q_k(t) - m_k \int_{-\infty}^{t} \mathrm{d}\tau \gamma_k(t-\tau) \dot{q}_k(\tau) + f_k(t) \tag{2.141}$$

$$f_k(t) = \sum c_{kl} \delta x_l(t) \tag{2.142}$$

$$\gamma_k(t) = \frac{1}{2 m_k k_B T} \langle f_k(t) f_k(0) \rangle \tag{2.143}$$

where $\delta q_k(t)$ is the fluctuating part of the primary coordinate, ξ_{ik} is the real coupling constant between nuclear mode k and state i, m_k is the effective mass of mode k, $\delta x_l(t)$ is the fluctuating part of secondary mode l and c_{kl} is the coupling constant between q_k and x_l. The secondary mode act on the first modes as a random fluctuating force $f_k(t)$ and the associated coupling constant. The couplings ξ_{ik} and c_{kl} are considered constant, ie: invariant with time, q or x. Eq 2.141 is a Generalized Langevin equation. The behavior of secondary bath modes is of little interest, it matters only inasmuch as it affects the primary modes through the statistical forces $f_k(t)$ (fluctuation) and γ (dissipation). A common case is to assume the random force has

---

[1] We just draw sticks.

no memory, yielding: $\langle f_k(t) f_k(0)\rangle \propto \delta(t)$. This is called the Markov approximation, the associated dynamics are called Markovian dynamics[1].

The MBO model further assumes the primary bath modes are uncorrelated, which is a common approximation in classical statistical mechanics[2].

$$k \neq k' \implies \langle \delta q_k(t) \delta q_{k'}(0)\rangle = 0 \tag{2.144}$$

where $\langle \ldots \rangle$ indicate a stationary ensemble average, ie: average over the ensemble distribution and over initial times. This assumption yields the following expressions for the correlation functions:

$$\begin{aligned} C_{ij}(t) &= \langle \delta E_i(t) \delta E_j(0)\rangle && (2.145)\\ &= \sum_k \xi_{ik}\xi_{jk'} \langle \delta q_k(t) \delta q_{k'}(0)\rangle && (2.146)\\ &= \sum_k \xi_{ik}\xi_{jk} \langle \delta q_k(t) \delta q_k(0)\rangle && (2.147)\end{aligned}$$

ie: all correlation functions can be expressed as a sum of autocorrelation functions. They all have the same symmetries. Furthermore, the correlation functions of the energy levels must obey the Cauchy-Schwarz inequality:

$$\left|C_{ij}(t)\right|^2 \leq \left|C_{ii}(t) C_{jj}(t)\right|. \tag{2.148}$$

---

[1] This term should only be employed in the presence of a well-defined Generalized Langevin equation. Theoreticians get susceptible otherwise.

[2] Otherwise you're in heavy trouble [21, 22].

This further allows the separation of the lineshape function into multiple independent components:

$$g_{ij}(t) = \sum_k \xi_{ik}\xi_{jk} g_{ij}^{(k)}(t) \tag{2.149}$$

This equation allows the mix and matching of lineshape functions. We will see an example of this in chapter 5.

The MBO model separates the nuclear motions into modes with an explicit treatment, the primary modes q_k, and modes which are averaged out, the secondary modes x_l. The primary modes then obey a generalized Langevin equation, with fluctuations and dissipation arising from their coupling to the secondary modes. This is the description of a projection operator where the electronic degrees of freedom and the primary coordinates (and their momenta) are part of the system, and the secondary coordinates form the bath. This forms a closed set of integro-differential equations for which the correlation functions are known. This situation is different from the orthodox system-bath partitioning of quantum open systems, in which all nuclear motions are part of the bath.[1]

2.4 2D spectroscopy

The stage has been set to discuss the most advanced experiment contained in this thesis: 2D spectroscopy. The use of advanced tools like DSFDs will be much more natural for the description of 2D spectroscopy. Hopefully, the detailed treatment of linear spectroscopy allows an efficient description of 2DE where the focus is on the specifics of CMDS instead of formalism. The assignation of features in a 2D spectrum is usually carried out with the help of DSFD. The modeling of coherent lineshape

---

[1] An excellent display of ambiguous jargon. Well done Prof. Mukamel!

dynamics will be achieved with the help of the cumulant expansion of the 4-point correlation function and the MBO model.

2.4.1 Third order response pathways in Liouville space

The third order response contains many more terms than the linear response. The third order response is given by:

$$\chi^{(3)} = \Big(\mu|\hat{\hat{G}}(t_3)\hat{\hat{\mu}}\hat{\hat{G}}(t_2)\hat{\hat{\mu}}\hat{\hat{G}}(t_1)\hat{\hat{\mu}}|\rho_{\mathrm{eq}}\Big)\,. \tag{2.150}$$

The equation can thus be expanded to where each electric field superoperator μ expands to two terms, one acting on the bra and one acting on the ket (eq 2.46). As discussed previously, the expansion results in 8 terms, 4 of which are the complex conjugates of the others:

$$\chi^{(3)} = R_1 + R_2 + R_3 + R_4 + \text{c.c.}. \tag{2.151}$$

The conventional assignment of these terms is presented on Fig 2.4. The anatomy of a DSFD is recalled on panel a. All the diagrams follow a similar pattern: evolution in a coherence during t_1 then in a population during t_2 and finally again in a coherence during t_3. This allows the separation of the four terms in two families of light-matter interactions and two phase-matching conditions. All the signals have the same sign (positive).

The physical phenomena correspond to stimulated emission (SE) and ground state bleach (GSB). The SE pathways have two distinguishing features: the evolution during t_2 corresponds to the excited state population $|aa)$. These diagrams thus probe the excited state dynamics. Furthermore, the third light-matter interaction is an emission, as shown by the corresponding arrow. Conversely, the GSB pathways evolve in the ground state population $|gg)$ during delay t_2. The third light-matter

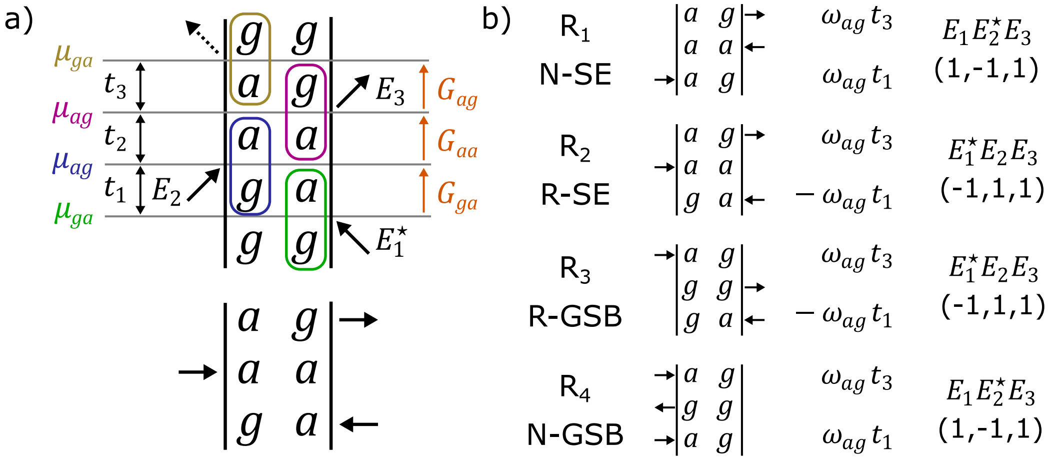

Figure 2.4: Double sided Feynman diagrams for a two-level system. (a) Dissecting a third-order DSFD. Transition dipoles correspond to transitions in the bra or ket, read vertically. Temporal evolution corresponds to the rows of the diagrams, read horizontally. DSFD will be presented in abbreviated form, as shown below. (b) Conventional DSFD for the third order response of a two-level system, R_1 to R_4.

interaction corresponds to absorption. These two signal categories correspond to bleach.

The signals can arise from two different series of interactions with the components of the light fields. The rephasing (R) diagrams correspond to interactions with $E_1^\star E_2 E_3$. The frequency of the oscillation along t_1 is thus reversed with respect to the evolution during t_3. A consequence of this is that some dephasing processes are reversed, yielding an echo signal. The rephasing signals correspond to photon-echo experiments [3, 12]. The non-rephasing signals (N) arise from interactions with $E_1 E_2^\star E_3$. The time-reversal does not happen, and this is sometimes called an anti-echo [23].

The rephasing and non-rephasing signals correspond to different series of light-matter interactions. As such, they have different phase-matching conditions, enumerated on the right. The phase matching condition can be expressed using coherence transfer pathways $\boldsymbol{\alpha}_j$ for signal j. The pathways $\boldsymbol{\alpha}_j$ are vectors of integers of length N for N pulses. The components $\alpha_{i,j}$ indicate the total interaction with field i, with negatives indicating interaction with the conjugate part. Signals with different coherence transfer pathways can be separated by relying on the phases or directions of the input fields. This will be important for the design and understanding of the experiments.

The situation becomes relatively more complicated for a multi-level system. Each of the four responses expand into many terms, depending on which paths the system may take under the influence of any given pulses. In the absence of relaxation, the pathways can be written as follows:

$$R_1 = \sum_{g,a,b,c} (\mu_{ba}|\hat{\hat{G}}_{ba,ba}(t_3)\hat{\hat{\mu}}_{ba,ca}\hat{\hat{G}}_{ca,ca}(t_2)\hat{\hat{\mu}}_{ca,cg}\hat{\hat{G}}_{cg,cg}(t_1)\hat{\hat{\mu}}_{cg,gg}|gg) \tag{2.152}$$

$$R_2 = \sum_{g,a,b,c} (\mu_{cb}|\hat{\hat{G}}_{cb,cb}(t_3)\hat{\hat{\mu}}_{cb,ca}\hat{\hat{G}}_{ca,ca}(t_2)\hat{\hat{\mu}}_{ca,ga}\hat{\hat{G}}_{ga,ga}(t_1)\hat{\hat{\mu}}_{ga,gg}|gg) \tag{2.153}$$

$$R_3 = \sum_{g,a,b,c} (\mu_{cb}|\hat{\hat{G}}_{cb,cb}(t_3)\hat{\hat{\mu}}_{cb,gb}\hat{\hat{G}}_{gb,gb}(t_2)\hat{\hat{\mu}}_{gb,ga}\hat{\hat{G}}_{ga,ga}(t_1)\hat{\hat{\mu}}_{ga,gg}|gg) \tag{2.154}$$

$$R_4 = \sum_{g,a,b,c} (\mu_{cg}|\hat{\hat{G}}_{cg,cg}(t_3)\hat{\hat{\mu}}_{cg,bg}\hat{\hat{G}}_{bg,bg}(t_2)\hat{\hat{\mu}}_{bg,cg}\hat{\hat{G}}_{cg,cg}(t_1)\hat{\hat{\mu}}_{cg,gg}|gg) \tag{2.155}$$

where indices a, b, c are any states of the system, including the ground state. The order of the indices may seem unintuitive, but will be made clearer later. The third order response can thus be decomposed into a sum of pathways involving 4 states each.

The inclusion of multiple states generates new types of pathways, illustrated on Fig 2.5, for a system consisting of a single ground state g, two singly excited states d, e and three doubly excited states k, l and m. State l can be accessed from both d and e, but not states k and m. This system is represented on Fig 2.5a. The energy of the excited states is shifted by their binding energy: $E_k = 2E_d - \Delta_k$, $E_l = E_d + E_e - \Delta_l$,

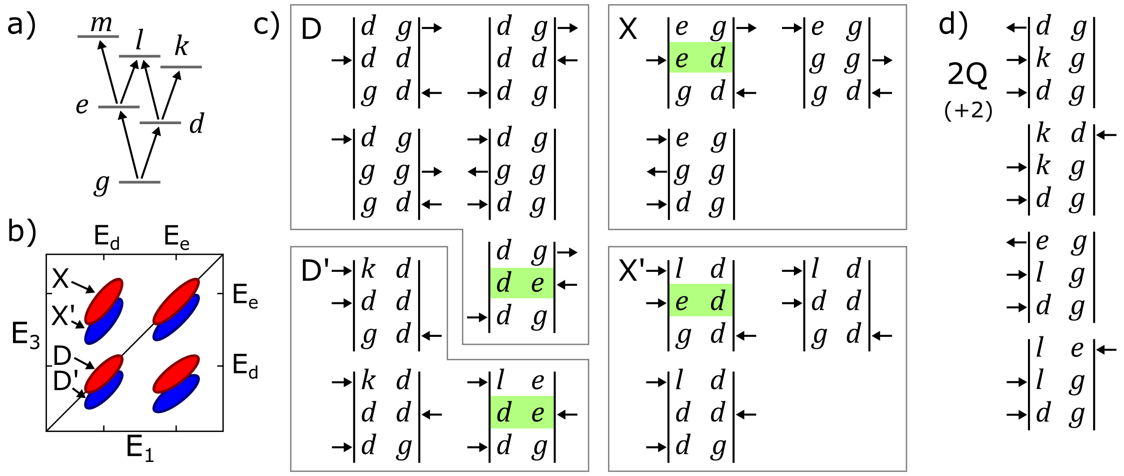

Figure 2.5: DSFD for a multi-level system. (a) Energy level diagram with two singly-excited states and three doubly excited states. (b) Schematic 2D spectrum identifying diagonal peaks D and D′ and cross-peaks X and X′. (c) DSFD. Only diagrams corresponding to initial transition to d are considered. Pathways with a coherent oscillation during t_2 are highlighted. (d) Double quantum (2Q) diagrams.

$E_m = 2E_e - \Delta_m$. For the sake of discussion, the binding energies will be assumed to be small positive numbers causing a redshift in the induced absorption, although this is by no means necessary.

This scheme gives rise to multiple peaks on a 2D spectrum, illustrated on Fig 2.5b. Bleach contributions are indicated in red, induced absorption in blue. The spectrum contains two diagonal peaks, at E_d and E_e. The diagonal peaks arise from SE and GSB contributions. The diagrams corresponding to this peak are listed in the corresponding box of Fig 2.5c for initial transitions $g \rightarrow d$. The diagrams contain the four terms discussed previously, which arise from considering the manifolds formed by g, d or g, e. An extra signal occurs in peak D, where the evolution during t_2 is not in population state $|gg)$ but in a coherent superposition of singly excited states $|de)$. This evolution does not change the peak's location on the 2D spectrum which is dictated by the evolution during t_1 and t_3. However, this signal oscillates during t_2 with frequency ω_{de} and reveals information about the elusive electronic coherences [24, 25]. This signal is a N-SE contribution; there is no corresponding rephasing signal.

The addition of excited states opens up induced absorption (IA) pathways and the corresponding peak D′. The manifold of states g, d, k gives rise to an R-IA and N-IA signal. The induced absorption pathways have an odd number of interactions on the bra, and thus they are negative. The frequency of the oscillation during t_3 is $\omega_{kd} = \omega_{dg} - \Delta_k/\hbar$. The inclusion of states e and l again adds a signal that oscillates during t_2. This is a N-IA signal; along E_3 it is located at $E_{le} = E_{dg} - \Delta_l$. It is thus not located exactly at the same position as the other IA contributions, but should be near if the binding energies are small.

A similar analysis can be repeated for the cross-peaks X and X′. The cross peaks both contain two R and one N contributions. One of the R contribution oscillates. There is the same number of positive (GSB, SE) and negative (IA) pathways. If the features overlap and the contributions have similar amplitudes, the X and X′ peaks will cancel each other.

The existence of a doubly excited state also adds another set of pathways which access states k, l, m from a coherence instead of a population. Examples are shown on Fig 2.5d. The system evolves in a $|kg)$ coherence during t_2, with a frequency that is about double the laser frequency. These pathways are named double-quantum (2Q) pathways (sometimes the pathways are named 0-quantum). The observation of 2Q in electronic spectroscopy has proved elusive, but has been achieved using specific experimental configurations [24, 26–28].

This formalism can also be applied to transient absorption (TA) spectroscopy. In TA, the first two light-matter interactions occur with the first pulse. For the case of impulsive δ pulses, this implies $t_1 = 0$. In the Fourier domain, the TA signal

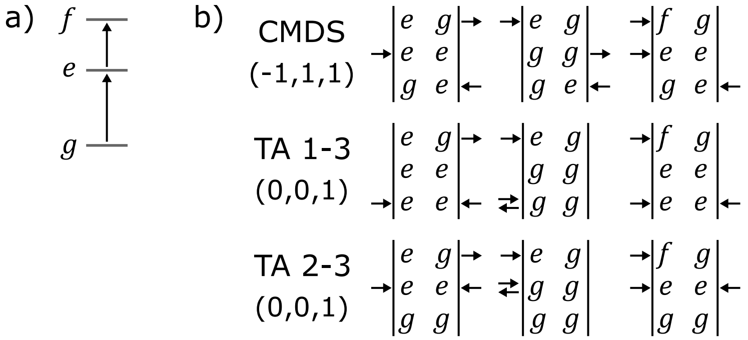

Figure 2.6: Diagrammatic representation of TA experiments. (a) Simple three-level system. (b) Comparison of the signals arising from CMDS contributions and TA signals. TA arising from interactions with pulses 1,3 and 2,3 shown. The TA signals does not depend on the phase of pulses 1,2 as shown by their phase matching vectors. TA from pulses 1,2 not shown. Rephasing signals only.

can be obtained from the 2D signal by integration along ω_1. This equality can be demonstrated using the Fourier projection-slice theorem. Delay t_2 thus corresponds rigorously with the pump-probe delay of TA. On DSFD this is often represented using a pair of arrows interacting at a given time point, as shown on Fig 2.6. Usually, this is done in the context of signal isolation, for a given experiment. For example, a three pulse experiment contains the CMDS signals as well as TA signals arising for any pair of pulses. Every diagram in Figs 2.4 or 2.5 has a two-pulse TA equivalent.

The emblematic observation allowed by TA is relaxation. It is surprising it has not been discussed yet. Indeed, the focus in the literature is to describe the mechanism by which the CMDS signals arise. Relaxation processes are thus a secondary concern with regards to the theoretical description. There is no such inhibitions in experimental works, where dynamical peak intensities are routinely used to extract population kinetics [29–32]. It is a shortcoming of DSFD that they do not represent incoherent relaxation processes easily. They are tailored to represent dynamics corresponding to diagonal elements of the Liouville space Green function. Indeed,

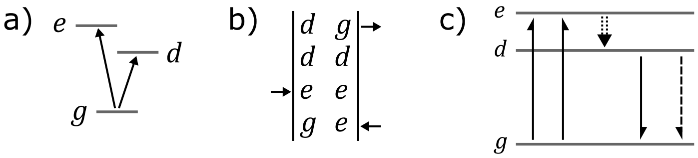

Figure 2.7: Diagrammatic representation of the third order response with relaxation. (a) Simple three-level system. (b) R-SE diagram including relaxation. (c) Example representation of the same process on an energy level diagram. Full lines: light-matter interaction. Dotted lines: incoherent relaxation. Dashed line: Polarization.

equations 2.152 to 2.155 only contain diagonal population dynamics of the form $G_{ii,ii}$. Population transfer can be included by considering off-diagonal terms $G_{jj,ii}$, corresponding to $i \to j$ incoherent relaxation.

The case of CMDS including relaxation is shown on Fig 2.7. The DSFD on panel a contains an extra row, but still three light-matter interactions. It is thus still a third-order process, since the order is defined in respect to the light-matter interaction Hamiltonian as defined in equation 2.16. This pathway can be written using elements of the superoperators:

$$(\mu|G_{dg,dg}(t_3)\mu_{dg,dd}\underline{G_{dd,ee}}(t_2)\mu_{ee,ge}G_{ge,ge}(t_1)\mu_{ge,gg}|gg), \tag{2.156}$$

where it is apparent that the process is a third order process with respect to light-matter interaction. Population relaxation is highlighted by an underline. The computation of the relaxation Green function $G_{dd,ee}(t)$ may require integration over one (or more) delays, but it is a property of the material Hamiltonian. Care has to be taken when including relaxation. The coherence Green functions need to include relaxation of the corresponding populations [3]. The different elements of $\hat{\hat{G}}$ have to obey the detailed balance condition, to avoid the spontaneous creation of matter.

It is clumsy to add relaxation to a DSFD; time-evolution during t_2 now covers two rows, which is not the standard notation. Indeed, there seems to be no standard notation to describe this. Sometimes dashed lines are added, wiggly arrows, and so on. It can be helpful in that case to represent the process on an energy level diagram, as is done on Fig 2.7c. The side of the harpoon indicates interaction with the ket (left) or bra (right). Line styles can be used to represent different types of interaction, though this is not subject to a strong convention in the literature[1].

The preceding discussion illustrates the use of DSFD to understand and analyze 2DE spectra. Fig 2.5 covers most of the common cases, but is not exhaustive. As such, a similar analysis has to be carried out on a case-by-case basis. For example, a system with two ground states would yield a different pattern of peaks. The analysis is greatly facilitated by the use of DSFD. Studying the DSFD reveal the location of the signals on a 2D spectrum, as well as the oscillation frequency during t_2 — if any. The analysis of the light-matter interaction reveals the coherence transfer pathways, which informs experimental design and operation. The transcription of DSFD into equations can be used to realize quantitative models including transition dipoles, transition energies, population relaxation and phenomenological lineshapes.

2.4.2 Four-point correlation functions in Hilbert space

We now turn to the rigorous description of lineshapes in 2DE using lineshape functions as was outlined in section 2.3.3. The derivation follows the same lines. In Hilbert space, the third order polarization can be written as:

$$\chi^{(3)}(t_1, t_2, t_3) = \frac{\mathrm{i}}{\hbar^3} \left\langle [\mu(t_3), [\hat{\mu}(t_2)\, [\hat{\mu}(t_1), \hat{\mu}(0)]]] \right\rangle_{\mathrm{eq}} . \tag{2.157}$$

---

[1] The diagram on Fig 2.7c has an issue. It does not represent which component of E causes the interaction as obviously as conventional DSFD.

Fully expanding the commutators yield 8 terms, 4 of which are complex conjugates of the other. All terms can be written as the product of 4 dipole operators with permutations of the arguments. Cast into this form, this equation is known as the four-point correlation function of the transition dipole:

$$\Phi(\tau_1, \tau_2, \tau_3, \tau_4) = \langle \hat{\mu}(\tau_1)\hat{\mu}(\tau_2)\hat{\mu}(\tau_3)\hat{\mu}(\tau_4)\rangle \tag{2.158}$$

$$= \sum_{g,a,b,c} \langle \mu_{ga}(\tau_1)\mu_{ab}(\tau_2)\mu_{bc}(\tau_3)\mu_{cg}(\tau_4)\rangle_{\mathrm{eq}} \tag{2.159}$$

where the second equation is obtained from the first by expanding each μ into a basis of states. This is valid in the absence of relaxation.

Computing the expectation value for eq 2.159 takes the system through a loop consisting of four states:

$$g \leftrightarrow a \leftrightarrow b \leftrightarrow c \leftrightarrow g. \tag{2.160}$$

This path is known as the third-order Hilbert space path (or Hilbert path). This can be understood by decomposing $\hat{\mu}$ in the basis of states:

$$\hat{\mu} = \sum_{i,j} \mu_{ij} |i\rangle \langle j| . \tag{2.161}$$

Using this in the transition dipole operator in Hilbert space:

$$\hat{\mu}(t) = \exp_{-}\left(\mathrm{i}\int_{-\infty}^{t} \mathrm{d}\tau \hat{H}_0(\tau)\right) \hat{\mu} \exp_{+}\left(-\mathrm{i}\int_{-\infty}^{t} \mathrm{d}\tau \hat{H}_0(\tau)\right) \tag{2.162}$$

$$\mu_{ij}(\tau) = |i\rangle \exp_{-}\left(\mathrm{i}\int_{-\infty}^{t} \mathrm{d}\tau \hat{H}_i(\tau)\right) \mu_{ij} \exp_{+}\left(-\mathrm{i}\int_{-\infty}^{t} \mathrm{d}\tau \hat{H}_j(\tau)\right) \langle j| . \tag{2.163}$$

Conceptually, $\mu(t)$ propagates the system forward in time for duration t, the transition $i \rightarrow j$ occurs, and the system is restored back to its initial time position by the reverse propagator. The net result is the accumulation of a phase factor, due

Table 2–1: Correspondence between Hibert and Liouville paths. State g corresponds to any ground state, e to any first excited state and f to any doubly excited state.

	Delays				Path			
Type	τ_1	τ_2	τ_3	τ_4	a	b	c	Signal
N-SE	t_1	t_1+t_2	$t_1+t_2+t_3$	0	e	g	e	R_1
R-SE	0	t_1+t_2	$t_1+t_2+t_3$	t_1	e	g	e	R_2
R-GSB	0	t_1	$t_1+t_2+t_3$	t_1+t_2	e	g	e	R_3
N-GSB	$t_1+t_2+t_3$	t_1+t_2	t_1	0	e	g	e	R_4
R-IA	t_1	t_1+t_2	$t_1+t_2+t_3$	0	e	f	e	$-R_1^\star$
N-IA	0	t_1+t_2	$t_1+t_2+t_3$	t_1	e	f	e	$-R_2^\star$
2Q-IA	0	t_1	$t_1+t_2+t_3$	t_1+t_2	e	f	e	$-R_3^\star$
2Q-SE	$t_1+t_2+t_3$	t_1+t_2	t_1	0	e	f	e	R_4

to the forward and backwards evolution occurring in different states. Furthermore, time-dependent system Hamiltonians will induce dephasing.

The correspondence between the Hilbert space description using eq 2.159 and the Liouville space pathways of eqs 2.152 to 2.155 is presented in Table 2–1. Different permutations of the time arguments give rise to the different pathways R_1 to R_4. The pathway elements a and c are any states with an allowed transition from the ground state, any singly excited states. The pathway element b is any state accessible from said singly excited state, thus any ground state or doubly excited state. The application of conventional rules of DSFD results in the complex conjugation of the induced absorption pathways.

The complete expansion of eq 2.159 using eq 2.163 is rather tedious. It follows the procedure outlined in section 2.3.3. The main steps are recalled here. The system Hamiltonians are separated in an average and fluctuating part $\hat{H}_i(t) = \hbar\omega_{ig} + \hat{V}_{ig}(t)$. The ground state Hamiltonian is taken as a frame of reference and $\hat{\mu}$ expressed in the corresponding interaction picture. The positive and negative time-ordered exponents are expanded in a series, up to second order. The products are taken, once again keeping only terms up to second order. Finally, a math trick is required in order to convert every term to a lineshape function. The lineshape functions are converted back to exponential assuming they are the first term in a truncated expansion. The whole process is detailed in section 8A of [3]. The result is as follows:

$$R_1(t_1,t_2,t_3) = \sum_{g,a,b,c} \mu_{ga}\mu_{ab}\mu_{bc}\mu_{cg} \exp\left(-\omega_{ab}t_3 - \omega_{ac}t_2 - \omega_{ag}t_1\right) F_1(t_1,t_2,t_3) \tag{2.164}$$

$$R_2(t_1,t_2,t_3) = \sum_{g,a,b,c} \mu_{ga}\mu_{ab}\mu_{bc}\mu_{cg} \exp\left(-\omega_{ab}t_3 - \omega_{ac}t_2 + \omega_{cg}t_1\right) F_2(t_1,t_2,t_3) \tag{2.165}$$

$$R_3(t_1,t_2,t_3) = \sum_{g,a,b,c} \mu_{ga}\mu_{ab}\mu_{bc}\mu_{cg} \exp\left(-\omega_{ab}t_3 + \omega_{bg}t_2 + \omega_{cg}t_1\right) F_3(t_1,t_2,t_3) \tag{2.166}$$

$$R_4(t_1,t_2,t_3) = \sum_{g,a,b,c} \mu_{ga}\mu_{ab}\mu_{bc}\mu_{cg} \exp\left(-\omega_{cg}t_3 - \omega_{bg}t_2 - \omega_{ag}t_1\right) F_4(t_1,t_2,t_3) \tag{2.167}$$

where ω_{ij} is the average transition energy in angular frequency, and F_i is a dephasing function. The dephasing functions are:

$$\begin{aligned} F_1(t_1,t_2,t_3) = \exp[&- g^\star_{cc}(t_2) - g^\star_{bb}(t_3) - g_{aa}(t_1+t_2+t_3) \\ &- g^\star_{cb}(t_2+t_3) + g^\star_{cb}(t_2) + g^\star_{cb}(t_3) \\ &+ g_{ca}(t_1+t_2) - g_{ca}(t_1) + g^\star_{ca}(t_2+t_3) \\ &- g^\star_{ca}(t_3) + g_{ba}(t_1+t_2+t_3) - g_{ba}(t_1+t_2) \\ &+ g^\star_{ba}(t_3)] \end{aligned} \tag{2.168}$$

$$\begin{aligned} F_2(t_1,t_2,t_3) = \exp[&- g^\star_{cc}(t_1+t_2) - g^\star_{bb}(t_3) - g_{aa}(t_2+t_3) \\ &- g^\star_{cb}(t_1+t_2+t_3) + g^\star_{cb}(t_1+t_2) + g^\star_{cb}(t_3) \\ &+ g_{ca}(t_2) + g^\star_{ca}(t_1+t_2+t_3) - g^\star_{ca}(t_1) \\ &- g^\star_{ca}(t_3) + g_{ba}(t_2+t_3) - g_{ba}(t_2) \\ &+ g^\star_{ba}(t_3)] \end{aligned} \tag{2.169}$$

$$F_3(t_1,t_2,t_3) = \exp[- g^\star_{cc}(t_1) - g^\star_{bb}(t_2+t_3) - g_{aa}(t_3)$$

$$\begin{aligned}
&- g^{\star}_{cb}(t_1 + t_2 + t_3) + g^{\star}_{cb}(t_1) + g^{\star}_{cb}(t_2 + t_3) \\
&+ g^{\star}_{ca}(t_1 + t_2 + t_3) - g^{\star}_{ca}(t_1 + t_2) - g^{\star}_{ca}(t_2 + t_3) \\
&+ g^{\star}_{ca}(t_2) + g_{ba}(t_3) - g^{\star}_{ba}(t_2 + t_3) \\
&+ g^{\star}_{ba}(t_2)]
\end{aligned} \tag{2.170}$$

$$\begin{aligned}
F_4(t_1, t_2, t_3) = \exp[&- g_{cc}(t_3) - g_{bb}(t_2) - g_{aa}(t_1) \\
&- g_{cb}(t_2 + t_3) + g_{cb}(t_2) + g_{cb}(t_3) \\
&- g_{ca}(t_1 + t_2 + t_3) + g_{ca}(t_1 + t_2) + g_{ca}(t_2 + t_3) \\
&- g_{ca}(t_2) - g_{ba}(t_1 + t_2) + g_{ba}(t_1) \\
&+ g_{ba}(t_2)].
\end{aligned} \tag{2.171}$$

where g_{ij} are lineshape function as defined in section 2.3.3. Contrary to eq 2.129, the dephasing functions depend on the correlation between the fluctuations of different states — a critial component of dynamical lineshapes.

The equations 2.164 to 2.171 are rather long and complicated, but straightforward. The cumulant expansion is easily taught to a computer. A spectroscopic model can be fully specified by three ingredients:

1. Transition dipoles;
2. Energy levels;
3. Lineshape functions, for all pairs of states.

The lineshape functions are not only necessary for states coupled via a spectroscopic transition, but for all states. A convenient numerical code can be realized by designing a data structure to contain these ingredients. It is easy for a computer to compute the responses over a 3-dimensional grid of time delays. The sum over possible Hilbert space paths is similarly easy to abstract out. A module for the `Julia` programming language has been coded[1] and is available online [33]. The modeling of coherent lineshape dynamics is easily realized with this toolkit. As an added bonus, the same parameters can be used to compute a model linear absorption spectrum, PL spectrum, etc.

The numerical calculation of the 2D spectra is a very useful tool. The multiple terms with opposite signs can give rise to subtle cancellation effects. This can outright remove the dependence on some delays[2]. For example, the 2D lineshapes for homogeneous (eq 2.130) and inhomogeneous (eq 2.131) dephasing do not depend on t_2 despite the explicit dependence in eqs 2.168 to 2.171. The lineshapes are shown on Fig 2.8. The 2D spectrum for pure homogeneous dephasing, shown on panel a, has a star-like shape which should be familiar from NMR. Its projections along E_1 and E_3 are Lorentzian lineshapes. The addition of inhomogeneous dephasing stretches the lineshape along the diagonal, as shown on Fig 2.8b. This behavior can be understood as a Gaussian distribution of oscillators. The spectrum can also be obtained by the convolution of a 2D Lorentzian with a 1D Gaussian distribution of central frequencies.

The Kubo lineshape gives rise to spectral dynamics during t_2. Figure 2.9 shows 2D spectra obtained with this lineshape function at two values of delay t_2. This spectrum was obtained by using homogeneous and Kubo lineshapes, with parameters γ=10 meV, σ=20 meV, τ=50 fs. The homogeneous term serves to avoid truncation in the time domain at small values of t_2/τ. The spectrum is initially stretched along the diagonal as in the inhomogeneous case. The different oscillators in the

---

[1] Hand-written by yours truly. Hopefully fast, hopefully easy to use.

[2] I call this Mukamel magic.

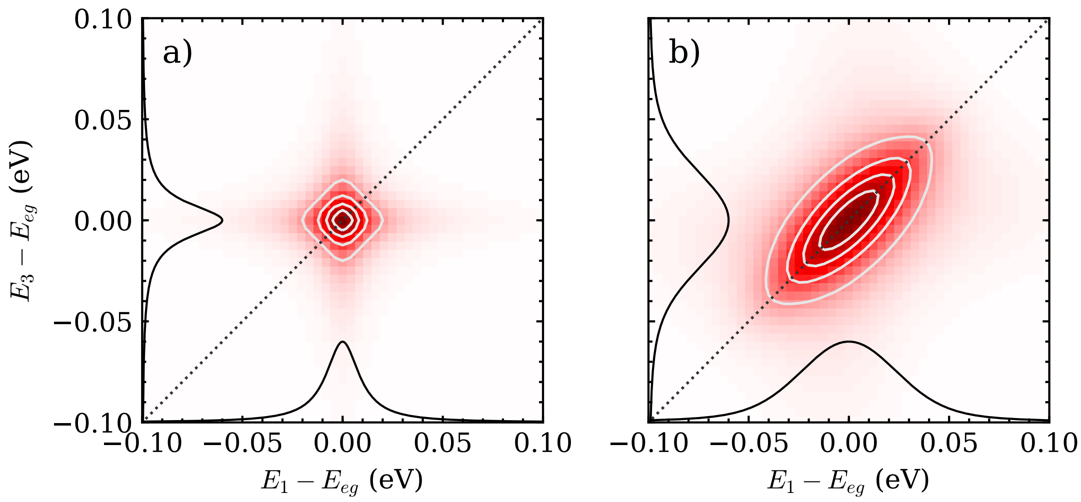

Figure 2.8: Real absorptive 2D spectra for homogeneous and inhomogeneous dephasing. These lineshapes do not change with delay t_2. Projections along E_1 and E_3 shown in black. (a) Homogeneous dephasing only, $\gamma = 10$ meV) (b) Homogeneous dephasing and inhomogeneous dephasing, $\gamma = 10$ meV, $\sigma = 20$ meV.

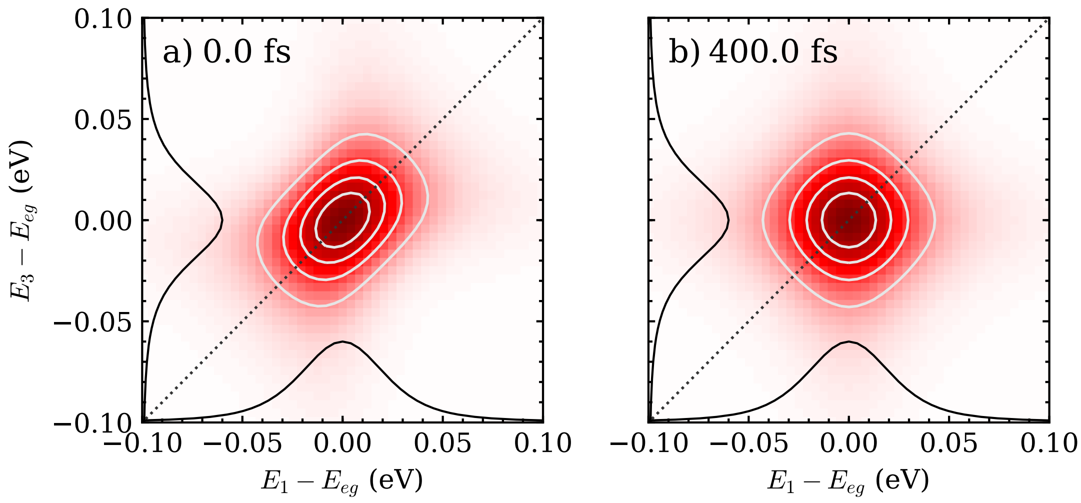

Figure 2.9: The Kubo lineshape gives rise to spectral dynamics. 2D spectrum obtained using homogeneous dephasing and the Kubo lineshape. Parameters: γ=10 meV, σ = 20 meV, τ = 50 fs. (a) t_2=0 fs (b) t_2=400 fs.

ensemble have a distribution of frequencies. As time progresses, the feature rounds off as the oscillators loose memory of their initial resonance frequency. Each vertical slice (fixed E_1) returns to the equilibrium distribution. This behavior is indicative of spectral diffusion. The projections are unaffected by this process. Note the long time spectrum is a round two-dimensional Gaussian, different from the star shape of the homogeneous case. The feature is not perfectly circular as the homogeneous contribution distorts the spectrum a bit.

The Huang-Rhys lineshape corresponds to the well known Frank-Condon transitions describing an electronic transition accompanied by a change in the vibrational number Δv. The lineshape has 3 parameters: the Huang-Rhys coupling strength S, vibrational frequency ω_{vib} and temperature T. The impact of these parameters is well known [19]: S modulates the intensity of the various vibronic lines as a function of $|\Delta v|$, ω_{vib} correspond to the spacing between the bands and T adjusts the relative intensity of the $\Delta v > 0$ vs the $\Delta v < 0$ bands. Model 2D spectra for two-level system are shown on Fig 2.10 for two parameter sets. The two cases differ only by the value of S: 0.2 for panels a and b, 2.0 for panels c and d. In both cases, the spectra is obtained by summing homogeneous dephasing (eq 2.130, γ=10 meV), inhomogeneous dephasing (eq 2.131, σ =20 meV) and Huang-Rhys coupling (eq 2.133, ω_{vib}=103 meV, kT=80 meV). The homogeneous and inhomogeneous contributions dictate the lineshape of individual bands.

The spectra have rich oscillatory dynamics with period $2\pi/\omega_{\text{vib}}$=40 fs. The spectra are shown for integer periods (a, c) and half periods (b, d). The behavior of the spectra is rather complicated, and quite interesting in video format. The two parameter sets discussed above show qualitatively distinct dynamics. In the weak coupling case, the diagonal and off diagonal peaks oscillate out of phase, corresponding to

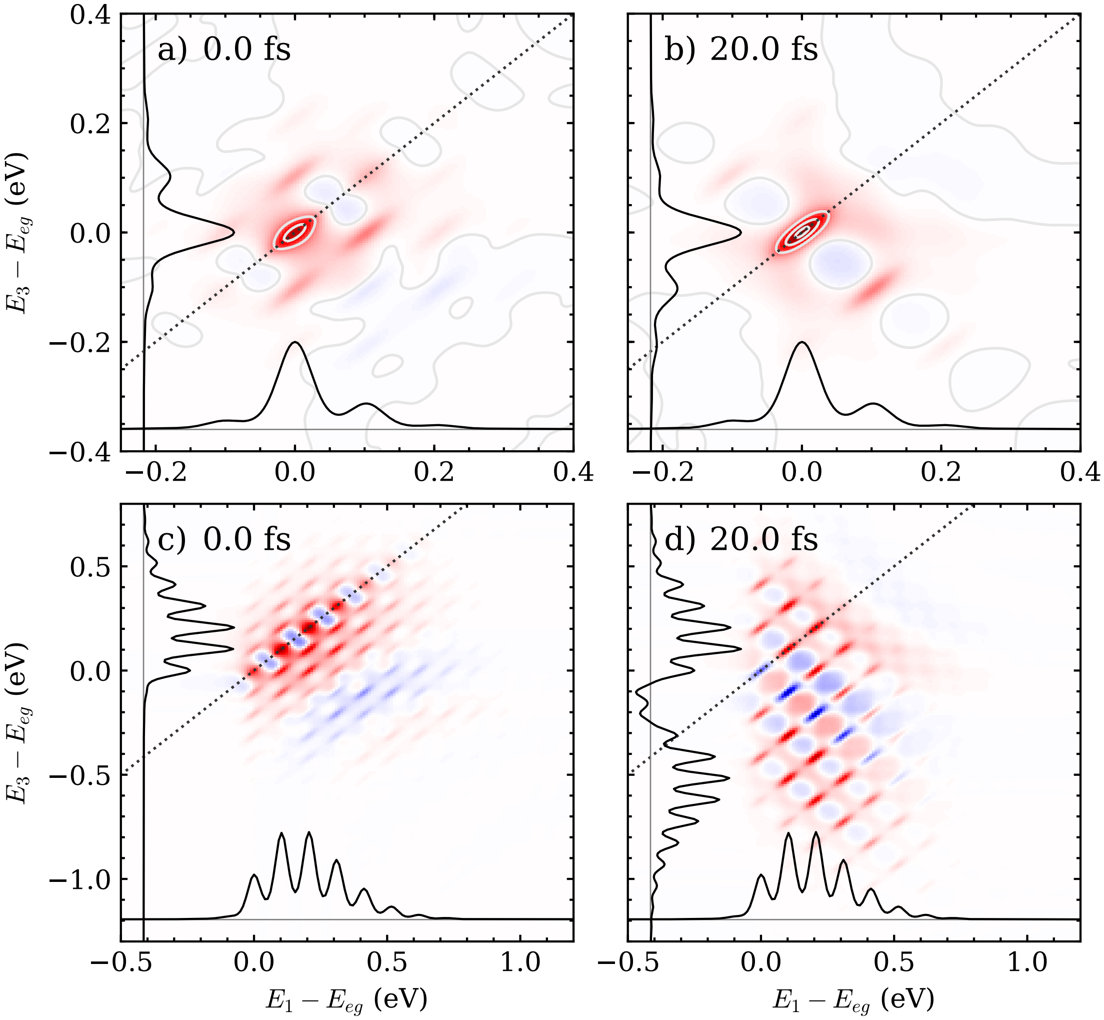

Figure 2.10: Model 2D spectra using the Huang-Rhys lineshape. Cases for weak coupling (S=0.2, top) and strong coupling (S=2.0, bottom) at initial time (left) and after half a period. The spectra can be interpreted as the Frank-Condon peaks oscillating with varying phases.

coupled oscillators. For strong coupling, the entire feature waves out along the diagonals and cross-diagonal, in a manner suggestive of wavepacket dynamics. This rich behavior gives rise to coherent modulations of the 2D lineshape [34]. The result can be obfuscated depending on the value of the lineshape parameters, motivating the use of modeling even for simple microscopic models.

Vibrational wavepacket dynamics are one possible source of coherent lineshape dynamics; the only common source for two-level systems. Coherent oscillations in the 2D spectrum also arise in the case of electronic coherences between two singly excited states. A model 2D spectrum for a three-level system (g, e, d) is shown on Fig 2.11. The DSFD for the signals oscillating as a function of t_2 are highlighted in Fig 2.5. These dynamics contributions oscillate as $\cos(\omega_{ab} t_2)$. After half a period, the oscillating contributions are negative and reduce the peak amplitudes. The cancellation is almost perfect for the cross-peak; the residue arises for slight phase shifts of the oscillation in the E_1, E_3 plane. The specific lineshape parameters are: $\gamma_{dd} = \gamma_{ee} = \gamma_{de} = \gamma$=10 meV, $\sigma_{dd} = \sigma_{ee} = \sigma_{de} = \sigma$=20 meV.

The duration of the electronic coherence depends on the degree of correlation between the states involved in the coherence. Using the cumulant expansion approach detailed here, this is governed by the lineshape functions with mixed indices. Fig 2.12 shows the cross-peak dynamics for two cases: $\gamma_{de} = \sqrt{\gamma_{ee}\gamma_{dd}} = \gamma$ and $\gamma_{de} = 0$. In the first case, the correlation is perfect and the interexcitonic coherence never dephases. This case occurs when eq 2.148 is an equality. In the second case, the $|e\rangle\langle d|$ coherence dephases with an homogeneous dephasing rate of $\gamma_{dd} + \gamma_{ee}$. The associated peak dynamics dampen out on the corresponding time scale. It is interesting to realize the electronic coherence is present even in the case of uncorrelated fluctuations [35]. For a 3-level system, the electronic coherence has a minimum lifetime related to

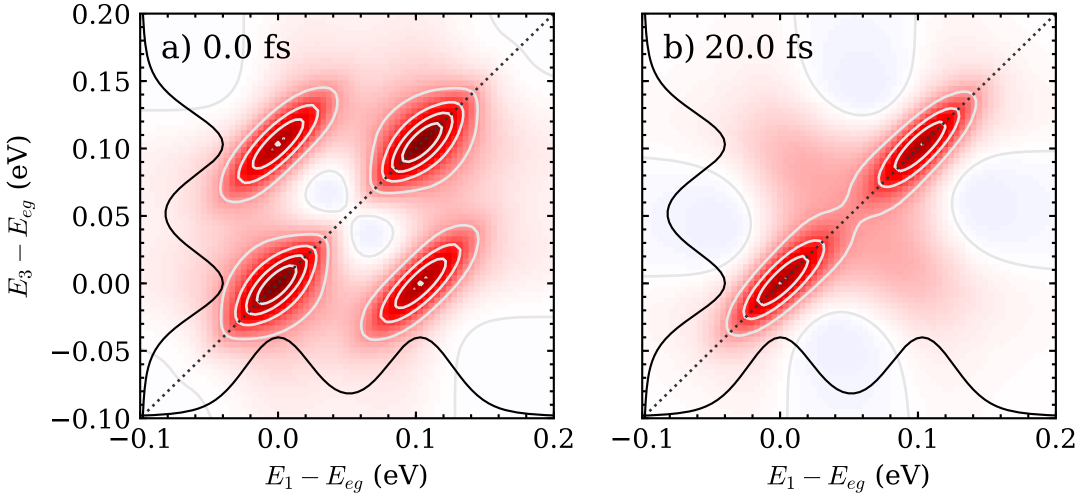

Figure 2.11: Spectral dynamics arising from an electronic coherence. The spectra are shown of t_2=0 and after half a cycle. Lineshape parameters identical to Fig 2.8b for both states.

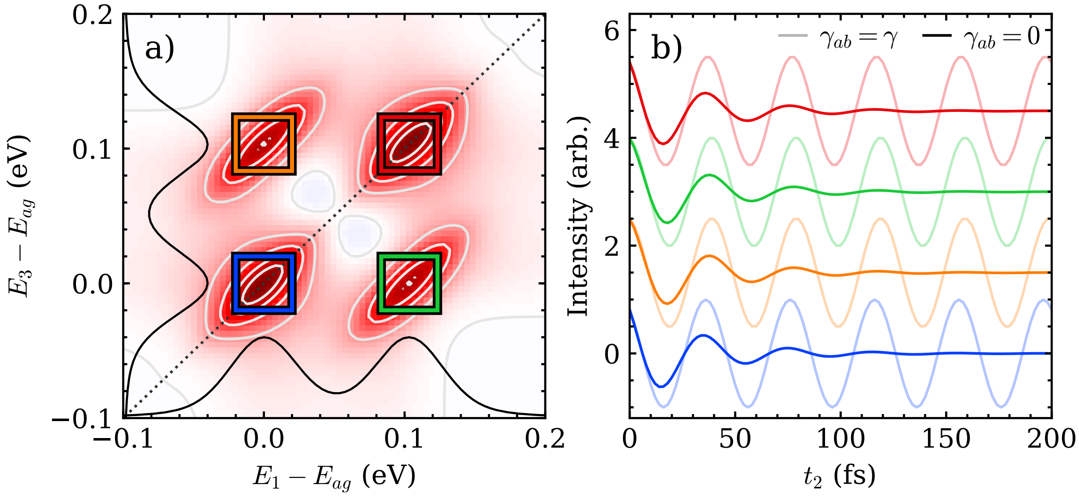

Figure 2.12: Dephasing of electronic coherences. The duration of electronic coherences is governed by the cross-correlation functions and the associated lineshapes, $g_{ij}(t)$. (a) Model 2D spectrum indicating the regions of interest. (b) Kinetic transients integrated over the region in (a). Two cases are shown: perfect correlation (pale) and perfect decorrelation (dark).

the linewidths of the linear spectra of the individual transitions. This fact will be important in the discussion of chapter 5.

2.5 Concluding remarks

This concludes the presentation of the theoretical tools commonly used to describe 2DE experiments. During the derivations, a number of approximations were made, which will be kept throughout the manuscript.

- The perturbation applied by the EM wave is assumed to be a weak perturbation. Indeed, CMDS experiments are normally tickling the weakest electronic excitations. This approximation breaks down in the strong field limit, which is more common in the fields of THz and high harmonic generation.
- The susceptibility can depend on the angle between the wavevectors of the incident beams, as well as on their polarizations. These aspects were neglected.
- The susceptibility of a macroscopic system was assumed proportional to the average behavior of microscopic chromophores. This is not the case for extended coupled systems, although the correction normally requires extending the size of the microscopic system.
- When nuclear motions are considered, the dynamics are assumed to obey the Born-Oppenheimer approximation. The description of coupled vibrational-electronic coherences is possible however [36].
- The vibrational wavepacket dynamics were assumed to change the electronic energy gap, and not the transition dipole moment. This is the Condon approximation. Corrections to eqs 2.152 to 2.155 are available to treat non-Condon cases [37].

- The cumulant expansion explicitly limits the fluctuations to Gaussian processes. This is a limit of this specific modeling scheme, certainly not of 2DE in general[1].
- The MBO model considers uncoupled fluctuations of the primary mode coordinates.

These approximations limit the range of application of the theory. I am confident some features of 2DE are rather robust and hold even when the above approximations break down. Essentially, a 2D spectrum measures the change in the optical response at E_3 due to the previous excitation at E_1, delayed by t_2. Resolution along E_1 is obtained using an interferometer, delay t_2 uses the finite speed of light and resolution along E_3 is obtained by a spectrometer. None of these experimental features depend on the above approximations.

The above description applies to common nonlinear optical processes as used in the design of experiments. Considerations such as phase-matching vectors and coherence transfer vectors $\boldsymbol{\alpha}$ will be used throughout the presentation of experimental details in chapter 3. The case of self-phase modulation in Argon will be central to chapter 4, where the nonlinear response will be expanded up to 11th order.

Semiclassical nonlinear optical response theory was formulated both in Liouville space and in Hilbert space. The Liouville space representation conveniently tracks the state of both the bra and the ket during a multi-pulse experiment. It naturally separates population and coherences, which correspond to different experimental features. It is the source of the standard description using DSFD which facilitates

---

[1] Similarly, the shape of a drop of water is not limited by our inability to compute the exact value of π.

assignment of the complicated 2DE spectra. The Hilbert space description is closer to basic quantum mechanics. It allows the modeling of coherent lineshape dynamics since it treats all delays equivalently. Both will be used in chapter 5.

These formalisms also apply to other common experiments such as photoluminescence (PL) and Raman spectroscopy. Both are third order experiments. The fact that PL is a third order experiment with three time/frequency axes explains why PL can be time-resolved as will be done in chapter 6. The PL lifetime of most optical chromophores is on the order of a few ps to μs, which is much longer than the lifetime of electronic coherences (tens of fs). The time-resolved PL dynamics are thus usually discussed in terms of population dynamics, which greatly simplifies their description.

References

1. Kuhn, T. S. *The Structure of Scientific Revolutions* 3rd (University of Chicago Press, 1996).
2. Hamm, P. & Zanni, M. *Concepts and methods of 2D infrared spectroscopy* 1–286 (2011).
3. Mukamel, S. *Principles of nonlinear optical spectroscopy* xviii, 543 p. (1995).
4. Cho, M. *Two-dimensional optical spectroscopy* 385 (CRC Press, 2009).
5. Chandler, D. *Introduction to Modern Statistical Mechanics* (Oxford University Press, New York-Oxford, 1987).
6. Hansen, J.-P. P. & McDonald, I. R. *Theory of Simple Liquids* 416 (Elsevier Academic Press, 2006).
7. Loriot, V., Hertz, E., Faucher, O. & Lavorel, B. Measurement of high order Kerr refractive index of major air components. *Optics Express* **17,** 13429 (Aug. 2009).
8. Loriot, V., Hertz, E., Faucher, O. & Lavorel, B. Measurement of high order Kerr refractive index of major air components: erratum. *Optics Express* **18,** 3011 (Feb. 2010).
9. Brée, C., Demircan, A. & Steinmeyer, G. Kramers-Kronig relations and high-order nonlinear susceptibilities. *Physical Review A - Atomic, Molecular, and Optical Physics* **85,** 1–8 (2012).
10. Richter, M., Patchkovskii, S., Morales, F., Smirnova, O. & Ivanov, M. The role of the Kramers-Henneberger atom in the higher-order Kerr effect. *New Journal of Physics* **15,** 083012 (2013).

11. Vacher, M., Bearpark, M. J., Robb, M. A. & Malhado, J. P. Electron Dynamics upon Ionization of Polyatomic Molecules: Coupling to Quantum Nuclear Motion and Decoherence. *Physical Review Letters* **118,** 083001 (Feb. 2017).
12. Hochstrasser, R. M. Two-dimensional spectroscopy at infrared and optical frequencies. *Proceedings of the National Academy of Sciences* **104,** 14190–14196 (Sept. 2007).
13. Schlau-Cohen, G. S., Ishizaki, A. & Fleming, G. R. Two-dimensional electronic spectroscopy and photosynthesis: Fundamentals and applications to photosynthetic light-harvesting. *Chem. Phys.* **386,** 1–22 (July 2011).
14. Laughlin, R. B. The physical basis of computability. *Computing in Science and Engineering* **4,** 27–30 (2002).
15. Kubo, R. The fluctuation-dissipation theorem. *Reports on Progress in Physics* **29,** 255–284 (Jan. 1966).
16. Mori, H. Transport, Collective Motion, and Brownian Motion. *Progress of Theoretical Physics* **33,** 423–455 (Mar. 1965).
17. Zwanzig, R. Memory Effects in Irreversible Thermodynamics. *Physical Review* **124,** 983 (1961).
18. Turner, D. B., Hassan, Y. & Scholes, G. D. Exciton superposition states in CdSe nanocrystals measured using broadband two-dimensional electronic spectroscopy. *Nano letters* **12,** 880–6 (Feb. 2012).
19. De Jong, M., Seijo, L., Meijerink, A. & Rabouw, F. T. Resolving the ambiguity in the relation between Stokes shift and Huang–Rhys parameter. *Phys. Chem. Chem. Phys.* **17,** 16959–16969 (2015).

20. Duan, H.-G. *et al.* Nature does not rely on long-lived electronic quantum coherence for photosynthetic energy transfer. *Proceedings of the National Academy of Sciences* **114,** 8493–8498 (2017).
21. Götze, W. in *Liquides, Cristallisation et Transition Vitreuse / Liquids, Freezing and Glass Transition* (eds Hansen, J. P., Levesques, D. & Zinn-Justin, J.) chap. 5 (Elsevier Science Publishers, 1991).
22. Götze, W. & Sjörgen, L. Relaxation processes in supercooled liquids. *Reports on Progress in Physics* **55,** 241 (1992).
23. Ernst, R. R. *et al. Principles of nuclear magnetic resonance in one and two dimensions* 349 (1987).
24. Li, H., Bristow, A. D., Siemens, M. E., Moody, G. & Cundiff, S. T. Unraveling quantum pathways using optical 3D Fourier-transform spectroscopy. *Nature Communications* **4,** 1390 (2013).
25. Ball, P. Still seeking coherence. *Nature Materials* **17,** 220 (Mar. 2018).
26. Mueller, S. *et al.* Fluorescence-Detected Two-Quantum and One-Quantum-Two-Quantum 2D Electronic Spectroscopy. *Journal of Physical Chemistry Letters* **9,** 1964–1969 (2018).
27. Stone, K. W., Turner, D. B., Gundogdu, K., Cundiff, S. T. & Nelson, K. A. Exciton - Exciton Correlations Revealed by Two-Quantum, Two-Dimensional Fourier Transform Optical Spectroscopy. *Accounts of chemical research* **42** (2009).
28. Bristow, A. D. *et al.* A versatile ultrastable platform for optical multidimensional Fourier-transform spectroscopy. *Review of Scientific Instruments* **80,** 073108 (July 2009).

29. Enriquez, M. M. *et al.* Energy transfer dynamics in trimers and aggregates of light-harvesting complex II probed by 2D electronic spectroscopy. *Journal of Chemical Physics* **142.** `http://dx.doi.org/10.1063/1.4919239` (2015).
30. Niedringhaus, A. *et al.* Primary processes in the bacterial reaction center probed by two-dimensional electronic spectroscopy. *Proceedings of the National Academy of Sciences* **115,** 3563–3568 (Apr. 2018).
31. Dean, J. C. & Scholes, G. D. Coherence Spectroscopy in the Condensed Phase: Insights into Molecular Structure, Environment, and Interactions. *Accounts of Chemical Research* **50,** 2746–2755 (Nov. 2017).
32. Monahan, D. M. *et al.* Room-Temperature Coherent Optical Phonon in 2D Electronic Spectra of CH3NH3PbI3Perovskite as a Possible Cooling Bottleneck. *Journal of Physical Chemistry Letters* **8,** 3211–3215 (2017).
33. Palato, S. *Multimode Brownian Oscillator* 2018. `https://github.com/spalato/Mbo.jl`.
34. Seiler, H., Palato, S. & Kambhampati, P. Investigating exciton structure and dynamics in colloidal CdSe quantum dots with two-dimensional electronic spectroscopy. *The Journal of Chemical Physics* **149,** 074702 (Aug. 2018).
35. Caram, J. R. *et al.* Persistent Interexcitonic Quantum Coherence in CdSe Quantum Dots. *The Journal of Physical Chemistry Letters* **5,** 196–204 (Jan. 2014).
36. Tiwari, V., Peters, W. K. & Jonas, D. M. Electronic resonance with anticorrelated pigment vibrations drives photosynthetic energy transfer outside the adiabatic framework. *Proceedings of the National Academy of Sciences* **110,** 1203–1208 (2013).

37. Bizimana, L. A., Carbery, W. P., Gellen, T. A. & Turner, D. B. Signatures of Herzberg-Teller coupling in three-dimensional electronic spectroscopy. *Journal of Chemical Physics* **146,** 084311 (Feb. 2017).

CHAPTER 3

Experimental nonlinear spectroscopy.

The nonlinear response of materials forms the basis of both the manipulation of femtosecond pulses and CMDS spectroscopy experiments. The nonlinear processes are exploited for both pulse measurement techniques and as light sources for spectroscopy. These processes can be described using the formalism covered in the previous chapter: the response of typical nonlinear media such as doubling crystals can be described as an instantaneous nonlinear response [1, 2]. The known, simple nonlinear response is used to manipulate and characterize the femtosecond pulse, which is in turn used to measure the complicated nonlinear response of an interesting sample.

First, the femtosecond pulse is introduced. Elements of nonlinear optics are then presented, including phase cycling. This aspect also applies to CMDS experiments. Nonlinear optics are applied to the measurement of femtosecond pulses. Two such methods are in use in the Kambhampti lab: FROG and c-scans. The implementation of 2D spectroscopy in the pump-probe geometry is finally discussed.

3.1 The femtosecond pulse

The description of the spectroscopic response in terms of nonlinear response theory allows separation of the perturbing electromagnetic field from the molecular response. Each can be treated in a regime where it is most convenient. Due to the large amplitude of the electric field, it will be described classically.

Classical EM waves obeying Maxwell's equations are real-valued fields depending on 3 spatial dimensions and time. It is convenient to express them as the real part of a complex electric field:

$$\mathcal{E}(t) = \Re E(t) \tag{3.1}$$

$$E(t) = A(t) \exp\left[i(\boldsymbol{k} \cdot \boldsymbol{x} - \omega_0 t)\right] \tag{3.2}$$

for a linearly polarized pulse propagating along $\boldsymbol{x}$. In eq 3.1, $\mathcal{E}(t)$ is the real field and $E(t)$ is its convenient complex analogue. Femtosecond pulses are typically decomposed into a carrier and an envelope, as per eq 3.2. The temporal envelope $A(t)$ is a complex-valued function describing the pulse, ω_0 is a reference angular frequency. Spatial dimensions have been dropped from the envelope: spectroscopic experiments described herein are carried out on isolated chromophores in solution, providing a specific point in space at which to measure the electric field. The polarization was similarly dropped, the work presented herein does not use it. The envelope $A(t)$ in eq 3.2 is defined with respect to a reference frequency ω_0. It is a complex valued function of time. Its magnitude gives the time-dependent intensity:

$$A(t) = \sqrt{I(t)} \exp\left[-i\phi(t)\right] \tag{3.3}$$

where $I(t)$ is the real positive time-dependent intensity of the pulse and $\phi(t)$ is the temporal phase.

The electric field can be discussed in the frequency or time domain. Both representations are shown on Fig 3.1. Computation of the emitted polarization is often

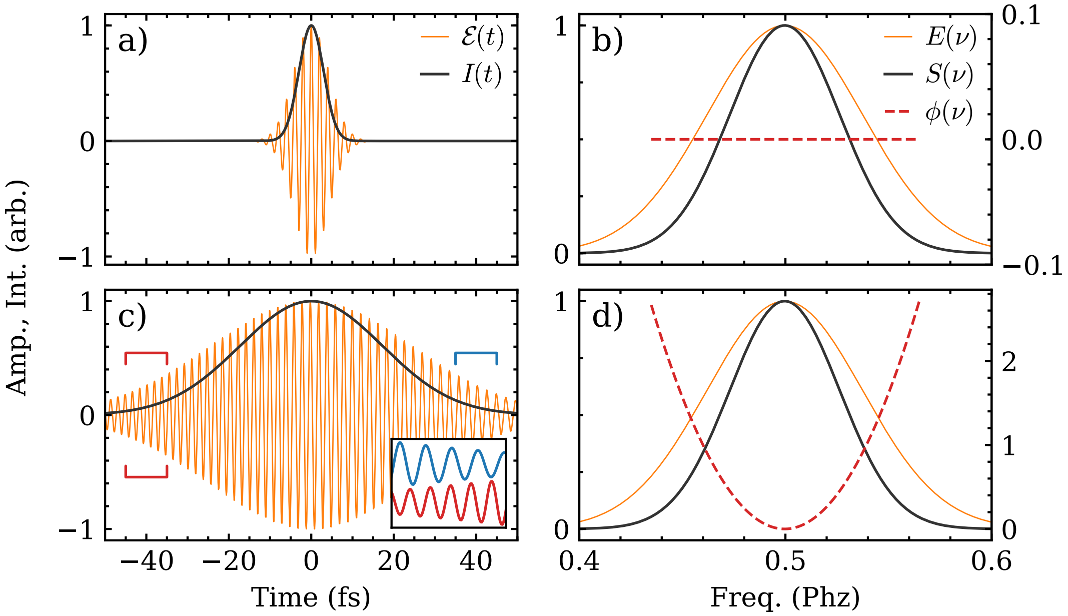

Figure 3.1: Example femtosecond pulse in the time and frequency domains. Intensity FWHM=7 fs. (a) FTL pulse in the time domain. Real electric field (orange) and temporal intensity (black). (b) Frequency domain representation of the FTL pulse in (a): Amplitude (orange), spectral intensity (black) and phase (dashed). (c) Chirped pulse in the time domain. $\varphi_2 = 2000$ fs^2 The change in frequency is subtle. Inset shows the oscillation at the two ends of the pulse, highlighted by square brackets. (d) Chirped pulse in the frequency domain.

carried out in the time domain, and the time-domain representation is normally preferred for theoretical work. It was the case in the previous chapter. The spectrum, however, is more easily measured and forms the basis of much of the experimental discussion. The temporal phase is typically not discussed, its frequency analogue is more conventional:

$$E(\omega) = A'(\omega)\exp\left[i\boldsymbol{k}\cdot\boldsymbol{x}\right] \tag{3.4}$$

$$A'(\omega) = \sqrt{S(\omega)}\exp\left[-i\varphi(\omega)\right] \tag{3.5}$$

where $E(\omega) = \mathcal{F}E(t)$ is the complex spectral field, $S(\omega)$ is the spectral intensity and $\varphi(\omega)$ is the spectral phase. Note that whereas $E(\omega)$ and $E(t)$ are related by the Fourier transform, this is not the case for $A(t)$ and $A'(\omega)$. Instead, $A(t) = \mathcal{F}A'(\omega-\omega_0)$ as a matter of convention. Similarly, $I(t)$ and $S(\omega)$ as well as $\phi(t)$ and $\varphi(\omega)$ form related pairs, but are not related directly by a mathematical transform. For the full picture, see the excellent book of Trebino [3].

The spectral phase can be expanded in a series around ω_0:

$$\varphi(\omega) = \sum_n \frac{\varphi_n}{n!}(\omega-\omega_0)^n \tag{3.6}$$

The first three of these terms are discussed. The first term φ_0 is the absolute phase or constant phase. It is often said to be unimportant since it vanishes in any single pulse measurement. For multiple pulses, the difference between φ_0 of the pulses can be observed in an interference pattern. This phase difference will also be used to isolate signals in 2D experiments, and hence will be used extensively. The description of phase cycling in the later parts of this chapter will refer exclusively to this term. The second term φ_1 is an absolute delay of the entire pulse. Again, this is unimportant for isolated pulses, but will be very important in multiple-pulse experiments, as it corresponds to interpulse delays.

The higher order terms are known as dispersion or chirp. φ_2 is the second order dispersion or first order chirp. The group delay of the envelope can be obtained from $\varphi(\omega)$:

$$t_{\text{group}}(\omega) = \frac{\mathrm{d}\varphi}{\mathrm{d}\omega} \tag{3.7}$$

One can readily see that the terms φ_2 and higher result in a frequency dependent group delay. The different frequencies do not arrive in sync. Chirp thus stretches the pulse and distorts spectroscopic measurements. The elimination of phase distortions is desirable in experiments. A pulse with no chirp ($\omega_n = 0 \; \forall \; n \geq 2$) is referred to as a Fourier-Transform limited (FTL) pulse. It is the shortest pulse that can be obtained from a given spectrum. The experiments are carried out with FTL pulses as much as possible in order to avoid chirp-induced distortions and optimize temporal resolution. Chirp is a constant experimental consideration, impacting the experimental design and motivating the implementation of pulse measurement techniques.

The short duration of pulsed lasers confers them a very high peak power. For example, the amplifier of the Kambhampati lab has an output of 8 W at a pulse repetition rate of 1 kHz. The pulse duration is about 130 fs FWHM, yielding a peak power of 57.8 GW. The spatial mode has a beam waist (intensity radius $1/e^2$) of 12 mm, yielding a peak fluence of 25 GW/cm^2. The large electric field is just low enough to propagate trough transparent optics without distortions due to nonlinear effects. It is very easy, upon slight focusing, to observe nonlinear optical effects arising from such a beam.

3.2 Nonlinear optics and phase matching

The nonlinear optical phenomena arising from the large peak fluence of femtosecond pulsed lasers form a rich toolkit for the femtosecond spectroscopist. Nonlinear processes come in a variety of forms. The commonly used phenomena contain 2$^{\text{nd}}$ order processes: sum-frequency generation (SFG), Optical Parametric amplification (OPA), and 3$^{\text{rd}}$ order processes: Transient-Grating (TG) and self-phase modulation (SPM). These phenomena allow the manipulation and measurement of the femtosecond pulse. The full picture, as required for the correct design of devices such as optical parametric amplifiers, is much more complicated than what is covered here [3, 4]. An aspect that requires immediate discussion, however, is phase matching. The phase matching conditions are an important aspect of nonlinear processes, applying to both CMDS experiments and other nonlinear processes.

As detailed in the previous chapter, the nonlinear response can be computed from a perturbative expansion of the density matrix. Recall that the nonlinear response in the time-domain can be expressed as a non-separable n-dimensional convolution:

$$P_i^{(n)}(t) = \overline{E}_i^{(n)} \otimes \chi_i^{(n)} \tag{3.8}$$

where $\chi_i^{(n)}$ is the j^{th} component of $\chi^{(n)}$ and $\overline{E}_i$ is the corresponding n-dimensional electric field kernel.

Let us pick a specific term in the expansion of the third order response, corresponding to $E_1 E_2^\star E_3$, $\chi_1^{(3)}$. The electric field kernel is then:

$$\begin{aligned}
\overline{E}_1^{(3)}(t_1, t_2, t_3) &= E_3(t_3) E_2^\star(t_3 + t_2) E_1(t_3 + t_2 + t_1) && (3.9)\\
&= e^{-i[(\boldsymbol{k}_3 - \boldsymbol{k}_2 + \boldsymbol{k}_1)\cdot\boldsymbol{x} + \phi_3 - \phi_2 + \phi_1)]} A_3(t_3) A_2^\star(t_3 + t_2) A_1(t_3 + t_2 + t_1) && (3.10)\\
&= \exp\left(-i\left[\boldsymbol{k}_{\text{sig},1} \cdot \boldsymbol{x} + \phi_{\text{sig},1}\right]\right) A_{\text{sig}}(t_1, t_2, t_3) && (3.11)
\end{aligned}$$

where eq 3.1 was used, assuming FTL pulses. In this equation, $\boldsymbol{k}_i$ is the wavevector of pulse i and ϕ_i is the absolute phase of pulse i. The envelope $A_i(t)$ contains the time and frequency dependent parts of pulse i. Each different signal $E_{\mathrm{sig},j}$ thus has a specific dependence on the wavevectors and phases of the pulses, a phase-matching condition. This phase matching condition can be expressed compactly using the coherence transfer vectors presented in section 2.4, $\boldsymbol{\alpha}_j$:

$$E^{(n)}_{\mathrm{sig},j}(x,t) = \exp\left[-\mathrm{i}\left(\boldsymbol{k}_{\mathrm{sig},j}\cdot\boldsymbol{x} + \phi_{\mathrm{sig},j}\right)\right] E^{(n)}_{\mathrm{sig},j}(t) \tag{3.12}$$

$$\boldsymbol{k}_{\mathrm{sig},j} = \boldsymbol{\alpha}_j\cdot\boldsymbol{k} = \sum_i^m \alpha_{ij}\boldsymbol{k}_i \tag{3.13}$$

$$\omega_{\mathrm{sig},j} = \boldsymbol{\alpha}_j\cdot\boldsymbol{\omega} = \sum_i^m \alpha_{ij}\omega_i \tag{3.14}$$

$$\phi_{\mathrm{sig},j} = \boldsymbol{\alpha}_j\cdot\boldsymbol{\phi} = \sum_i^m \alpha_{ij}\phi_i \tag{3.15}$$

where $\boldsymbol{\alpha}_j$ is the phase matching vector of signal j, $\boldsymbol{k}$ is a matrix of the wavevectors of the pulses $\boldsymbol{k}_i$ and $\boldsymbol{\phi}$ is a vector of the absolute phases of the pulses.

Every nonlinear signal thus has a specific dependence on the phase of the incident pulses and their propagation directions. We already mentioned this can be used to separate the rephasing and non-rephasing contributions to the 2D signal. This however applies to all nonlinear processes. For example, the sum-frequency generation (SFG) signal can be described as arising from the second-order response of a two-pulse experiment with:

$$\alpha_{\mathrm{SFG}} = (1,1) \tag{3.16}$$

$$\boldsymbol{k}_{\mathrm{SFG}} = \boldsymbol{k}_1 + \boldsymbol{k}_2 \tag{3.17}$$

$$\omega_{\mathrm{SFG}} = \omega_1 + \omega_2. \tag{3.18}$$

This results in the sum-frequency signal being emitted between the two incident pulses. This is depicted on Fig 3.2b. Similar phase matching considerations can be applied to all nonlinear processes. The transient grating (TG) geometry involving 3 crossed beams is depicted on Fig 3.2c. The signal is emitted at an angle, which can be thought of as the diffraction of beam 3 off the grating formed by the first two beams. This geometry can be used to measure the rephasing signals discussed previously. The phase matching conditions allows for the isolation of the nonlinear signals, whether for pulse measurement or spectroscopy experiments.

3.3 Pulse measurements: FROG and chirp-scans

The full characterization of a femtosecond pulse requires the determination of the spectra amplitude and phase. Measurement of the spectrum is relatively easy with a standard spectrometer. Measurement of the phase, however, is more challenging. The simplest way is to use spectral interferometry of the unknown pulse with a reference [5]. This method is reasonably straightforward but requires a phase-locked reference pulse covering at least the same bandwidth, a rare species. In order to measure the spectral phase of an unknown pulse, a few methods are available. Two will be covered here: frequency-resolved optical gating (FROG) and chirp scans.

3.3.1 Frequency Resolved Optical Gating

The standard way to measure the spectral phase in the ultrafast community is to use FROG. The basic anatomy of a FROG is shown on Fig 3.2. The pulse to be measured is first sent to an interferometer, which creates pulse replicas with a controllable delay τ. The FROG acts on the pulse envelopes, as such the interferometer doesn't need to be phase stable, jitter of the optical path lengths has to be small when compared to the pulse envelope. The specific form of the interferometer is quite flexible. The second element of the FROG is the nonlinear mixing process. This is

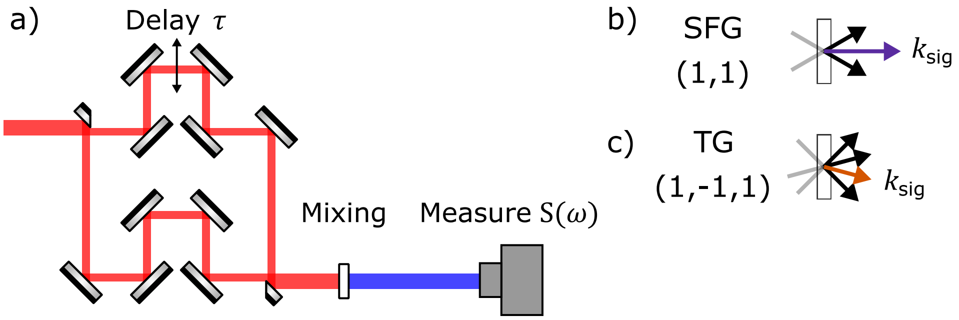

Figure 3.2: Working principle of FROG. (a) Scheme of a dispersion-free FROG. D-shaped cut mirrors are used to split the beam. The mobile arm is subject to a variable delay τ. The beams are recombined for the nonlinear mixing process, and the spectrum of the nonlinear signal is recorded. (b) Geometry for the SFG process. (c) Geometry for the TG process.

3

a core element of a FROG design, but can be picked at convenience. The mixing is carried out in nonlinear media with an instantaneous response. Different nonlinear processes have different tradeoffs which are described in details in the works of Trebino [3, 5]. Two processes are used in the laboratory: transient grating (TG) and sum frequency generation (SFG). The last element of the FROG is the measurement apparatus, a standard spectrometer which detects the non-linear signal.

The physical implementation of the FROG is presented on Fig 3.3. For the measurement of very short pulses (<20 fs), the use of transmissive optics inside the FROG should be avoided. An all-reflective FROG can be realized by using d-shaped mirrors to split the beam instead of beamsplitters. The process is carried out by putting a mask in the beam path before the splitting mirrors. The mask is made of a sheet of black material with a few holes, as illustrated on Fig 3.3c. The masks can be selected to optimize overall transmission, although a clear vertical separation line must be present to allow splitting of the paths. Once split into sub-beams, a

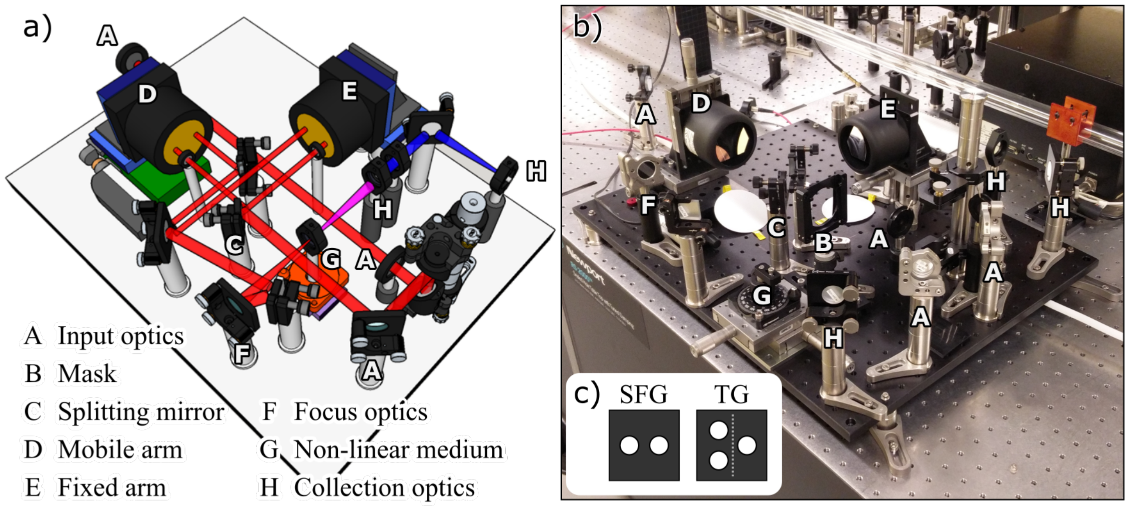

Figure 3.3: Implementation of a FROG, switchable between SFG and TG configurations. (a) Plans of the apparatus in the SFG configuration. Input mask is absent. (b) Experimental apparatus, missing the nonlinear medium and the input mask. (c) Input masks for SFG and TG FROG measurements.

d-shaped mirror picks up one side of the resulting pattern[1]. The beams are sent to the fixed arm of the interferometer. The undeflected beam propagates to the mobile arm. Both arms consist of retroreflectors mounted in translation stages for tuning and alignment. The mobile arm is moved using a motorized actuator. The reflected beams are then made parallel using a second d-shaped mirror and sent to the focusing mirror and nonlinear medium. The focusing is currently achieved using an off-axis parabolic (OAP) mirror. The same mirror is used for all beams. The beams are focused to overlap in the nonlinear medium, the signal is collected and sent to a spectrometer. Irises allow the removal of scattered light and other non-linear signals.

The FROG apparatus shown in Fig 3.3 is made modular such that it is possible to switch between SFG and TG operation. SFG requires the use of a $\chi^{(2)}$ crystal with

---

[1] Currently the port-side beam. In TG FROG, this is the pair of beams.

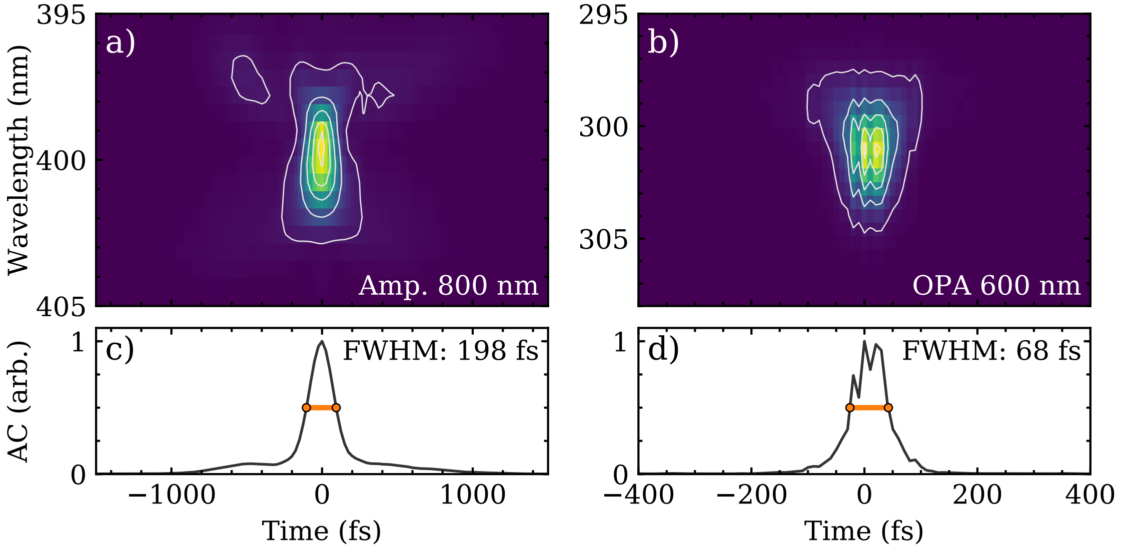

Figure 3.4: Example SFG FROG traces for (a) the output of the amplifier at 800 nm and (b) the output of an OPA at 600 nm. Time marginal, corresponding to autocorrelation signals, are shown for (c) the amplifier and (d) the OPA output.

a limited phase-matching bandwidth, but has a much higher signal level. It is the preferred geometry for longer, narrowband pulses such as the output of the amplifier or OPAs. SFG FROG is also known as frequency-resolved autocorrelation. TG has a very large phase-matching bandwidth (essentially unlimited for our purposes) and can thus be used to characterize broadband white-light pulses without distortion. It is a less efficient process, requiring decently compressed broadband pulses. It is the preferred means of characterization of pulses for 2D spectroscopy.

Example SFG FROG traces are shown on Fig 3.4 for the output of the amplifier (left) and of an OPA (right). SFG FROG traces can be quite abstract, and are not always easy to interpret. The addition of chirp makes the trace wider (along delay), with higher order dispersion changing the shape of the wings. The autocorrelation signal can be obtained by integrating the SFG FROG trace along wavelength. This provides an easily computed metric to estimate the pulse duration.

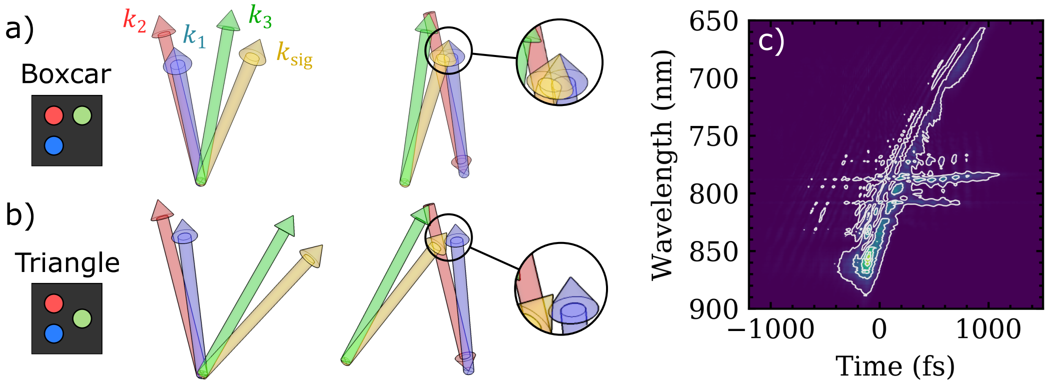

Figure 3.5: TG FROG. (a) Phase matching is achieved in the boxcars or rectangular geometry. (b) Phase matching is not achieved if a triangular pattern is used. (c) Example FROG trace obtained after a hollow-core fiber compressor.

The TG FROG trace results from the interaction of 3 beams, one of which is delayed. This results in two variants, yielding equations identical to FROGs realized with self-diffraction (SD) and polarization gating (PG). The geometry implemented in the lab corresponds to the PG equation where the diffracted beam is delayed, yielding equation 3.22. TG FROGs are much easier to interpret. For smooth temporal envelopes, the TG FROG trace can be read as instantaneous frequency vs time. This makes TG FROG traces easy to read and very helpful in troubleshooting. An example FROG trace with a rich structure is shown on Fig 3.5c.

The implementation of TG FROG is relatively straightforward: focus the three beams in a $\chi^{(3)}$ material such as a sapphire plate or fused silica. The intensity must not be increased to the point of white-light generation. However, some attention must be paid to the phase-matching geometry, as illustrated on Fig 3.5. The signal field must obey both conservation of momentum, eq 3.13, and conservation of energy, eq 3.14. The sum of the wavevectors must thus yield $\boldsymbol{k}_{\text{sig}}$ with the same length as the other vectors. This is easily obeyed in the boxcars geometry, or any rectangular geometry, but not when input beams are arranged in a triangular pattern. Experimentally, the pattern can be adjusted without changing the pointing by using the adjustment screws of the retroreflectors assemblies.

The acquisition of a FROG trace proceeds similarly to a TA experiment. First, it is necessary to ensure the measured spectrum arises from the nonlinear mixing process. Scatter from the input beams will give rise to interference patterns, and should be avoided. Once acquisition parameters are set and signal is optimized, a background is acquired by translating the mobile stage by a large distance. Then, the delay axis τ is scanned and the spectrum is acquired at every step. The background is subtracted from every spectrum. The FROG trace is simply the stack of spectra acquired at different τ. The entire scan is repeated multiple times to average over fluctuations on longer timescales.

The FROG signal can easily be computed for arbitrary pulses. The FROG process can be described as a sonogram, where the electric field of the laser pulse is modulated by a gate function $g(t-\tau)$, also derived from the laser pulse. This modulation is carried out by the non-linear process, which determines the form of the gate function[1]. The mathematical description of the FROG trace is given by:

$$E_{\mathrm{sig}}(t,\tau) = E(t)g(t-\tau), \tag{3.19}$$

$$I_{\mathrm{FROG}}(\omega,\tau) = \left|E_{\mathrm{sig}}(\omega,\tau)\right|^2, \tag{3.20}$$

where $E(t)$ is the electric field of the pulse under study, $E_{\mathrm{sig}}(t,\tau)$ is the emitted FROG signal and $I_{\mathrm{FROG}}(\omega,\tau)$ is the detected FROG trace. The shape of the gate

---

[1] There are interesting extensions of FROG in the case where the gate is derived from a different beam. It's called X-FROG. See Trebino

function is determined by the non-linear process:

$$g_{\mathrm{SFG}}(t) = E(t), \tag{3.21}$$

$$g_{\mathrm{TG}}(t) = |E(t)|^2 . \tag{3.22}$$

Substitution of these equations in eq 3.19 yields the mathematical description of a FROG trace.

Inspection of a FROG trace yields indications about the pulse duration. The time-marginal, computed by integrating the trace along wavelength, gives an indication of the pulse length. For SHG FROG, this corresponds to the intensity autocorrelation. With some practice, one can also learn to read a FROG trace. However, the important advantage of using FROGs is the ability to retrieve the complex spectrum from the FROG trace. A FROG trace can be inverted to a complex spectrum that is essentially unique, ie: a FROG trace corresponds to a single spectrum $E(\omega)$. There are a few exceptions to this rule, for example, SHG FROGs are symmetric upon inversion of τ and thus the sign of the phase is ambiguous (ie: $|E(\omega)|\, e^{-\mathrm{i}\phi(\omega)}$ and $|E(\omega)|\, e^{\mathrm{i}\phi(\omega)}$ yield the same trace). In practice this is seldom a concern [3]. This constraint also implies FROG traces with too many experimental artifacts cannot be inverted, as they correspond to unphysical pulses.

The complex spectrum can be obtained from the FROG trace using a number of FROG retrieval algorithms [3, 6]. The initial algorithms were derived in analogy with phase retrieval problems. They tend to be somewhat fragile: small errors in the precise determination of $\tau = 0$ cannot be compensated and the algorithm will fail to converge. The calculation of the trace from a given electric field is straightforward using eqs 3.21 and 3.22. The problem is thus tractable using standard nonlinear least-squares fitting algorithms, where the parameters are the real and imaginary

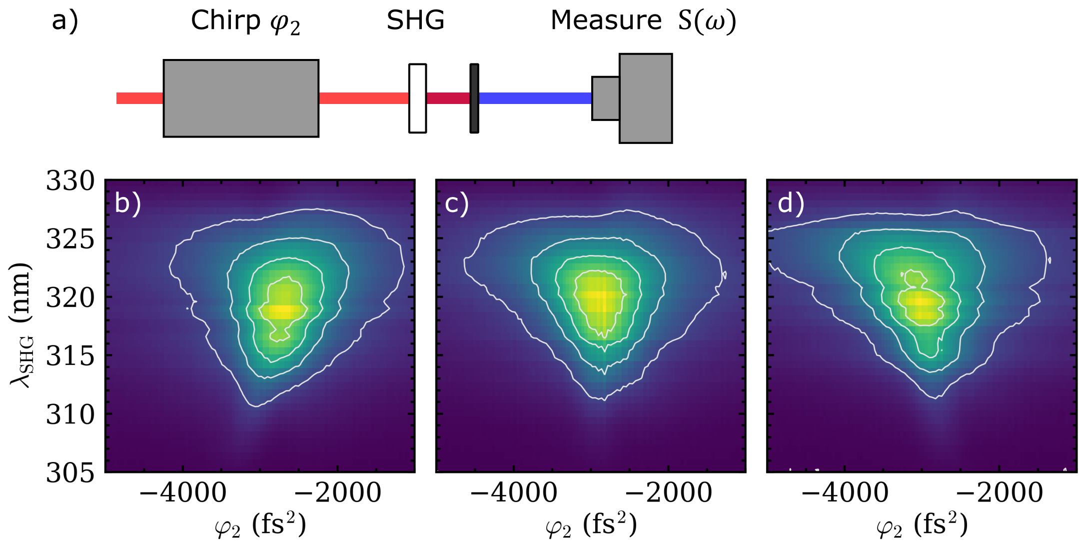

Figure 3.6: Chirp scans. (a) Scheme of a chirp scan. A compressor applies a known chirp φ_2. The chirped pulse is sent to a SHG crystal and the spectrum of the SHG signal is recorded. (b-d) Experimental c-scan for a white-light pulse. (b) $\varphi_3 > 0$. (c) $\varphi_3 \approx 0$ (d)$\varphi_3 < 0$

part of the electric field, for every frequency bin. The parameter space for the optimization problem is rather large (a few hundred parameters). Non-linear least square otpimization algorithms were made for smaller parameter spaces, and performance suffers a bit. In the Kambhampati lab, we encountered some success using the Powell optimization algorithm, as well as using Simplex. Recent approaches try to leverage modern optimization algorithms, such as differential evolution algorithms[1].

3.3.2 Chirp scans

The use of FROG, especially TG FROG, requires the pulse to be already reasonably well compressed. Power decreases with chirp, and thus the nonlinear signal can be reduced to below measurable levels. In order to measure absolutely unknown

---

[1] Prof. Günter Steinmeyer has a conference proceedings out on this, protected behind a paywall. No paper yet.

pulses, the use of chirp scans (c-scans) is preferred [7]. A scheme of this method is illustrated on Fig 3.6. The technique is rather straightforward: the unknown pulse is sent to a stretcher applying a known amount of chirp φ_2. The beam is then sent to a SHG crystal, the second harmonic is collected and its spectrum is measured. The result is a map of spectral intensity vs applied chirp. Examples for varying values of positive, null and negative values of φ_3 are shown on Fig 3.6b-d. Indeed, scanning a compressor while monitoring a SHG signal is a common way to optimize a pulse. The c-scan realizes the full potential by measuring the spectrum of the nonlinear signal.

While c-scans can be realized using conventional compressors, the use of a pulse shaper is preferred. A pulse shaper can apply a precise phase mask to the pulse. The entire assembly can thus be realized very simply. Dazzler acousto-optical pulse shapers apply a phase mask $H(\omega)$, in this case:

$$H(\omega) = \exp\left[\frac{\mathrm{i}\varphi_2}{2}(\omega - \omega_0)^2\right] \tag{3.23}$$

$$E_{\mathrm{sig}}(t, \phi_2) = \left[\mathcal{F}^{-1}E(\omega)H(\omega)\right]^2 \tag{3.24}$$

$$I_{\mathrm{cscan}}(\omega, \phi_2) = \left|\mathcal{F}E_{\mathrm{sig}}(t, \phi_2)\right|^2 \tag{3.25}$$

where φ_2 is the applied chirp. Conceptually, the signal is maximal when the applied chirp φ_2 compensates the second derivative of the spectral phase $\varphi''(\omega)$. As a result, a chirp scan is easily read off: the position of the maximum signal vs frequency corresponds to the chirp in that frequency band, the maximum traces $-\varphi''(\omega)$. A vertical trace at a fixed value of φ_2 corresponds to a pulse whose only distortion is chirp, of value φ_2. This technique allows scanning of a broad range of chirp values, and thus allows the measurement of a completely unknown pulse. It is easily read off, greatly accelerating the adjustment of a pulse shaper.

Finally, the chirp scans can in theory be used to measure the spectral phase from only two measurements. If a large amount of chirp is applied (> 5000 fs^2), the pulse is completely stretched in the time domain, and the frequencies are separated in time. The different frequencies in the pulse do not mix in the SHG crystal, they are doubled individually. In this limit, the signal follows the far-field equation:

$$I_{\text{cscan}}(2\omega, \phi_2) \approx \frac{S(\omega)^2}{|\varphi_2 + \varphi''(\omega)|}, \tag{3.26}$$

where $S(\omega)$ is the spectrum of the pulse. This equation in principle allows the determination of the phase $\varphi''(\omega)$ from only two chirped measurements [6, 8]. In practice, it can be hard to ensure the far field limit applies while maintaining decent signal level.

The two techniques covered above, FROG and chirp scans, are used to ensure the pulses used for a 2D experiment are compressed and well-behaved. The chirp scans facilitate the tuning of the pulse shapers: the signal is easy to obtain, the traces are easily read off and map directly to the parameters of the pulse-shapers. The bandwidth of the SHG crystal can be an issue for broadband pulses, however. Final pulse characterization is carried out with TG-FROG, which is more sensitive and free of limits due phase-matching bandwidth. The availability of both SFG and TG FROG is also generally useful in a femtosecond lab, allowing enhanced troubleshooting vs the 1D autocorrelation.

3.4 Broadband two-dimensional spectrometer.

The experimental implementation of 2DE maps very well to the theoretical description involving the perturbative expansion in the interaction picture, eq 2.150. The use of three pulses corresponds to three light-matter interactions, yielding a

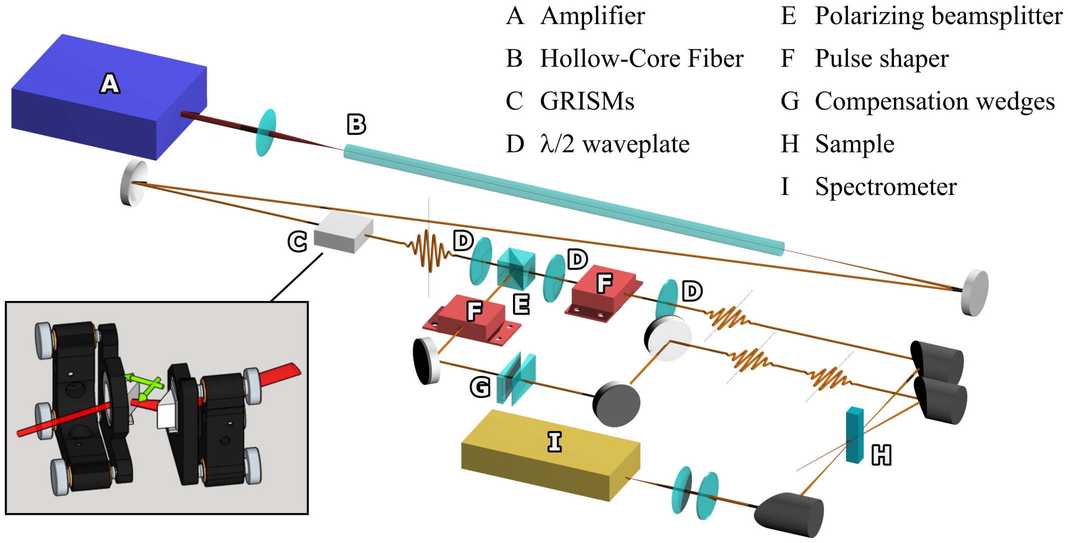

Figure 3.7: Anatomy of the 2D spectrometer. The regenerative amplifier and Hollow-core fiber (HCF) supply the light. The pulse shapers control the pump and probe arms, controlling phase and delay. The signal is detected by a spectrometer. Adapted with permission from Seiler, H. *et al.* Investigating exciton structure and dynamics in colloidal CdSe quantum dots with two-dimensional electronic spectroscopy. *The Journal of Chemical Physics* **149,** 074702 (Aug. 2018).

third-order polarization. A number of 2D spectrometer configurations have been realized, with varying tradeoffs [9–11]. These designs vary in their experimental complexities, accessible bandwidth and possible signal isolation.

3.4.1 Description of the instrument

The spectrometer presented here is a broadband 2D spectrometer in the pump-probe geometry using pulse shapers. The anatomy of this 2D spectrometer is shown on Fig 3.7. In general, a 2D experiment requires 4 parts: a light source, a pulse control element, a sample and a detector.

The light source is an important factor in determining the performance of the spectrometer, especially with regards to which samples can be studied. In order to take full advantage of the detailed overview provided by 2DE, a broad bandwidth is necessary. In order to study couplings between two transitions, the bandwidth should be sufficient to cover the two bands under study. For the quantitative study of lineshapes by 2DE, the pulse should be broader than the linewidth of the band of interest. Even that second prerequisite is hard to meet: electrons are strongly interacting particles, and thus linewidths in the visible range can easily be rather large. Even bright single-color dyes have FWHM around or in excess of 150 meV: 146 meV for rhodamine B, 186 meV for malachite green and 211 meV for nile blue. These widths concern only the center of the peak, not the interesting edges. This motivates the search for white-light sources for 2D spectroscopy. For benchmarking experiments, or in the rare case where the bandwidth of the sample is very narrow, an OPA might suffice [13].

The 2D spectrometer of the Kambhampati lab [1] can be run with either OPAs or a hollow-core fiber (HCF) white-light source. In both cases, light is generated using a Ti:Sapphire femtosecond oscillator [14] and amplified using a regenerative chirped pulse amplifier (CPA) — an award wining design [15, 16]. The regenerative amplifier supplies 8 mJ pulses, at a repetition rate of 1 kHz. The pulse duration is 130 fs FWHM and the central wavelength is 800 nm. An example SHG FROG trace of the pulse is shown on Fig 3.4 The beam is split across the multiple experiments. The oscillator, amplifier and OPAs are commercially available products of mature designs. They will not be covered in detail here. The HCF generates white-light pulses by self-phase modulation in Argon. This source will be covered in detail in chapter 4.

The white-light pulses out of the fiber are sent to a pair of GRISMs (Grating-pRISM) for dispersion management. The GRISMs use both transmission gratings and

---

[1] Nickname: Gupta.

prisms to compensate both second and third order dispersion. They are illustrated on the inset of Fig 3.7. The assembly is made of two identical units, rotated by 180°. The beam penetrates through a transmission grating. The first diffraction order then traverses a glass prism and exits the first sub-unit. After a small air gap (a few mm), the beam enters the second unit via the prism, traverses to the diffraction grating and exits. The beam is back-reflected using a right angle prism as a retroreflector. The returning beam traverses the entire assembly in reverse, parallel to the input beam but about 1 mm below. The GRISMs have a very compact form factor, compensate for $>10^4$ fs^2 of dispersion, but have a low total transmission, typically less than 30 % [17]. The principal role of the GRISMs is to pre-compensate for the second and third order dispersion of the pulse shapers.

After dispersion management, the beam is split and sent to a pair of acousto-optical programmable dispersive filters (Dazzlers, Fastlight inc.). One arm is responsible for generating pulses 1 and 2 (the pumps), the other arm generates the probe. The diffracted beams out of the shapers are then focused and crossed at the sample position. The spectrum of the probe is measured using a CCD spectrometer. The experiment is repeated for varying delays t_1 and t_2. The signal is isolated by a mix of phase matching and phase cycling, which exploits the capacity of the pulse shapers to control the phase of the pulses. The pulse shapers are responsible for final adjustment of the spectral amplitude and phase, generation of pulse replicas and control of the pulses phases. The pulse shaping setup is discussed extensively elsewhere [18, 19]. Some elements will be briefly recalled, others covered in slightly more details.

The great flexibility of the pulse shapers allows fine tuning of the spectral amplitude and shape. The amplitude should be adjusted to obtain a smooth spectrum in the region of spectroscopic interest. The spectral phase is adjusted to obtain a

FTL pulse, or a good enough approximation thereof. Currently, this is achieved in two stages. During the pre-adjustment stage, chirp scans (section 3.3.2) are used to monitor the pulse while iteratively adjusting the phase parameters. Due to hardware constraints, this operation needs to be realized with two computers, one for the control of the Dazzlers and one for the acquisition of the spectra. As a consequence, the process is somewhat tedious and it is not currently possible to automate the compression[1]. Once satisfactory chirp scans are obtained[2], the pulse is measured using the TG FROG which is more sensitive to small phase distortions. Final adjustments to the spectral phase are again made by iteratively adjusting the Dazzler parameters. The process needs to be repeated for both Dazzlers.

Once pulse compression is achieved, the parameters are stored and serve as a basis for the experiments. During the experiments, the pulse shapers will vary the zero and first order phases (ie: absolute phase shifts φ_0 and delays φ_1), but no higher phase terms. The computer-controlled Dazzlers enable the acquisition sequence of multiple ultrafast experiments, including phase cycling and amplitude chopping. These modulation schemes will be discussed later. The entire process is computer-controlled, and thus rather straightforward.

After the pulse shapers, the pulses are focused on the sample. One of the lines is equipped with a manual delay stage used to balance the delays in both arms. In order to avoid both dispersion and aberration at the sample, the beams are focused using off-axis parabolic mirrors. The first two pulses come from the same path, while

---

[1] The USB drivers for the Avantes spectro of the CEP feedback loop would collide with the *actual* Avantes drivers. Blame Fastlite.

[2] By which I mean, once you're tired of fiddling with parameters...

the probe and signal beams are collinear. This geometry is known as the pump-probe geometry, due to its similarity with pump-probe spectroscopy. This geometry exhibits reduced phase mismatch and geometrical distortions with respect to its boxcars equivalent [20].

The sample consists of a quartz cuvette containing the solution under study. The analyte should be dissolved such that the total sample has an OD of about 0.3 (50% transmission). During normal operation, the sample is flowed by using a flow cell and perstaltic pump. In order to minimize the addition of chirp as the pulse travels through the sample, a 200 μm optical path length is used.

The spectrum of the probe beam is monitored using a CCD spectrometer capable of acquisition at 1 kHz. The spectra are stored in the on-board memory. The number of spectra that can be stored limits the acquisition rate. The pulse sequence has to be interrupted in order to transfer the spectra from the CCD RAM to the computer. Each spectrum is saved to the disc for future processing and automatically synchronized to a data server.

The spectrometer acquiring the signal needs to be synchronized with the pulse shaper in order to track the various pulses. The triggering chain that achieves this feat is shown on Fig 3.8. The initial trigger source is the synchronization and delay generator (SDG) of the amplifier. It emits a 1kHz trigger generated from the oscillator pulse train in countdown mode. The SDG has a total of 8 outputs, delay 5 is currently used for the 2DE instrument. This signal is used to trigger the Fastlite Octopuzz, a computer-controlled delay generator with logical gating. The Octopuzz also has multiple outputs with controllable delays. Outputs 1 and 2 are sent to trigger the two Dazzlers (one each). This causes the next pulse of the sequence to be sent. In order to prevent missed shots, these triggers must be sent only if the Dazzlers are

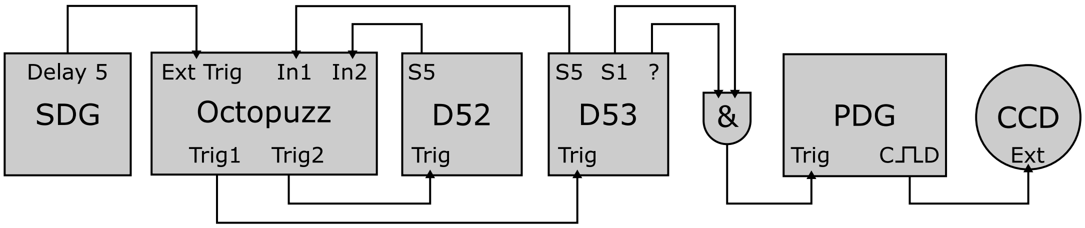

Figure 3.8: Triggering chain for the synchronization of the 2D instrument. Arrows indicate the logical direction. Where applicable, front panels at the bottom, rear panels at the top. D52 is the pump Dazzler (Master), D53 is the probe Dazzler (Slave)

ready for the next shot. This is enforced using a logical condition: the triggers are sent only if both ports In1 and In2 of the Octopuzz are high. The signal to these ports come from the output ports S5 of the Dazzlers.

The Dazzlers in turn trigger the CCD detector. This duty falls to the Dazzler controlling the probe beam. Sadly no logical output corresponds directly to the required trigger signal. It can be obtained by combining programmable output S1 with an undocumented and unlabeled output port, now called ?. The programmable output S1 is set to behavior `[2] GATE`. This signal is combined with ? using a logical `AND` gate and sent to another programmable delay generator (PDG). This PDG has 2 pairs of controllable delay outputs. The current chain uses the `C AND NOT D`, denoted using a little positive pulse symbol. The signal turns high after delay C, and turns low after delay D, allowing the adjustment of the trigger duration.

Delay C should be set to prevent ghosting of the CCD image. The acquisition rate of 1 kHz is close to the maximum rate of the CCD; it spends most of the precious millisecond reading out the charges. If the pulse arrives while the charges are migrating along the parallel registers, a given laser shot will be split between two acquisition frames. There is no way to recover the data from this. The proper procedure to adjust delay C is thus to setup a chopping sequence on the probe pulse, without the pump beam or sample. The recorded signal should vanish to the background level during an OFF shot. A duty cycle of 1/4 (ie: 1-0-0-0) helps the adjustment: it becomes clear whether the trigger is too early or to late. Delay D is conveniently set with respect to C and thus sets the trigger duration. It should simply be set to be long enough for the CCD specifications, 30 µs. The entire chain operates on 5 V, 50 Ω TTL signals. Using this trigger chain, the acquisition usually proceeds flawlessly. When a mistake does occur, it results in obvious errors such as missing or truncated data files. The errors can also be tracked using the acquisition timestamps supplied by the spectrometer.

3.4.2 Signal isolation

The detection of the 2D signal is carried out by the spectrometer in the pump-probe geometry. The spectrometer is a square-law detector sensitive to the intensity. It detects signal emitted along the third pulse direction. Recall the phase matching condition, and the total signal:

$$\boldsymbol{k}_j = \sum_i \alpha_{ij} \boldsymbol{k}_i \tag{3.27}$$

$$\phi_j = \sum_i \alpha_{ij} \phi_i \tag{3.28}$$

$$E_{\mathrm{sig}}^{(n)} = \sum_j e^{\mathrm{i} \boldsymbol{\alpha}_j \cdot \boldsymbol{\phi}} \chi_j^{(n)} \tag{3.29}$$

where $\boldsymbol{k}_j$ is the wavevector of signal j (ϕ_j is its phase), $\boldsymbol{k}_i$ is the wavevector of pulse i (ϕ_i is its phase) and $\boldsymbol{\alpha}_j$ is the coherence transfer pathways of signal j. The total signal $E_{\mathrm{sig}}^{(n)}$ is made of the sum of all signals and has the structure of a discrete Fourier transform. This equation forms the basis of most of phase cycling theory [21–24]. Indeed, signal j can be obtained by combining the recorded signals at varying values of the phases ϕ_i in steps, indexed by k:

$$\chi_j^{(n)} = \sum_k E_{\mathrm{sig},k}^{(n)} W_{jk} \tag{3.30}$$

$$W_{jk} = e^{-\mathrm{i}\boldsymbol{\alpha}_j \cdot \boldsymbol{\phi}_k} \tag{3.31}$$

where $\chi_j^{(n)}$ is a desired contribution, k indexes different repetitions of the experiment with varying phases $\boldsymbol{\phi}_k$ and W_{jk} is a weight factor. Using this technique, the weight factors can be derived systematically.

A phase cycling scheme is noted $N_1 \times N_2 \times \ldots$ where N_i indicates the phase of pulse i is cycled in steps of $2\pi/N_i$. The standard 2-step phase cycling scheme can be described as either $2 \times 1 \times 1$ or $1 \times 2 \times 1$. It is easy to check the weights will be 1 and -1. A common 4-step scatter removal scheme is 2x2x1.

The use of optical detection adds constraints to the detection process. This can be both an advantage and a disadvantage. The emitted signal is collected in the direction of the probe pulse, k_3 for a 3 pulse experiment. The spectrometer is a square-law detector which records the interference pattern formed of the signal and the third pulse:

$$\begin{aligned} I_{\mathrm{tot}}(\omega) &= \left|E_3(\omega) + E_{\mathrm{sig}}(\omega)\right|^2 \\ &= \left|E_3(\omega)\right|^2 + \left|E_{\mathrm{sig}}(\omega)\right|^2 + 2\Re\left[E_3^\star(\omega) E_{\mathrm{sig}}(\omega)\right] \\ &\approx \left|E_3(\omega)\right|^2 + 2\Re\left[E_3^\star(\omega) E_{\mathrm{sig}}(\omega)\right] \end{aligned} \tag{3.32}$$

where the total signal intensity $\left|E_{\mathrm{sig}}\right|^2$ is considered negligible. Note that the interference process will systematically remove the dependence of the signal on ϕ_3. Furthermore, the bandwidth of the spectrometer is limited: the signal frequency must be close to the single coherence frequency (ie: no SFG). These constraints can be cast to equations:

$$\boldsymbol{k}_j = \boldsymbol{k}_3 \tag{3.33}$$

$$\sum_i \alpha_{ij} = 1 \tag{3.34}$$

$$\sum_i |\alpha_{ij}| \leq K \tag{3.35}$$

where j indexes signals, and i indexes pulses. Eq 3.33 enforces the detection direction. Eq 3.34 removes signals in other bandwidths (ie: SFG, THG, DC). Eq 3.35 limits the signals to those of order K or less. These conditions limit the acquisition of some signals in the pump-probe geometry. The 2Q signals shown on Fig 2.5 will not obey condition 3.33 above. Their acquisition is impossible in this geometry. The linear response to the third pulse as well as TA, R and NR third order signals all obey the above constraints and can be detected.

The formalism above is inherited from NMR. It is very useful, but has weaknesses. First, it has difficulty representing the intricacies of the optical detection process. Adaptations can be made to correct for this. The second limit, however, is more difficult to get around [22, 23]. The formalism above cannot represent amplitude modulation. It treats together all signals of the same α, even though they may have different dependence on the amplitudes. This formalism cannot represent a TA signal: it will always be "hidden" by the linear response. This motivates the need for another approach. The tedious expansion of all signals, including their phase and wavevector dependence can seem untractable except for the most simple problems. However, the whole thing is just a simple sum, albeit a very long one.

The process can be made tractable with the aid of computer algebra systems such as Sympy. Sympy is a module for the Python programming language, making it ideally suited to develop a toolkit. The writing of a specialized signal object and helper functions make the whole enterprise rather straightforward[1]. It allows the validation of amplitude and phase modulation schemes such as the 8-step scatter removal cycle [11, 25] and the 32-step collinear scheme from our group [24]. This latter problem expands to over 200 signals, neglecting signal intensities as in eq 3.32 (over 1000 otherwise...). Amplitude modulation is easily represented by expanding every electric field as a complex number in polar coordinates:

$$E_i \propto a_i e^{\mathrm{i}\phi_i} \tag{3.36}$$

where a_i is a real positive amplitude factor and ϕ_i is the phase, as previously. The computed-based approach has advantages. Among other things, it makes every approximation explicit. It supplements standard phase cycling theory very well.

3.4.3 Data acquisition and processing

The data processing for 2D spectroscopy follows rather straightforwardly from the previous discussion. The experiment is repeated with identical input pulses while varying delays t_1, t_2 and phases ϕ_i. Delay t_1 will be subject to Fourier Transform, as such it should be scanned in constant steps starting from 0. The delay t_2 is not always subject to such constraints, the acquisition of a few time points is perfectly reasonable. The analysis of coherent lineshape dynamics however will usually require delay t_2 to be scanned in constant steps. The phases ϕ_i are cycled for every value of t_1 and t_2 in order to allow signal isolation.

The isolation of the 2D signal relies on the combination of spectra acquired with various phases using eq 3.30. The spectral intensity contains a rather large background due to the probe pulse, eq 3.32. In the dataset discussed in chapter 5, the

---

[1] I have not made the code available online yet.

2D signal corresponds to a 5% modulation of the detected spectrum. Fluctuations in the spectrum profile can thus negatively affect the subtraction process and introduce noise. As such, it is preferable to acquire different spectra to be subtracted in rapid succession to prevent decorrelation of the laser spectrum [26, 27]. As such, the cycling of the phases should be the innermost cycling loop. A similar consideration applies to t_1: excessive background noise will morph the spectrum, and t_1 should be the second innermost loop.

Each step in this multi-parameter scan is repeated in order to reduce noise by averaging. The repetition pattern is split in two sequences: pattern repetition and experiment repetition. The pattern repetition sequence repeats the pulses every 38 shots, due to the structure of the Dazzlers' memory. The entire experiment is acquired with this fast averaging sequence. The entire experiment is then repeated to average over fluctuation on a much longer time scale. The pattern repetition sequence is time efficient and efficiently averages short time noise of the laser spectrum. The experiment repetition allows averaging over much slower processes such as environmental fluctuations, laser drifts and sample decay. Every spectrum is stored, allowing troubleshooting and clipping of the acquisition sequence if a problem arises.

The data analysis pipeline needs to carry out the following operations: combinations to isolate the signal, averaging and Fourier transforms. All these operations are linear mappings, and can be carried out in any order. To limit the amount of data to be transferred, the averaging is thus often carried out early in the process. The spectra are transferred to a network-assisted storage (NAS) server during the acquisition process. The data processing can be carried out directly on the server in order to avoid unnecessary data transfer. In particular, the averaging reduces the size of the dataset.

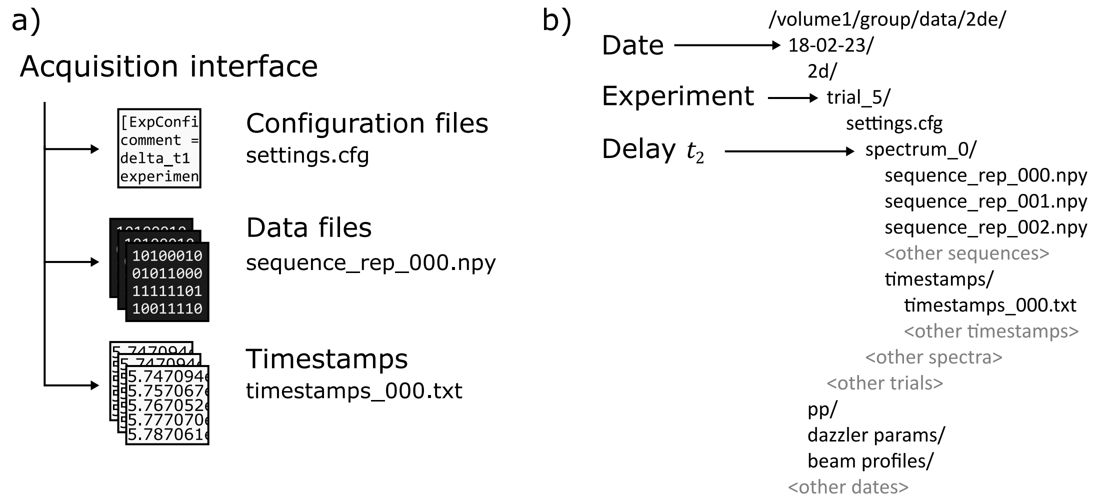

Figure 3.9: Data structure following acquisition. (a) The acquisition software generates data files, configuration information and timing information. (b) Example directory structure following acquisition.

The current data structure at the end of an experiment is shown on Fig 3.9. The acquisition interface generates data files, in binary format as well as plain text experimental configuration information and timestamps. The timestamps can be used to find timing errors, but are otherwise not required for data analysis. The data is stored in a directory organized as shown in Fig 3.9b. A given trial folder `trial_XXX/` contains a specific experiment. The different values of t_2 are stored as different `spectrum_YYY/`. This folder contains multiple data files, corresponding to different experimental repetitions. The data files, named `sequence_rep_ZZZ.npy` contain the spectra for different values of t_1, ϕ_i as well as pattern repetition.

The current data analysis pipeline is illustrated on Fig 3.10. The binary data files are first averaged and reorganized to yield data files, containing the spectra for varying values of t_1 and ϕ_i. The data files of various `spectrum_YYY/` folders are collected in a compressed multi-array archive, also containing the values of t_1, t_2, wavelengths, etc. This archive is easily extended to include all necessary information

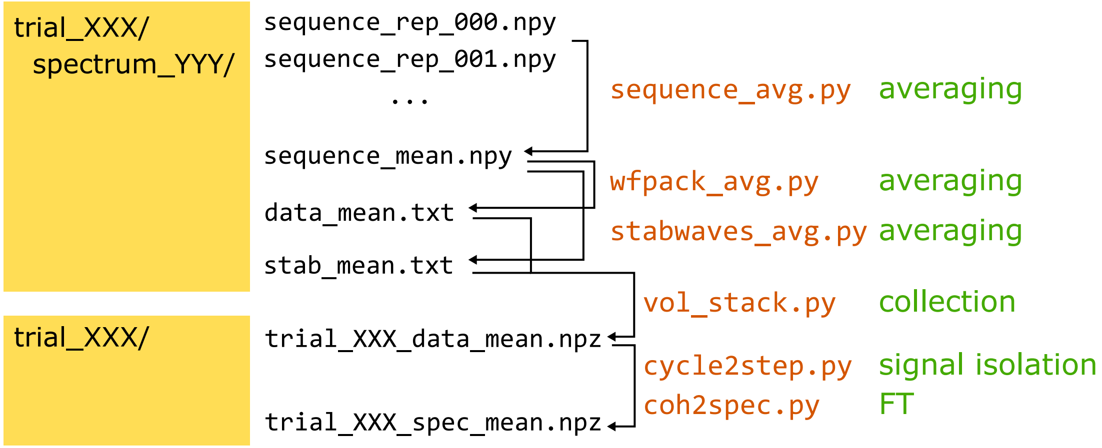

Figure 3.10: Current data analysis pipeline

without having to carry around multiple files. This archive is also easily processed to yield the frequency axes, the spectra, etc.

An example dataset is shown on Fig 3.11 for CdSe NCs at t_2=1200 fs. The sequence after averaging is shown on panel a. The shots are obtained for increasing values of t_1, in steps of 0.5 fs. Each value of t_1 is repeated twice, for $\Delta\phi_{12} = 0$ and $\Delta\phi_{12} = \pi$. Small oscillations are visible for the first shots; this is the 2D signal. The signal is isolated from the background by subtraction using eq 3.30. The result is shown on Fig 3.11b. The coherence is obtained as a function of both detection wavelength λ_3 and coherence time t_1. The projection of the coherence signal is shown as black dots, the black line is a guide to the eye. The coherence is then Fourier-transformed along t_1 to obtain a 2D spectrum, shown on panel c. The conversion from detection wavelength λ_3 to detection energy E_3 is not a linear mapping. The Jacobian of the transformation needs to be included. In numerical form, this can be expressed as:

$$S(E_i)\Delta E_i = S(\lambda_i)\Delta\lambda_i \tag{3.37}$$

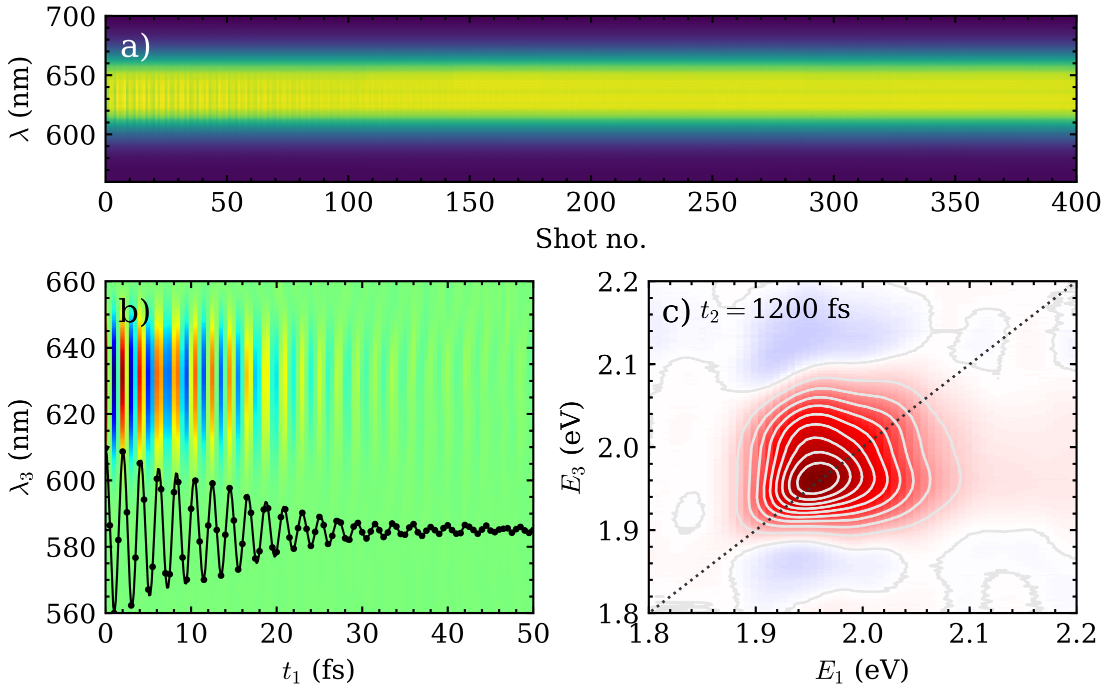

Figure 3.11: Example dataset during analysis for t_2=1200 fs. (a) Averaged sequence of increasing t_1 and two-step phase cycling. (b) Coherence obtained by subtracting shot $2i+1$ from shot $2i$ in panel a. The black dots are the integrated coherence for all frequencies. Black line as a guide to the eye. (c) Resulting 2D spectrum.

where E_i is the energy of pixel i, $S(E_i)$ is the corresponding intensity, ΔE_i is the energy bin width, λ_i is the wavelength of pixel i, $S(\lambda_i)$ is the corresponding intensity and $\Delta\lambda_i$ is the wavelength bin width.

The real part of the 2D spectrum, shown on Fig 3.11c is known as the real absorbtive 2D spectrum. The imaginary part corresponds to dispersion, and is usually not discussed. The signal is dominated by a bleach feature on the diagonal. Two weaker induced absorption features can be seen at $E_3 = 1.85$ eV and $E_3 = 2.15$ eV. The main bleach feature corresponds to bleach and stimulated emission from the first two exciton states X_1 and X_2. This feature has a square-like shape arising from two diagonal peaks and their cross peaks. The contour line give a glimpse of the underlying diagonal lineshapes. The induced absorption signatures correspond to well-known experimental TA results. This spectrum is really rich. It has been the subject of a few papers [12, 28, 29]. Its dynamical lineshape will be the main topic of interest in chapter 5.

References

1. Wahlstrand, J. K., Cheng, Y.-H., Chen, Y.-H. & Milchberg, H. M. Optical Nonlinearity in Ar and N2 near the Ionization Threshold. *Physical Review Letters* **107,** 103901 (Aug. 2011).
2. Steinmeyer, G., Demircan, A. & Brée, C. Comment on: nonlinearity in Ar and N2 near the ionization threshold. *arXiv* **107,** 2–3 (2011).
3. Trebino, R. *Frequency-Resolved Optical Gating: The Measurement of Ultrashort Laser Pulses* `http://link.springer.com/10.1007/978-1-4615-1181-6` (Springer US, Boston, MA, 2000).
4. Boyd, R. W. *Nonlinear Optics* (2008).
5. Trebino, R. *et al.* Measuring ultrashort laser pulses in the time-frequency domain using frequency-resolved optical gating. *Review of Scientific Instruments* **68,** 3277–3295 (1997).
6. Wilcox, D. E. & Ogilvie, J. P. Comparison of pulse compression methods using only a pulse shaper. *Journal of the Optical Society of America B* **31,** 1544 (2014).
7. Loriot, V., Gitzinger, G. & Forget, N. Self-referenced characterization of femtosecond laser pulses by chirp scan. *Optics express* **21,** 24879–24893 (2013).
8. Loriot, V., Hertz, E., Faucher, O. & Lavorel, B. Measurement of high order Kerr refractive index of major air components. *Optics Express* **17,** 13429 (Aug. 2009).
9. Hamm, P. & Zanni, M. *Concepts and methods of 2D infrared spectroscopy* 1–286 (2011).

10. Fuller, F. D. & Ogilvie, J. P. Experimental Implementations of Two-Dimensional Fourier Transform Electronic Spectroscopy. *Annual Review of Physical Chemistry* **66,** 667–690 (Apr. 2015).
11. Shim, S.-H. & Zanni, M. T. How to turn your pump–probe instrument into a multidimensional spectrometer: 2D IR and Vis spectroscopiesvia pulse shaping. *Phys. Chem. Chem. Phys.* **11,** 748–761 (Feb. 2009).
12. Seiler, H., Palato, S. & Kambhampati, P. Investigating exciton structure and dynamics in colloidal CdSe quantum dots with two-dimensional electronic spectroscopy. *The Journal of Chemical Physics* **149,** 074702 (Aug. 2018).
13. Li, H., Bristow, A. D., Siemens, M. E., Moody, G. & Cundiff, S. T. Unraveling quantum pathways using optical 3D Fourier-transform spectroscopy. *Nature Communications* **4,** 1390 (2013).
14. Keller, U., 'tHooft, G. W., Knox, W. H. & Cunningham, J. E. Femtosecond pulses from a continuously self-starting passively mode-locked Ti:sapphire laser. *Optics Letters* **16,** 1022 (July 1991).
15. Strickland, D. & Mourou, G. Compression of Ampified Chirped Optical Pulses. *Optics Communications* **55,** 447–449 (1985).
16. Strickland, D. & Mourou, G. *Nobel Prize in Physics 2018* 2018. `https://www.nobelprize.org/prizes/physics/2018/summary/`.
17. Forget, N., Crozatier, V. & Tournois, P. Transmission Bragg-grating grisms for pulse compression. *Applied Physics B* **109,** 121–125 (Sept. 2012).
18. Seiler, H. *et al.* Kilohertz generation of high contrast polarization states for visible femtosecond pulses via phase-locked acousto-optic pulse shapers. *Journal of Applied Physics* **118** (2015).

19. Seiler, H. *Development of coherent two-dimensional spectroscopy at optical frequencies and application to model chromophores* PhD thesis (McGill University, 2017).
20. Yetzbacher, M. K., Belabas, N., Kitney, K. A. & Jonas, D. M. Propagation, beam geometry, and detection distortions of peak shapes in two-dimensional Fourier transform spectroscopy. *Springer Series in Chemical Physics* **88,** 338–340 (2007).
21. Ernst, R. R. *et al. Principles of nuclear magnetic resonance in one and two dimensions* 349 (1987).
22. Tan, H.-S. Theory and phase-cycling scheme selection principles of collinear phase coherent multi-dimensional optical spectroscopy. *The Journal of chemical physics* **129,** 124501 (Sept. 2008).
23. Zhang, Z., Wells, K. L., Hyland, E. W. J. & Tan, H.-S. Phase-cycling schemes for pump–probe beam geometry two-dimensional electronic spectroscopy. *Chemical Physics Letters* **550,** 156–161 (2012).
24. Seiler, H., Palato, S. & Kambhampati, P. Coherent multi-dimensional spectroscopy at optical frequencies in a single beam with optical readout. *Journal of Chemical Physics* **147** (2017).
25. Lewis, K. L. M., Myers, J. A., Fuller, F., Tekavec, P. F. & Ogilvie, J. P. *Strategies for Scatter Removal in Two-Dimensional Electronic Spectroscopy in the Pump-Probe Geometry* in *Ultrafast Phenomena* (2010), 1–2.
26. Kearns, N. M., Mehlenbacher, R. D., Jones, A. C. & Zanni, M. T. Broadband 2D electronic spectrometer using white light and pulse shaping: noise and signal evaluation at 1 and 100 kHz. *Optics Express* **25,** 7869 (2017).

27. Son, M., Mosquera-Vázquez, S. & Schlau-Cohen, G. S. Ultrabroadband 2D electronic spectroscopy with high-speed, shot-to-shot detection. *Optics Express* **25,** 18950 (2017).

28. Turner, D. B., Hassan, Y. & Scholes, G. D. Exciton superposition states in CdSe nanocrystals measured using broadband two-dimensional electronic spectroscopy. *Nano letters* **12,** 880–6 (Feb. 2012).

29. Seiler, H., Palato, S., Sonnichsen, C., Baker, H. & Kambhampati, P. Seeing Multiexcitons through Sample Inhomogeneity: Band-Edge Biexciton Structure in CdSe Nanocrystals Revealed by Two-Dimensional Electronic Spectroscopy. *Nano Letters* **18,** 2999–3006 (May 2018).

CHAPTER 4

Hollow-core fiber for femtosecond visible spectroscopy.

Advances in femtosecond visible spectroscopy motivate the investigation into new pulsed sources of broadband visible light. This section details the performance of an Ar-filled hollow core fiber for femtosecond visible spectroscopy. This source is characterized by high overall transmission and good spatial mode. Broadening is achieved by self-phase modulation. Notably, the uncompressed visible part of the output is shorter than the input pulse. The design space for this source is explored and compared with established modeling procedures. The fiber should be amenable to broadening across the entire visible range, down to 450 nm. This passive design can provide an interesting alternative to achieve broadband visible pulses for femtosecond spectroscopy.

4.1 Introduction

Femtosecond time-resolved spectroscopy has many requirements for a broadband source. First, the pulse duration should be short to obtain good temporal resolution. The bandwidth necessary to support a short pulse, however, is typically not the most stringent requirement: the pulse must also match the absorption bands of the sample under study. This requirement becomes especially challenging at optical frequencies, due to the large spectral widths of electronic transitions. Broadband transient-absorption (TA) and two-dimensional electronic (2DE) spectroscopies are often limited by insufficient bandwidth to cover multiple spectroscopic transitions of interest. Indeed, samples such as biological light harvesting proteins and nanostructures possess spectral features located anywhere in the visible range, the near infrared or the ultraviolet [1–7]. A source that is free of bandwidth limitations arising from resonance or phase-matching considerations is thus highly desirable.

A pulse with a large bandwidth must be amenable to compression, and thus show a high level of coherence and noise robustness [8]. A smooth spectral phase consisting mostly of low order dispersion allows the use of simple pulse compression techniques. This smooth spectral phase also permits the use of modern pulse shaping devices to their full potential [9]. Furthermore, a smooth spectral phase indicates minor spatio-temporal distortions such as spatial chirp [10]. Femtosecond experiments usually rely on modulation of the amplitude and phase of the pulses to isolate the signal of interest. This puts a stringent need on the shot-to-shot stability of the spectral amplitude and phase. Furthermore, demanding femtosecond experiments such as 2DE spectroscopy often last for many hours [11, 12]. Accordingly, both the spectrum and phase of the broadband source should be stable over the long-term, and reasonably robust to unavoidable environmental fluctuations.

Time-resolved spectroscopy probes resonant processes, and as such the power requirements are typically modest. However, the source is usually the first element in a series of lossy optical devices. This accentuates the need for pulse energies in the tens of μJ/pulse range. Tunablity of the pulse energy is also desirable. Varying the intensity of the laser pulses is a common occurrence in spectroscopy experiments.

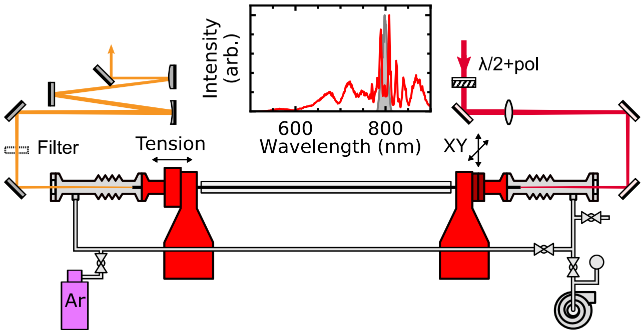

Figure 4.1: Stretched hollow-core fiber setup. Input pulse from regenerative amplifier enters the fiber through an evacuated chamber. Output chamber is pressurized (Ar). Collimation telescope and all routing optics shown. Inset: input spectrum (gray) and typical output spectrum (red).

Furthermore, downstream optical elements have requirements and limits in terms of powers. Being able to adjust the power output of the source to a range acceptable to downstream optics simplifies the design and operation of the experiment.

4.2 Methods

Hollow-core fibers are a possible broadband source for optical spectroscopy. A typical implementation is depicted in Fig 4.1 [13, 14]. Typical input and output spectra of the fiber are shown as an inset to Fig 4.1. The output of a femtosecond amplifier is coupled to the entrance of a straight hollow-core fiber. A variable attenuator, consisting of a half waveplate and polarizer, allows for fine control over the input power. The fiber, which is essentially a flexible glass capillary, is stretched between two holders which allow for adjustments to the fiber alignment and tension. Fibers of varying inner diameters can be used, with thinner fibers enhancing the nonlinear interaction at the expense of overall transmission. The input and output of the fiber are enclosed in gas chambers to control the pressure and nature of the gas in the fiber. Best performance is obtained using a pressure gradient. The input is under vacuum, which reduces plasma defocusing and thus enables efficient and stable coupling at the fiber input [13]. The output chamber is pressurized, resulting in a pressure gradient inside the fiber. Although only Argon is used in this thesis, the nature of the gas can be varied. The output of the fiber is collimated before being sent to a home-built all reflective TG-FROG or to the experiment. For visible spectroscopy, the near-IR part of the continuum is discarded using a short-pass filter inserted after the output chamber (cutoff 700 nm).

The fiber assembly offers multiple adjustable parameters. Some parameters are determined by hardware design, such as fiber length L, inner diameter (ID) and gas type. Input pulse characteristics, such as central wavelength, bandwidth and beam radius, are similarly constrained by available hardware. The beam should be focused down such that the waist $w = 0.65a$, where a is the radius of the fiber [13, 15]. The gas pressure and input pulse energy can be tuned continuously during operation, and thus can be finely adjusted. The fiber assembly was tested with up to 4 mJ input pulses and 3 atm gas pressure. For 2DE experiments, we typically use 580 μJ pulses from a Ti:Sapphire amplifier with a duration of 130 fs, central wavelength of 800 nm and repetition rate of 1 kHz. The amplifier output has a beam waist of about 12 mm. This is focused down to 260 μm at the fiber tip in order to efficiently couple to the fiber with an ID of 400 μm. The fiber has a length of 2.57 m. Sufficient broadening is achieved by maintaining a pressure of 3 bar Ar in the output chamber. The output beam is collimated to 1.06 mm. The total transmission in the differential pumping scheme is above 80%, with an overall conversion to the visible of 7–10%.

Broadening in inert gases is well-understood and dominated by self-phase modulation (SPM) of the laser pulse in the gas. The broadening is described by the nonlinear Schrödinger equation (NLSE) [14, 15]:

$$\partial_z \tilde{\varepsilon} = \tilde{D}\tilde{\varepsilon} + ik_0 T \widetilde{\Delta n} \tilde{\varepsilon} - \frac{\tilde{\alpha}}{2}\tilde{\varepsilon} \tag{4.1}$$

where $\tilde{\varepsilon}$ is the Fourier-transform of the slowly-varying envelope $\varepsilon(t, z)$. This equation accounts for dispersion ($\tilde{D}$), self-steepening ($T = 1 + i\tau_{\text{shock}}\partial_t$, $\tau_{\text{shock}} \approx 1/\omega_0$ and ω_0 is the central frequency of the pulse), instantaneous Kerr effects (Δn) and optical losses (α). The equation above is called the 1D+1 NLSE (z, time). It is integrated using the split-step Fourier method [14, 15]. The index of refraction n are obtained using the Sellmeier equations for Ar at 1 bar. The pressure correction is applied as $n(p) = \sqrt{1 + p(n(1)^2 - 1)}$. In the current case, Kerr coefficients up to n_{10} are necessary to reproduce the experimental results. These coefficients have been measured at 800 nm, and were extrapolated to other frequencies using the Generalized Miller formula [16, 17]. The Kerr coefficients are proportional to pressure. The origin of these so-called high-order Kerr effect terms has been subject to considerable debate [16, 18–21].

Table 4–1: Characteristic nonlinear lengths obtained for coupling an input pulse 130 fs FWHM, $E_{\text{in}} = 580$ µJ into a fiber of 400 µm ID under 3 atm Ar.

Nonlinear effect	Characteristic length	Value (m)
Kerr (3rd order)	$\lvert c/(\omega_0 n_2 \lvert\epsilon\rvert^2)\rvert$	0.0538
Kerr (5th order)	$\lvert c/(\omega_0 n_4 \lvert\epsilon\rvert^4)\rvert$	1.84
Kerr (7th order)	$\lvert c/(\omega_0 n_6 \lvert\epsilon\rvert^6)\rvert$	0.216
Kerr (9th order)	$\lvert c/(\omega_0 n_8 \lvert\epsilon\rvert^8)\rvert$	0.643
Kerr (11th order)	$\lvert c/(\omega_0 n_{10} \lvert\epsilon\rvert^{10})\rvert$	15.7
Kerr (full)	$\left\lvert c/(\omega_0 \sum_{m=1}^{5} n_{2m} \lvert\epsilon\rvert^{2m})\right\rvert$	0.0472
Self-Steepening	$\left\lvert c\sigma_t/(\sum_{m=1}^{5} n_{2m} \lvert\epsilon\rvert^{2m})\right\rvert$	12.3
Dispersion	$\lvert\sigma_t^2/\beta_2\rvert$	196

The relative importance of the different contributions to eq 4.1 are usually evaluated using characteristic lengths, with shorter lengths indicating a stronger effect [14, 15, 22]. The characteristic lengths for the current experimental configuration are presented in table 4–1. In that table, c is the speed of light in vacuum, n_{2m} is the Kerr coefficient at ω_0, ϵ is the peak field amplitude, σ_t is the temporal width of the pulse ($1/e$ intensity half-width) and β_2 is the group velocity dispersion ($\beta_2 = \mathrm{d}^2k(\omega)/\mathrm{d}\omega^2$).

Assuming Gaussian temporal and transverse envelopes, $|\epsilon|^2 = \sqrt{2\pi} I_0/\sigma_t w^2$ where I_0 is the pulse energy and w is the beam waist. These lengths have to be compared to the effective length of the fiber $L_{\text{eff}} = \left(1 - e^{-\alpha L}\right)/L$, where L is the geometrical length of the fiber. In the current case, $L_{\text{eff}} = 2.13$ m. Table 4–1 clearly shows that Kerr effects dominate. Nevertheless, all effects need to be taken into account to accurately reproduce the output spectrum.

The duration of the femtosecond white-light pulse is measured using a home-built dispersion-free transient grating (TG) FROG [23]. In this geometry, chirp is visible as a tilt in the TG-FROG traces. A Fourier-transform limited (FTL) pulse shows as a vertical TG-FROG trace. Unless specified, the beam path from the fiber's output chamber to the FROG is free of transmissive optics. For ultrafast experiments, compression is achieved using a GRISM assembly and acousto-optical pulse-shapers (Dazzlers, Fastlite Inc.). A complete description of the spectroscopy apparatus is presented in previous work [24].

4.3 Results

The performance of the fiber can be measured through several indicators. Fig 4.2 illustrates the suitability of this fiber for femtosecond optical spectroscopy. The overall transmission of the fiber is shown on Fig 4.2a. In operational conditions, the transmission of the fiber is above 80%. Transmission drops when pressure and input energy are increased past a certain threshold, consistent with previous work [13]. This is a consequence of ionization of the gas. The collimated output mode is shown on Fig 4.2b, as imaged by a camera. This high quality of the spatial mode makes this source suited for spatially resolved femtosecond spectroscopy [5, 25, 26]. The continuum can readily be compressed for use in a spectroscopy experiment. Fig 4.2c shows the spectrum after amplitude and phase shaping achieved using GRISMs and

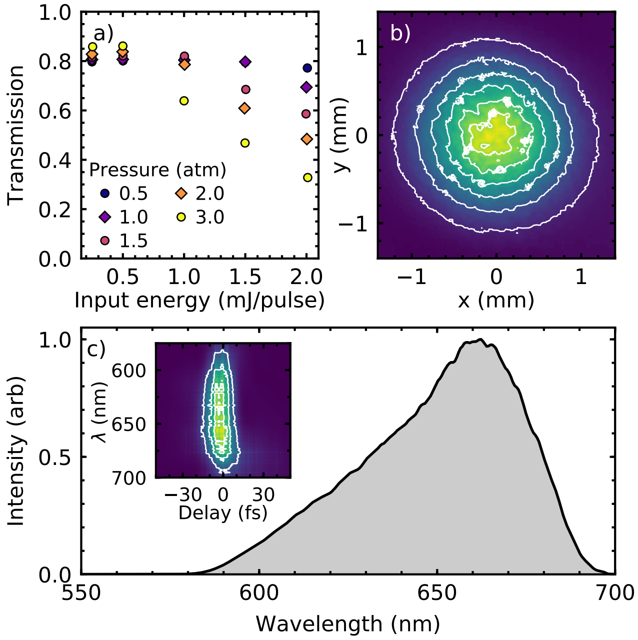

Figure 4.2: Fiber performance. (a) Transmission is typically above 80%. Plasma generation at high pressures and powers decreases transmission. (b) Image of the fiber mode after collimation. (c) Broadband visible pulse obtained from the visible part of the fiber output after compression. Inset: TG-FROG of the compressed pulse. Time projection has a FWHM of 16 fs.

an acousto-optical pulse shaper (Dazzlers, Fastlite Inc.) [24]. The main role of the GRISMs is to compensate the large second and third order dispersion of the pulse shapers. The compression of the pulse is measured using a dispersion-free TG-FROG. The inset of Fig 4.2c shows the resulting trace. The temporal projection has a FWHM of 16 fs.

Nonlinear optical spectroscopy experiments usually take multiple hours to reach completion [11, 12, 27]. Furthermore, both amplitude and phase modulation of the pulses can be used to isolate the signal of interest [9, 28–30]. As such, it is desirable for the source to be stable over both the long and short terms. Variations in the spectrum of the source are shown on Fig 4.3. Both fast (shot to shot) and slow (over a day) measurements are shown. Relative fluctuations of the total power and bandwidth

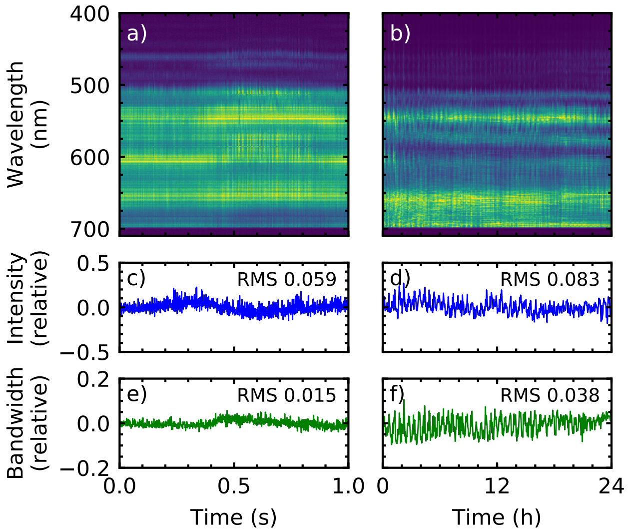

Figure 4.3: Fluctuations of the visible power and bandwidth. (a) Temporal evolution of the spectrum shot-to-shot and (b) over 24 h. (c) Fluctuations of the total visible intensity shot-to-shot and (d) over 24 h. (e) Fluctuations of the visible bandwidth shot-to-shot and (f) over 24 h.

are also shown. Due to the asymmetric shape of the spectrum, the bandwidth is measured as the square-root of the second central moment of the spectrum. The shot-to-shot RMS fluctuation is about 6%, which is remarkable considering the large bandwidth and highly nonlinear process involved. The laser spectrum is stable over the course of multiple days, although some sensitivity to environmental fluctuations is visible for long-term measurements. A modulation with a period of 40 minutes is visible on panels b, d and f, which is attributed to a temperature control loop in the laser chillers.

Due to the nature of the nonlinear propagation process, pulses with increased bandwidth also tend to be increasingly sensitive to fluctuations and thus less stable. There is a trade-off between bandwidth and stability for large broadening. The fiber assembly is entirely passive: the instability is due to the amplification of preexisting fluctuations by the nonlinear SPM process. These fluctuations can be due both to power fluctuations in the amplifier as well as pointing fluctuations. The stability performance displayed in Fig 4.3 were obtained without active pointing stabilization, and without humidity control of the laser room. Correcting for this is expected to significantly increase the stability of the source.

Having described the general properties of the fiber, we now look at the impact of power and pressure on the fiber output. Fig 4.4 shows the fiber output for three input powers, at a fixed pressure of 1.34 atm for a 2.5 m fiber of 400 µm ID. Both TG-FROGs and output spectra are shown. The spectra exhibit the signature shape of SPM broadening. The comparison with model spectra obtained by propagating eq 4.1 are shown in red. The agreement is excellent. The FROG traces are also typical of broadening by SPM, with the exception of an elongated tail lasting 1 ps at around 795 nm. This tail is also present in the direct output of the amplifier, and does not participate in the broadening process. It is far from the spectral region used in experiments, and has been safely ignored. Linear chirp shows as a tilt in TG-FROGs, with increased angle from the vertical indicating increased chirp [23]. It is remarkable to observe the TG-FROG become increasingly vertical at larger power. This indicates the bandwidth of the pulse increases at a faster rate than its duration in this regime.

Fig 4.5 shows the fiber output for three gas pressures, at a fixed input energy of 800 µJ/p. The general shapes of the FROG traces and spectra are once again indicative of SPM. The pulse at the highest pressure setting is becoming unstable, and ionization reduces the visible part of the spectrum. The properties of the traces are otherwise similar to the previous case. The complete overview of parameter space is shown on Fig 4.6. Indeed, both gas pressure and power increase the impact of nonlinear effects and increase broadening. As such, input power and gas pressure are

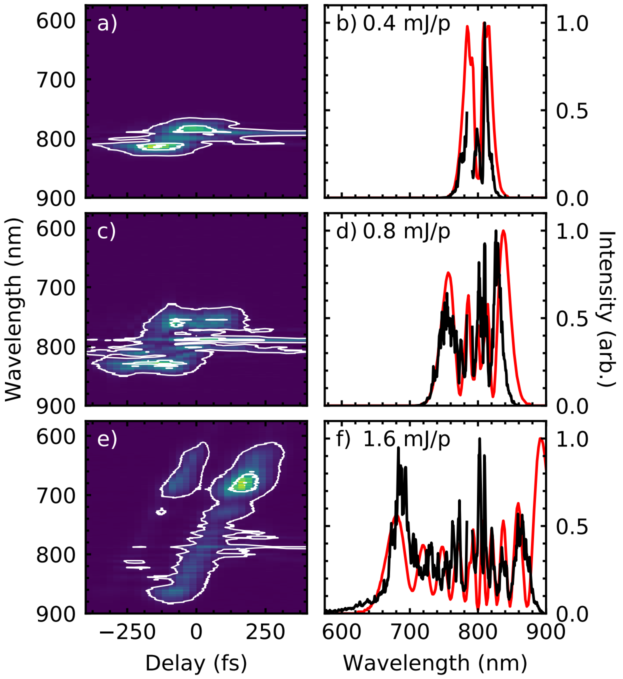

Figure 4.4: Pulse energy increases broadening. TG-FROG traces (a,c,e) and output spectrum (b,d,f) of the full fiber output for increasing input pulse energy. Red lines are model spectra obtained for the same input conditions. Ar pressure: 1.34 atm.

two degrees of freedom that can be used to obtain a target output bandwidth and power. This flexibility thus allows the fiber to accommodate the constraints imposed by other elements of the optical setup, such as operational thresholds.

4.4 Discussion

The reduction of the chirp with increased broadening displayed in Fig 4.4 is interesting. As a consequence, selecting part of the output spectrum using filters yields a pulse of shorter duration than the input pulse. This self-compression is demonstrated in Fig 4.7a. The TG-FROG trace obtained after the use of a 700 nm shortpass filter has a temporal FWHM of 45 fs before compression, compared to 159 fs for the input pulse. The chirp of the experimental pulse includes contributions from two transmissive filters: neutral density and 700 nm shortpass. The resulting chirp was not taken

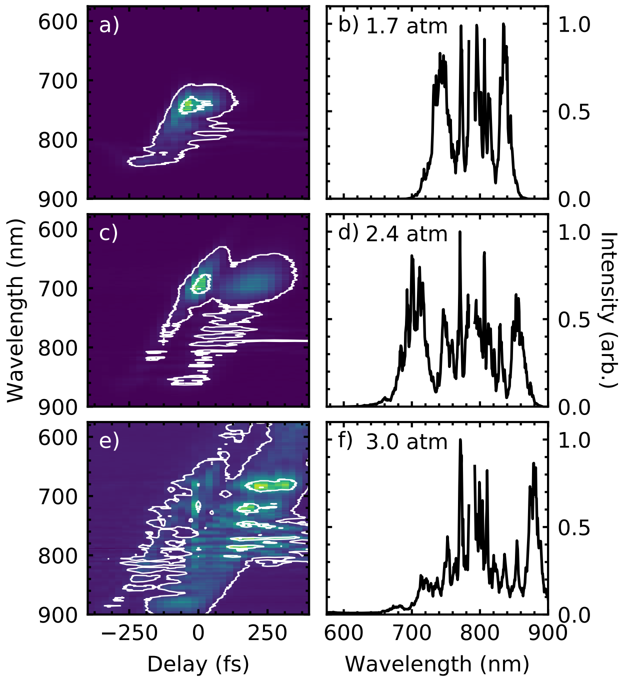

Figure 4.5: Gas pressure increases broadening. TG-FROG traces (a,c,e) and output spectrum (b,d,f) of the full fiber output for increasing pressure. Input pulse energy: 800 μJ/p.

into account for the model trace. Self-compression has not been reported in fibers of this kind. Modeling carried out with the NLSE (eq 4.1) qualitatively reproduces this feature, as shown on Fig 4.7b.

This fiber achieves a stable broadband continuum by relying mostly on a stable self-phase modulation process. The smooth broadening is illustrated in Fig 4.8, showing the spectrum as a function of distance obtained from modeling. The bandwidth increases almost linearly with distance [15]. No sudden bandwidth changes are observed, as is the case for soliton propagation or filamentation [8, 31]. The impact of the fiber length on the output pulse is thus easily assessed.

The tunability of the HCF for visible spectroscopy as a function of input energy and pressure conditions has been demonstrated. Further tunability can be achieved

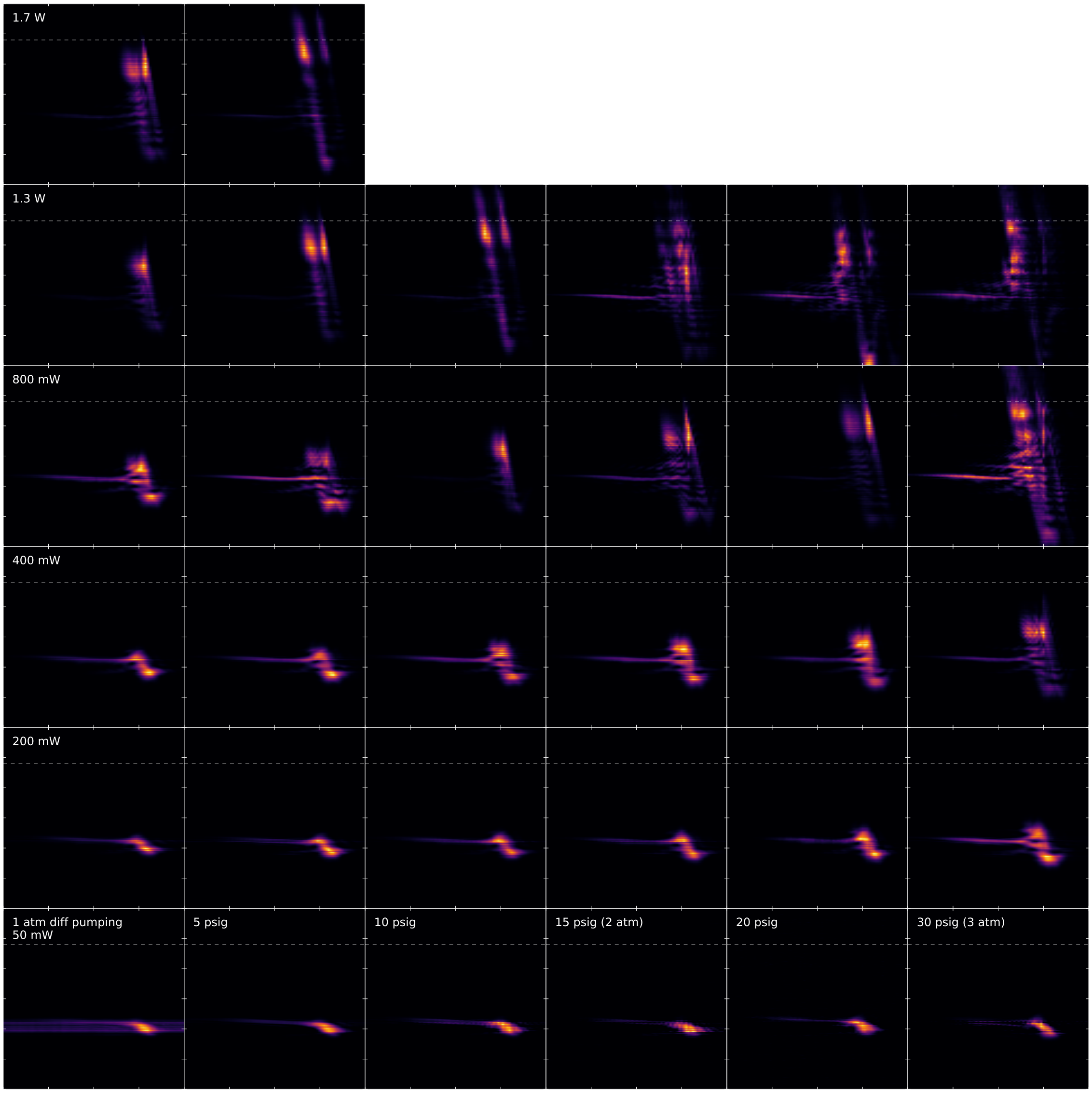

Figure 4.6: Detailed view of the HCF output. TG FROG traces. Delay axis is reversed with respect to convention. Power increases going up, pressure increases going right.

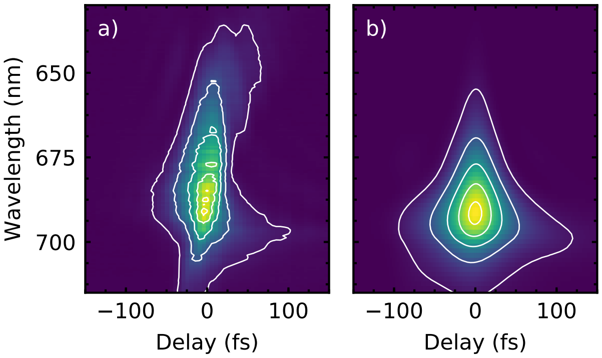

Figure 4.7: Model calculations reproduce the experimental self-compression. (a) Experimental TG-FROG trace displaying self-compression of the visible part. Temporal projection FWHM: 45 fs. (b) TG-FROG trace from model calculations similarly exhibit a duration inferior to input pulse. Temporal projection FWHM: 54 fs. Ar pressure: 3.0 atm, input pulse energy: 550 μJ/p, fiber ID 400 μm.

by varying design parameters, such as fiber length and inner diameter, or characteristics of the input pulse, such as duration and wavelength. This large number of parameters stimulates the need for an efficient way to evaluate and predict fiber performance as a function of these parameters. The NLSE provides the basis for reliable modeling of the nonlinear processes at work in the HCF. The code employed for the nonlinear pulse propagation was benchmarked in previous work [14] as well as in Fig 4.4 of the present work. The calculations presented in 4.9 were realized efficiently by naively porting an existing algorithm to a modern high performance language. Propagation over the length of a 2.5 m fiber takes about 2 minutes on a common laptop. The code is made available online [32].

Fig 4.9 displays the expected broadening when pumping the HCF with OPAs available in our laboratory. Fig 4.9a shows typical output spectra for pumping with 150 μJ/p, 100 fs pulses across the visible bandwidth. Fig 4.9b shows the broadening factor for varying input pulse wavelengths (color) and energies, for two fiber IDs (symbols). Broadening is computed as the ratio of the spectral FWHM of the output

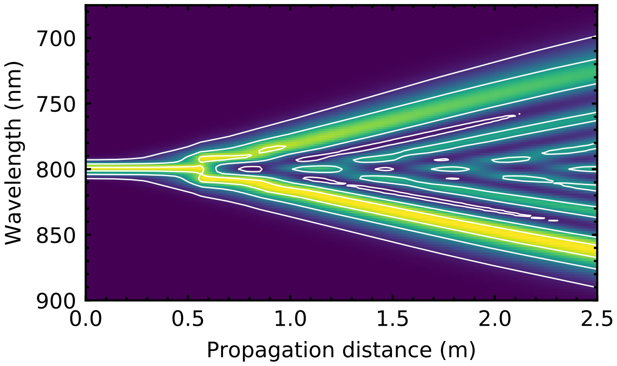

Figure 4.8: Modeling of pulse propagation. Normalized spectra as a function of propagation distance. Same conditions as Fig 4.7b.

and input pulses. These simulation results suggest this fiber can be used over the whole visible bandwidth, down to 450 nm. Broadening in the UV is impossible due to an increase in plasma generation at 400 nm or bluer wavelengths. This increase in plasma density causes an important reduction in the transmission, down to ∼10%. All other parameters yield an identical transmission due to the negligible impact of plasma. The use of a gas with a larger ionization potential (Ne, He) should extend the bandwidth accessible to the UV.

4.5 Conclusion

HCFs are fully passive, stable broadband white-light sources with a high overall transmission and excellent spatial mode. The broadening can be increased by using smaller fiber inner diameter, longer fiber length, higher gas pressure and higher input laser energy. The broadening operates mostly through self-phase modulation, yielding a smooth spectral phase. Selection of the visible part of the fiber output using a shortpass filter yields a pulse of shorter duration than the input pulse. This behavior is reproduced by numerical modeling of nonlinear propagation in HCFs. The design of the fiber is facilitated by the availability of efficient and well-established modeling techniques.

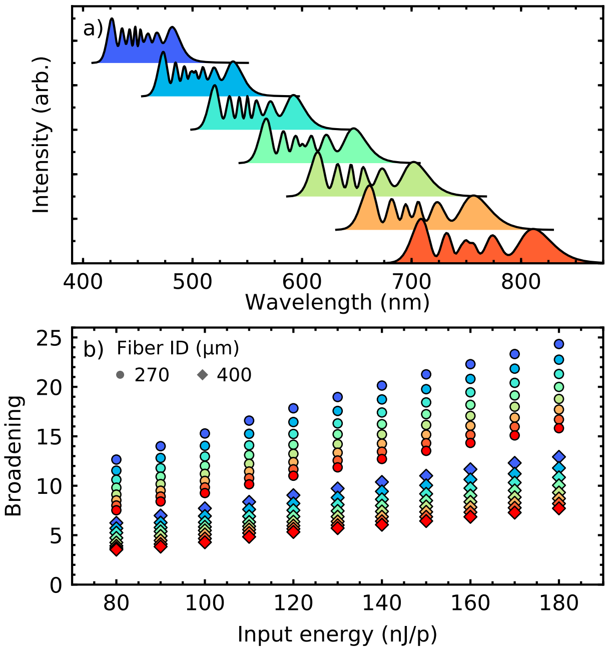

Figure 4.9: Ar-filled hollow fibers can broaden over the complete visible range. (a) Output spectra for OPA pumping (100 fs, 150 µJ/p, 270 µm ID). Central wavelength is varied in steps of 50 nm from 450 nm to 750 nm. (b) Spectral broadening as a function of power for different model parameters (see text). Color: central wavelength (matches colors in a). Symbols indicate fiber inner diameter: 270 µm (circles) or 400 µm (diamonds).

References

1. Niedringhaus, A. *et al.* Primary processes in the bacterial reaction center probed by two-dimensional electronic spectroscopy. *Proceedings of the National Academy of Sciences* **115,** 3563–3568 (Apr. 2018).
2. Paleček, D., Edlund, P., Westenhoff, S. & Zigmantas, D. Quantum coherence as a witness of vibronically hot energy transfer in bacterial reaction center. *Science Advances* **3,** e1603141 (Sept. 2017).
3. Duan, H.-G. *et al.* Nature does not rely on long-lived electronic quantum coherence for photosynthetic energy transfer. *Proceedings of the National Academy of Sciences* **114,** 8493–8498 (2017).
4. Monahan, D. M. *et al.* Room-Temperature Coherent Optical Phonon in 2D Electronic Spectra of CH3NH3PbI3Perovskite as a Possible Cooling Bottleneck. *Journal of Physical Chemistry Letters* **8,** 3211–3215 (2017).
5. Aeschlimann, M. *et al.* Coherent Two-Dimensional Nanoscopy. *Science* **333,** 1723–1726 (2011).
6. Cassette, E., Pensack, R. D., Mahler, B. & Scholes, G. D. Room-temperature exciton coherence and dephasing in two-dimensional nanostructures. *Nature Communications* **6,** 6086 (Dec. 2015).
7. Petti, M. K., Lomont, J. P., Maj, M. & Zanni, M. T. Two-Dimensional Spectroscopy Is Being Used to Address Core Scientific Questions in Biology and Materials Science. *Journal of Physical Chemistry B* **122,** 1771–1780 (2018).
8. Dudley, J. M., Genty, G. & Coen, S. Supercontinuum generation in photonic crystal fiber. *Reviews of Modern Physics* **78,** 1135–1184 (2006).

9. Shim, S.-H. & Zanni, M. T. How to turn your pump–probe instrument into a multidimensional spectrometer: 2D IR and Vis spectroscopiesvia pulse shaping. *Phys. Chem. Chem. Phys.* **11,** 748–761 (Feb. 2009).

10. Ma, X., Dostál, J. & Brixner, T. Broadband 7-fs diffractive-optic-based 2D electronic spectroscopy using hollow-core fiber compression. *Optics Express* **24,** 20781 (Sept. 2016).

11. Son, M., Mosquera-Vázquez, S. & Schlau-Cohen, G. S. Ultrabroadband 2D electronic spectroscopy with high-speed, shot-to-shot detection. *Optics Express* **25,** 18950 (2017).

12. Kearns, N. M., Mehlenbacher, R. D., Jones, A. C. & Zanni, M. T. Broadband 2D electronic spectrometer using white light and pulse shaping: noise and signal evaluation at 1 and 100 kHz. *Optics Express* **25,** 7869 (2017).

13. Robinson, J. S. *et al.* The generation of intense, transform-limited laser pulses with tunable duration from 6 to 30 fs in a differentially pumped hollow fibre. *Applied Physics B: Lasers and Optics* **85,** 525–529 (2006).

14. Béjot, P., Schmidt, B. E., Kasparian, J., Wolf, J. P. & Legaré, F. Mechanism of hollow-core-fiber infrared-supercontinuum compression with bulk material. *Physical Review A - Atomic, Molecular, and Optical Physics* **81,** 2–7 (2010).

15. Agrawal, G. *Nonlinear Fiber Optics* 648. `https://doi.org/10.1016/C2011-0-00045-5` (Academic Press, 2012).

16. Loriot, V., Hertz, E., Faucher, O. & Lavorel, B. Measurement of high order Kerr refractive index of major air components. *Optics Express* **17,** 13429 (Aug. 2009).

17. Ettoumi, W., Petit, Y., Kasparian, J. & Wolf, J.-P. Generalized Miller Formulæ. *Optics Express* **18,** 6613 (Mar. 2010).

18. Wahlstrand, J. K., Cheng, Y.-H., Chen, Y.-H. & Milchberg, H. M. Optical Nonlinearity in Ar and N2 near the Ionization Threshold. *Physical Review Letters* **107,** 103901 (Aug. 2011).
19. Brée, C., Demircan, A. & Steinmeyer, G. Saturation of the all-optical Kerr effect. *Physical Review Letters,* 183902 (2011).
20. Borchers, B., Brée, C., Birkholz, S., Demircan, A. & Steinmeyer, G. Saturation of the all-Optical Kerr Effect in Solids and Gases. *Opt. Lett.* **13429,** 1541 (2012).
21. Richter, M., Patchkovskii, S., Morales, F., Smirnova, O. & Ivanov, M. The role of the Kramers-Henneberger atom in the higher-order Kerr effect. *New Journal of Physics* **15,** 083012 (2013).
22. Brabec, T. & Krausz, F. Intense few-cycle laser fields: Frontiers of nonlinear optics. *Reviews of Modern Physics* **72,** 545–591 (Apr. 2000).
23. Trebino, R. *Frequency-Resolved Optical Gating: The Measurement of Ultrashort Laser Pulses* `http://link.springer.com/10.1007/978-1-4615-1181-6` (Springer US, Boston, MA, 2000).
24. Seiler, H., Palato, S., Schmidt, B. E. & Kambhampati, P. Simple fiber-based solution for coherent multidimensional spectroscopy in the visible regime. *Optics Letters* **42,** 643 (Feb. 2017).
25. Tiwari, V. *et al.* Strongly coupled bacteriochlorin dyad studied using phase-modulated fluorescence-detected two-dimensional electronic spectroscopy. *Optics Express* **26,** 22327 (Aug. 2018).
26. Mueller, S. *et al.* Fluorescence-Detected Two-Quantum and One-Quantum-Two-Quantum 2D Electronic Spectroscopy. *Journal of Physical Chemistry Letters* **9,** 1964–1969 (2018).

27. Lomsadze, B. & Cundiff, S. T. Frequency combs enable rapid and high-resolution multidimensional coherent spectroscopy. *Science* **357,** 1389–1391 (2017).

28. Hamm, P. & Zanni, M. *Concepts and methods of 2D infrared spectroscopy* 1–286 (2011).

29. Tan, H.-S. Theory and phase-cycling scheme selection principles of collinear phase coherent multi-dimensional optical spectroscopy. *The Journal of chemical physics* **129,** 124501 (Sept. 2008).

30. Bolzonello, L., Volpato, A., Meneghin, E. & Collini, E. Versatile setup for high-quality rephasing, non-rephasing, and double quantum 2D electronic spectroscopy. *Journal of the Optical Society of America B* **34,** 1223 (2017).

31. Bethge, J. *et al.* Self-compression of 120fs pulses in a white-light filament. *Journal of Optics* **13** (2011).

32. Zifkin, R. & McGowan, J. *Self-Phase Modulation* 2018. `https://github.com/ry-dgel/self-phase`.

CHAPTER 5

Atomic disorder gives rise to dissipation of electronic coherences in semiconductor nanocrystals.

Coherent femtosecond spectroscopy allows the investigation of coherent electronic dynamics. The observation of quantum beats, periodic modulation of the lineshape, have sparked discussion pertaining to the characterization, design and performance of materials. This chapter uses the theory presented in chapter 2 and the instrument presented in chapter 3 to analyze the coherent optical response of CdSe semiconductor nanocrystal via two-dimensional electronic spectroscopy (2DE). Coherence map analysis reveals the observed oscillations in the 2D spectra arise from coherent optical phonons. Contrary to predictions of standard continuum-based models, no electronic coherences were observed between the first two excitons. The absence of measurable electronic coherence is modeled using *ab initio* molecular dynamics of a single realistic nanocrystal. Rapid dephasing of interexcitonic coherences is due to the complicated electronic structure intrinsic to a NC represented at an atomistic level of details. This dephasing mechanism is expected to be of general importance to nanostructures. The study of coherent dynamics by 2DE is a general and sensitive experiment that allows detailed analysis of the source of electronic disorder in complex materials.

5.1 Introduction

Quantum coherences are a fundamental quantum mechanical phenomenon which occurs whenever two quantum states with a fixed phase relationship interfere. They can be observed for any quantum degree of freedom: spin, rotational, vibrational or electronic [1–4]. Such coherences are important spectroscopic probes of structural and kinetic disorder: magnetic resonance imaging technology manipulates spatial inhomogeneity to obtain spatial resolution and exploits coherence lifetime to obtain contrast [5]. Rotational coherences have been controlled to image molecules in their own reference frame [6, 7]. Vibrational and electronic coherences are more challenging to observe due to their high frequencies, short lifetimes and exquisite sensitivity to system details. While electronic coherences can be observed in femtosecond and attosecond pump-probe measurements, these spectroscopies have typically been confined to clean and cold systems such as dilute gases and metal surfaces [4, 8–11]. The advent of coherent multidimensional spectroscopy enables the investigation of electronic coherences in condensed matter systems supporting many-body physics such as biological light-harvesting proteins and nanomaterials [12–18].

In addition to the high frequencies and short dephasing times of electronic coherences, their observation in complex systems is often complicated by the simultaneous presence of vibrational coherences. This challenge is illustrated by the intense debate regarding the existence of long-lived coherences in light-harvesting systems [12, 19–23]. Distinguishing vibrational from electronic oscillations is essential as it completely changes the interpretation of the signal. Coherent electronic dynamics are profoundly sensitive to details of the system's structure and dynamics: any conclusions about their occurrence remains highly system specific. As such, parameters that impact the observation and preservation of electronic coherences can vary widely, from gas pressure in gas-phase atoms [10] to vibrational structure in biological light harvesting complexes [12, 24, 25] and exciton-exciton interactions in epitaxial quantum wells [26, 27]. A similar understanding is still in its infancy for colloidal nanostructures.

Semiconductor nanocrystals are an ideal model system to probe electronic coherences. These colloidal nanocrystals are characterized by a well-resolved vibrational and electronic structure. Their well understood vibrational manifold enables the use of coherent phonons as an internal standard for coherent dynamics [28]. These nanocrystals have a rich electronic structure that has been described at various levels of theory. Inter-excitonic coherences provide a sensitive experimental signature to test these theories [29–32]. There have been reports of pure electronic coherences in colloidal semiconductor nanostructures such as nanoplatelets [15, 33] and nanocrystals [34–38]. However, such reports are intermittent, and the coherence signals are always weak and short-lived. This is surprising: the discrete colocalized exciton states should yield a long-lived inter-excitonic coherence. This discrepancy underlines a current need to identify the phenomena relevant to the observation and preservation of inter-excitonic coherences in colloidal nanostructures.

Here 2DE spectroscopy is applied to probe coherences in CdSe nanocrystals (NCs). The implementation of 2DE spectroscopy enables coherence mapping thereby revealing a detailed view of coherent dynamics. The coherence maps confirm coherent optical phonons. In contrast to 1D experiments, these 2D coherence maps uniquely enable assignment of the microscopic quantum mechanical contributions to the signals [39, 40]. The experimental signals do not show the presence of electronic coherences that would have been predicted under standard continuum effective mass approximation theories. Atomistic *ab initio* molecular dynamics rationalizes the absence of electronic coherences due to disorder arising naturally from atomistic details,

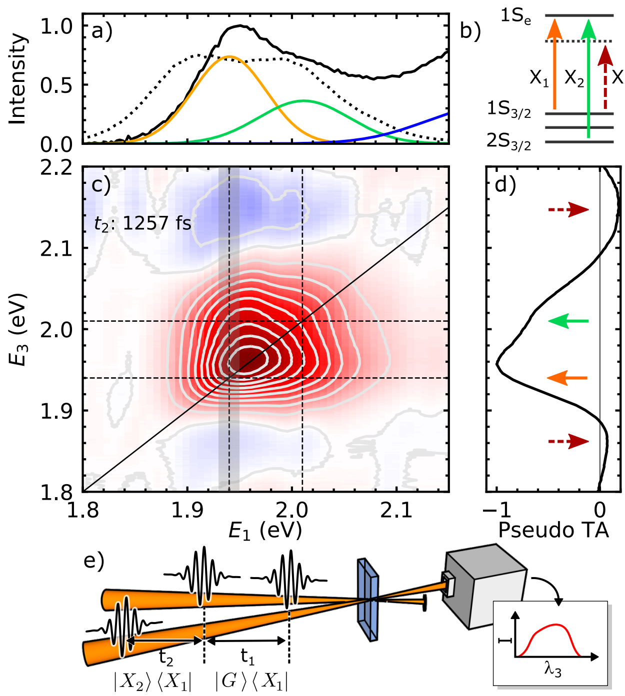

Figure 5.1: Electronic spectroscopy of CdSe NCs. (a) Linear absorption spectrum (black) and constituent peaks (colors match panel b). Laser spectrum shown as a dotted line. (b) Minimal energy level diagram. Solid arrows: excitons, dashed: biexcitons. (c) Representative 2DE spectrum, offering a detailed view of the electronic response. Inter-excitonic coherences should appear where the dashed lines meet. Red: bleach (GSB, SE), blue: induced absorption. (d) Pseudo-TA spectrum, shaded region in c. (e) Schematic diagram of 2DE spectroscopy in the pump-probe geometry.

even in single nanostructures. Results on this model system implies the study of electronic coherences by 2DE may be used to identify the sources of electronic disorder in complex materials.

Semiconductor NCs have a rich electronic structure that has been described at various levels of theory, from continuum to atomistic models [29–32]. Fig 5.1 shows the electronic structure and spectroscopy of CdSe NCs. The prevailing model of semiconductors NCs is called the multiband $k{\cdot}p$ effective mass approximation (EMA). Despite its simplicity, this model has successfully provided the framework of decades of spectroscopic investigations, from fluorescence to multidimensional spectroscopy.

More refined theories are available and mature, but usually unnecessary [29–32, 41, 42]. In the EMA model, the Bloch waves of the bulk semiconductor are confined in a nanoparticle. As a result, the conduction and valence bands split, yielding discrete electron and hole states. These in turn yield a manifold of discrete exciton states, which are more strongly bound than in the bulk. The absorption spectrum reveals discrete excitonic transitions (Fig 5.1a). The first two exciton transitions and their electrons and hole states are indicated on Fig 5.1b. Notably, this model predicts the first two excitons share an electron state (1Se), but have different hole states (X_1: $1S_{3/2}$, X_2: $2S_{3/2}$) [29, 35, 43–45]. They should sustain a long lived inter-excitonic coherence as only hole dynamics contribute to dephase a $|X_2\rangle \langle X_1|$ coherence.

Furthermore, the NCs can host multiple excitations, in the form of bound biexcitons and multiexcitons. First observed in time-resolved photoluminescence, biexcitons are apparent as red-shifted induced absorption (IA) in the time-resolved absorption spectra, Figs 5.1c,d [46, 47]. Calculations using the EMA model suggests this binding is dominated by exchange interactions [30]. Due to the small (∼10 meV) binding energy of the band edge biexciton, the induced absorption overlaps with the bleach signal and the contributions are hard to separate [48]. Time-resolved spectroscopy of CdSe experiments have reported oscillations due to both the optical and acoustic phonons [28, 49–51]. Weak and short lived electronic coherences have been reported by broadband transient absorption (TA) and 2DE for $|X_1\rangle \langle X_2|$ [35, 36]. Surprisingly long coherences lasting ∼100 fs have been reported for $|X_1\rangle \langle X_3|$ [34].

Coherent dynamics can be studied using 2D spectroscopy, which has been described in detail elsewhere [14, 52–57]. A representative 2D spectrum is shown on Fig 5.1c, experimental scheme on Fig 5.1e. Briefly, this experiment is a three-pulse experiment similar to a pump-probe measurement where a pair of phase-stable broadband pulses acts as the pump. The first delay t_1 is scanned; its Fourier transform yields a detection axis E_1. Delay t_2 is analogous to the pump-probe delay of TA. During this delay, the system can be in a population (eg: $|\mathrm{G}\rangle\langle\mathrm{G}|$ or $|\mathrm{X}_i\rangle\langle\mathrm{X}_i|$) or inter-excitonic coherence (eg: $|\mathrm{X}_j\rangle\langle\mathrm{X}_i|$). It evolves under the field-free Hamiltonian. The third pulse acts as the probe. Its transmission is monitored using a spectrometer yielding a spectral detection axis E_3. The result is a 2D spectrum $S(E_1, t_2, E_3)$. The 2D spectrum can reveal coupled transitions, relaxation processes, reduce spectral congestion and deconvolve lineshape contributions [13, 53, 58, 59]. Of particular interest, coherent processes are revealed by oscillations of the peak intensities as a function of t_2. The experiment reported here is carried out in the pump-probe geometry, which can be realized simply by inserting a pulse shaper in the pump arm of a TA spectrometer. In this geometry, the absorptive 2D spectrum is easily acquired without the need for delicate phasing and filtering procedures. It is directly related to the basic phenomena of absorption and dispersion: the intensity of the real absorptive spectrum (shown here) can be interpreted as arising from ground state bleach (GSB), stimulated emission (SE) and induced absorption (IA) [52, 53, 60–62].

5.2 Methods

5.2.1 Two-dimensional electronic spectroscopy

The experimental setup is identical to previous work [55]. The output of a 1 kHz 130 fs 800 nm Ti:Sapphire regenerative amplifier (Coherent Legend Elite HE+) is coupled to a 2.5 m long, 400 μm inner diameter hollow core fiber (few-cycle) filled with Argon (gradient, 3 bar). The visible part of the broadband output is selected using a low-pass filter (<700 nm). Transmission GRISMs (GRating + prISM, Fastlite) are used for dispersion management. The visible continuum pulse is split and each arm is sent to a pulse shaper (AOPDF, Dazzler, Fastlite) to generate the three pulses and control their delays, spectral amplitudes and phases. The pulses are characterized using a home-built all-reflective TG-FROG. Recovered pulse durations are typically 11-13 fs. Spot size is estimated to 100 μm at the sample position using a CCD camera. Pulse energies were 10 nJ/pulse for each of the three pulses. The spectrum of the transmitted probe was monitored using a spectrometer (Acton 2500i, Pixis 100B Excelon). A two-step phase cycling scheme was used [56]. CdSe nanocrystals (NCs) in toluene where purchased from NNLabs. Their band edge absorption was 640 nm with a Wurtzite lattice and octadecylamine ligands. The experiment was carried out in a 200 μm optical path length glass flow cell (Starna). The samples were constantly flowed during the experiment. OD of the samples was 0.3 in the 200 μm cuvette.

5.2.2 Details of AIMD calculation

The simulations were performed on a $Cd_{33}Se_{33}$ cluster with a diameter of 1.3 nm constructed using bulk wurtzite lattice. $Cd_{33}Se_{33}$ is one of the smallest stable CdSe NCs that support a crystalline-like core making it an excellent model for studying electronic and vibrational properties of semiconductor NCs [63, 64]. A the plane-wave density functional theory approach is employed to describe the electronic properties of the system, as implemented in QUANTUM ESPRESSO [65] program package. The cluster geometry was optimized using the Perdew-Burke-Ernzerhof (PBE) [66] exchange-correlation functional with norm-conserving pseudopotential. The kinetic energy cutoff for wave function was set to 30 Ry. The simulations were performed in a periodically replicated cubic cell with at least 10 Å of vacuum in each direction between NC replicas. Following the geometry optimization, the fully optimized structure was heated to 300 K with repeated velocity rescaling for 1000 fs using the Andersen thermostat. A 1.5 picosecond-long ground state molecular dynamics (MD)

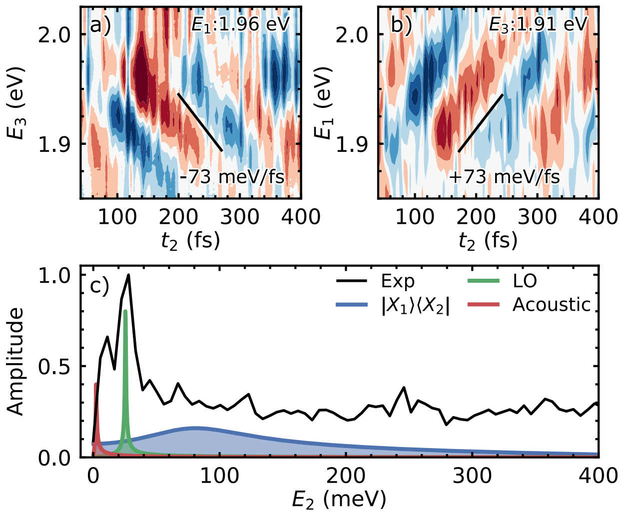

Figure 5.2: Unraveling oscillations in the time-resolved spectra. (a,b) Oscillations can be studied along either E_1 (a) or E_3 (b). Color indicates amplitude relative to peak 2D signal. (c) Spectrum of the oscillations, amplitude integrated for E_1, E_3 from 1.85 to 2.10 eV. Expected peaks for the LO phonon, acoustic phonons and $|\mathrm{X}_1\rangle\langle\mathrm{X}_2|$ are shown for reference.

trajectory at 300 K was then generated using the Verlet algorithm and the Andersen thermostat with a time step of 1 fs.

5.3 Results

In 2DE, coherent oscillations can be reported as a function E_3 (Fig 5.2a) or E_1 (Fig 5.2b). The latter is not possible in other techniques. Following common procedures, incoherent dynamics are removed by global analysis using a multi-exponential decaying model [12, 67–69]. The residuals show a dominant contribution from the longitudinal optical (LO) phonon, with a period of ∼160 fs. The phase of the oscillations shifts as a function of both detection and excitation energy, consistent with frequency modulation arising from coupling to the LO phonon [70–74]. The existence of a substantial phase shift implies that a technique that averages over a large excitation bandwidth will attenuate the relative amplitude of the oscillations.

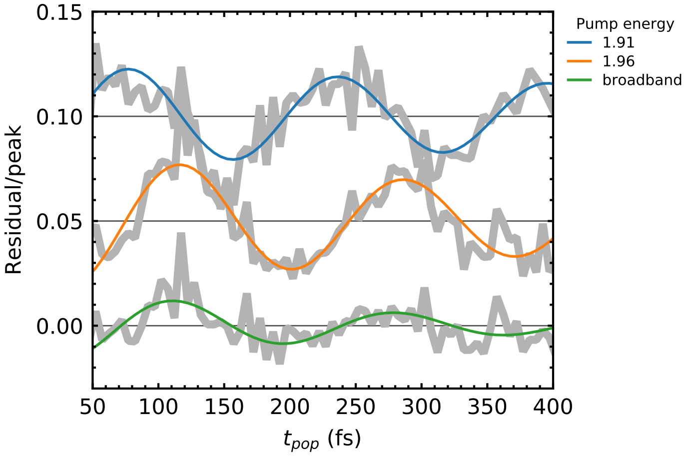

Figure 5.3: Apparent amplitude and phase of oscillations depend on central frequency and bandwidth of both pump and probe. Two narrowband slices of 12 meV bandwidth at 1.91 and 1.96 eV show larger relative oscillations than a broadband slice of 200 meV bandwidth at 1.95 eV. Coloured lines are fits to a single damped oscillation. Curves offset for clarity.

Fig 5.3 shows the oscillations at E_3=1.91 eV at two pump energies and for the broadband case. The two narrowband curves are obtained by integrating over a bandwidth of 12 meV. The broadband signal uses a bandwidth of 200 meV. Broadband transient absorption risks underestimating the amplitude of the phonon oscillation, depending on their phase shifts which are dependent on the system Hamiltonian. Pump bandwidth thus further complicates the comparison of TA experiments with varying bandwidths [36]. This emphasizes the necessity of a technique that completely characterizes the third order response.

The residual oscillations can be Fourier transformed to study directly their spectral components. This operation yields a 3D spectrum. Fig 5.2c shows the amplitude of the oscillations integrated over the region spanning 1.85 to 2.1 eV along both E_1 and E_3. Expected signatures are also shown [34, 51]. The strongest signature arises from the LO phonon (∼25 meV). Another peak can be seen at lower energies, which

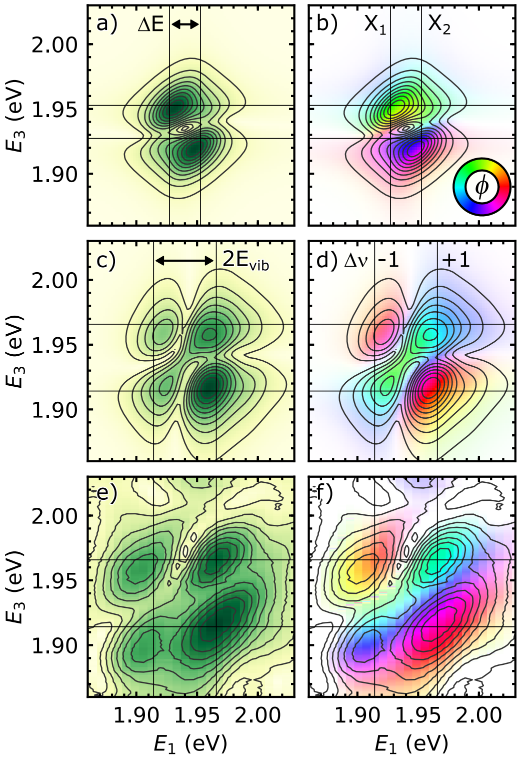

Figure 5.4: Simulated and experimental coherence maps for the strongest signature, E_2=25 meV. (a) Amplitude and (b) phase for a model electronic coherence. (c) Amplitude and (d) phase for a model vibrational coherence. (e) Amplitude and (f) phase for the experimental coherence map at 25 meV, indicating it is of vibrational origin. Inset in b: color scale for phase.

can be associated with known acoustic phonons [59]. Due to the short time range used here, it is poorly resolved and will thus not be discussed further. The coherent LO phonon serves as an internal standard for the measurement of other coherences [75]. Fig 5.2 indicates oscillations of less than 2% of the peak signal amplitude are well resolved.

A more detailed picture can be obtained by taking projections at fixed E_2, yielding coherence maps [39, 76–79]. Fig 5.4 shows model and experimental coherence maps for the signal at E_2=25 meV. Separating the signal by mixing energy allows the selection of spectroscopic signatures by their coupling to specific excitations [26, 76, 77, 80]. Coherence mapping allows the assignation of whether they are electronic or vibrational coherences without relying on separate acquisitions of the rephasing and non-rephasing contributions. The distinction is usually carried out using patterns of peaks on the coherence maps [80, 81]. However, lineshape parameters and induced absorption obfuscate the pattern of the underlying peaks. As such, simple model calculations are carried out using the cumulant expansion to second order, neglecting relaxation [58, 78, 81–83]. This technique allows the modeling of nonlinear spectra using few parameters: the states' average energy, the transition dipoles and lineshape functions.

The calculation was carried out using the methods outlined in sections 2.4.2 and 2.3.4. The code is available online [84]. Throughout the manuscript, Bloch dynamics are used as model lineshapes (ie: homogeneous dephasing, eq 2.130 and gaussian inhomogeneous broadening, eq 2.131). Coupling to a vibrational mode is added using the Huang-Rhys lineshape function, eq 2.133. The choice of these lineshape functions is justified by the lack of spectral dynamics in NCs [59]. The use of undamped vibrational modes is justified by the short time window used here, shorter than the dephasing time of the LO phonon.

The model coherence maps were obtained by considering systems simplified with respect to previous work by the group of Pullerits [78, 81]. The model coherence map for electronic coherence is obtained by considering a 4-level system consisting of a ground state G, two excitons states X_1, X_2 and a biexciton state XX. The energies of the two excitons are E_{X1} and E_{X2}. They are separated by an energy difference $\Delta E_{21} = E_{\mathrm{X2}} - E_{\mathrm{X1}}$=25 meV. This energy sets the frequency of the oscillation along E_2. The biexciton has an energy $E_{\mathrm{XX}} = E_{\mathrm{X1}} + E_{\mathrm{X2}} - \delta E$, with small binding energy δE=10 meV. The lineshape functions use the homogeneous and inhomogeneous lineshape functions (eqs 2.130 and 2.131) with γ=10 meV and σ= 10 meV. All transition dipole moments are set to 1.

The model coherence map for vibrational coupling is obtained by considering a 3-level system consisting of a ground state G, a single exciton state X_1 and a biexciton state XX. Coupling to vibrations is modeled as an undamped classical vibrational bath mode (E_{vib}=25.5 meV) using the Huang-Rhys lineshape function (eq 2.133) with S=0.2 at 298 K. Vibrational dephasing is neglected since the experimental time window is much shorter than the lifetime of the vibrational oscillations ($>$1 ps) [85]. In this model, the lineshape function is made of 3 contributions: homogeneous and inhomogeneous dephasing (as previously) and Huang-Rhys coupling. It was verified that using smaller values for the Huang-Rhys parameter doesn't change the coherence map shape or phase.

Fig 5.4a,b shows the amplitude and phase of the coherence maps for an electronic coherence. The amplitude (Fig 5.4a) reveals two symmetric features, with a relative phase shift of π (Fig 5.4b). This structure arises from the interference of stimulated emission (top) and induced absorption (bottom) [80]. Results for the model vibrational coherence are shown on Fig 5.4c,d. It shows 4 features on the corners of a square, roughly separated by twice the beat energy. These correspond to the diagonal and cross peaks formed by the +1 and -1 phonon line [81]. The diagonal peaks are π phase shifted with respect to the off-diagonal contributions.

Fig 5.4e,f show the experimental coherence maps obtained for E_2= 25 meV. Both the progression of the intensities and the phases shows an excellent agreement with the vibrational model coherence maps considering the use of a simplified model. Using the shape and phase of model coherence maps, it is possible to assign the

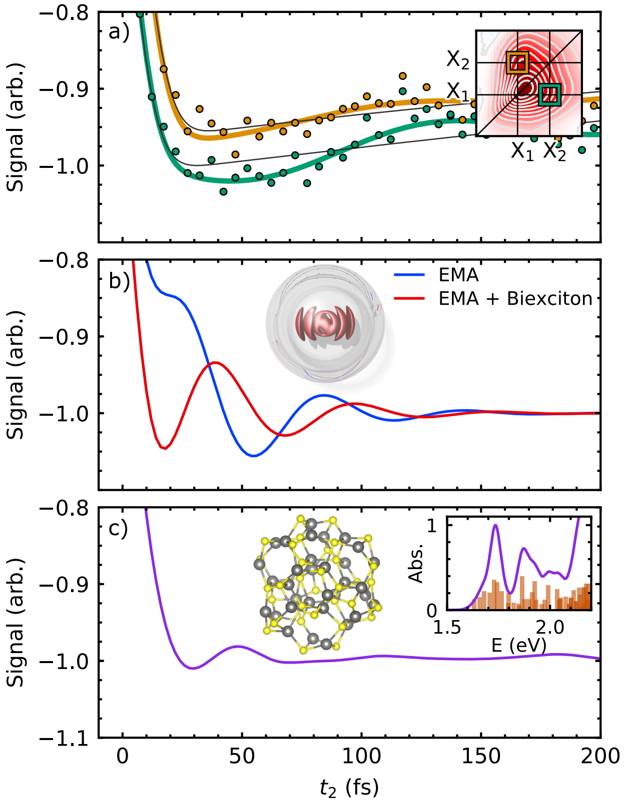

Figure 5.5: No electronic coherences can be observed between the X$_1$ and X$_2$ excitons. (a) Cross peak dynamics show no oscillations other than the LO phonon. Inset: location of the cross peaks. (b) Predictions based on the discrete states of the EMA yields an observable coherence of large magnitude (see text). Biexciton contributions does not reduce the relative amplitude of the coherence. (c) Atomistic details induce very fast dephasing. Cross-peak dynamics obtained using AIMD trajectories. Inset: linear spectrum (line), individual transitions and their transition dipoles (sticks).

nature of an oscillatory component using 2DE in the pump-probe geometry. The use of model calculations permits this assignment despite overlapping contributions.

5.4 Discussion

The strongest oscillatory component was assigned to the weak LO phonon, in agreement with the literature [28, 49–51]. Most intriguing is that no signatures can be assigned to electronic coherence. A more detailed look at the X$_1$, X$_2$ cross peaks is warranted. Fig 5.5a shows transients over square regions 40 meV across around the cross peaks which should reveal oscillations due to electronic coherences. The data can be fully accounted for by population decay and the LO phonon. There is no $|X_1\rangle\langle X_2|$ coherence in Wurtzite CdSe NCs at room temperature. This observation is unexpected: the discrete manifold predicted by the EMA should yield an observable coherence.

5.4.1 Description of model EMA calculation

First, the expected properties of the $|X_1\rangle\langle X_2|$ coherence in NCs are estimated quantitatively. Dephasing of coherences arises from two contributions: incoherent relaxation processes and decorrelation of the states participating in the coherence [86]. The $X_2 \rightarrow X_1$ hole relaxation occurs with a timescale of 200 fs, which is much slower than other dephasing mechanisms and is thus safely neglected [87]. Decorrelation of the energy of the states is described using lineshape functions, using eqs 2.149, 2.130 and 2.131. Each lineshape function is made of two contributions: homogeneous dephasing and gaussian inhomogeneous broadening. The lack of spectral dynamics in NCs justifies the use of Bloch dynamics [53, 58, 83]. The LO phonon is not considered, due to its different frequency.

The experimental data can be captured by using a single ground state and two excitons, X_1 and X_2. The energies of the excitons are made of the constituent electrons and holes:

$$E_{X_1} = E_e - E_{h_1} \tag{5.1}$$

$$E_{X_2} = E_e - E_{h_2} \tag{5.2}$$

$$\tag{5.3}$$

As such, the fluctuations of the exciton energies can be separated in a hole and electron part. In order to reduce the number of parameters, a few experimentally justified assumptions are made.

As a limiting case, the fluctuations of the fast homogeneous dephasing are considered uncorrelated for all electrons and holes involved. The homogeneous dephasing of the electron and holes are assumed to be uncorrelated and of equal magnitude γ. This estimate puts a lower bound on the pure dephasing time of the inter-excitonic coherence: a first-principles calculation is likely to result in correlation between the energy fluctuations of the two holes as they share a phonon bath [27, 34, 41, 42].

The correlation functions can be derived as follows, using the homogeneous dephasing lineshape function $g^{(\mathrm{H})}$ of the X_1 exciton as an example:

$$\begin{aligned}
\delta E^{(\mathrm{H})}_{\mathrm{X}_1}(t) &= \delta E^{(\mathrm{H})}_{\mathrm{e}}(t) - \delta E^{(\mathrm{H})}_{\mathrm{h}_1}(t) && (5.4)\\
C^{(\mathrm{H})}_{\mathrm{X}_1,\mathrm{X}_1}(t) &= \langle \delta E_{\mathrm{X}_1}(t)\delta E_{\mathrm{X}_1}(t)\rangle_{\mathrm{eq}} && (5.5)\\
&= \left\langle \left(\delta E^{(\mathrm{H})}_{\mathrm{e}}(t) - \delta E^{(\mathrm{H})}_{\mathrm{h}_1}(t)\right)\left(\delta E^{(\mathrm{H})}_{\mathrm{e}}(0) - \delta E^{(\mathrm{H})}_{\mathrm{h}_1}(0)\right)\right\rangle_{\mathrm{eq}} && (5.6)\\
&= \langle \delta E_{\mathrm{e}}(t)\delta E_{\mathrm{e}}(0)\rangle_{\mathrm{eq}} - \langle \delta E_{\mathrm{e}}(t)\delta E_{\mathrm{h}_1}(0)\rangle_{\mathrm{eq}} \\
&\quad - \langle \delta E_{\mathrm{h}_1}(t)\delta E_{\mathrm{e}}(0)\rangle_{\mathrm{eq}} + \langle \delta E_{\mathrm{h}_1}(t)\delta E_{\mathrm{h}_1}(0)\rangle_{\mathrm{eq}} && (5.7)\\
C^{(\mathrm{H})}_{\mathrm{X}_1,\mathrm{X}_1}(t) &= \langle \delta E_{\mathrm{e}}(t)\delta E_{\mathrm{e}}(0)\rangle_{\mathrm{eq}} + \langle \delta E_{\mathrm{h}_1}(t)\delta E_{\mathrm{h}_1}(0)\rangle_{\mathrm{eq}} && (5.8)\\
C^{(\mathrm{H})}_{\mathrm{X}_1,\mathrm{X}_1}(t) &= \gamma_{\mathrm{e}}\delta(t) + \gamma_{\mathrm{h}_1}\delta(t) && (5.9)
\end{aligned}$$

yielding:

$$g^{(\mathrm{H})}_{\mathrm{X}_1,\mathrm{X}_1}(t) = (\gamma_{\mathrm{e}} + \gamma_{\mathrm{h}_1})t. \tag{5.10}$$

In the above equations, $\delta E_i(t)$ is the fluctuating part of the energy of particle i, the angular brackets denote averaging over equilibrium conditions (i.e.: stationary average), $\delta(t)$ is the Dirac delta (the correlation function for homogeneous dephasing). Uncorrelated fluctuations of electrons and holes are used to obtain eq 5.8 from equation 5.8. Eq 5.10 is obtained from eq 5.9 using eq 2.128. In the same way, the other lineshape functions are obtained:

$$g^{(\mathrm{H})}_{\mathrm{X}_2,\mathrm{X}_2}(t) = (\gamma_{\mathrm{e}} + \gamma_{\mathrm{h}_2})t, \tag{5.11}$$

$$g^{(\mathrm{H})}_{\mathrm{X}_1,\mathrm{X}_2}(t) = g^{(\mathrm{H})}_{\mathrm{X}_2,\mathrm{X}_1}(t) = \gamma_{\mathrm{e}}t. \tag{5.12}$$

For simplicity, it is assumed that all electrons and holes have identical homogeneous dephasing rates: $\gamma_{\mathrm{e}} = \gamma_{\mathrm{h}_1} = \gamma_{\mathrm{h}_2} = \gamma$.

The inhomogeneous broadening is usually considered to be dominated by size inhomogeneity, which is perfectly correlated for all states. This has a major implication: whereas size distribution dominates the dephasing of single excitons, its impact is reduced for inter-excitonic coherences. Estimation of the effect of inhomogeneous size distribution relies on well-established values for the size-dependence of the spectroscopic transitions, shown to be compatible with the EMA [29, 88]. The energy gap between the first two excitons is related linearly to the X_1 transition energy, such that $\delta E_{\mathrm{X}_2} = r\delta E_{\mathrm{X}_1}$ and $\sigma_{\mathrm{X}_2} = r\sigma_{\mathrm{X}_1}$. Using this quantity, we obtain the following correlation functions for inhomogeneous broadening:

$$C^{(\mathrm{I})}_{\mathrm{X}_1,\mathrm{X}_1}(t) = \langle \delta E_{\mathrm{X}_1}(t)\delta E_{\mathrm{X}_1}(0)\rangle_{\mathrm{eq}} = \sigma^2_{\mathrm{X}_1} \tag{5.13}$$

yielding:

$$g^{(\mathrm{I})}_{\mathrm{X}_1,\mathrm{X}_1}(t) = \frac{1}{2}\sigma^2_{\mathrm{X}_1}t^2 \tag{5.14}$$

Similarly:

$$g^{(\mathrm{I})}_{\mathrm{X}_2,\mathrm{X}_2}(t) = \frac{1}{2}\sigma^2_{\mathrm{X}_2}t^2 = \frac{1}{2}r^2\sigma^2_{\mathrm{X}_1}t^2 \tag{5.15}$$

Table 5–1: Parameters used for model inter-excitonic coherence under the EMA.

Parameter	Value	Source
E_{X_1}	1.94 eV	Linear spectrum
E_{X_2}	2.01 eV	Linear spectrum
γ	8.75 meV	[59, 89]
r	1.3	[29]
σ_{X_1}	14.86 meV	[89]

$$g^{(\mathrm{I})}_{\mathrm{X}_1,\mathrm{X}_2}(t) = g^{(\mathrm{I})}_{\mathrm{X}_2,\mathrm{X}_1}(t) = \frac{1}{2} r \sigma^2_{\mathrm{X}_1} t^2 \tag{5.16}$$

Using this analysis, the lineshape functions can be entirely described by 3 parameters: γ, σ_{X_1} and r. The complete set of parameters, derived from previous experimental work, is included in table 5–1. Parameters are estimated from previous experimental work. A value of $2\gamma_{\mathrm{X}_1,\mathrm{X}_1}$=35 meV can be extracted from the antidiagonal FWHM of the 2D spectrum [59, 89]. From curve b on Figure 4 of ref [29], we can extract r=1.3. An experimental FWHM of 35 meV for the inhomogeneous linewidth has been reported [89].

The lifetime of the excitons are minor contributions to dephasing processes. The lowest exciton X_1 has a lifetime of ∼30 ns, measured by time-resolved photoluminescence. The X_2 exciton relaxes to X_1 with a lifetime between 200 and 300 fs depending on particle size, ligand and shell [87, 89]. Both processes are too slow to have a measurable impact on the coherences and are neglected (200 fs corresponds to $\gamma \approx 3$ meV).

The amplitude of the interfering biexciton induced absorption depends on biexciton binding energy, transition dipole moments for the X→XX transitions, and biexciton lineshape parameters (γ and σ). Biexciton fine structure and degeneracy potentially have to be taken into account. Such a detailed calculation is beyond the

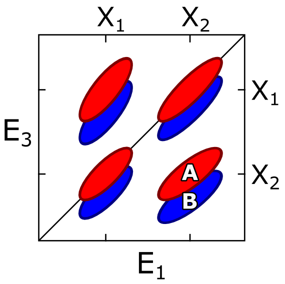

Figure 5.6: Cartoon of 2D spectrum indicating contributions to lower cross peak. Red indicates bleach, blue indicates induced absorption.

scope of this work and does not change the resulting effect: the oscillating and non-oscillating contributions cancel at the same rate. The biexciton signal presented in Fig 5.5 has been obtained by assuming a constant binding energy of 10 meV and a transition dipole moment of 0.8 for all biexciton transitions.

This calculation is carried out using the multimode brownian oscillator model (see section 2.3.4) and the results are convolved with the experimental instrument response function (IRF, FWHM=24 fs). The contributions to the cross peaks are identified on Fig 5.6 and table 5–2. The analysis focuses on early time dynamics, before $X_2 \rightarrow X_1$ relaxation occurs. Contributions arising from relaxation are neglected. The amplitude of the oscillating signal is a substantial part of the total cross-peak amplitude: the oscillating and non-oscillating contributions contain the same transition dipole moments. The results are shown as a blue curve in Fig 5.5b. Clearly, taking into account generous estimates for dephasing, the cross peak should be strongly modulated by the inter-excitonic coherences for 100 fs. Therefore, the EMA is insufficient to predict the experimentally observed lack of coherent electronic dynamics in NCs.

Table 5–2: Double-sided Feynman diagrams (DSFF) contributing to cross-peaks of the 2D absorptive spectrum. $\mathrm{X_1X_2}$ indicates a biexciton formed of the $\mathrm{X_1}$ and $\mathrm{X_2}$ excitons. Location refers to Fig 5.6.

DSFD	Type	Amplitude	Location
$\begin{array}{r\|ll\|l} & \mathrm{X_1} & \mathrm{G} & \rightarrow \\ \rightarrow & \mathrm{X_1} & \mathrm{X_2} & \\ & \mathrm{G} & \mathrm{X_2} & \leftarrow \end{array}$	R-SE oscillating	$\mu^2_{\mathrm{G,X_2}}\mu^2_{\mathrm{G,X_1}}$	A
$\begin{array}{r\|ll\|l} \rightarrow & \mathrm{X_1} & \mathrm{G} & \\ & \mathrm{G} & \mathrm{G} & \rightarrow \\ & \mathrm{G} & \mathrm{X_2} & \leftarrow \end{array}$	R-GSB incoherent	$\mu^2_{\mathrm{G,X_2}}\mu^2_{\mathrm{G,X_1}}$	A
$\begin{array}{r\|ll\|l} \rightarrow & \mathrm{X_1} & \mathrm{G} & \\ \leftarrow & \mathrm{G} & \mathrm{G} & \\ \rightarrow & \mathrm{X_2} & \mathrm{G} & \end{array}$	NR-GSB incoherent	$\mu^2_{\mathrm{G,X_2}}\mu^2_{\mathrm{G,X_1}}$	A
$\begin{array}{r\|ll\|l} \rightarrow & \mathrm{X_1X_2} & \mathrm{X_2} & \\ \rightarrow & \mathrm{X_1} & \mathrm{X_2} & \\ & \mathrm{G} & \mathrm{X_2} & \leftarrow \end{array}$	R-IA oscillating	$-\mu_{\mathrm{G,X_2}}\mu_{\mathrm{G,X_1}}\mu_{\mathrm{X_2,X_1X_2}}\mu_{\mathrm{X_1,X_1X_2}}$	B
$\begin{array}{r\|ll\|l} \rightarrow & \mathrm{X_1X_2} & \mathrm{X_2} & \\ \rightarrow & \mathrm{X_2} & \mathrm{X_2} & \\ & \mathrm{G} & \mathrm{X_2} & \leftarrow \end{array}$	R-IA incoherent	$-\mu^2_{\mathrm{G,X_2}}\mu^2_{\mathrm{X_2,X_1X_2}}$	B
$\begin{array}{r\|ll\|l} \rightarrow & \mathrm{X_1X_2} & \mathrm{X_2} & \\ & \mathrm{X_1} & \mathrm{X_2} & \leftarrow \\ \rightarrow & \mathrm{X_2} & \mathrm{G} & \leftarrow \end{array}$	NR-IA incoherent	$-\mu^2_{\mathrm{G,X_2}}\mu^2_{\mathrm{X_2,X_1X_2}}$	B

5.4.2 2D spectrum from AIMD trajectories.

The previous analysis ignored the impact of exciton-exciton interactions. Biexcitons in NCs give rise to an induced absorption feature on the 2D spectra. The red curve on Fig 5.5b shows the impact of the IA signal, which also gives rise to quantum beats. In semiconductor NCs, IA and SE contributions overlap and cancel over most of the cross-peak [48]. The net result shown in Fig 5.5b is a phase shift of the oscillation, dictated by the biexciton binding energy, transition dipole and degeneracy as well as the region of integration.

A higher level of theory including atomic details is required to explain the lack of coherent inter-excitonic dynamics in NCs. Despite its successes, the EMA has been criticized for its lack of microscopic details [90, 91]. Fig 5.5c shows the cross-peak dynamics computed from an atomistic model. Realistic microscopic models of small semiconductor NCs are within reach of modern ab-initio molecular dynamics (AIMD) [63, 64, 92, 93]. A 1.5 ps AIMD trajectory of a $Cd_{33}Se_{33}$ model nanocrystal was carried out to evaluate the impact of microscopic disorder on the dephasing time [92–95].

The linear and third order optical responses were computed from the trajectories using the cumulant expansion [58, 83]. The AIMD calculations yield the energies of all states as a function of time. In principle, the required correlation functions can be computed directly using eq 2.128. Normally, the dynamics are repeated with different initial conditions in order to average out slow modes. This is called the inhomogeneous cumulant expansion [58]. This requirement is prohibitive: the AIMD calculation with microscopic details is a very expensive calculation.

Direct application of the cumulant expansion using lineshape functions computed from a single AIMD trajectory causes the third order response to diverge due to coincidental correlations between slow modes. In order to improve the statistical properties of the cross-correlation functions, we compute the cross-correlation from the autocorrelation functions of the states' energies and their energy separations. This can be demonstrated as follows. As usual, let:

$$\omega_i(t) = \frac{E_i(t)}{\hbar} = \overline{\omega}_i + \delta\omega_i(t) \tag{5.17}$$

where $E_i(t)$ is the energy of state i. ω_i is decomposed in an average value $\overline{\omega}_i$ and a fluctuating part $\delta\omega_i(t)$. Under the multimode Brownian oscillator model, the fluctuations are caused by fluctuations of classical bath modes:

$$\delta\omega_i(t) = \sum_k \xi_{ik}\delta q_k(t) \tag{5.18}$$

where $\delta q_k(t)$ is the fluctuating part of mode k and ξ_{ik} is a time-independent real coupling constant.

Let:

$$\varepsilon_{ij}(t) = \omega_i(t) - \omega_j(t) = \overline{\varepsilon}_{ij} + \delta\varepsilon_{ij}(t) \tag{5.19}$$

be the frequency difference between states i and j. Its fluctuating part is given by:

$$\delta\varepsilon_{ij}(t) = \delta\omega_i(t) - \delta\omega_j(t) = \sum_k \left(\xi_{ik} - \xi_{jk}\right)\delta q_k(t). \tag{5.20}$$

As for the MBO, we assume uncorrelated bath modes:

$$k \neq k' \implies \langle \delta q_k(t)\delta q_k(0)\rangle_{\text{eq}} = 0, \tag{5.21}$$

where $\langle \ldots \rangle_{\text{eq}}$ designate a stationnary ensemble average. This assumption yields the following correaltion functions (in the absence of relaxation):

$$\langle \delta\omega_i(t)\delta\omega_i(0)\rangle_{\text{eq}} = \sum_k \xi_{ik}^2 \langle \delta q_k(t)\delta q_k(0)\rangle_{\text{eq}} \tag{5.22}$$

$$\langle \delta\omega_i(t)\delta\omega_j(0)\rangle_{\text{eq}} = \sum_k \xi_{ik}\xi_{jk} \langle \delta q_k(t)\delta q_k(0)\rangle_{\text{eq}} \tag{5.23}$$

$$\langle \delta\varepsilon_{ij}(t)\delta\varepsilon_{ij}(0)\rangle_{\text{eq}} = \sum_k \left(\xi_{ik}\xi_{jk}\right) \langle \delta q_k(t)\delta q_k(0)\rangle_{\text{eq}}. \tag{5.24}$$

By expanding the square in 5.24 and substituting eqs 5.22 and 5.23, we get:

$$\langle \delta\omega_i(t)\delta\omega_j(0)\rangle_{\text{eq}} = \frac{1}{2}\left(\langle \delta\omega_i(t)\delta\omega_i(0)\rangle_{\text{eq}} + \langle \delta\omega_j(t)\delta\omega_j(0)\rangle_{\text{eq}} - \langle \delta\varepsilon_{ij}(t)\delta\varepsilon_{ij}(0)\rangle_{\text{eq}}\right) \tag{5.25}$$

Thus, the cross-correlation of the fluctuation of the energy levels can be expressed in terms of autocorrelation functions, which are statistically well-behaved (or better behaved, at least). The resulting cross-correlation functions all obey the Cauchy-Schwarz inequality, and the third order response stays finite.

The calculation of the 2DE spectrum from the AIMD proceeds as follows. The average state energy and the transition dipole moments are obtained from the AIMD calculation. The correlation functions are computed from state trajectories using eq 5.25, and the corresponding lineshape functions are computed using eq 2.128. The total response is computed using equations 2.164 to 2.171. Inhomogeneous dephasing due to size distribution was added ($g_{ij}(t) = g_{ij}^{(\mathrm{AIMD})}(t) + g_{ij}^{(\mathrm{I})}(t)$). Inhomogeneous dephasing was considered perfectly correlated and identical across all states, which only serves to isolate the effect of the AIMD calculation.

The calculation uses only singly excited states: allowed transitions always involve the ground state. As such, all Hilbert path require $b = g$ in equations 2.164 to 2.171 (ie: $b \neq g$ yields $\mu_{cb} = \mu_{ba} = 0$). The other two states a and c can be any of the singly excited state, the sum runs over all possibilities. The calculation was truncated at 21 states, which is the amount necessary to converge the linear spectrum in the region of interest.

The correlation functions obtained from the AIMD calculations have a time dependent part, which yield non-Markovian dynamics. One might wonder if this has a determinant role in reducing the amplitude of observed coherences. In order to separate the contributions of the electronic structure from the fluctuation dynamics, a pure dephasing rate is extracted from the covariance matrix of the fluctuations of the states. This essentially dismisses the dynamic part of the correlation functions.

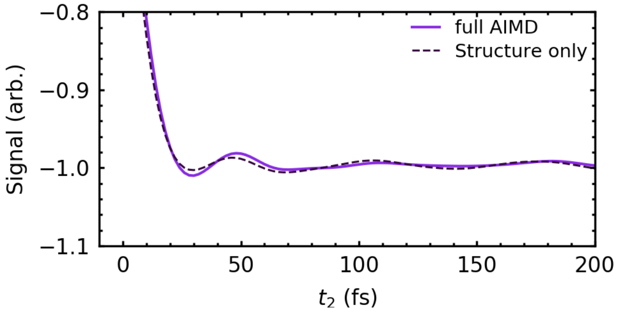

Figure 5.7: Separating kinetic vs structure effects in the AIMD calculation. Cross peak dynamics obtained using the full AIMD results (solid) and using electronic structure and pure dephasing (dashed). Both curves are convolved with the experimental IRF.

Fig 5.7 compares the results of this calculation, labeled "structure only", with the full AIMD results. Both curves have been convolved with the experimental IRF.

The model 2D spectrum obtained from the AIMD trajectories includes the disorder arising from an atomistic picture of the nanocrystal. The detailed position of atoms break the symmetry of the system: a realistic NC is not a sphere. The states predicted by the EMA mix, degeneracies lift and forbidden transitions become allowed. This results in dense manifolds of transitions [94]. The inset of Fig 5.5c shows the linear absorption spectrum obtained from this calculation. The first two spectroscopic features require taking into account 21 distinct states, an order of magnitude more than the standard EMA model suggests. This disorder very quickly damps the oscillations of the cross-peak. Note that this occurs without the introduction of defects such as extra atoms [95].

The modeling was carried out on a single NC without the introduction of defects such as extra atoms or surface defects. The rapid dephasing of the inter-excitonic coherence thus occurs even for single nanocrystals in the absence of ensemble disorder. The model NC was built from a perfect lattice; the deviations from the ideal shape are thermally accessible and thus inherent to the NC. AIMD studies of multiple chemical composition shows that such an intrinsic electronic disorder is a general property of quantum-confined NCs. Disorder induced by atomistic details is thus expected to be a dominant effect in reducing the lifetime of inter-excitonic coherences in nanostructures.

5.5 Conclusion

CdSe NCs have long been a model system in which to study the impact of many-body physics on electron dynamics. Here we have studied coherent oscillations in the time-resolved electronic response of CdSe NCs. Coherence mapping experiments with high time resolution and high sensitivity failed to observe any electronic coherences. In contrast, coherence maps containing the expected experimental signatures were observed for the optical phonon. A strong electronic coherence is predicted using the standard EMA model, which lacks atomistic details. The absence of electronic coherence was successfully modeled using time-domain ab initio calculations. In semiconductor nanostructures, atomistic details present in single nanostructures play a dominant role in determining the lifetime of electronic coherences. Application of coherence mapping on a model system of semiconductor nanocrystals suggests that electronic coherence may be used as a measure of electronic disorder. This technique should be generally applicable to discriminate between competing dephasing processes in complex materials.

References

1. Ernst, R. R. *et al. Principles of nuclear magnetic resonance in one and two dimensions* 349 (1987).
2. Sussman, B. J., Underwood, J. G., Lausten, R., Ivanov, M. Y. & Stolow, A. Quantum control via the dynamic Stark effect: Application to switched rotational wave packets and molecular axis alignment. *Physical Review A* **73,** 053403 (May 2006).
3. Rosker, M. J., Wise, F. W. & Tang, C. L. Femtosecond relaxation dynamics of large molecules. *Physical Review Letters* **57,** 321–324 (1986).
4. Ten Wolde, A., Noordam, L. D., Lagendijk, A. & van Linden van den Heuvell, H. B. Observation of Radially Localized Atomic Electron Wave Packets. *Physical Review Letters* **61,** 2099–2101 (Oct. 1988).
5. McRobbie, D. W., Moore, E. A., Graves, M. J. & Prince, M. R. *MRI from picture to proton* 1–397 (2006).
6. Marceau, C. *et al.* Molecular Frame Reconstruction Using Time-Domain Photoionization Interferometry. *Physical Review Letters* **119,** 083401 (Aug. 2017).
7. Mikosch, J. *et al.* Channel- and Angle-Resolved Above Threshold Ionization in the Molecular Frame. *Physical Review Letters* **110,** 023004 (Jan. 2013).
8. Yeazell, J. A., Mallalieu, M. & Stroud, C. R. Observation of the collapse and revival of a Rydberg electronic wave packet. *Physical Review Letters* **64,** 2007–2010 (Apr. 1990).
9. Hofer, U. *et al.* Time-Resolved Coherent Photoelectron Spectroscopy of Quantized Electronic States on Metal Surfaces. *Science* **277,** 1480–1482 (1997).

10. Cao, W., Warrick, E. R., Fidler, A., Leone, S. R. & Neumark, D. M. Near-resonant four-wave mixing of attosecond extreme-ultraviolet pulses with near-infrared pulses in neon: Detection of electronic coherences. *Physical Review A* **94,** 021802 (Aug. 2016).
11. Mauritsson, J. *et al.* Attosecond Electron Spectroscopy Using a Novel Interferometric Pump-Probe Technique. *Physical Review Letters* **105,** 053001 (July 2010).
12. Duan, H.-G. *et al.* Nature does not rely on long-lived electronic quantum coherence for photosynthetic energy transfer. *Proceedings of the National Academy of Sciences* **114,** 8493–8498 (2017).
13. Li, H., Bristow, A. D., Siemens, M. E., Moody, G. & Cundiff, S. T. Unraveling quantum pathways using optical 3D Fourier-transform spectroscopy. *Nature Communications* **4,** 1390 (2013).
14. Cundiff, S. T. & Mukamel, S. Optical multidimensional coherent spectroscopy. *Physics Today* **66,** 44 (2013).
15. Cassette, E., Pensack, R. D., Mahler, B. & Scholes, G. D. Room-temperature exciton coherence and dephasing in two-dimensional nanostructures. *Nature Communications* **6,** 6086 (Dec. 2015).
16. Nagy, A., Prokhorenko, V. & Miller, R. D. Do we live in a quantum world? Advances in multidimensional coherent spectroscopies refine our understanding of quantum coherences and structural dynamics of biological systems. *Current Opinion in Structural Biology* **16,** 654–663 (2006).
17. Dubin, F. *et al.* Macroscopic coherence of a single exciton state in an organic quantum wire. *Nature Physics* **2,** 32–35 (Jan. 2006).

18. Scholes, G. D. *et al.* Using coherence to enhance function in chemical and biophysical systems. *Nature* **543,** 647–656 (Mar. 2017).
19. Engel, G. S. *et al.* Evidence for wavelike energy transfer through quantum coherence in photosynthetic systems. *Nature* **446,** 782–786 (Apr. 2007).
20. Chin, A. W. *et al.* The role of non-equilibrium vibrational structures in electronic coherence and recoherence in pigment-protein complexes. *Nature Physics* **9,** 113–118 (2013).
21. Collini, E. *et al.* Coherently wired light-harvesting in photosynthetic marine algae at ambient temperature. *Nature* **463,** 644–647 (2010).
22. Wong, C. Y. *et al.* Electronic coherence lineshapes reveal hidden excitonic correlations in photosynthetic light harvesting. *Nature Chemistry* **4,** 396–404 (2012).
23. Ball, P. Still seeking coherence. *Nature Materials* **17,** 220 (Mar. 2018).
24. Maiuri, M., Ostroumov, E. E., Saer, R. G., Blankenship, R. E. & Scholes, G. D. Coherent wavepackets in the Fenna–Matthews–Olson complex are robust to excitonic-structure perturbations caused by mutagenesis. *Nature Chemistry* **10,** 177–183 (Jan. 2018).
25. Niedringhaus, A. *et al.* Primary processes in the bacterial reaction center probed by two-dimensional electronic spectroscopy. *Proceedings of the National Academy of Sciences* **115,** 3563–3568 (Apr. 2018).
26. Tollerud, J. O., Cundiff, S. T. & Davis, J. A. Revealing and Characterizing Dark Excitons through Coherent Multidimensional Spectroscopy. *Physical Review Letters* **117,** 097401 (Aug. 2016).
27. Stone, K. W., Turner, D. B., Gundogdu, K., Cundiff, S. T. & Nelson, K. A. Exciton - Exciton Correlations Revealed by Two-Quantum, Two-Dimensional Fourier Transform Optical Spectroscopy. *Accounts of chemical research* **42** (2009).

28. Kelley, A. M. Electron-phonon coupling in CdSe nanocrystals. *Journal of Physical Chemistry Letters* **1,** 1296–1300 (2010).
29. Norris, D. J. & Bawendi, M. G. Measurement and assignment of the size-dependent optical spectrum in CdSe quantum dots. *Physical Review B* **53,** 16338–16346 (June 1996).
30. Shumway, J., Franceschetti, A. & Zunger, A. Correlation versus mean-field contributions to excitons, multiexcitons, and charging energies in semiconductor quantum dots. *Physical Review B - Condensed Matter and Materials Physics* **63,** 1–13 (Mar. 2001).
31. Fu, H. X., Wang, L. W. & Zunger, A. Comparison of the k center dot p and the direct diagonalization approaches for describing the electronic structure of quantum dots. *Appl. Phys. Lett.* **71,** 3433–3435 (1997).
32. Hyeon-Deuk, K. & Prezhdo, O. V. Time-Domain ab Initio Study of Auger and Phonon-Assisted Auger Processes in a Semiconductor Quantum Dot. *Nano Letters* **11,** 1845–1850 (Apr. 2011).
33. Cassette, E., Dean, J. C. & Scholes, G. D. Two-Dimensional Visible Spectroscopy for Studying Colloidal Semiconductor Nanocrystals. *Small* **12,** 2234–2244 (Apr. 2016).
34. Caram, J. R. *et al.* Persistent Interexcitonic Quantum Coherence in CdSe Quantum Dots. *The Journal of Physical Chemistry Letters* **5,** 196–204 (Jan. 2014).
35. Turner, D. B., Hassan, Y. & Scholes, G. D. Exciton superposition states in CdSe nanocrystals measured using broadband two-dimensional electronic spectroscopy. *Nano letters* **12,** 880–6 (Feb. 2012).
36. Dong, S. *et al.* Observation of an Excitonic Quantum Coherence in CdSe Nanocrystals. *Nano Letters* **15,** 6875–6882 (Oct. 2015).

37. Tahara, H., Sakamoto, M., Teranishi, T. & Kanemitsu, Y. Harmonic Quantum Coherence of Multiple Excitons in PbS/CdS Core-Shell Nanocrystals. *Physical Review Letters* **119,** 1–6 (2017).
38. Tahara, H., Sakamoto, M., Teranishi, T. & Kanemitsu, Y. Quantum coherence of multiple excitons governs absorption cross-sections of PbS/CdS core/shell nanocrystals. *Nature Communications* **9,** 3179 (2018).
39. Paleček, D., Edlund, P., Westenhoff, S. & Zigmantas, D. Quantum coherence as a witness of vibronically hot energy transfer in bacterial reaction center. *Science Advances* **3,** e1603141 (Sept. 2017).
40. Bizimana, L. A., Carbery, W. P., Gellen, T. A. & Turner, D. B. Signatures of Herzberg-Teller coupling in three-dimensional electronic spectroscopy. *Journal of Chemical Physics* **146,** 084311 (Feb. 2017).
41. Takagahara, T. Electron-Phonon Interactions and Excitonic Dephasing in Semiconductor Nanocrystals. *Physical Review Letters* **71,** 3577–3580 (1993).
42. Krummheuer, B., Axt, V. M. & Kuhn, T. Theory of pure dephasing and the resulting absorption line shape in semiconductor quantum dots. *Physical Review B - Condensed Matter and Materials Physics* **65,** 195313 (2002).
43. Efros, A. L. & Rosen, M. The Electronic Structure of Semiconductor Nanocrystals. *Annual Review of Materials Science* **30,** 475–521 (Aug. 2000).
44. Kambhampati, P. Hot Exciton Relaxation Dynamics in Semiconductor Quantum Dots: Radiationless Transitions on the Nanoscale. *The Journal of Physical Chemistry C* **115,** 22089–22109 (Nov. 2011).
45. Caram, J. R. *et al.* Exploring size and state dynamics in CdSe quantum dots using two-dimensional electronic spectroscopy. *The Journal of Chemical Physics* **140,** 084701 (Feb. 2014).

46. Achermann, M., Hollingsworth, J. A. & Klimov, V. I. Multiexcitons confined within a subexcitonic volume: Spectroscopic and dynamical signatures of neutral and charged biexcitons in ultrasmall semiconductor nanocrystals. *Physical Review B - Condensed Matter and Materials Physics* **68,** 1–5 (2003).
47. Seiler, H., Palato, S., Sonnichsen, C., Baker, H. & Kambhampati, P. Seeing Multiexcitons through Sample Inhomogeneity: Band-Edge Biexciton Structure in CdSe Nanocrystals Revealed by Two-Dimensional Electronic Spectroscopy. *Nano Letters* **18,** 2999–3006 (May 2018).
48. Zhang, C., Do, T. N., Ong, X., Chan, Y. & Tan, H.-S. Understanding the features in the ultrafast transient absorption spectra of CdSe quantum dots. *Chemical Physics* **481,** 157–164 (Dec. 2016).
49. Mittleman, D. M. *et al.* Quantum size dependence of femtosecond electronic dephasing and vibrational dynamics in CdSe nanocrystals. *Physical Review B* **49,** 14435–14447 (May 1994).
50. Cerullo, G., De Silvestri, S. & Banin, U. Size-dependent dynamics of coherent acoustic phonons in nanocrystal quantum dots. *Physical Review B: Condensed Matter and Materials Physics* **60,** 1928–1932 (1999).
51. Sagar, D. M., Cooney, R. R., Sewall, S. L. & Kambhampati, P. State-resolved exciton-phonon couplings in CdSe semiconductor quantum dots. *Journal of Physical Chemistry C* **112,** 9124–9127 (June 2008).
52. Fuller, F. D. & Ogilvie, J. P. Experimental Implementations of Two-Dimensional Fourier Transform Electronic Spectroscopy. *Annual Review of Physical Chemistry* **66,** 667–690 (Apr. 2015).
53. Hamm, P. & Zanni, M. *Concepts and methods of 2D infrared spectroscopy* 1–286 (2011).

54. Hochstrasser, R. M. Two-dimensional spectroscopy at infrared and optical frequencies. *Proceedings of the National Academy of Sciences* **104,** 14190–14196 (Sept. 2007).
55. Seiler, H., Palato, S., Schmidt, B. E. & Kambhampati, P. Simple fiber-based solution for coherent multidimensional spectroscopy in the visible regime. *Optics Letters* **42,** 643 (Feb. 2017).
56. Zhang, Z., Wells, K. L., Hyland, E. W. J. & Tan, H.-S. Phase-cycling schemes for pump–probe beam geometry two-dimensional electronic spectroscopy. *Chemical Physics Letters* **550,** 156–161 (2012).
57. Monahan, D. M. *et al.* Room-Temperature Coherent Optical Phonon in 2D Electronic Spectra of CH3NH3PbI3Perovskite as a Possible Cooling Bottleneck. *Journal of Physical Chemistry Letters* **8,** 3211–3215 (2017).
58. Mukamel, S. *Principles of nonlinear optical spectroscopy* xviii, 543 p. (1995).
59. Gellen, T. A., Lem, J. & Turner, D. B. Probing Homogeneous Line Broadening in CdSe Nanocrystals Using Multidimensional Electronic Spectroscopy. *Nano Letters* **17,** 2809–2815 (May 2017).
60. Shim, S.-H. & Zanni, M. T. How to turn your pump–probe instrument into a multidimensional spectrometer: 2D IR and Vis spectroscopiesvia pulse shaping. *Phys. Chem. Chem. Phys.* **11,** 748–761 (Feb. 2009).
61. Myers, J. A., Lewis, K. L. M., Tekavec, P. F. & Ogilvie, J. P. Two-color two-dimensional Fourier transform electronic spectroscopy with a pulse-shaper. *Optics Express* **16,** 17420 (Oct. 2008).
62. Bolzonello, L., Volpato, A., Meneghin, E. & Collini, E. Versatile setup for high-quality rephasing, non-rephasing, and double quantum 2D electronic spectroscopy. *Journal of the Optical Society of America B* **34,** 1223 (2017).

63. Puzder, A., Williamson, A. J., Gygi, F. & Galli, G. Self-Healing of CdSe Nanocrystals: First-Principles Calculations. *Physical Review Letters* **92,** 217401 (May 2004).
64. Kilina, S., Ivanov, S. & Tretiak, S. Effect of Surface Ligands on Optical and Electronic Spectra of Semiconductor Nanoclusters. *Journal of the American Chemical Society* **131,** 7717–7726 (June 2009).
65. Giannozzi, P. *et al.* QUANTUM ESPRESSO: a modular and open-source software project for quantum simulations of materials. *Journal of Physics: Condensed Matter* **21,** 395502 (Sept. 2009).
66. Perdew, J. P., Burke, K. & Ernzerhof, M. Generalized Gradient Approximation Made Simple. *Physical Review Letters* **77,** 3865–3868 (Oct. 1996).
67. Van Stokkum, I. H. M., Larsen, D. S. & Van Grondelle, R. Global and target analysis of time-resolved spectra. *Biochimica et Biophysica Acta - Bioenergetics* **1657,** 82–104 (2004).
68. Milota, F. *et al.* Vibronic and vibrational coherences in two-dimensional electronic spectra of supramolecular J-aggregates. *Journal of Physical Chemistry A* **117,** 6007–6014 (July 2013).
69. Wells, K. L., Lambrev, P. H., Zhang, Z., Garab, G. & Tan, H.-S. Pathways of energy transfer in LHCII revealed by room-temperature 2D electronic spectroscopy. *Physical chemistry chemical physics : PCCP* **16,** 11640–6 (2014).
70. McHale, J. *Molecular Spectroscopy* (Prentice Hall, Upper Saddle River, 1999).
71. De Jong, M., Seijo, L., Meijerink, A. & Rabouw, F. T. Resolving the ambiguity in the relation between Stokes shift and Huang–Rhys parameter. *Phys. Chem. Chem. Phys.* **17,** 16959–16969 (2015).

72. Brito Cruz, C., Fork, R., Knox, W. & Shank, C. Spectral hole burning in large molecules probed with 10 fs optical pulses. *Chemical Physics Letters* **132,** 341–344 (Dec. 1986).

73. Fragnito, H., Bigot, J.-Y., Becker, P. & Shank, C. Evolution of the vibronic absorption spectrum in a molecule following impulsive excitation with a 6 fs optical pulse. *Chemical Physics Letters* **160,** 101–104 (Aug. 1989).

74. Pollard, W., Fragnito, H., Bigot, J.-Y., Shank, C. & Mathies, R. Quantum-mechanical theory for 6 fs dynamic absorption spectroscopy and its application to nile blue. *Chemical Physics Letters* **168,** 239–245 (May 1990).

75. Dong, S., Lian, J., Jhon, M. H., Chan, Y. & Loh, Z. H. Pump-Power Dependence of Coherent Acoustic Phonon Frequencies in Colloidal CdSe/CdS Core/Shell Nanoplatelets. *Nano Letters* **17,** 3312–3319 (May 2017).

76. Bakulin, A. A. *et al.* Real-time observation of multiexcitonic states in ultrafast singlet fission using coherent 2D electronic spectroscopy. *Nature Chemistry* **8,** 16–23 (Jan. 2016).

77. Butkus, V., Valkunas, L. & Abramavicius, D. Molecular vibrations-induced quantum beats in two-dimensional electronic spectroscopy. *Journal of Chemical Physics* **137,** 8231 (July 2012).

78. Seibt, J., Hansen, T. & Pullerits, T. 3D spectroscopy of vibrational coherences in quantum dots: Theory. *Journal of Physical Chemistry B* **117,** 11124–11133 (Sept. 2013).

79. Wang, L. *et al.* Controlling quantum-beating signals in 2D electronic spectra by packing synthetic heterodimers on single-walled carbon nanotubes. *Nature Chemistry* **9,** 219–225 (Mar. 2017).

80. Butkus, V., Zigmantas, D., Valkunas, L. & Abramavicius, D. Vibrational vs. electronic coherences in 2D spectrum of molecular systems. *Chemical Physics Letters* **545,** 40–43 (Aug. 2012).

81. Seibt, J. & Pullerits, T. Beating signals in 2D spectroscopy: Electronic or nuclear coherences? application to a quantum dot model system. *Journal of Physical Chemistry C* **117,** 18728–18737 (2013).

82. Mukamel, S. & Abramavicius, D. Many-body approaches for simulating coherent nonlinear spectroscopies of electronic and vibrational excitons. *Chemical Reviews* **104,** 2073–2098 (2004).

83. Cho, M. *Two-dimensional optical spectroscopy* 385 (CRC Press, 2009).

84. Palato, S. *Multimode Brownian Oscillator* 2018. `https://github.com/spalato/Mbo.jl`.

85. Sagar, D. M. *et al.* Size dependent, state-resolved studies of exciton-phonon couplings in strongly confined semiconductor quantum dots. *Physical Review B - Condensed Matter and Materials Physics* **77,** 235321 (June 2008).

86. Zhang, W. M., Meier, T., Chemyak, V. & Mukamel, S. Exciton-migration and three-pulse femtosecond optical spectroscopies of photosynthetic antenna complexes. *Journal of Chemical Physics* **108,** 7763–7774 (1998).

87. Cooney, R., Sewall, S., Anderson, K., Dias, E. & Kambhampati, P. Breaking the Phonon Bottleneck for Holes in Semiconductor Quantum Dots. *Physical Review Letters* **98,** 177403 (Apr. 2007).

88. Park, S. D. *et al.* Bandgap Inhomogeneity of a PbSe Quantum Dot Ensemble from Two-Dimensional Spectroscopy and Comparison to Size Inhomogeneity from Electron Microscopy. *Nano Letters* **17,** 762–771 (Feb. 2017).

89. Seiler, H., Palato, S. & Kambhampati, P. Investigating exciton structure and dynamics in colloidal CdSe quantum dots with two-dimensional electronic spectroscopy. *The Journal of Chemical Physics* **149,** 074702 (Aug. 2018).

90. Zunger, A. Pseudopotential theory of semiconductor quantum dots. *Physica Status Solidi (B) Basic Research* **224,** 727–734 (2001).

91. Zunger, A. On the Farsightedness (hyperopia) of the Standard k . p Model. *physica status solidi (a)* **190,** 467–475 (Apr. 2002).

92. Kilina, S. V., Kilin, D. S. & Prezhdo, O. V. Breaking the Phonon Bottleneck in PbSe and CdSe Quantum Dots: Time-Domain Density Functional Theory of Charge Carrier Relaxation. *ACS Nano* **3,** 93–99 (Jan. 2009).

93. Prezhdo, O. V. Photoinduced Dynamics in Semiconductor Quantum Dots: Insights from Time-Domain ab Initio Studies. *Accounts of Chemical Research* **42,** 2005–2016 (2009).

94. Prezhdo, O. V. Multiple excitons and the electron–phonon bottleneck in semiconductor quantum dots: An ab initio perspective. *Chemical Physics Letters* **460,** 1–9 (July 2008).

95. Pal, S., Nijjar, P., Frauenheim, T. & Prezhdo, O. V. Atomistic Analysis of Room Temperature Quantum Coherence in Two-Dimensional CdSe Nanostructures. *Nano Letters* **17,** 2389–2396 (Apr. 2017).

CHAPTER 6

Electron Dynamics at the Surface of Semiconductor Nanocrystals

In this chapter[1], we characterize the dynamics in the lineshape of the photoluminescence of CdSe NCs. The time-resolved PL (tPL) experiment differs from TA and 2D as it exclusively measures emissive states, ie: excited states. The timescale is also much slower, the lineshape dynamics are mostly due to population transfers. The tPL dynamics are a potential signature of electron transfer between core and surface electrons.

Semiconductor nanocrystals emit light from excitons confined to their core, as well as from their surfaces. Time-resolving the emission from the core yields information on the band edge exciton, which is now well understood. In contrast, the emission from the surface is ill-characterized and remains poorly understood, especially on long time scales. In order to understand the kinetics of charge trapping to the surface and electronic relaxation within the surface, time-resolved photoluminescence spectroscopy is performed on CdSe nanocrystals with strong surface emission.

---

[1] Adapted with permission from Palato, S. *et al.* Electron Dynamics at the Surface of Semiconductor Nanocrystals. *The Journal of Physical Chemistry C* **121,** 26519–26527 (Nov. 2017), Copyright 2017 American Chemical Society.

The time-resolved spectra reveal a time scale of electron transfer from core to surface much slower than previously thought. These spectra also unveil electron dynamics in the surface band, which gives rise to an average lifetime spectrum. These dynamics are explained by invoking two surface states. This simple model further rationalizes the role of ligands in tuning the surface emission of nanocrystals. These experimental results provide a critical test of our understanding of the electronic structure of the surface.

6.1 Introduction

The optical properties of colloidal semiconductor nanocrystals (NCs) are tunable through many material parameters such as size, chemical composition, crystal structure, and ligand chemistry. Coupled with cheap solution-based processing compatible with flexible substrates, NCs are a promising platform for device development. Current applications leverage the emissive properties of the NC, which arise from confined excitons in the core. These core excitons are well understood. Continuous wave (CW), time-resolved, and temperature-dependent experiments on core emission supplied important kinetic information on radiative and non-radiative processes. These experiments yielded a detailed understanding of the electronic structure of the band-edge exciton, revealing the origins of the Stokes shift and the existence of a dark exciton [2–4]. This understanding has enabled rational development of these materials for various optoelectronic applications [5].

In addition to the core, NCs also have a surface. In the case of bulk semiconductors, these surface electronic states are well investigated, typically using time-resolved photoluminescence, to yield their electronic structure and dynamics [6–9]. In the case of NCs, the surface is of increased importance by virtue of their sizes [2, 10]. Various aspects of nanocrystal surface science have recently been reviewed by ourselves and others [11–16]. Our group has focused on the steady-state spectroscopy of the surface [17–19]. The main spectroscopic observable is a broad photoluminescence (PL) band red-shifted from the core band. While PL from the surface of NCs is ubiquitous, especially at low temperatures, it remains poorly understood. This surface PL shows a rich dependence upon temperature, size, ligands, and other material parameters. These observations were rationalized using semiclassical electron transfer theory [17, 20, 21]. Based on steady-state experiment, this theory invokes assumptions for the electron dynamics that may be tested by time-resolving the PL. Specifically, the time-resolved PL spectrum can address the time scale for charge trapping from the core to the surface. In addition, spectral dynamics can reveal electronic processes at the NC surface. In summary, time-resolved PL can test the nature of the core to surface exchange, discriminating between the thermodynamic and kinetic regimes. Time-resolved PL spectroscopy is performed on CdSe NCs that exhibit dual emission at room temperature, enabling evaluation of the kinetics of both core and surface spectral bands. The results reveal the kinetics of electron transfer at the surface and dynamics within the surface band. The core and surface bands decay at different rates, implying an electron transfer time comparable to or longer than the fluorescence lifetime. The spectral dynamics within the surface band unveil dynamics of the electrons at the surface of semiconductor NCs. Both of these results provide critical tests of previous understanding of electronic structure and dynamics of surface electrons in these materials. These kinetic measurements provide an advance in our understanding of the surface of NCs, and the ways in which the surface may be exploited for light emissive applications.

6.2 Background

Spectroscopic investigations into the electronic properties of NCs have yielded a detailed picture of the core exciton energy levels and the associated relaxation processes. Figure 6.4a shows the salient features of this microscopic model. The confinement of the electrons and holes in the core of the NC gives rise to a manifold of exciton states (X_1,X_2, ...) which can be observed by CW absorption measurements. Temperature-dependent spectral measurements were instrumental in revealing the exciton fine structure and existence of the dark exciton [4]. This fine structure (a simplified version is shown as an inset in Figure 6.4a) explains both the large nonresonant Stokes shift observed in NC as well as the low-temperature exciton lifetime [2]. Time-resolved techniques, such as transient absorption (TA) and time correlated single photon counting (TCSPC), were necessary to disentangle the multiple electronic relaxation processes in these materials [3, 22–26]. This detailed understanding of the core electronics has been key to enable the design and synthesis of NCs for a wide range of applications.

In contrast, direct investigation of the spectroscopic properties of the surface state have only recently gained interest. A schematic level diagram for such a dual emitter is shown in Figure 6.4b. The most notable signature of surface electronics in NCs is a broad photoluminescence (PL) feature, red-shifted from the core PL. This spectral signature is prevalent in CdS and CdSe NCs with radius < 1.1 nm, although the PL appears at low temperature for most types of NCs as well as for other nanostructured materials [17, 27]. Single NC spectroscopic investigations have also shown the broad surface PL to be present in individual NCs and therefore not due to a heterogeneous ensemble of emitters, as was initially thought [28, 29]. This is also consistent with the spectroscopic properties of “atomically precise” CdSe clusters, which exhibit similar broad PL despite a very narrow size distribution [30]. Consistent with these observations, the surface PL is now thought to come from a "shallow surface state". This model was used by our group to reproduce the complicated variation of the relative amplitudes of the two emissive bands down to liquid helium temperature [31]. The occurrence of a shallow surface state is currently emerging as the dominant model for NCs across a range of chemical compositions [17, 32–35].

The dual emission from NCs cannot be observed if the transfer between the two emitting states is unidirectional and fast. This observation is known as Kasha's rule. The non-Kasha behavior of small NCs implies either slow electron transfer or thermodynamic equilibrium between the two emissive states. In previous work from our group, the electron transfer between the core and surface was assumed to be fast. This assumption was derived from TA experiments reporting surface trapping time constants of ∼2 ps in CdSe NCs [3, 36]. The hypothesis of fast surface trapping is also supported by fluorescence upconversion experiments, reporting PL rise times as low as <300 fs, with smaller NCs exhibiting faster rates [37, 38]. These observation, together with the assumption of equilibrium, results in a picture where the surface and core emitting states are in a thermodynamical equilibrium with a ps time constant, much faster than the ns timescale of the PL. In a kinetic scheme, the fast equilibrium would validate the steady-state approximation, where the ratio of core to surface ratio is constant. This model results in a prediction for the time-resolved fluorescence: the lineshape of the PL spectrum should not vary with time, or conversely, the spectrum should show uniform decay kinetics. This behavior is inconsistent with previous measurements which have shown different behaviors for the core and surface states. The surface state to be very long-lived, with observable populations still present >1 μs after excitation [39]. Systematic application of TCSPC

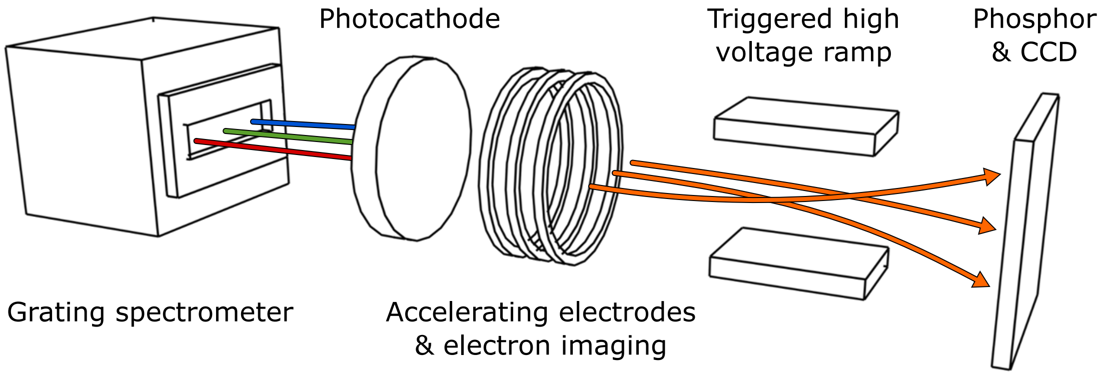

Figure 6.1: Operating principle of a Streak Camera. The light out of the spectrometer is sent to a photocathode which converts the photons to electrons. The horizontal position of the electron encodes the wavelength of the light. The electrons are accelerated and imaged to a detector. As they traverse the tube, the electrons are deviated vertically by a time-varying high voltage ramp. The vertical position of the electrons out of the streak tube thus encodes the arrival time of the light. The image at the detector thus measures both the PL wavelength and time.

has already suggested the existence of two surface states in the surface band of CdS NCs which could resolve this contradiction [33]. Furthermore, the electronic fine structure of the surface and the dynamic processes of surface electrons are poorly understood.

Investigations of the surface PL are further complicated by its large spectral overlap with the core PL. In order to address this difficulty, the time-resolved PL is obtained using a streak camera which provides simultaneous temporal and spectral resolution. The working principle of this instrument is shown on Fig 6.1. This experiment is performed on CdSe NCs with radius < 1.2 nm. The easily observed surface fluorescence makes these systems ideal subjects to investigate the dynamics of electrons at the surface of semiconductor NCs. A total of four sizes were studied, with estimated radii of 0.80, 0.89, 1.08, and 1.16 nm [40]. They were dispersed in toluene with tetradecylphosphonic acid (TDPA) as a capping ligand. Their synthesis has been described elsewhere [41]. Ligand exchange with 1-dodecanethiol (DDT) was carried out on the smallest and largest NCs due to the large spectral shifts it induces [19, 42]. The samples, flowed in toluene, are excited using a femtosecond UV pulse obtained by frequency doubling the output of a Ti:Sapphire CPA amplifier. The resulting fluorescence is collected and sent to a streak camera equipped with a grating spectrometer, operating on a 1 μs time range.

6.3 Experimental methods

6.3.1 Synthesis

The samples are prepared using standard published procedures [19, 40]. The available samples are described in table 6–1. The nanocrystal sizes are estimated from their band-edge absorption using standard sizing curves. The absorption spectra are shown on Fig 6.2.

6.3.2 Time-Resolved Fluorescence Spectroscopy.

The sample is dispersed in toluene and flowed in a 1 mm path length cell (Starna Type 48) using a peristaltic pump (Masterflex 77390-00). The time-resolved PL setup is presented on Fig 6.3. The sample is excited using 0.5 μJ pulses at 400 nm of duration < 100 fs obtained by frequency doubling the output of a Ti:Sapphire regenerative amplifier (Legend Elite Duo HE+, 1 kHz rep. rate) in a 100 μm BBO. The focusing conditions are shown on Fig 6.3c. The PL is collected at 90deg and image the streak camera entrance slit using a pair of off-axis parabolic mirrors. A hole in the collection mirror allows the use of the backscatter geometry, which is easier to align and yields higher signal levels, at the cost of increased scatter. The streak camera (Axis TRS, Axis Photonique Inc.) is equipped with a spectrometer (Acton SP2358i, 50 g/mm, 600 nm blaze), a bilamellar streak tube (Photonis P820), and an air cooled CCD (Spectral Instruments 1200 Series). The streak tube is electronically triggered, with an approximately 1 μs time range streak ramp. The triggering chain is shown on

Table 6–1: Description of the samples.

TDPA Band edge abs. (nm)	Est. radius (nm)	Ligands
405	0.80	TDPA, DDT
453	0.98	TDPA
480	1.08	TDPA
498	1.16	TDPA, DDT

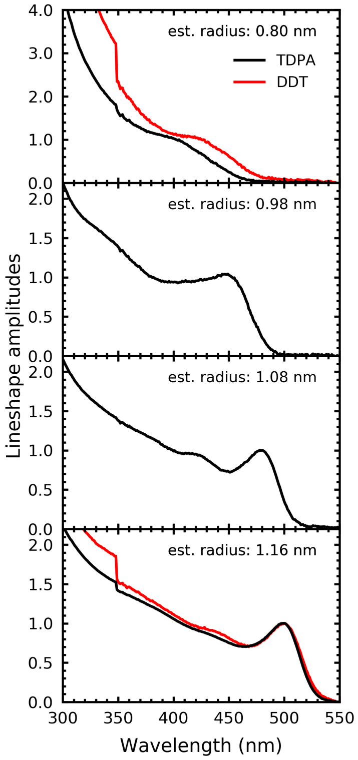

Figure 6.2: Linear spectra of the small NC samples.

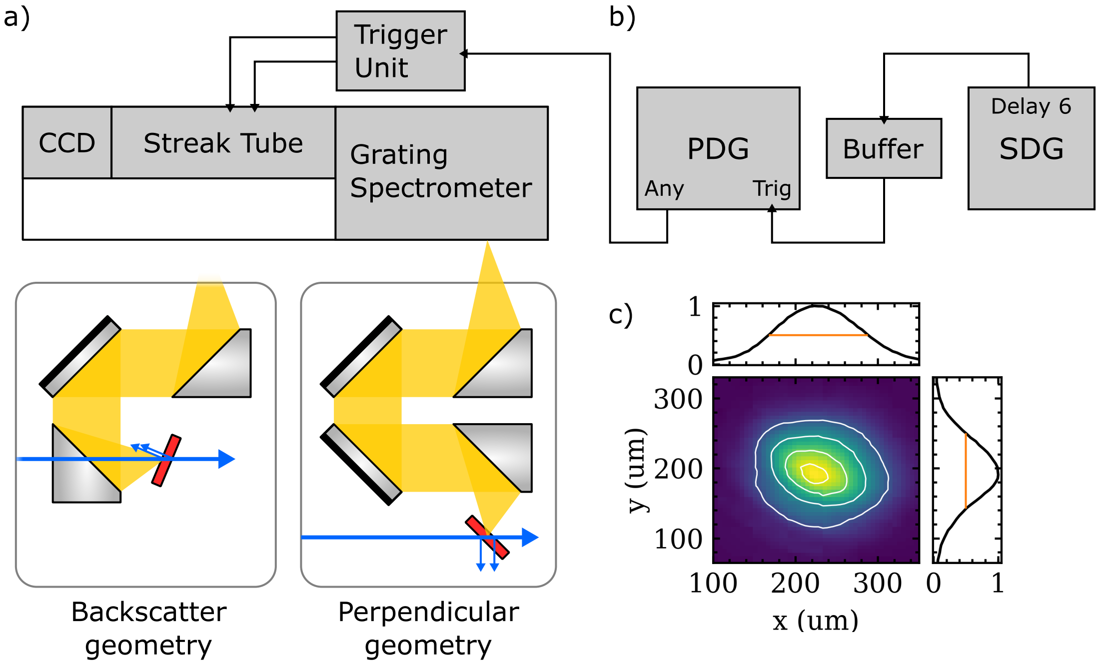

Figure 6.3: Time-resolved PL using a Streak camera. (a) Diagram of the Streak camera and collection optics. The collection mirror can be used at 90deg or in the backscatter geometry. (b) Electronic triggering chain. The trigger buffer serves to match the impendences. The PDG allows adjustement of the timing for the various modes. (c) Focusing conditions. Image of the focal spot with projections along x (top) and y (right). FWHM along x (y): 118 (105) µm.

Fig 6.3b. Only minor corrections are required for quantitative analysis. The trace has an average resolution of 2.31 ns and 4.05 nm for time and wavelength, respectively. Each trace is obtained from the average of 10 exposures of 10 s each. Including CCD readout time, each image was acquired in around 3 min. For each sample, a background trace is acquired in the same manner but with the pump blocked.

The streak was checked to be free from rotational and barrel distortions. A 1% shear correction was applied to the trace to correct for the alignment of the electrodes and detector. This value was obtained by analyzing the trace obtained using a static bias. The baseline using the part of the trace with $t < -10$ ns was subtracted. It consisted only of noise. The signal was corrected for the wavelength dependence of the detector and grating response using a stabilized Tungsten-Halogen lamp (Thorlabs SLS201L). The intensity was corrected for the uneven time bins. For plotting, the trace was converted from wavelength to energy along the spectral axis, including the jacobian correction [43].

6.4 Results

An example time-resolved PL spectrum is shown in Fig 6.4. The streak trace shows the two bands have different decay kinetics. Close inspection also suggests the surface band undergoes previously unreported spectral dynamics. The analysis proceeds in steps. First, a detailed inspection of the traces is performed by taking slices at a fixed time or fixed wavelength. This reveals a variation of the lifetime across the surface band. This is quantified using fluorescence lifetime spectra. Following this, the underlying spectral dynamics are quantified by extracting spectral parameters of both core and surface bands as a function of time.

The evolution of the shape and intensities of the two bands can be studied by taking slices of the time-resolved PL. Figure 6.5a,c,e displays spectra taken at

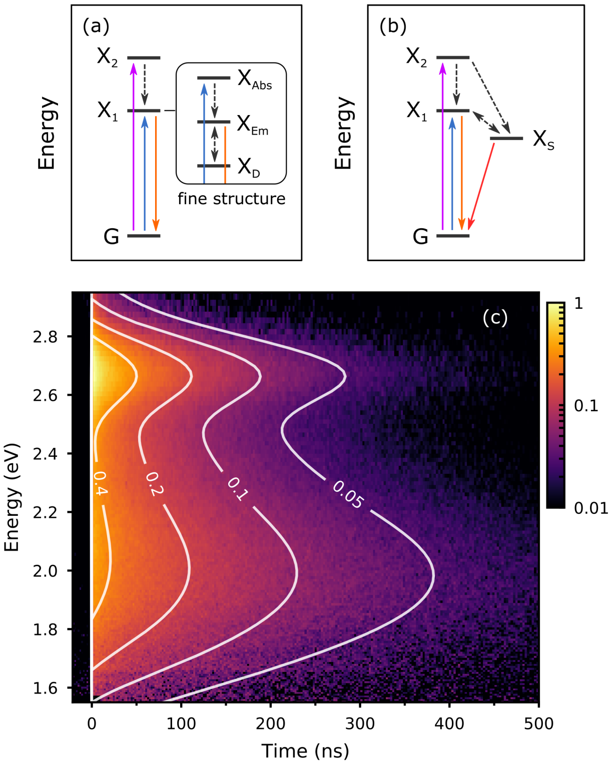

Figure 6.4: Kinetics of photoluminescence (PL) from the core and surface bands of semiconductor nanocrystals (NC). (a) Minimal energy level diagram for the core excitons. Confinement yields a spectrum of excitons. Further perturbations yield a fine structure (inset). (b) Minimal energy level diagram for the PL from NCs, with inclusion of a surface state. (c) Time-resolved PL from ultrasmall CdSe NC, showing different dynamics for the core and surface bands. Colormap on log scale, with contours evenly spaced on log scale as a guide to the eye. The CdSe NC has a band edge exciton absorption peak at 405 nm, corresponding to an estimated radius of 0.80 nm.

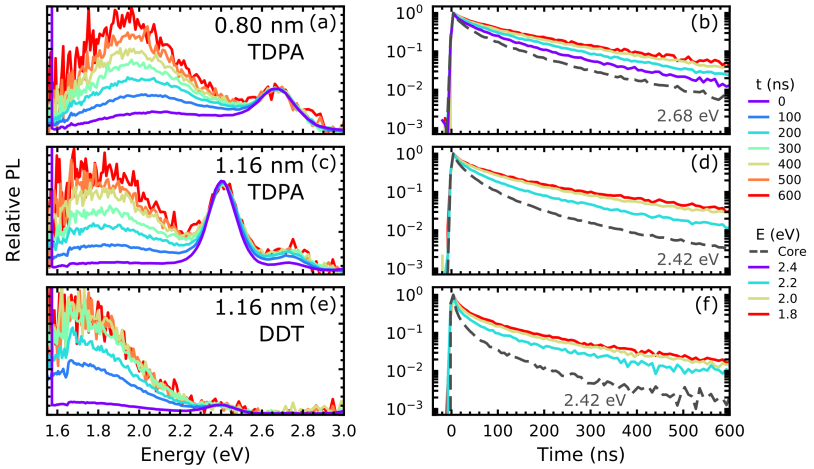

Figure 6.5: PL spectral dynamics within the surface band are sensitive to particle size and ligand. (a, c, e) Transient PL spectra, normalized to the core, in 100 ns increments. (b, d, f) Normalized kinetic transients for the core and across the surface band. The right column notes the NC radii and ligands. cell

100 ns intervals, normalized to the core PL intensity. Two main observations can be made about the evolving PL spectra. First, the surface band grows to dominate the PL lineshape at long times. This implies the core and surface bands undergo different decay kinetics. Second, the surface band shifts and narrows over hundreds of nanoseconds. This effect is present for all TPDA capped samples, but absent in the case of samples capped with DDT. In contrast, the core state shows no spectral dynamics. Note that both effects seem to stabilize after ~400 ns. Both observations contradict the assumptions of fast thermodynamical equilibrium made in previous work from our group. As previously detailed, thermodynamic equilibrium between the core and surface states with a time scale of 100 ps would result in identical decay kinetics for both states on the ns timescale. Furthermore, the spectral dynamics of the surface band are incompatible with the assumption of a single surface state with a fixed PL energy.

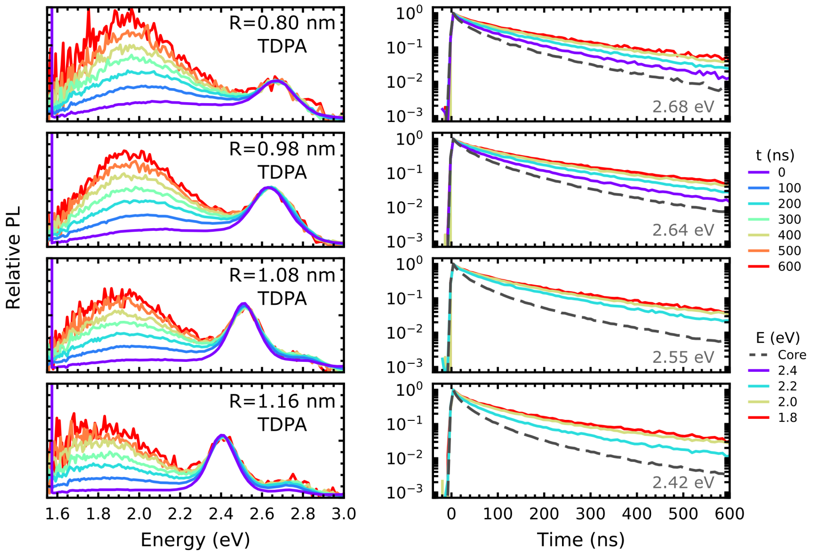

Figure 6.6: Impact of nanocrystal size on tPL. (left) Spectra as a function of time, in 100 ns increments, normalized to core PL intensity. (right) Kinetic transients, normalized to initial value.

A complementary analysis can be made by taking slices at fixed PL energy. Figure 6.5b,d,f displays normalized kinetic transients taken for the core peak and across the surface peak. As expected, the blue edge of the spectrum shows a faster decay than the red edge, corresponding to the shorter lifetime of the core. Due to the large spectral overlap of the core and surface emission bands, a kinetic slice at the core emission peak shows contributions from both core and surface states. Furthermore, the kinetic transients in the surface band are not identical. This observation implies the average lifetime varies across the surface band. The average lifetime increases toward the red edge of the surface band.

The effect of size on the time-resolved PL can be observed by comparing the top two rows of Figure 6.5, for R = 0.80 nm and R = 1.16 nm. The complete comparison of all sizes is shown on Fig 6.6. Changing the size impacts the relative amplitude of the core and surface bands, with smaller NCs showing proportionally larger surface

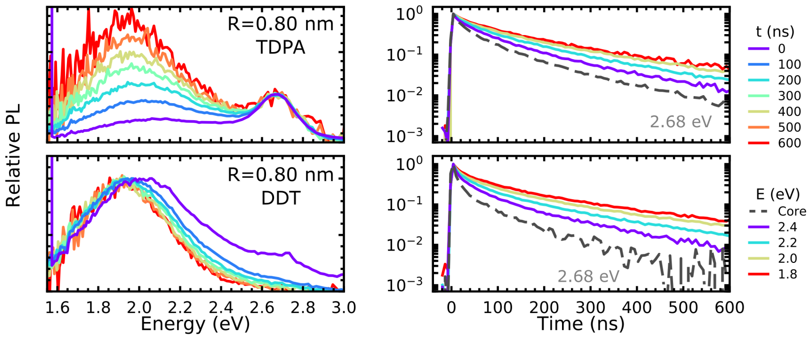

Figure 6.7: Impact of ligand on tPL for smallest NC. (left) Spectra as a function of time, in 100 ns increments, normalized to core PL intensity. (right) Kinetic transients, normalized to initial value.

emission. However, size seems to have little impact on the spectral dynamics. The kinetic transients yield a similar picture, although the transition between the faster decay on the blue edge and the slower decay on the red edge is smoother for smaller NCs.

The bottom two rows of Figure 6.5 and Fig 6.7 show the results for TDPA and DDT ligands at a fixed size, which allows an overview of the impact of ligands. DDT quenches the PL from the core by acting as a hole trap [19, 44]. Inspection of the time-dependent spectra suggests peak dynamics are less pronounced when thiol ligands (DDT) are used instead of phosphonic acid. The relative amplitude of the core and surface peaks still varies on a similar time scale, although the surface accounts for a larger fraction of the total PL.

This quenching effect can be accounted for by normalizing the kinetic transients to their initial value. Changing the ligands from TDPA to DDT increases the importance of early time decay but otherwise does not change the overall qualitative picture. This trend suggests the spectral dynamics are still present in DDT samples and of similar nature. The observed differences in apparent behavior between ligands

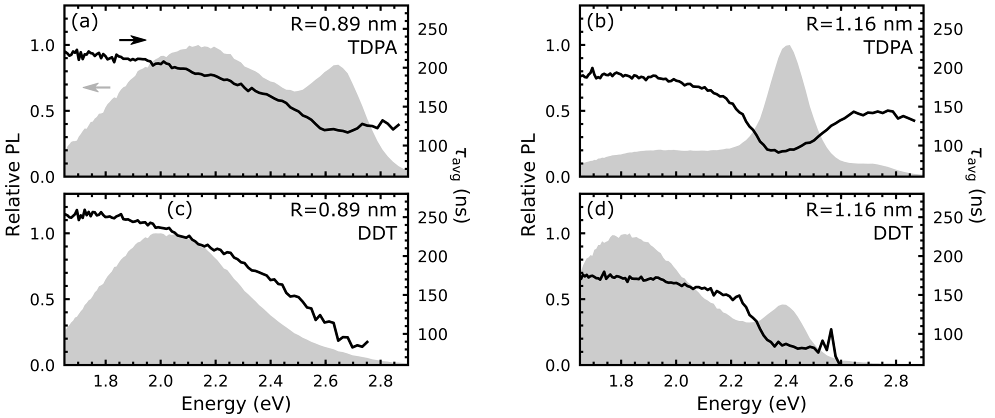

Figure 6.8: Time-resolved PL reveals a lifetime spectrum spanning the core and surface bands. Average fluorescence lifetime spectra for two sizes and two ligands. Shown are the time-integrated PL spectra (gray, left axes) and average lifetime spectra (black, right axes) for two sizes and two ligands. See text for details on obtaining the average lifetime spectra.

are thus an amplitude effect: the reduction in both the overall and core PL intensity makes the spectral dynamics harder to observe and quantify.

One of the readily observable features of the kinetics of the surface PL is the dependence of lifetime on emission energy, which gives rise to an average lifetime spectrum. Figure 6.8 shows the average lifetime spectra for four samples. A comparison for all NC sizes is shown on Fig 6.9. These lifetime spectra (black) show features which correlate with the time-integrated PL intensity (shown in gray). The fluorescence lifetime spectra are influenced by changes in both amplitude and lifetime. They present two distinct regimes: a long-lifetime plateau on the red side, corresponding to the surface state, and a short lifetime dip associated with PL from the core exciton. The transition between these two regimes is generally smooth, a crossover regime extending for most of the spectral range in TDPA capped samples (see Fig 6.9). This crossover regime can cause changes of a few orders of magnitude in the average lifetime of the surface. The use of a streak camera enables quick and direct observation

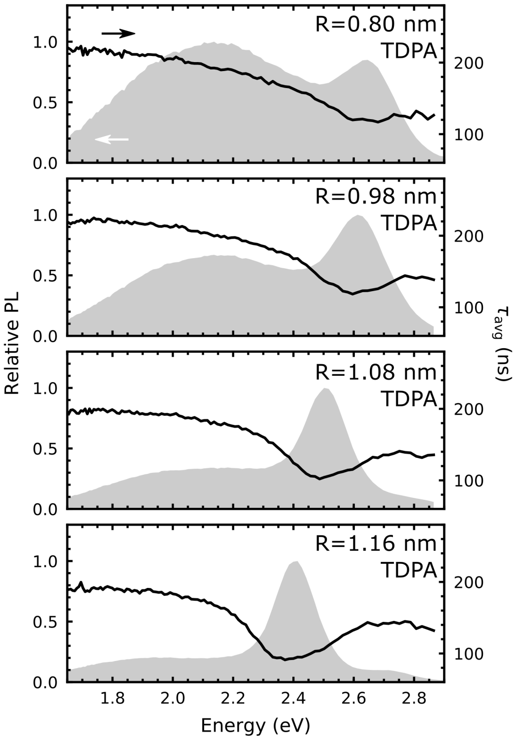

Figure 6.9: Impact of size on average lifetime spectra. Total PL intensity, (light gray, left axis) and average lifetime (black line, right axis). Samples are ordered from smallest (top) to largest (bottom).

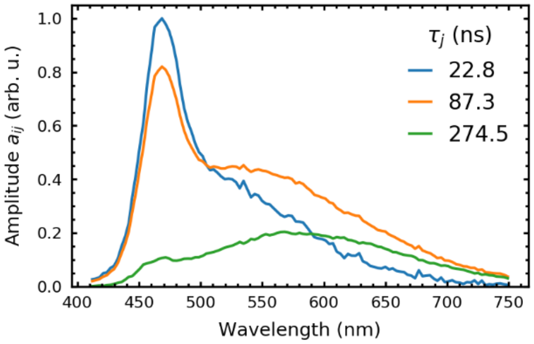

Figure 6.10: Example DAS analysis for R=0.80nm, TDPA ligands. Index i indicates spectrum pixel (wavelength), j indicates lifetime component.

of these changes despite the large bandwidth and low quantum yield of the samples. Note that these lifetime spectra contain contributions from both the core and surface states which arise due to spectral overlap.

The average lifetime spectrum was obtained from the results of a DAS global analysis tail fit ($t > 10$ ns) [45]. Three exponential components were required for all samples. For every wavelength slice, the average lifetime was computed from the DAS spectra following standard procedure for multi-exponential decays. For a given wavelength pixel i with components j:

$$\langle \tau \rangle_i = \frac{\sum_j a_{ij} \tau_j^2}{\sum_j a_{ij} \tau_j} \tag{6.1}$$

An example of the DAS components for the sample with R=0.80nm, TDPA ligands is reported on figure 6.10. All samples had only two important singular values, and required 3 exponential decays. We note that in principle, the DAS analysis can reveal the spectra of individual emitting species. Sadly, DAS analysis makes the assumption that individual components exhibit single exponential decays. This assumption is violated by semiconductor NCs due to a number of processes ranging from blinking to competitive decay pathways.

The relative contributions of the two PL features can be separated by fitting the two PL bands with a pair of peaks. Performing this analysis as a function of time allows a quantification of the spectral changes of the surface. The dual peak analysis was performed by fitting a dual Gaussian lineshape independently to each time-slice of the trace following rebinning by a factor of 15 along wavelength and 30 along time. The model lineshape function is a pair of gaussians. This model for the lineshape is converted to a model for the wavelength-dependent PL intensity according to [43]:

$$I(\lambda) \propto E^2 I(E) \propto E^5 f(E) \tag{6.2}$$

Where $I(\lambda)$ is the observed wavelength-dependent fluorescence intensity, $I(E)$ is the energy-dependent fluorescence intensity, $E = hc/\lambda$ is the emission energy and $f(E)$ is the model lineshape, a pair of Gaussian peaks. The fit is performed directly in wavelength. The wavelength-dependent standard deviation of a background trace was used as a noise estimate.

Figure 6.11a shows an example fit result. This analysis yields a line shape position, amplitude, and width for each peak, as a function of time. Typical resulting parameters for the surface state are shown in Figure 6.11b–d for selected samples. The complete set is shown on fig 6.12

The peak position shows little dynamics. As shown in Figure 6.11b, the surface PL red shifts by up to 50 meV over the course of the first 200 ns. The core stays at a fixed position (see Figure S8a). The dynamics are more pronounced for the FWHM, illustrated in Figure 6.11c. TDPA samples show a large reduction in FWHM (>400 meV), with most of the change happening in the first ~200 ns, whereas DDT samples exhibit almost no FWHM reduction. The change is concurrent with the red shift in the peak position. Interestingly, the surface peaks converge to a similar FWHM,

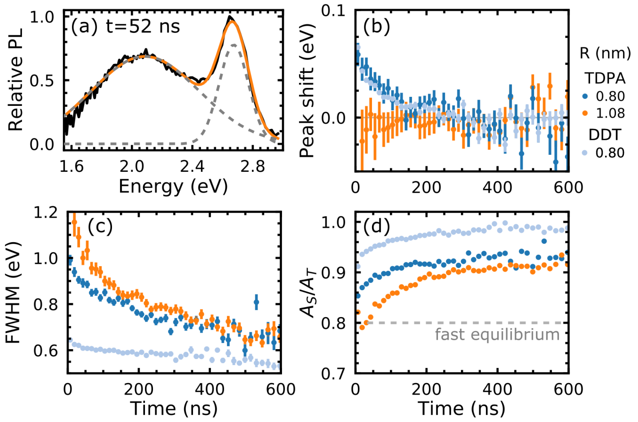

Figure 6.11: Surface band undergoes spectral dynamics. (a) The two bands can be isolated, as shown here for R = 0.89 nm, TDPA ligands at 52 ns. (b) Evolution of the surface band position for different radii and ligands. (c) Evolution of the PL linewidth. (d) Evolution of contribution of the surface to the total PL lineshape. Results for all samples, including core, shown in Figure S8.

irrespective of size and ligand type, suggesting a similar surface band is present at long times. The relative lack of spectral dynamics for DDT samples suggests their PL spectrum exhibits mostly this final state. Overall, the surface PL dynamics are dominated by an FWHM reduction, controlled by ligands, with size playing a minor role in the initial peak position and FWHM.

Previous understanding of the surface electronic dynamic involved a fast electron transfer between the core and surface of the NC, which should result in a fixed relative amplitude of the two bands. Figure 6.11d shows the evolution of the ratio of the area of the surface band to the total line shape area. According to the previous assumptions of fast electron transfer rate, this ratio should be a fixed value. This is not the observed behavior. TDPA samples reach an asymptote > 0.9 on a time scale > 120 ns. The asymptotic behavior is consistent with a slow equilibrium between surface and core state. Most importantly, the numeric value of the asymptotic ratio is different from what steady-state measurements suggest: the NC radius influences only

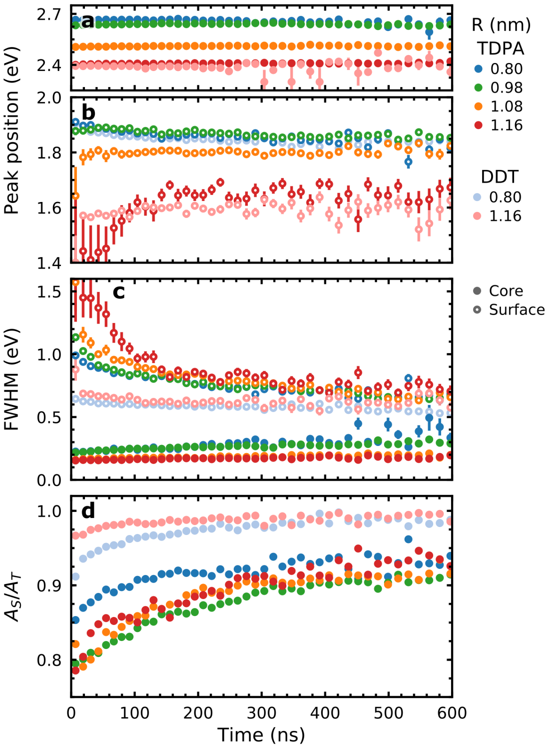

Figure 6.12: Complete result set for dual peak deconstruction analysis for both core (filled) and surface (open). Evolution of the peak position for the (a) core and (b) surface; (c) FWHM and (d) relative lineshape area, for all samples. The largest dot studied here (dark red) stands out and seems to show a different trend, although the Gaussian peaks model used here cannot easily reproduce the extreme breadth and flatness of this sample's surface PL at early times.

the initial values. As a consequence, steady-state measurements are inappropriate in addressing the thermodynamics of the surface of NCs, as they convolve kinetics and thermodynamic effects

6.5 Discussion

The previous analysis revealed and quantified spectral dynamics within the surface band of dual-emitting NCs. These dynamics occur on a time scale of $>$100 ns. In this section, an explanation for this effect is proposed in terms of two surface states with a large spectral overlap. This model aims at revealing the cause of these spectral dynamics and focuses on spectral aspects of the salient observables. Quantitative modeling of the PL kinetics, taking into account all possible phenomena, is beyond the scope of this work. Using model calculations, we outline the role of kinetic effects on the fluorescence lifetime spectrum. These calculations are applicable to any dual emitter. Implications of the proposed model are then discussed in the broader context of NC nanoscience.

The interesting PL dynamics unraveled by the dual peaks analysis occur on a time scale comparable to the fluorescence lifetime of the emission bands. This observation motivates us to explore the existence of multiple spectrally overlapping states with different lifetimes as the origin for these spectral dynamics. Figure 6.13a,b illustrates the spectral and kinetic behavior of three bands used to reproduce a time-resolved PL spectrum. Each time-resolved PL spectrum is fitted with a single model composed of multiple emission bands with fixed spectra and independent decay kinetics. Each band i emits a fixed PL spectrum $S_i(\lambda)$, a Gaussian line shape, whose amplitude decays according to a kinetic model $K_i(t)$, a triple exponential decay [46]. The triple exponential kinetic model is common in the analysis of time-resolved PL of NCs and should be thought of simply as flexible enough to fit the transient well [46]. In order to eliminate contributions due to hot excitons cooling or multi-exciton effects, PL from $t < 10$ ns was eliminated from the analysis. These effects are known to occur on time scales < 100 ps at room temperature [22, 47]. The complete time-resolved PL is, for n such states:

$$I(t, \lambda) = \sum_{i=1}^{n} S_i(\lambda) K_i(t) \tag{6.3}$$

We note that the lack of a well-defined kinetic model for NC PL decay precludes the use of standard global analysis schemes such as species associated spectra [45, 48, 49].

The model functions are, respectively, a Jacobian-corrected Gaussian lineshape and a triple exponential decay, given by:

$$S_i\left(\frac{hc}{E}\right) = E^5 g(E, E_{i0}, \sigma_i) \tag{6.4}$$

$$K_i(t) = \sum_{j=1}^{3} a_{ij} \exp\left(-\frac{t}{\tau_{ij}}\right) \tag{6.5}$$

where $g(E, E_0, \sigma)$ is a Gaussian function. The Gaussian lineshape model has been selected for simplicity as the bands' lineshape is dominated by inhomogeneous broadening. The triple exponential kinetic model is common in the analysis of NC time-resolved PL [46], and should be thought of simply as flexible enough to fit the transient well. With 3 states, each streak trace is fit using 24 parameters. This total is much smaller than for the dual peak model used to quantify spectral dynamics, which used a total of 6x95=570 parameters for a complete trace.

We find all time-resolved PL spectra can be fit well using three bands: the core (X_C) and two surface bands (X_{S1}, X_{S2}). Compared to spectral deconstruction of CW PL, this procedure for time-resolved PL separates the states using their kinetic behavior. This simple three state picture explains not only the spectral dynamics but

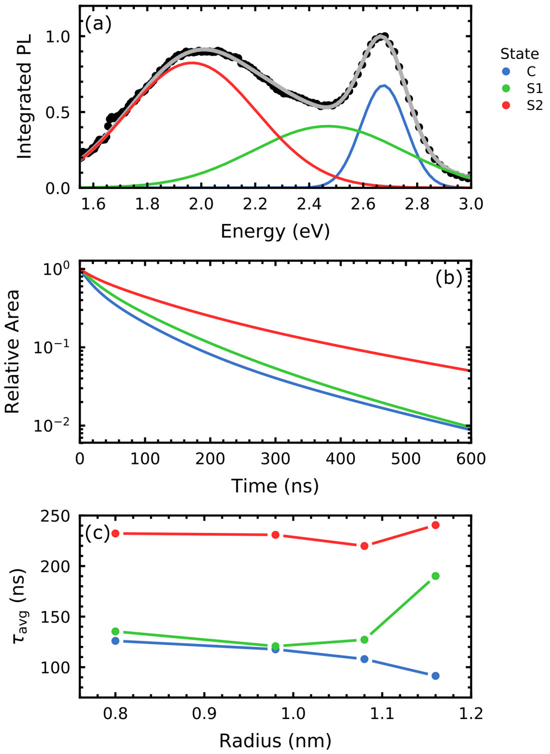

Figure 6.13: Spectral dynamics requires three emission bands: Core exciton X_C (blue) and two surface bands X_{S1} (green), X_{S2} (red). (a) Shown is the time-integrated spectrum for the experimental data (black dot), the three components (colored lines), and their sum (gray line). (b) Kinetic components of each of the three spectral bands (see text for details). (c) Average lifetimes for the three bands as a function of NC size.

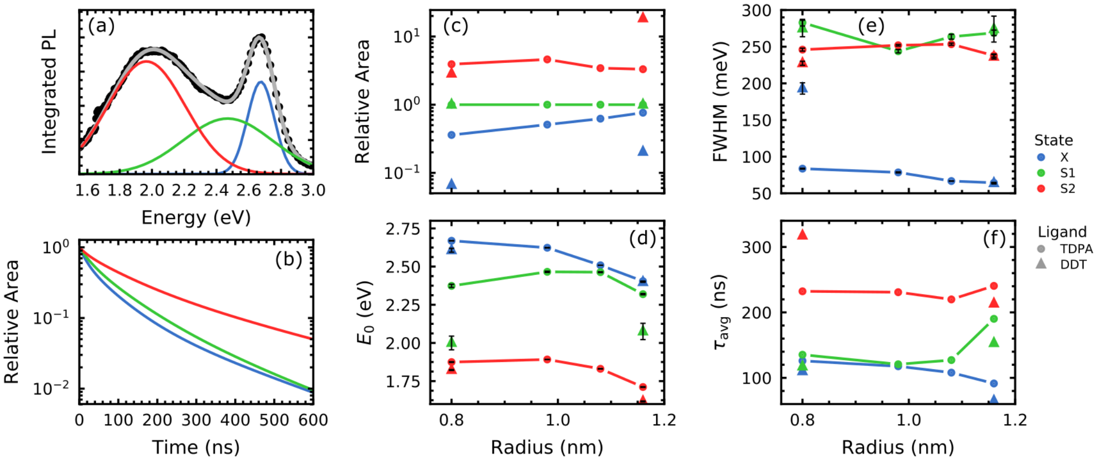

Figure 6.14: Complete parameter set for the triple-peak analysis. (a) Time-integrated spectrum for the experimental data (black dot), the three components (colored lines), their sum (gray line). (b) Kinetic components of each of the three spectral bands. Size and ligand dependence of spectral properties: (c) relative lineshape areas, (d) peak positions, (e) peak width and (f) average lifetimes. Errors on fit parameters reported at the 3σ level, obtained from the diagonal of the covariance matrix.

also the differences in behavior between ligands. Moreover, this picture is similar to models recently suggested by others [33, 39].

This analysis allows disentangling of two surface states, which show different decay kinetics. Figure 6.13c shows the average lifetimes for all sizes. The most interesting trend is in the average lifetime of the core and $\mathrm{X_{S1}}$ states. Whereas they are indistinguishable for the smallest NCs size, they separate as size increases: the $\mathrm{X_C}$ state becomes progressively shorter lived, while the rmX_{S1} state becomes longer lived. This suggests a change in the transfer kinetic between these states, as will be emphasized later. The $\mathrm{X_{S2}}$ state shows a lifetime of around 230 ns for most samples.

The complete result, shown on Fig 6.14, shows robust trends for the spectral components. Results for the core PL are consistent with previous results for these samples. The central position of the $\mathrm{X_{S1}}$ state is close to the core peak, whereas $\mathrm{X_{S2}}$

is much redder, suggesting a position deeper in the band gap. The two surface bands have similar widths, consistent with similar sources of broadening.

Figure 6.14c shows the time-integrated lineshape areas, relative to the surface state XS1. The ratio of the two surface states is roughly constant over the size range studied. The core monotonously increases, consistent with an increased coupling to the surface as NC size is reduced. The peak positions redshift with increasing size, as seen on Figure 6.14d. This is consistent with surface state where one charge carrier is still confined in the bulk while the second charge carrier is pinned at the surface.

The triple peak target fit was performed directly on the streak trace using a wavelength-dependent noise estimate as previously described. The fit parameters were loosely constrained. The surface peaks were allowed to overlap, and the green surface state was allowed to overlap or go beyond the core peak.

The kinetic exchange between the core exciton $\mathrm{X_C}$ and first surface state $\mathrm{X_{S1}}$ is now explored. Figure 6.15a shows a minimal model for a dual emitting nanocrystal with kinetic coupling between the two states. Let's consider a system of 4 states: Ground G, core exciton X, and surfaces S1 and S2. The core and surface states are excited states and decay spontaneously to the ground state. The intrinsic decay rate of the population p_i from state i to the ground state is:

$$k_{\mathrm{d},i} = k_{\mathrm{r},i} + k_{\mathrm{nr},i} = 1/\tau_{\mathrm{d},i} \tag{6.6}$$

with quantum yield:

$$\eta_i = \frac{k_{\mathrm{r},i}}{k_{\mathrm{d},i}} \tag{6.7}$$

The two excited states are potentially in equilibrium, with a forward (X to S1) transfer rate k_f and backwards transfer rate k_b. If both are non-zero, the equilibrium constant is given by:

$$K_{\mathrm{X,S1}} = p_{S1}/p_X = k_f/k_b \tag{6.8}$$

The total change in the populations is the sum of all such contributions. The resulting differential equations are cast in matrix form:

$$\dot{\boldsymbol{P}} = \boldsymbol{T} \cdot \boldsymbol{P} \tag{6.9}$$

with T_{ij} containing transfer from state j to i. The diagonal terms contain all the terms withdrawing population from a given state. For the sake of simplicity, the ground state is not included in these calculations. The decay to the ground state $k_{\mathrm{d},i}$ is included in the diagonal elements T_ii. If we assume S2 to be kinetically uncoupled, the matrices are:

$$\boldsymbol{P} = \begin{bmatrix} p_X \\ p_{S1} \\ p_{S2} \end{bmatrix} \tag{6.10}$$

$$\boldsymbol{T} = \begin{bmatrix} -k_{\mathrm{d},C} - k_f & k_b & 0 \\ k_f & -k_{\mathrm{d},S1} - k_b & 0 \\ 0 & 0 & -k_{\mathrm{d,S2}} \end{bmatrix} \tag{6.11}$$

Given a set of parameters and initial conditions, the equation can be integrated to yield a trajectory $\boldsymbol{P}(t)$. We note that given the bloc diagonal structure of $\boldsymbol{T}$, S2 can be excluded from the equations and integrated separately. The integration is carried out for duration Δt with the populations recorded every step δt.

The PL intensities are proportional to the populations, rates and quantum yields. The quantum yields merely act as a scaling factor for the intensities, they drop out of all equations used here:

$$I_i(t) = \eta_i k_{\mathrm{d},i} p_i(t). \tag{6.12}$$

Table 6–2: Calculation parameters for kinetic model. The forward electron transfer rate is varied as described in the text. The population of state S2 irrelevant to the calculation due to the bloc diagonal structure of the transfer matrix $\boldsymbol{T}$.

Parameter	Value
k_{X}	$1/50\ \mathrm{ns}^{-1}$
k_{S1}	$1/250\ \mathrm{ns}^{-1}$
k_{S2}	$1/250\ \mathrm{ns}^{-1}$
$K_{\mathrm{X,S1}}$	2
k_f	$1/\tau_{\mathrm{ET}}$
$p_{\mathrm{X}}(0)$	0.8
$p_{\mathrm{S1}}(0)$	0.2
Δt	4 µs
δt	1 ns

The average lifetimes are computed as:

$$\langle\tau\rangle_i = \frac{\int_0^\infty \mathrm{d}t\ tI_i(t)}{\int_0^\infty \mathrm{d}tI_i(t)} = \frac{\int_0^\infty \mathrm{d}t\ tp_i(t)}{\int_0^\infty \mathrm{d}tp_i(t)} \tag{6.13}$$

For multiexponential decays, this yields the well known expression:

$$\langle\tau\rangle = \frac{\sum_j a_j\tau_j^2}{\sum_j a_j\tau_j} \tag{6.14}$$

The results are obtained using the values in table 6–2.

Figure 6.15b shows the resulting average lifetime of the two states as the electron transfer rate is varied between the limits of fast thermodynamic equilibrium ($\tau_{\mathrm{ET}} < 1$ ns) and uncoupled kinetics ($\tau_{\mathrm{ET}} > 10^3$ ns). For fast equilibrium, the kinetics of both states are tightly coupled, and the populations undergo a common evolution. For slow equilibrium, the states evolve toward their intrinsic, uncoupled kinetics. For fast equilibrium, the presence of a slowly decaying surface state enhances the effective lifetime of the surface state: the surface acts as a reservoir for the core state. The required time scale for electron transfer is rather slow: an equilibrium time $\tau = 10$ ns is sufficient to entirely couple the kinetics, and effects of the coupling can be felt beyond $\tau = 10^3$ ns. These calculations are consistent with the observed behavior of the average lifetimes of the X_C and X_{S1} bands shown in Figure 6.13c. Thus, our results are consistent ET rate governed by size: the smallest NCs studied here show kinetics consistent with $\tau_{ET} < 10$ ns, increasing to $\tau_{ET} \approx 100$ ns in the larger NCs. Most importantly, these calculations suggest the electron transfer between core and surface occurs on the time scale of nanoseconds, much slower than previously assumed.

This transition between fast thermodynamic equilibrium and decoupled kinetics gives rise to a fluorescence lifetime spectrum. Figure 6.15c shows the lifetime spectra for a model dual emitter with well separated peaks. For fast equilibrium, the lifetime is a fixed value across the spectrum. An average lifetime spectrum develops as the ET time increases. In this case, the spectrum has two regions, one for each band. The crossover region is narrow: it cannot exceed the width of the narrowest peak. Thus, the existence of a lifetime spectrum is indicative of an electron transfer that is on the order of, or slower than, the excited state decay.

The previous model calculation rationalizes the existence of a fluorescence lifetime spectrum for any dual emitter using simple kinetics but does not explain the spectral dynamics of the surface band. This behavior can be reproduced using two surface states, one of which is in exchange with the core state. Figure 6.16a shows a simple level diagram corresponding to such a model. This model can reproduce all the salient features of the observed lifetime spectra by varying the electron transfer time τ_{ET}. As previously, all states have a fixed intrinsic decay rate. For simplicity, this rate is taken to be the same for both surface states. The core state X_C and the first surface state X_{S1} are in equilibrium with a time scale given by the forward electron transfer time τ_{ET}. The second surface state X_{S2} is taken to be a deep trap, kinetically

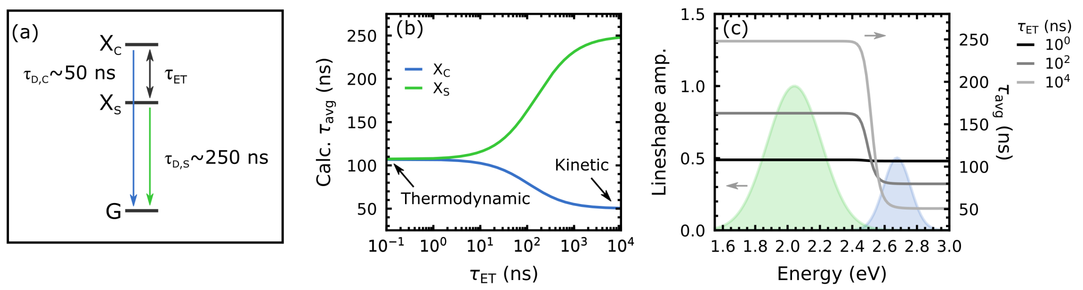

Figure 6.15: Unraveling the time scale for charge transfer in a dual emissive system. A dual emissive system may span the limits from thermodynamic (fast electron transfer) or to decoupled kinetics (slow charge transfer) limit. (a) Minimal level structure for a dual emitter with fixed intrinsic decay rates but varying electron transfer rate. (b) Calculated average lifetime of the two states as a function of the electron transfer time. The thermodynamic limit is approached on the 10 ns time scale in this system. (c) Development of a PL lifetime spectrum based upon time scale of electron transfer. The presence of a lifetime spectrum indicates an electron transfer that is not in the (fast) thermodynamic limit.

decoupled from the other states. Figure 6.16b shows lifetime spectra obtained for various electron transfer times τ_{ET} using fixed spectral parameters borrowed from the previous triple states fit (shown in Figure 6.13a). By varying a single parameter, this model qualitatively reproduces the complicated features of the experimental lifetime spectra for all sizes of NCs.

Furthermore, the current dual surface states model rationalizes the influence of ligands in shaping the surface PL spectrum. Thiols are currently investigated as hole traps [19, 44]. They reduce the overall quantum yield by quenching emission from $\mathrm{X_C}$ and $\mathrm{X_{S1}}$. The observed red shift of the surface PL is thus due to quenching of a state instead of the shifting of an energy level. The opposite effect has been demonstrated for amine ligands, which blue shift the surface peak and increase the quantum yield [18]. This observation is consistent with an elimination of PL from $\mathrm{X_{S2}}$ while retaining PL from $\mathrm{X_C}$ and $\mathrm{X_{S1}}$.

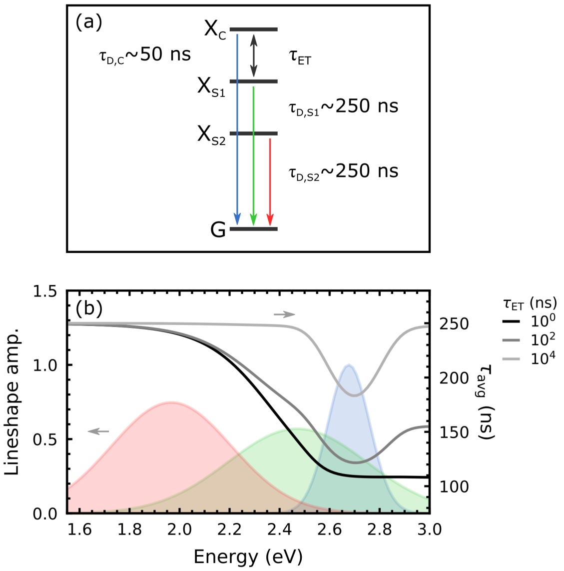

Figure 6.16: Two surface states are required to reproduce the spectral dynamics. (a) Minimal level structure for an NC with two surface states. The surface state X_{S1} is coupled to the core exciton, whereas the red state X_{S2} is kinetically decoupled from the other excited states. (b) Two surface states yield lifetime spectra consistent with experiments.

Here, we have considered competitive kinetics of multiple emissive states as the source of the spectral dynamics of the surface band in CdSe NCs. Other hypotheses can be considered. Thermal effects must be considered as an alternative explanation, as the exciting laser deposits 3eV of energy in the absorbing NCs [50]. Low temperature time-resolved PL measurements on NCs similar to those carried out here have shown the phonon thermalization to happen well within 100 ps, and to be governed by heat diffusion to the solvent [51, 52]. This time scale is comparable to the usual picture for out-of-equilibrium phonon distributions in semiconductors [53]. This leaves the increased temperature of the illuminated volume and ensuing heat diffusion as a potential source of spectral dynamics on the nanosecond time scale. The magnitude of this effect would be dependent on the temperature gradient, thus on the total energy of the pump pulse. In the context of this work, no change could be observed with pump energies ranging from 0.25 μJ/pulse to 2 μJ/pulse, thus disproving this hypothesis.

Alternatively, an inhomogeneous distribution of decay kinetics can yield spectral dynamics. The spectral dynamics of the surface band reported here could be explained by invoking a correlation between the lifetime and emission energy in this ensemble distribution. This hypothesis cannot be ruled out using the current ensemble measurements. Size inhomogeneity effects seem unlikely however. Changing the NC radius from 1.2 nm size down to 0.8 nm results mostly in an enhancement of the surface PL; the position of the band stays mostly fixed [54]. An argument based on sample inhomogeneity would thus need to be specific to the NC surface.

Models based on ensemble distributions are easy to invoke on a qualitative level. However, they turn out to be hard to investigate quantitatively due to difficulty in specifying the underlying distribution. Recent analysis of the temperature dependence of the PL kinetics of dual-emitting CdS NCs in terms of trap distributions was carried out by the Jones group [33]. Their analysis requires a bimodal distribution of trap states, consisting of shallow and deep traps. This is compatible with our current model.

A direct evaluation of the distribution of emissive states could be done by accessing the spectroscopic properties of single nanocrystals [25, 26, 55, 56]. This would allow the assessment of the properties of the underlying distributions of PL energies and lifetimes. Single NC experiments would also address heterogeneity of the PL kinetics. NCs are known to exhibit blinking, and there is no reason to expect the surface state to be exempt of such effects. Single NC spectroscopy studies in this size regime have found a population of emitters emit from the core only [28]. Furthermore, the degree of correlation between the core and surface blinking is unknown.

To our knowledge, no extensive study of the statistics of surface PL of small NCs has been reported in the literature.

The current work suggests the electron transfer rate between the core and surface can be much slower than normally accepted. Spectral dynamics of the surface PL on the nanosecond time scale suggest an electron transfer rate on the order of tens of nanoseconds, whereas femtosecond transient absorption studies have assigned a < 30 ps decay component to surface trapping [22, 47]. The current work clearly establishes that this fast transfer rate is not compatible with a shallow trap. This fast trapping rate could be related to transfer to the deep surface state suggested here (X_{S2}), or can be an indication of trapping to dark states that cannot be observed in this experiment. Again, we hope single NC spectroscopy studies would directly address this issue [25, 56].

The predominant role played by ligands in determining the electronic properties of the surface state of NCs is already well established. The current work suggests ligands do not merely tweak these properties: they can select which states are accessible. A shallow surface state in thermodynamic exchange with the core can be a new tool in the hands of designers. Potential applications of the surface PL for lighting and sensing have already been demonstrated [12, 18, 57–59]. Shallow surface states in equilibrium with the core could be leveraged in the design of light-harvesting or emitting devices as they provide a pathway for charge carriers to be injected into or extracted from the core, with an ET timescale of 10–10^3 ns. In NC superlattices, they could provide a migration path through the device. Due to their long intrinsic lifetime, shallow surface states can act as reservoirs for charge carriers, enhancing the lifetime of the core PL [60].

6.6 Conclusion

We have time-resolved PL from semiconductor nanocrystals that support intrinsic dual emission from core and surface. The measurements reveal the time scale for electron transfer to the surface as well as dynamics within the surface band. The spectral dynamics gives rise to rich fluorescence lifetime spectra. The evolution of the relative amplitudes of the PL bands was shown to be incompatible with preceding theories of nanoscale surfaces. Time-resolved PL provides an estimate for the surface electron transfer time of 10–10^3 ns, dependent on size. Furthermore, the surface band exhibits large spectral dynamics on the time scale of hundreds of nanoseconds, which is indicative of surface electron dynamics. These spectral dynamics have been explained using a model involving two surface bands with different decay kinetics. Time-resolved PL reveals a spectrum of states is responsible for surface emission, and that their dynamics are in the kinetic rather than thermodynamic regime.

References

1. Palato, S. *et al.* Electron Dynamics at the Surface of Semiconductor Nanocrystals. *The Journal of Physical Chemistry C* **121,** 26519–26527 (Nov. 2017).
2. Burda, C., Chen, X., Narayanan, R. & El-Sayed, M. A. Chemistry and properties of nanocrystals of different shapes. *Chemical Reviews* **105,** 1025–1102 (2005).
3. Kambhampati, P. Hot Exciton Relaxation Dynamics in Semiconductor Quantum Dots: Radiationless Transitions on the Nanoscale. *The Journal of Physical Chemistry C* **115,** 22089–22109 (Nov. 2011).
4. Nirmal, M. *et al.* Observation of the "dark exciton" in CdSe quantum dots. *Physical Review Letters* **75,** 3728–3731 (Nov. 1995).
5. Kagan, C. R., Lifshitz, E., Sargent, E. H. & Talapin, D. V. Building devices from colloidal quantum dots. *Science* **353,** aac5523–aac5523 (Aug. 2016).
6. Schmidt, O. *et al.* Time-resolved two photon photoemission electron microscopy. *Applied Physics B: Lasers and Optics* **74,** 223–227 (Mar. 2002).
7. Smith, N. V. Inverse photoemission. *Reports on Progress in Physics* **51,** 1227–1294 (Sept. 1988).
8. Hansson, G. V. & Uhrberg, R. I. Photoelectron spectroscopy of surface states on semiconductor surfaces. *Surface Science Reports* **9,** 197–292 (Aug. 1988).
9. Tisdale, W. A. *et al.* Hot-Electron Transfer from Semiconductor Nanocrystals. *Science* **328.** `http://science.sciencemag.org/content/328/5985/1543` (2010).
10. Kovalenko, M. V. *et al.* Prospects of Nanoscience with Nanocrystals. *ACS Nano* **9,** 1012–1057 (Feb. 2015).

11. Kambhampati, P. On the kinetics and thermodynamics of excitons at the surface of semiconductor nanocrystals: Are there surface excitons? *Chemical Physics* **446,** 92–107 (2015).
12. Kambhampati, P., Mack, T. & Jethi, L. Understanding and Exploiting the Interface of Semiconductor Nanocrystals for Light Emissive Applications. *ACS Photonics* **4,** 412–423 (Mar. 2017).
13. Boles, M. A., Ling, D., Hyeon, T. & Talapin, D. V. The surface science of nanocrystals. *Nat Mater* **15,** 141–153 (Feb. 2016).
14. Owen, J. The coordination chemistry of nanocrystal surfaces. *Science* **347.** `http://science.sciencemag.org/content/347/6222/615` (2015).
15. Houtepen, A. J., Hens, Z., Owen, J. S. & Infante, I. On the Origin of Surface Traps in Colloidal II–VI Semiconductor Nanocrystals. *Chemistry of Materials* **29,** 752–761 (Jan. 2017).
16. Hines, D. A. & Kamat, P. V. Recent Advances in Quantum Dot Surface Chemistry. *ACS Applied Materials & Interfaces* **6,** 3041–3057 (Mar. 2014).
17. Mooney, J., Krause, M. M., Saari, J. I. & Kambhampati, P. Challenge to the deep-trap model of the surface in semiconductor nanocrystals. *Physical Review B* **87,** 081201 (Feb. 2013).
18. Krause, M. M., Mooney, J. & Kambhampati, P. Chemical and Thermodynamic Control of the Surface of Semiconductor Nanocrystals for Designer White Light Emitters. *ACS Nano* **7,** 5922–5929 (July 2013).
19. Jethi, L., Mack, T. G., Krause, M. M., Drake, S. & Kambhampati, P. The Effect of Exciton-Delocalizing Thiols on Intrinsic Dual Emitting Semiconductor Nanocrystals. *ChemPhysChem* **17,** 665–669 (2016).

20. Barbara, P. F., Meyer, T. J. & Ratner, M. a. Contemporary Issues in Electron Transfer Research. *The Journal of Physical Chemistry* **100,** 13148–13168 (1996).

21. Jortner, J. Temperature dependent activation energy for electron transfer between biological molecules. *The Journal of Chemical Physics* **64,** 4860–4867 (June 1976).

22. Knowles, K. E., McArthur, E. A. & Weiss, E. A. A Multi-Timescale Map of Radiative and Nonradiative Decay Pathways for Excitons in CdSe Quantum Dots. *ACS Nano* **5,** 2026–2035 (Mar. 2011).

23. Jones, M. & Scholes, G. D. On the use of time-resolved photoluminescence as a probe of nanocrystal photoexcitation dynamics. *Journal of Materials Chemistry* **20,** 3533 (2010).

24. Caram, J. R. *et al.* Persistent Interexcitonic Quantum Coherence in CdSe Quantum Dots. *The Journal of Physical Chemistry Letters* **5,** 196–204 (Jan. 2014).

25. Schlegel, G., Bohnenberger, J., Potapova, I. & Mews, A. Fluorescence decay time of single semiconductor nanocrystals. *Physical review letters* **88,** 137401 (Mar. 2002).

26. Nirmal, M. *et al.* Fluorescence intermittency in single cadmium selenide nanocrystals. *Nature* **383,** 802–804 (Oct. 1996).

27. Dohner, E. R., Jaffe, A., Bradshaw, L. R. & Karunadasa, H. I. Intrinsic White-Light Emission from Layered Hybrid Perovskites. *Journal of the American Chemical Society* **136,** 13154–13157 (Sept. 2014).

28. Dukes, A. D. I. *et al.* Single-Nanocrystal Spectroscopy of White-Light-Emitting CdSe Nanocrystals. *Journal of Physical Chemistry A* **115,** 4076 (2011).

29. Layek, A., De, S., Thorat, R. & Chowdhury, A. Spectrally Resolved Photoluminescence Imaging of ZnO Nanocrystals at Single-Particle Levels. *The Journal of Physical Chemistry Letters* **2,** 1241–1247 (June 2011).

30. Beecher, A. N. *et al.* Atomic structures and gram scale synthesis of three tetrahedral quantum dots. *Journal of the American Chemical Society* **136,** 10645–10653 (July 2014).

31. Lifshitz, E. *et al.* Optical properties of CdSe nanoparticle films prepared by chemical deposition and sol?gel methods. *Chemical Physics Letters* **288,** 188–196 (May 1998).

32. Mooney, J., Krause, M. M., Saari, J. I. & Kambhampati, P. A microscopic picture of surface charge trapping in semiconductor nanocrystals. *Journal of Chemical Physics* **138,** 204705 (2013).

33. Woodall, D. L., Tobias, A. K. & Jones, M. Resolving carrier recombination in CdS quantum dots: A time-resolved fluorescence study. *Chemical Physics* **471,** 2–10 (2016).

34. Caram, J. R. *et al.* PbS Nanocrystal Emission Is Governed by Multiple Emissive States. *Nano Letters* **16,** 6070–6077 (2016).

35. Smith, M. D., Jaffe, A., Dohner, E. R., Lindenberg, A. M. & Karunadasa, H. I. Structural origins of broadband emission from layered Pb–Br hybrid perovskites. *Chem. Sci.* **8,** 4497–4504 (May 2017).

36. Tyagi, P. & Kambhampati, P. False multiple exciton recombination and multiple exciton generation signals in semiconductor quantum dots arise from surface charge trapping. *The Journal of Chemical Physics* **134,** 094706 (Mar. 2011).

37. Bowers II, M. J. *et al.* Structure and Ultrafast Dynamics of White-Light-Emitting CdSe Nanocrystals. *Journal of the American Chemical Society* **131,** 5730–5731 (Apr. 2009).

38. Underwood, D. F., Kippeny, T. & Rosenthal, S. J. Ultrafast Carrier Dynamics in CdSe Nanocrystals Determined by Femtosecond Fluorescence Upconversion Spectroscopy. *The Journal of Physical Chemistry B* **105,** 436–443 (Jan. 2001).

39. Abdellah, M. *et al.* Ultra Long-Lived Radiative Trap States in CdSe Quantum Dots. *The Journal of Physical Chemistry C* **118,** 21682–21686 (Sept. 2014).

40. Yu, W. W., Qu, L., Guo, W. & Peng, X. Experimental determination of the extinction coefficient of CdTe, CdSe, and CdS nanocrystals. *Chemistry of Materials* **15,** 2854–2860 (2003).

41. Peng, Z. A. & Peng, X. Formation of High-Quality CdTe, CdSe, and CdS Nanocrystals Using CdO as Precursor. *Journal of the American Chemical Society* **123,** 183–184 (Jan. 2001).

42. Baker, D. R. & Kamat, P. V. Tuning the emission of CdSe quantum dots by controlled trap enhancement. *Langmuir* **26,** 11272–11276 (July 2010).

43. Mooney, J. & Kambhampati, P. Get the Basics Right: Jacobian Conversion of Wavelength and Energy Scales for Quantitative Analysis of Emission Spectra. *The Journal of Physical Chemistry Letters* **4,** 3316–3318 (Oct. 2013).

44. Wuister, S. F., De Mello Donegá, C. & Meijerink, A. Influence of thiol capping on the exciton luminescence and decay kinetics of CdTe and CdSe quantum dots. *Journal of Physical Chemistry B* **108,** 17393–17397 (2004).

45. Van Stokkum, I. H. M., Larsen, D. S. & Van Grondelle, R. Global and target analysis of time-resolved spectra. *Biochimica et Biophysica Acta - Bioenergetics* **1657,** 82–104 (2004).

46. Resch-Genger, U., Grabolle, M., Cavaliere-Jaricot, S., Nitschke, R. & Nann, T. Quantum dots versus organic dyes as fluorescent labels. *Nature Methods* **5,** 763–775 (Sept. 2008).
47. Sewall, S. L. *et al.* State-resolved studies of biexcitons and surface trapping dynamics in semiconductor quantum dots. *Journal of Chemical Physics* **129,** 1–8 (2008).
48. Al Salman, A., Tortschanoff, A., van der Zwan, G., van Mourik, F. & Chergui, M. A model for the multi-exponential excited-state decay of CdSe nanocrystals. *Chemical Physics* **357,** 96–101 (Feb. 2009).
49. Loefroth, J. E. Time-resolved emission spectra, decay-associated spectra, and species-associated spectra. *The Journal of Physical Chemistry* **90,** 1160–1168 (Mar. 1986).
50. Pennycook, T. J., McBride, J. R., Rosenthal, S. J., Pennycook, S. J. & Pantelides, S. T. Dynamic Fluctuations in Ultrasmall Nanocrystals Induce White Light Emission. *Nano letters* **16,** 3038 (2012).
51. Hannah, D. C. *et al.* Observation of Size-Dependent Thermalization in CdSe Nanocrystals Using Time-Resolved Photoluminescence Spectroscopy. *Physical Review Letters* **107,** 177403 (2011).
52. Rainò, G. *et al.* Exciton Dynamics within the Band-Edge Manifold States: The Onset of an Acoustic Phonon Bottleneck. *Nano Letters* **12,** 5224–5229 (Oct. 2012).
53. Othonos, A. Probing ultrafast carrier and phonon dynamics in semiconductors. *Journal of Applied Physics* **83,** 1789–1830 (1998).

54. Jethi, L., Mack, T. G. & Kambhampati, P. Extending Semiconductor Nanocrystals From the Quantum Dot Regime to the Molecular Regime. *The Journal of Physical Chemistry C,* acs.jpcc.7b08439 (Oct. 2017).

55. Cui, J. *et al.* Evolution of the Single-Nanocrystal Photoluminescence Linewidth with Size and Shell: Implications for Exciton-Phonon Coupling and the Optimization of Spectral Linewidths. *Nano Letters* **16,** 289–296 (Jan. 2016).

56. Jones, M., Lo, S. S. & Scholes, G. D. Quantitative modeling of the role of surface traps in CdSe/CdS/ZnS nanocrystal photoluminescence decay dynamics. *Proceedings of the National Academy of Sciences* **106,** 3011–3016 (2009).

57. Jethi, L., Krause, M. M. & Kambhampati, P. Toward Ratiometric Nanothermometry via Intrinsic Dual Emission from Semiconductor Nanocrystals. *The Journal of Physical Chemistry Letters* **6,** 718–721 (Feb. 2015).

58. Bowers, M. J., McBride, J. R. & Rosenthal, S. J. White-Light Emission from Magic-Sized Cadmium Selenide Nanocrystals. *Journal of the American Chemical Society* **127,** 15378–15379 (Nov. 2005).

59. Schreuder, M. A. *et al.* Encapsulated white-light CdSe nanocrystals as nanophosphors for solid-state lighting. *Journal of Materials Chemistry* **18,** 970 (2008).

60. Vlaskin, V. A., Janssen, N., Van Rijssel, J., Beaulac, R. & Gamelin, D. R. Tunable dual emission in doped semiconductor nanocrystals. *Nano Letters* **10,** 3670–3674 (Sept. 2010).

CHAPTER 7

Conclusion and future directions

In this thesis, we have shown how lineshape analysis reveals dynamics in materials. The analysis of dynamical lineshapes complements the more common observables of dynamical peak shifts and intensity changes. This approach is particularly fertile for 2D spectroscopy, where the linewidths along all three dimensions are not entirely independent. Chapter 2 was necessary to introduce the advanced tools necessary to the dissection of 2D spectra, as well as the modeling of lineshapes. This chapter is rather long and comprehensive, hopefully it can be built upon by future generation of students in the Kambhampati group. Experimental aspects of 2DE were covered in chap 3, with an emphasis on modern pulse measurement methods. These methods were instrumental in enabling the use of the HCF for 2D spectroscopy, detailed in chapter 4. Indeed, pulse bandwidth is one of the main obstacles stifling the growth of 2DE as a method of general use.

Equipped with the theory and 2DE apparatus, it was then possible to submit CdSe NCs to an increased level of scrutiny. Chapter 5 exemplifies this. The oscillatory components of the 2D spectra are extracted and found to be in reasonable agreement with a simple model of coupling to the LO phonon. The main scientific contribution of this chapter comes from the realization that the dephasing time along t_2 is not independent of the linewidth of the linear spectrum. The absence of an observable electronic coherence motivated the search for a theoretical description beyond the EMA. The ability of 2DE to discriminate between a hierarchy of theories is a testament to the power of this approach. This chapter is perhaps the strongest contribution in this thesis, bringing together elements from all the preceding chapters. The analysis of coherent lineshape dynamics in other materials will surely yield similar insights.

The understanding of the electronic properties of materials can hardly be derived from 2DE alone. Indeed, 2DE is still a challenging experiment with its host of constraints — among them a difficult interpretation and a limited audience. The work on CdSe presented in this thesis could build upon more than a decade of TA work. The synergistic integration of 2DE with other experiments can provide a smoother path into the unknown. To this end, a streak camera was installed and used to study samples of dual emitting NCs in chapter 6. Concurrent dynamics of the linewidth and peak position on the timescale of 100 ns suggested the occurrence of multiple overlapping PL bands.

The thesis covered most work done during the installation of a new spectroscopy lab. The lab is merely a foundation for future students to build on. This can be provided both by experimental improvements such as ratiometry as well as by the design of new experiments. For example, fluence and temperature dependence studies are commonly undertaken in either TA, PL and tPL in order to gather detailed insight.

7.1 Outlook: biexciton revisited

As a demonstration of possible future research, the study of the biexciton by TA, tPL and 2DE can be undertaken. Preliminary results of 2D and tPL are presented

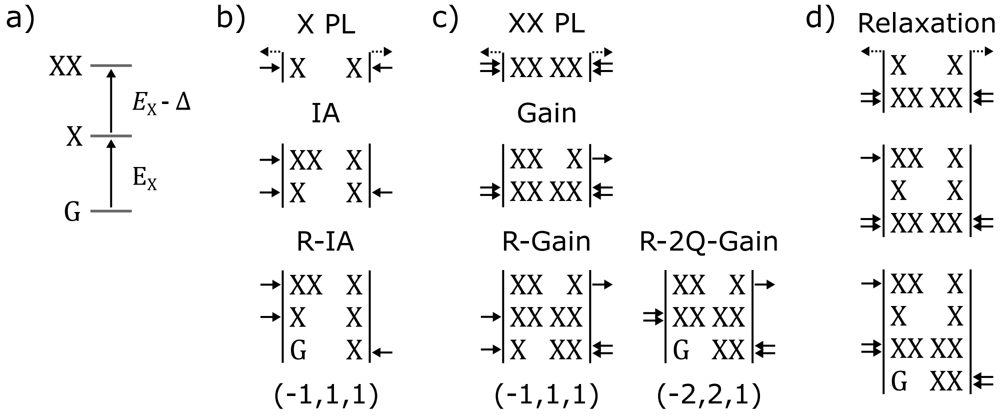

Figure 7.1: DSFD for the bandedge exciton and biexciton in CdSe. (a) Minimal energy level diagram. Δ is the biexciton binding energy. (b) Example DSFD for third order processes for tPL, TA and 2DE. (c) Example DSFD for fifth order processes. The 2Q spectrum can be obtained by phase cycling. (d) Relaxation restores the third order signal for all techniques.

here. The band edge biexciton of CdSe NCs has been the subject of extensive study by our group and others. Despite this, determination of the binding energy of the biexciton has proved elusive. We can now try to study the biexciton by all three techniques. Example DSFD corresponding to tPL, TA and 2DE are shown on Fig 7.1, for third and fifth order signals. In the case of tPL, an increase to higher pump fluence allows the observation of direct emission from the biexciton via a fifth order process [1].

The tPL spectrum of CdSe NCs (620 nm BE absorption) are shown on Fig 7.2, for two values of the pump energy. The long-time behavior is identical in both cases. Rescaling by this long-time value allows subtraction of the traces, yielding a differential tPL trace. This differential trace isolates the higher order contributions. In both cases, the pump power is so strong as to yield large biexciton signals. The dynamics are rather rich, with likely contribution from exciton cooling, Auger annihilation, etc. Still, the early IRF limited trace can be selected and analyzed separately. The

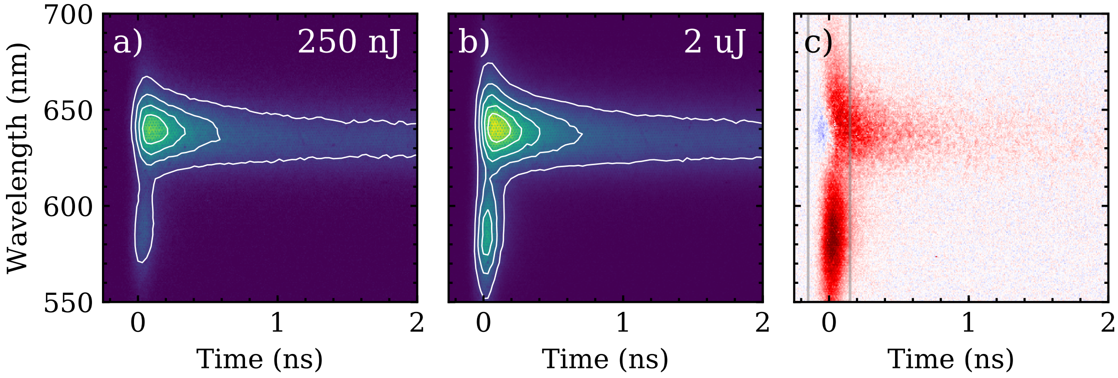

Figure 7.2: Streak traces allow the observation of the biexciton. (a) Streak trace for lower power. Biexcitons are visible as a transient shoulder to the red edge. IRF limited PL from hot excitons is also visible around 585 nm. (b) Streak trace at higher power. XX and MX are more prevalent. (c) Subtraction of the previous traces, isolating the high-fluence contribution.

early time differential spectrum, integrated for t going from -0.2 to 0.2 is shown on Fig 7.3 and compared to the single exciton PL, obtained from late time data. The difference between the peaks is 56 meV.

Two signatures of the biexciton can be observed by TA. At low fluence, the 3rd order TA signal shows an induced absorption feature redshifted from the band-edge peak [2, 3]. At high fluence, stimulated emission from the biexciton can give rise to gain in CdSe and related structures [4]. Analogues to all the TA signals can be observed by 2DE. The third order IA feature has already been subject to analysis, leveraging the increased resolution of 2DE [5]. The high fluence case is unexplored however. The DSFD for the fifth order signals are illustrated on Fig 7.1c. In particular, two interactions with the first pulse can give rise to 2Q coherences during t_1 with coherence transfer vector $(-2, 2, 1)$. The use of a $4 \times 1 \times 1$ phase cycling scheme allows the simultaneous acquisition of both the 2Q and 1Q signals. Following the description of chapter 2, this phase cycle consists in the following phases for the first pulse: $0, \pi/2, \pi, 3\pi/2$. The weights allowing the isolation of both signals

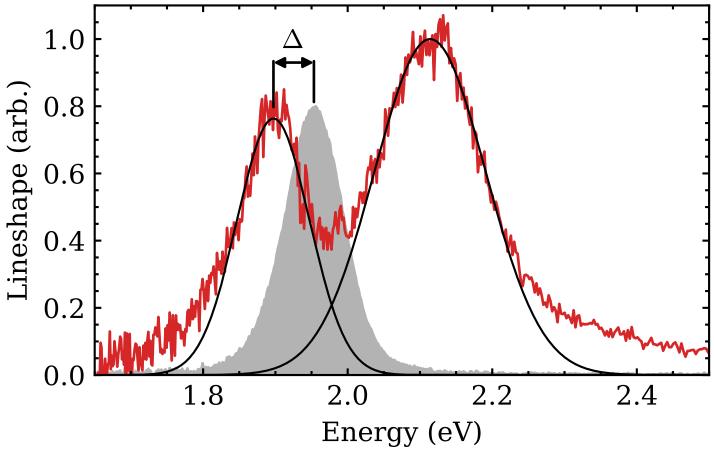

Figure 7.3: Early-time biexciton PL (red) vs single exciton PL (gray). Peak energy difference Δ=56 meV.

Table 7–1: Phase cycle for the acquisition of 1Q and 2Q signals. The phases of the pulses are $0, \pi/2, \pi, 3\pi/2$.

Signal type	Phase matching vectors	Weights	Rotation frame
1Q	$(-1,1,1)$, $(1,-1,1)$	$1,-i,-1,i$	ω_{frame}
2Q	$(-2,2,1)$, $(2,-2,1)$	$1,-1,1,-1$	$2\omega_{\text{frame}}$

are shown on table 7–1. The 2Q signals oscillate with approx. twice the frequency of the regular 2D signal, a finer acquisition grid must be used along t_1 to prevent aliasing of the signal. The resulting 2D spectra are shown on Fig 7.4 for a sample of CdSe NCs (640nm BE absorption).

There is a lot to be analyzed even in that limited dataset. At late time, the relaxation to the single exciton should dominate as the detected species should be mostly X_1. The detected spectrum should be very similar in both cases, and more information is contained in the lineshape along E_1. A simple analysis is reported comparing the 1Q signal at low power, corresponding to single photon absorption, to the high power 2Q signal, corresponding to two-photon absorption. The spectra integrated for E_3 between 1.92 and 1.96 eV are shown on Fig 7.5. Such slices are referred

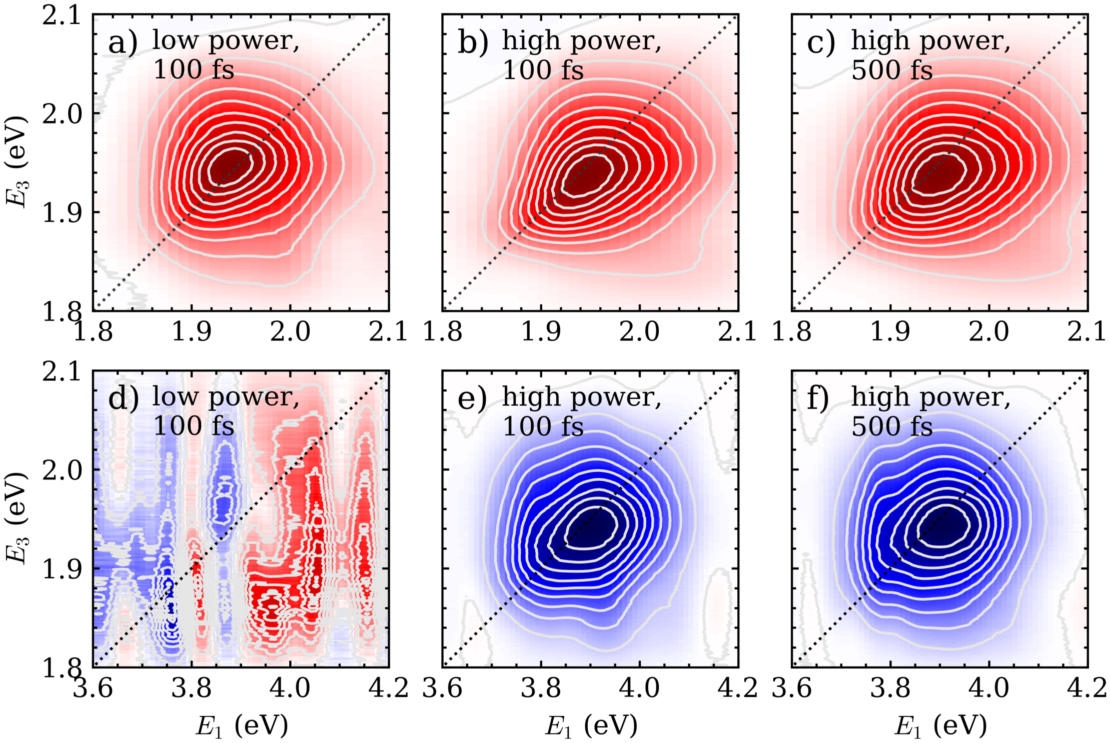

Figure 7.4: 1Q (top) and 2Q (bottom) 2D spectra. (a) Early time, low pump power, 2D spectrum. (b) Early time, high pump power spectrum. Elongation along the diagonal can be indicative of XX. (c) Late time, high power 2D spectrum. Relaxation is noticeable. (d) 2Q signal is absent at low power. (e) The early time 2Q signal. (f) Late-time 2Q signal.

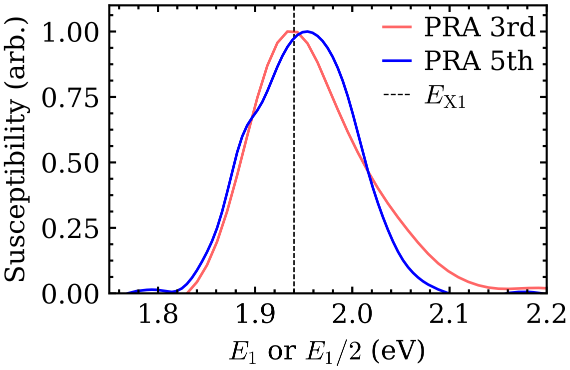

Figure 7.5: Absorption lineshapes for X vs XX. The energy axis has been divided by two for the 2Q spectrum. Vertical line indicates the position of the band-edge absorption obtained from the linear spectrum.

to as pump-resolved absorption spectra (PRA). This reveals the susceptibility as a function of pump wavelength, a form of action spectrum. Two things can be noticed: the 2Q exhibits a shoulder redshifted from the linear absorption peak, which seems to correspond to absorption into XX. Furthermore, the peak of the 2Q spectrum is blue shifted with respect to the 1Q signal, which can be due mixed X_1X_2 biexcitons. This is apparent on the corresponding 2D spectrum on Fig 7.4f. There is likely a spectrum of biexciton states, arising from both the exciton fine structure and mixed biexcitons. This preliminary data suggests the biexciton absorption spectrum can be obtained directly using a 2D instrument in the pump-probe geometry.

The detailed comparison of spectroscopy data acquired in both absorption and emission, using time resolution spanning a continuous range range from a few fs to μs is a powerful tool to unravel processes in materials. The application of this toolkit to the model system of CdSe NCs allows unprecedented observations, despite decades of investigations. One might hope that their timely application to systems of modern interest will be similarly enlightening.

References

1. Achermann, M., Hollingsworth, J. A. & Klimov, V. I. Multiexcitons confined within a subexcitonic volume: Spectroscopic and dynamical signatures of neutral and charged biexcitons in ultrasmall semiconductor nanocrystals. *Physical Review B - Condensed Matter and Materials Physics* **68,** 1–5 (2003).
2. Zhang, C., Do, T. N., Ong, X., Chan, Y. & Tan, H.-S. Understanding the features in the ultrafast transient absorption spectra of CdSe quantum dots. *Chemical Physics* **481,** 157–164 (Dec. 2016).
3. Sewall, S. L., Franceschetti, A., Cooney, R. R., Zunger, A. & Kambhampati, P. Direct observation of the structure of band-edge biexcitons in colloidal semiconductor CdSe quantum dots. *Physical Review B - Condensed Matter and Materials Physics* **80,** 1–4 (2009).
4. Walsh, B. R. *et al.* Interfacial Electronic Structure in Graded Shell Nanocrystals Dictates Their Performance for Optical Gain. *Journal of Physical Chemistry C* **120,** 19409–19415 (2016).
5. Seiler, H., Palato, S. & Kambhampati, P. Investigating exciton structure and dynamics in colloidal CdSe quantum dots with two-dimensional electronic spectroscopy. *The Journal of Chemical Physics* **149,** 074702 (Aug. 2018).